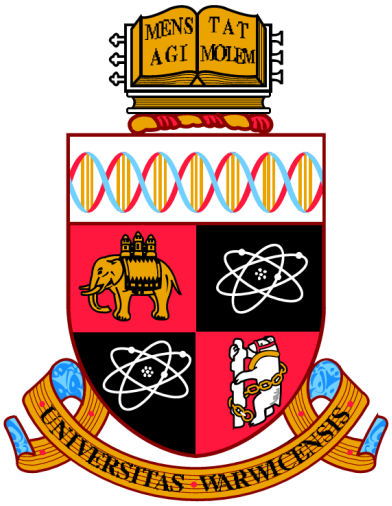

Investigating proteins that regulate the architecture of the plant Endoplasmic Reticulum

by

Natasha Ruth Iadzia Dzimitrowicz

A thesis submitted in partial fulfilment of the requirements for the degree of:

Doctor of Philosophy

University of Warwick
School of Life Sciences

February 2018

Contents

List of Figures

List of Tables

0.1 Acknowledgements

I would like to thank my supervisor, Prof. Lorenzo Frigerio for his guidance through this project. I would also like to thank past and present members of the C46 lab: Sarah Smith, Charlotte Carol, Rachel Clewes, Misti-Ann Feeney. Particular thanks goes to Emily Breeze, as without her support this may not have happened. Emily is also the "Queen of Cloning", and helped me in cloning the protein interactors, a rather crucial aspect of this project.

I would like to thank Prof. Stanley W. Botchway, who helped me with FRET-FLIM experiments and analysis at the Central Laser Facility at the Rutherford Appleton Laboratory, Harwell Oxford.

I would of course like to thank my friends and family for their encouragement during this project! Finally, I would like to very dearly thank Arron Maytum, who has provided constant support and encouragement during this journey.

0.2 Declaration

This thesis is presented in accordance with the regulations for the degree of Doctor of Philosophy. It has been composed by myself, under the supervision of Dr Lorenzo Frigerio, and has not been submitted in any previous application for any degree. All of the work in this thesis has been undertaken by myself except where otherwise stated. All sources of information have been acknowledged by means of a reference. The research was funded by a BBSRC Doctoral Training Grant through the Midlands Integrative Bioscience Training Partnership (MIBTP).

Some of this work presented in this thesis will be published in the following book:

Dzimitrowicz, N., Breeze, E., and Frigerio, L. (Dec 2017). *Long-term imaging of ER morphology in embryos during seed germination,* volume 1691 of *Methods in Molecular Biology*, **The Plant Endoplasmic Reticulum, Methods and Protocols**, Chapter 14. Humana Press. Springer.

0.3 Abstract

The plant endoplasmic reticulum (ER), a highly dynamic membrane-bound organelle, is not only the site of secretory protein production and lipid synthesis, but also responsible for calcium storage. It is currently hypothesised that the shape of the ER network relates to these functions. The sheets, large flat areas of network are proposed to be the sites of protein production and the tubules, thin, highly-mobile and interconnected, the regions of lipid production and calcium storage.

The reticulon protein family has been shown to bend the ER lipid bilayer to form tubules and the edges of sheets. Identifying protein interactors to reticulons may help to understand how the morphology of the ER is controlled or influenced. Mass spectrometry and co-immunoprecipitation techniques were used to identify protein interactors to the *Arabidopsis thaliana* seed-specific reticulon, RTN13. Five non-reticulon proteins were found to interact with RTN13 in developing *A. thaliana* seed; GTP-binding protein 2, lysophospholipase 1, NADH: Cytochrome B5 Reductase 1, sterol methyltransferase 2 and synaptotagmin a. Microscopy analysis of the ER in over-expression lines and T-DNA insertions lines for each putative interactor, showed that only sterol methyltransferase 2 and synaptotagmin a influenced the ER morphology.

Additionally, the morphology of the ER was analysed during seed development and germination through confocal microscopy. An image analysis macro was used to determine the percentage of sheet morphology in the network. Significant changes in the amount of sheet morphology were recorded in the ER of cotyledon cells during seed development and over the first six days of germination. Wild type embryos were also compared to mutants known to have altered ER morphology. The analysis suggested that the amount of sheet morphology is maximal at times of maximum protein production, highlighting the link between ER form and function.

0.4 Abbreviations

℃	Degrees celsius
3AT	3-Amino-1,2,4-triazole
APS	Ammonium persulphate
amiRNA	Artificial Micro RNA
BiFC	Bimolecular fluorescence complementation
BME	beta-mercaptoethanol
CBR1	NADH: Cytochrome b5 reductase
cDNA	Complementary DNA
Col-0	Wild type *A. thaliana* columbia, strain Col-0
COPI/II	COat Protein complex I / II
DMF	Dimethylformamide
DMSO	Dimethyl sulfoxide
DNA	Deoxyribonucleic acid
DTT	Dithiothreitol
ECL	Electrochemiluminescence
EDTA	Ethylenediaminetetraacetic acid
ER	Endoplasmic reticulum
FLAG	a short, hydrophilic 8-amino acid peptide (Asp-Tyr-Lys-Asp-Asp-Asp-Asp-Lys)
g/mg/μg	Gram / milligram / microgram
GB2	*A.thaliana* GTP-binding protein (Also known as AtRab2C/AtRabB1b)
GFP	Green fluorescent protein
GTP	Guanosine-5'-triphosphate
HA	Human influenza hemagglutinin
HDEL	Four letter amino acid code (His-Asp-Glu-Leu)
HRP	Horseradish Peroxidase
KCl	Potassium chloride
l/ml/μl	Litre / millilitre / microlitre
LB Broth	Luria-Bertani broth
LPL	Lysophospholipase (also known as CSE, Caffeoyl shikimate esterase)

mAmp	Milliamps
MgSO4	Magnesium Sulphate
MS salts	Murashige and Skoog Basal salt mixture
MS0	Murashige and Skoog Basal salt mixturewith 0g/l sucrose
NaCl	Sodium chloride
NP-40	Nonylphenoxypolyethoxylethanol
PCR	Polymerase chain reaction
PM	Plasma membrane
PVDF	Polyvinyl
RFP	Red fluorescent protein
RHD3	Root hair defective 3 protein (atlastin homologue)
RL2	RHD3 like 2 protein (Seed specific atlastin homologue)
RNA	Ribonucleic acid
rpm	rotations per minute
RTN	Reticulon
SD	Synthetic defined
SD-Leu-Trp-His	Synthetic defined medium excluding leucine, tryptophan, histidine
SDS	Sodium dodecyl sulfate
SDS-PAGE	Sodium dodecyl sulfate polyacrylamide gel electrophoresis
SMT2	Sterol methyltransferase
SOC medium	Super Optimal Catabolite medium
ssDNA	Salmon sperm DNA
SYTa	Synaptotagmin a
TAE	Tris base, acetic acid and EDTA medium
TBST	Tris-buffered saline with Tween
TEMED	Tetramethylethylenediamine
Tris	Tris(hydroxymethyl)aminomethane
VAPs	VAMP-associated protein
VAMP	Vesicle-associated membrane protein
Y2H	Yeast-two-hybrid
YFP	Yellow fluorescent protein

Materials and Methods

0.5 Suppliers and materials

3M	Microporus tape
Bayer	Intercept™
BD Plastipak	1ml Syringe
BDH	NP-40
Becton Dickinson	0.5mm Microfine Insulin needles
Bemis	Parafilm
Bioline	Accuzyme
Biorad	Electrophoresis chamber
BioSpec, Thistle labs	3.2mm metal grinding beads
Biotium	GelRed™
Chromotek	GFP-Trap®_A, RFP-Trap®_A, Anti-RFP [6G6]
Desch Plant Pak	Plant trays / pots
Expedeon	InstantBlue™
Fisher	Aluminium foil, calcium chloride, DMF, DMSO, EDTA, glass slide (1 - 1.2mm), hydrochloric acid, isopropanol, lithium acetate, magnesium sulphate, $Na_2HPO_4 \bullet 12H_2O$, $NaH_2PO_4 \bullet H_2O$, potassium chloride, Tween-20
Fuji	Medical X-ray film
GE Healthcare	Filter paper, ImageQuant™ LAS 4000
Geneflow	Protogel (30% (w/v) acrylamide/methylene bisacrylamide solution (37.5:1 ratio))
Grace Biolabs	CoverWell™ Imaging chamber (1x20mm)
Hybond-N+	Nylon membrane
Implen	Nanodrop spectrophotometer
Invitrogen	1Kb+ DNA ladder, BP Clonase®, LR Clonase® II, Zeocin™
Levington	Compost
Loveland	Silwet-L77

Melford	LB Broth, Low salt LB broth
Menzel - Glaser	1.5 Cover slip (22x22mm)
Miltenyi Biotec	Anti-GFP-HRP
Nalgene	250ml Centrifuge bottles
New England Biolabs	Broad range pre-stained protein ladders (♯P7706 and ♯P7712s)
Panasonic	Plant growth chamber
Promega	Anti-mouse-HRP, anti-rabbit-HRP, ECL, RQ1 RNase-free DNase, sequencing grade Trypsin
Qiagen	RNeasy® Plant Mini Kit, QIAquick® PCR purification kit
Roche	C0mplete™ protease inhibitor
Retsch	Mixer Mill tissue grinder
Sigma Aldrich	3AT, acetosyringone, adenine, agarose, ammonium bicarbonate, anti-HA, anti-FLAG, APS, BME, calcium chloride, cDNA Ready Script, DTT, Extract-N-Amp™, glucose, iodoacetamine, lithium acetate, magnesium sulphate, MS salts, Nile red, orange g, peptone, primers, ReadyScript® cDNA synthesis kit, SD -Leu -Trp, SD -Leu -Trp -His, SDS, sodium chloride, ssDNA, sucrose, tris, tryptone
SLS	Bacto-Agar
Starstedt	50ml centrifuge tubes, microcentrifuge tubes, petri-dishes
Stratech Scientific	Rhodamine B
Tesco	Cling film, Marvel milk powder
Thermo Scientific	GeneJet plasmid mini-prep kit, Protein A, PVDF
UVP	BioDoc-IT^2® imager
VWR chemicals	Acetic acid, adenine, bromophenol blue, ethanol, glycerol, glycine, methanol, sodium hypochlorate, TEMED, yeast extract
Whatmann	Lens tissue

0.6 Vector list

BiFP 1 Gateway® destination vector in which the N-terminal half of e-YFP is fused to the C-terminus of the protein, as encoded by the gene of interest. Contains spectinomycin resistance for bacterial selection.

BiFP 2 Gateway® destination vector in which the N-terminal half of e-YFP is fused to the N-terminus of the protein, as encoded by the gene of interest. Contains spectinomycin resistance for bacterial selection.

BiFP 3 Gateway® destination vector in which the C-terminal half of e-YFP is fused to the N-terminus of the protein, as encoded by the gene of interest. Contains spectinomycin resistance for bacterial selection.

BiFP 4 Gateway® destination vector in which the C-terminal half of e-YFP is fused to the C-terminus of the protein, as encoded by the gene of interest. Contains spectinomycin resistance for bacterial selection.

pBin61 - P19 A pBin61 vector containing the RNA-silencing inhibitor protein, the tomato bushy stunt virus protein P19, under a 35s promoter (Voinnet et al., 2003; Bendahmane et al., 2000). Contains kanamycin resistance for bacterial selection.

pDest™22 Gateway® destination vector in which the Gal4 activation domain is fused to the N-terminus of the protein, as encoded by the gene of interest. Contains ampicillin resistance for bacterial selection.

pDest™32 Gateway® destination vector in which the Gal4 binding domain is fused to the N-terminus of the protein, as encoded by the gene of interest. Contains ampicillin resistance for bacterial selection.

pDonr™Zeo Gateway® entry vector containing Zeocin™ resistance for bacterial selection.

pDonr™207 Gateway® entry vector with gentamycin resistance for bacterial selection.

pEarleyGate 201 Gateway® destination vector in which an HA tag is fused to the N-terminus of the protein encoded by the gene of interest. Contains kanamycin resistance for bacterial selection.

pEarleyGate 202 Gateway® destination vector in which a FLAG tag is fused to the N-terminus of the protein encoded, as by the gene of interest. Contains kanamycin resistance for bacterial selection.

pGWB605 Gateway® destination vector in which e-GFP is fused to the C-terminus of the protein, as encoded by the gene of interest. Contains spectinomycin resistance for bacterial selection. Contains Basta® (a non-Selective herbicide) resistance for plant selection.

pGWB606 Gateway® destination vector in which e-GFP is fused to the N-terminus of the protein, as encoded by the gene of interest. Contains spectinomycin resistance for bacterial selection. Contains Basta® (a non-Selective herbicide) resistance for plant selection.

pGWB654 Gateway® destination vector in which RFP is fused to the C-terminus of the protein, as encoded by the gene of interest. Contains spectinomycin resistance for bacterial selection. Contains Basta® (a non-Selective herbicide) resistance for plant selection.

pGWB655 Gateway® destination vector in which RFP is fused to the N-terminus of the protein, as encoded by the gene of interest. Contains spectinomycin resistance for bacterial selection. Contains Basta® (a non-Selective herbicide) resistance for plant selection.

pVKH A plant binary vector in which e-YFP is fused to the N-terminus of the protein, as encoded by the gene of interest. Contains kanamycin resistance for bacterial selection. Contains hygromycin resistance for plant selection. Based on the pVKH18En6 series.

0.7 Primer lists

Primer Name	Primer Sequence (5' - 3')	Plasmid / Gene name	Intended Use
General Primers			
attB1 adapter	GGGGACAAGTTTGTACAAAAAAGCAGGCT	attB1 extention	To extend the half attB1 site
attB2 adapter	GGGGACCACTTTGTACAAGAAAGCTGGGT	attB2 extention	To extend the half attB2 site
Pre - attB1 F	CCATCCATACAACAAGTTTG	pDonr Zeo/207	Sequencing attB1 site and start of gene
Post - attB2 R	CCACCACCAACCACTTTG	pDonr Zeo/207	Sequencing attB2 site and end of gene
M13 F	GTAAAACGACGGCCAG	M13 sequence	Sequencing from froward M13 site
M13 R	CCAGGAAACAGCTATGAC	M13 sequence	Sequencing from reverse M13 site
pDONR207 F	GCCTGGCAGTTCCCTACTCTCGC	pDONR207	Sequencing gene of interest in pDONR207
pDONR207 R	GGGCCAGAGCTGCAGCTGGATGG	pDONR207	Sequencing gene of interest in pDONR207
35s Primer F	AGTGGAAAAGGAAGGTGGCT	35s Sequence	Sequencing froward from 35S site
35s Primer R	AAGGGTCTTGCGAAGGATAG	35S Sequence	Sequencing reverse from 35S site
YFP 5' Primer F	CTGGTCGAGCTGGACGGCGACG	5' end of YFP	Sequencing froward from eYFP
YFP 5' Primer R	CGTCGCCGTCCAGCTCGACCAG	5' end of YFP	Sequencing reverse from eYFP
BiFP1 Yn-YFP	GAACTTCAGGGTCAGCTTGC	eYFP in BiFP 1	Sequencing reverse from N-terminus eYFP
BiFP2 Yn-YFP	GACGACGGCAACTACAAGAC	eYFP in BiFP 2	Sequencing forward from N-terminus eYFP
BiFP3 Yc-YFP	GACAACCACTACCTGAGCTAC	eYFP in BiFP 3	Sequencing forward from C-terminus eYFP
BiFP4 Yc-YFP	GTAGCTCAGGTAGTGGTTGTC	eYFP in BiFP 4	Sequencing reverse from C-terminus eYFP
attB primers			
RL2 attb1 For	**GGGGACAAGTTTGTACAAAAAAGCAGGCT** ATGGGGGAAAACGATGATGG	RL2	Attach attB1 site to RL2
RL2 attB2 Rev	**GGGGACCACTTTGTACAAGAAAGCTGGGTGG** ATACATTTGTGAGATTTCTG	RL2	Attach attB2 site to RL2
RTN13 attB1 For	**GGGGACAAGTTTGTACAAAAAAGCAGGCT** ATGGCCAACGACGTGACCAAAG	RTN13	Attach attB1 site to RTN13
RTN13 attB2 Rev	**GGGGACCACTTTGTACAAGAAAGCTGGGTGG** ATACTCTGATTTTTTCACTTTC	RTN13	Attach attB2 site to RTN13
RTN13 attb Rev no stop	**CAAGAAAGCTGGGTC** GTACTCTGATTTTTTCACTTTCTCTTC	RTN13	Attach attB2 site to RTN13 with no stop codon
RTN1 attb For	**AAAAAAGCAGGCTTC** ATGGCGGAAGAACATAAGCATGATG	RTN1	Attach attB1 site to RTN1
RTN1 attb Rev	**CAAGAAAGCTGGGTC** CTAATCTTTCTTCTTGTTCTTCAACG	RTN1	Attach attB2 site to RTN1
RTN1 attb Rev no stop	**CAAGAAAGCTGGGTC** GTAATCTTTCTTCTTGTTCTTCAACG	RTN1	Attach attB2 site to RTN1 with no stop codon
RTN4 attb For	**AAAAAAGCAGGCTTC** ATGGTGGAAGACCACAAGCACGAGG	RTN4	Attach attB1 site to RTN4
RTN4 attb Rev	**CAAGAAAGCTGGGTC** TTAATCCTTCTTCTTGTTCAGAGCTC	RTN4	Attach attB2 site to RTN4
RTN4 attb Rev no stop	**CAAGAAAGCTGGGTC** GTAATCCTTCTTCTTGTTCAGAGCTC	RTN4	Attach attB2 site to RTN4 with no stop codon
RTN5 attb For	**AAAAAAGCAGGCTTC** ATGGCGGAAGAAATTGAAAAATCTGTGC	RTN5	Attach attB1 site to RTN5
RTN5 attb Rev	**CAAGAAAGCTGGGTC** TTAACCCAATTTTGCCTTTGCCTTG	RTN5	Attach attB2 site to RTN5

Table 1: ***Primer list one.*** *List of primers used in this project, the sequence, which plasmid or gene they were used for and what the intended use of the primer was. Letters in bold highlight the non-specific, attB sequence.*

Primer Name	Primer Sequence (5' - 3')	Plasmid / Gene name	Intended Use
attB Primers continued			
RTN5 attb Rev no stop	**CAAGAAAGCTGGGTC** GTAACCCAATTTTGCCTTTGCCTTG	RTN5	Attach attB2 site to RTN5 with no stop codon
For - SMT2 attb	**AAAAAGCAGGCTTC** ATGGACTCTTTAACACTCTTCTTCACCGGT	SMT2	Attach attB1 site to SMT2
Rev - SMT2 attb	**AGAAAGCTGGGTC** AGAACTCTCCTCCGGTGACTCCGG	SMT2	Attach attB2 site to SMT2
For - FAH1 attb	**AAAAAGCAGGCTTC** ATGGAGTCTTCTATATCACAAACACTAAGC	FAH1	Attach attB1 site to FAH1
Rev - FAH1 attb	**AGAAAGCTGGGTC** AAGAGCACAGATGAGGCGCGTGG	FAH1	Attach attB2 site to FAH1
For - SYTa attb	**AAAAAGCAGGCTTC** ATGGGCTTTTTCAGTACGATACTAGGATTT	SYTa	Attach attB1 site to SYTa
Rev - SYTa attb	**AGAAAGCTGGGTC** AGAGGCAGTTCGCCACTCG	SYTa	Attach attB2 site to SYTa
For - Endo 70 attb	**AAAAAGCAGGCTTC** ATGGAGTTTTATAGAAGTTCTAGAAG	Endo 70	Attach attB1 site to Endo70
Rev - Endo 70 attb	**AGAAAGCTGGGTC** ATCGATCTTTACCGAGGAATAGATGAG	Endo 70	Attach attB2 site to Endo70
For - GB2 attb	**AAAAAGCAGGCTTC** ATGTCTTACGATTATCTCTTCAAGTACATAATC	GB2	Attach attB1 site to GB2
Rev - GB2 attb	**AGAAAGCTGGGTC** ACCACAACAGCCACCTCCCTG	GB2	Attach attB2 site to GB2
For - CBR1 attb	**AAAAAGCAGGCTTC** ATGGATACCGAGTTTCTCCGAACCCTAGAT	CBR1	Attach attB1 site to CBR1
Rev - CBR1 attb	**AGAAAGCTGGGTC** GAACTGGAATTGCATCTCCGGAGAG	CBR2	Attach attB2 site to CBR1
For - LPL2 attb	**AAAAAGCAGGCTTC** ATGCCGTCGGAAGCGGAGA	LPL2	Attach attB1 site to LPL2
Rev - LPL2 attb	**AGAAAGCTGGGTC** AGCGGTTTTAGATCCATACTTCTTAAC	LPL2	Attach attB2 site to LPL2
T-DNA Primers			
SALK LBb1.3	ATTTTGCCGATTTCGGAAC	SALK insertion	Border Primer for SALK
SAIL LB1	GCCTTTTCAGAAATGGATAAATAGCCTTGCTTCC	SAIL insertion	Border Primer for SAIL
SAIL LB2	GCTTCCTATTATATCTTCCCAAATTACCAATACA	SAIL insertion	Border Primer for SAIL
SAIL LB3	TAGCATCTGAATTTCATAACCAATCTCGATACAC	SAIL insertion	Border Primer for SAIL
GABI o8409	ATATTGACCATCATACTCATTGC	GK insertion	Border Primer for GK
GABI_205 E02 Left	GGAGTTTCGAGAACCCTATCG	SYTa	Left primer for GABI_205 E02 T-DNA insertion line
GABI_205 E02 Right	AACGATCAAGCGTGGACATAG	SYTa	Right primer for GABI_205 E02 T-DNA insertion line
GABI_368 D11 Left	CAAGTCAAATCGACGATACGG	LPL	"Left primer for GABI_368 D11 T-DNA insertion line"
GABI_368 D11 Right	ATGGTGAAATCAAAGGCACTG	LPL	"Right primer for GABI_368 D11 T-DNA insertion line"
GABI_371 A08 Left	TTGCGGATACATCTATTTGGC	CB5R	"Left primer for GABI_371 A08 T-DNA insertion line"
GABI_371 A08 Right	ATACCCTCATTTTAATGGCGG	CB5R	"Right primer for GABI_371 A08 T-DNA insertion line"
GABI_399 A09 Left	TTTCTTTCTACATCTCGCCCC	SMT2	"Left primer for GABI_399 A09 T-DNA insertion line"
GABI_399 A09 Right	GGCTTGCTTATTGGAGGAATC	SMT2	"Right primer for GABI_399 A09 T-DNA insertion line"

Table 2: ***Primer list two.*** *List of primers used in this project, the sequence, which plasmid or gene they were used for and what the intended use of the primer was. Letters in bold highlight the non-specific, attB sequence.*

Primer Name	Primer Sequence (5' - 3')	Plasmid / Gene name	Intended Use
T-DNA primers continued			
GABI_443 F03 Left	AGTGTGAGTTGGCCAAAATTG	SMT2	Left primer for GABI_443 F03 T-DNA insertion line
GABI_443 F03 Right	TCGTGTGTGGTAACTTCCTCC	SMT2	Right primer for GABI_443 F03 T-DNA insertion line
SAIL_252 E05 Left	AATGCTGGTTTGAACATACGG	SMT2	Left primer for SAIL_252 E05 T-DNA insertion line
SAIL_252 E05 Right	TTTTGACCAGGTTTGACTTGG	SMT2	Right primer for SAIL_252 E05 T-DNA insertion line
SAIL_775 A08 Left	AGGTCTCGCGATTTATTAGGG	SYTa	Left primer for SAIL_775 A08 T-DNA insertion line
SAIL_775 A08 Right	GCCTCCTGACAAGTATAGGGG	SYTa	Right primer for SAIL_775 A08 T-DNA insertion line
SALK_008202C Left	TGTAAAGACTCCGACCACCAC	LPL	Left primer for SALK_008202C T-DNA insertion line
SALK_008202C Right	CAACAGTTGGGTTGACAAAGG	LPL	Right primer for SALK_008202C T-DNA insertion line
SALK_009878C Left	CGCACCAACTCTCTACTGACC	LPL	Left primer for SALK_009878C T-DNA insertion line
SALK_009878C Right	TAAACGAACCCATGTAGCAGC	LPL	Right primer for SALK_009878C T-DNA insertion line
SALK_083103 Left	TTTAACCACAACAGCCACCTC	ATGB2	Left primer for SALK_083103 T-DNA insertion line
SALK_083103 Right	AGTTCACCAGTGCATTCCTTG	ATGB2	Right primer for SALK_083103 T-DNA insertion line
SALK_088781C Left	GGAGTTTCGAGAACCCTATCG	SYTa	Left primer for SALK_088781C T-DNA insertion line
SALK_088781C Right	AACAAGTCCCAATGAAATCCC	SYTa	Right primer for SALK_088781C T-DNA insertion line
SALK_129950C Left	TGGATCGATTCAAGAAAATGC	RTN5	Left primer for SALK_129950C T-DNA insertion line
SALK_129950C Right	GCACTATCCTGTGGAGCGTAG	RTN5	Right primer for SALK_129950C T-DNA insertion line
SALK_044472 Left	CATGTCCATTCATCAATTGTCC	SMT2	Left primer for SALK_044472 T-DNA insertion line
SALK_044472 Right	CCAATTGGAATTTTGCTTCTTC	SMT2	Right primer for SALK_044472 T-DNA insertion line
SAIL_445 H01 Left	GTTCACTCTTAAATGCACCCG	ATGB2	Left primer for SAIL_445 H01 T-DNA insertion line
SAIL_445 H01 Right	CATACTACAGAGGAGCAGCCG	ATGB2	Right primer for SAIL_445 H01 T-DNA insertion line
SALK_129878 Left	ATGGACGCCTATATGGAGTCC	CB5R	Left primer for SALK_129878 T-DNA insertion line
SALK_129878 Right	AAATAGAGATCGAACCTCTGCG	CB5R	Right primer for SALK_129878 T-DNA insertion line
SAIL_644 A11 Left	GATACCGAGTTTCTCCGAACC	CB5R	Left primer for SAIL_644 A11 T-DNA insertion line
SAIL_644 A11 Right	ACTTGGAACATGGGAGTGATG	CB5R	Right primer for SAIL_644 A11 T-DNA insertion line

Table 3: ***Primer list three.*** *List of primers used in this project, the sequence, which plasmid or gene they were used for and what the intended use of the primer was. .*

0.8 Methods

0.8.1 Growing *A. thaliana*

Two methods of growing *Arabidopsis thaliana* were used during this project.

Growing on soil

Seeds were imbibed for 1 hour in sterile distilled water, then pipetted onto compost containing Intercept™. Pots or trays of soil were covered in foil and incubated at 4℃ for 24-48 hours to break dormancy. The foil was replaced with cling film or a propagator lid and the seeds were then transferred to either a plant growth cabinet or a greenhouse compartment. Plants were grown under long daylight conditions (16 hours) at 21℃. The cling film and propagator lids were removed once plants had 5 or more leaves. The primary stem was removed once bolted to encourage secondary stems, thus increasing the number of flowers and seeds.

Growing on MS0 Agar

Seeds were sterilised using chlorine gas. Microcentrifuge tubes with seeds were left open in a plastic box, containing a beaker of 100ml sodium hypochlorite and 3ml hydrochloric acid. They were left to sterilise for four to six hours. Seeds were then pipetted, using minimal sterile distilled water, onto petri-dishes with MS0 agar (MS salts 4.4g/l, 0.5% agar, pH 5.7) and any necessary antibiotics for selection. Petri dishes were then sealed with microporus tape and placed in a plant growth chamber under long daylight conditions at 21℃. Plants were transferred onto compost with Intercept™ to grow to seed.

Harvesting seed

Once the plant had bolted after the primary stem was removed, the plants were bagged in 'bread bags'. Plants were grown until senescence began to occur, and then watering stopped. The plants were left to dry for two to three weeks, until all the siliques were yellow. The inflorescence was then collected into a paper bag, and the seeds left to dehydrate for a minimum of two weeks. The inflorescences were then threshed using a 500 micron sieve, to collect the seed. Seeds were then stored in a microcentrifuge tube at 4℃.

0.8.2 Growing *N. benthamiana*

Nicotiana Benthamiana seeds were placed in sterile 0.1% agarose and incubated at 4℃ for 24 to 48 hours to break dormancy. The seeds were then pipetted onto F2 and sand compost and covered with cling film until germinated. The plants were grown in a plant growth chamber for 5 weeks under long day conditions at 21℃, then removed and placed on a windowsill at room temperature to promote leaf growth, which enables better and easier infiltration, and delays flowering.

0.8.3 Collecting developing *A. thaliana* seed

A. thaliana plants were grown for approximately 30 days under long-day conditions (20℃ and 16 hour light)

Green siliques were harvested into liquid nitrogen and then transferred into a dry ice-chilled petri dish. The temperature change caused the siliques to pop open. This seed collection method was adapted from (Bates et al., 2013). The method is depicted in figure 1. Seeds were separated through a 500 micron sieve, cooled with liquid nitrogen, then collected in an microcentrifuge tube, and chilled in liquid nitrogen. The seeds were then stored at -80℃.

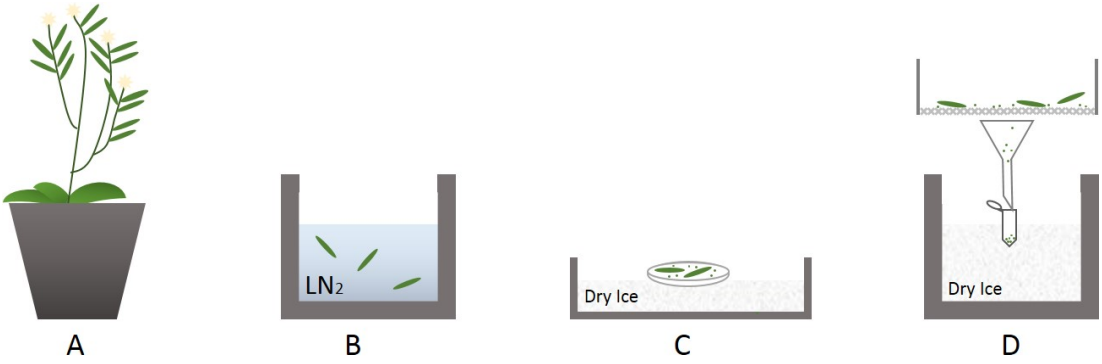

Figure 1: ***Collection of A. thaliana developing seed. A.*** *Green siliques on an Arabidopsis thaliana plant.* ***B.*** *Green siliques are removed from the plant and placed in liquid nitrogen.* ***C.*** *Siliques are then transferred into a petri dish that is chilled on dry ice. The siliques then pop open to release the seeds inside.* ***D.*** *Silique husks and seeds are put into a flash frozen sieve, which lets the seeds through into a chilled microcentrifuge tube.*

0.8.4 Co-immunoprecipiation from stable expression in *A. thaliana* seeds

0.3g of seeds were homogenised with a liquid nitrogen-chilled pestle and mortar, then scraped into pre-chilled microcentrifuge tubes. 1200μl of Lysis buffer [0.5%

NP-40, 10mM Tris pH 7.5, 150mM NaCl, 0.5mM EDTA, with 1 C0mplete™ protease inhibitor tablet per 200ml] was added and the microcentrifuge tubes were rotated for 1 hour at 4℃. The mixture was centrifuged at 14,000rpm for 10 minutes at 4℃ and 50μl of supernatant was taken as 'Homegenate' protein sample. The remaining supernatant was transferred to a pre-cooled microcentrifuge tube.

To equilibrate the GFP-Trap®_A (or RFP-Trap®_A beads as appropriate), 500μl of ice cold Wash buffer [10mM Tris pH 7.5, 150mM NaCl, 0.5mM EDTA] was added to 20μl of the slurry and then centrifuged at 2,000rpm for 2minutes at 4℃, the supernatant was then discarded. This equilibration process was repeated twice.

20μl of equilibrated GFP-Trap®_A beads and 1ml wash buffer was added to the plant supernatant. This mixture was then rotated for 1 hour at 4℃. The solution was then centrifuged at 2,000rpm for 2 minutes at 4℃. A 25μl aliquot of supernatant was taken as 'Unbound' protein sample. The remaining supernatant was discarded and the pellet re-suspended in 500μl of cold Wash buffer. The solution was centrifuged at 2,000rpm for 2 minutes at 4℃ and the supernatant was discarded. This was process was repeated twice.

For SDS-PAGE and western blotting, the pellet was re-suspended in 25μl of 2x Laemmli buffer (0.5M Tris-HCl pH 6.8, 4.4% SDS, 20% glycerol, 0.036% bromophenol blue, 2% BME) and boiled at 95℃ for 10 minutes to release the protein from the GFP-Trap A. It was then centrifuged at 2,000rpm for 2 minutes at 4℃ and the supernatant was loaded onto the gel. This was the 'Bound' protein sample.

For mass spectrometry analysis, all the supernatant was removed after the final wash. Then proceeded as in methods section 1.4.9.

0.8.5 Co-immunoprecipitation from transient expression in *N. benthamiana*

N.Benthamiana was co-infiltrated as outlined in (Sparkes et al., 2006). Infiltrated leaf sections were cut out with ethanol-cleaned scissors and then weighed. 0.25g of leaf material was placed in 2ml microcentrifuge tubes and frozen in liquid nitrogen. Three metal grinding beads were added to each microcentrifuge tube and samples were homogenised using the Mixer Mill tissue grinder for up to 10 minutes at 30 oscillations per second.

GFP/RFP co-immunoprecipitation

Following homogenisation, 1ml of Lysis buffer [0.5% NP-40, 10mM Tris pH 7.5, 150mM NaCl, 0.5mM EDTA with 1 C0mplete™ protease inhibitor tablet per 200ml] was added to each sample. The samples were rotated at 4℃ for 1 hour. To equilibrate the GFP-Trap®_A (or RFP-Trap®_A as appropriate), 500μl of ice cold Wash buffer [10mM Tris pH 7.5, 150mM NaCl, 0.5mM EDTA] was added to 20μl of the slurry and then centrifuged at 2,000rpm for 2 minutes at 4℃, the supernatant was then discarded. This equilibration process was repeated twice. The tissue samples were then centrifuged at 14,000rpm for 10 minutes at 4℃ and 50μl of supernatant was taken as 'Homegenate' protein sample. The remaining supernatant was transferred to a pre-cooled microcentrifuge tube. 20μl of equilibrated GFP/RFP-Trap_A and 500μl of Wash buffer was added to each sample. Tubes were rotated for 2 hours at 4℃. The solution was then centrifuged at 2,000rpm for 2 minutes at 4℃. A 25μl aliquot of supernatant was taken as 'Unbound' protein sample. The remaining supernatant was discarded and the pellet re-suspended in 500μl of cold Wash buffer. The solution was centrifuged at 2,000rpm for 2 minutes at 4℃ and the supernatant was discarded. This wash step was repeated twice.

HA/FLAG co-immunoprecipitation

Following homogenisation, 750μl of Lysis buffer [0.5% NP-40, 10mM Tris pH 7.5, 150mM NaCl, 0.5mM EDTA with 1 C0mplete™ protease inhibitor tablet per 200ml] was added to each sample. The samples were rotated at 4℃ for 1 hour. The tissue samples were centrifuged at 14,000rpm for 10 minutes at 4℃, and 50μl of supernatant was taken as 'Homegenate' protein sample. The remaining supernatant was transferred to a pre-cooled microcentrifuge tube. 8μl of anti-HA antibody was added to each sample. The samples were rotated at 4℃ for 2 hours. To equilibrate the Protein A sepharose, 400μl of Protein A was added to 1ml of cold Wash buffer [10mM Tris pH 7.5, 150mM NaCl, 0.5mM EDTA] and then centrifuged at 2,000rpm for 3 minutes. Supernatant was discarded, and 500μl of cold Wash buffer was then added to the pellet. This was then centrifuged at 2,000rpm for 3 minutes. This wash step was then repeated. 35μl of equilibrated Protein A was added to each sample, and then rotated for 2 hours at 4℃. Samples were centrifuged at 2,000rpm for 3 minutes at 4℃. A 25μl aliquot of supernatant was taken as 'Unbound' protein sample. The remaining supernatant was discarded. 500μl of chilled Wash buffer was added and samples were centrifuged at 2,000rpm for 3 minutes at 4℃. Supernatant was discarded

and this step was repeated four times.

0.8.6 SDS-PAGE

Samples were heated at 95℃ for 10minutes with x2 Laemmli buffer (0.5M Tris-HCl pH 6.8, 4.4% SDS, 20% glycerol, 0.036% bromophenol blue, 2% BME). Samples were then run on 12.5% SDS-PAGE. Protogel was used as an acrylamide source. (Separating gel [15% acrylamide , 375mM Tris/HCL (pH 8.8), 0.1% SDS, 0.05% APS, 0.0005% TEMED]. Stacking gel [4.5% acrylamide, 125mM Tris/HCL (pH 6.8), 0.1% SDS, 0.0003% APS, 0.0015% TEMED]).

40ml gels were run at 8mAmp for 16hours at 4℃. 12ml gels were run at 100 volts for 1 hour at room temperature. Protein bands were visualised with InstantBlue™ stain (hereafter referred to as Coomassie) and washed with distilled water until crisp bands were seen. If the gel was to be used for Western blotting, no Coomassie staining was performed.

0.8.7 Western blotting

Proteins were transferred from SDS-PAGE onto PVDF membrane using a semi-dry blot apparatus. Two sheets of chromatography paper were soaked in transfer buffer [25mM Tris pH 8.3, 192mM glycine, 20% methanol] and placed onto the lower plate. The PDVF membrane was soaked in 100% methanol and then equilibrated in transfer buffer and was then placed on top of the chromatography paper, without air bubbles. The SDS-PAGE was placed on top, along with another sheet of Transfer buffer-soaked chromatography paper. The proteins were transferred under a constant current of 300mA for 40 to 90 minutes depending on the size of the gel.

The PVDF membrane was blocked by gentle shaking in 20ml TBST [50mM Tris/HCL pH 8, 150mM NaCl, 0.05% Tween20] and 5% skimmed milk powder at 4℃ overnight. Blocking solution was removed and membrane was incubated with primary antibody in 20ml TBST with 5% milk for 1 hour shaking at room temperature. The membrane was then washed in 20ml TBST: three short washes, two 10 minute washes, and two additional short washes. If a secondary antibody was required, then the membrane was incubated in 20ml TBST with 5% milk and secondary antibody for 1 hour shaking at room temperature. The wash steps were then repeated as above. The antibody dilutions used are shown in table 4.

Bands were detected with ECL incubation (45 seconds) and visualised either

through developing on medical X-ray film, or using the chemiluminescence detector on the ImageQuant LAS4000 (with 10 to 20 minutes detection time). X-Ray films were developed using an Agfa Curix 60 automatic developer, with conditions and protocols recommended by the manufacturer.

0.8.8 Antibodies

Antibody name	Animal source	Binds to	Dilution
Anti-GFP-HRP	Rabbit, polyclonal	GFP/YFP	1/6,666
Anti-RFP	Mouse, polyclonal	RFP	1/1,000
Anti-mouse-HRP	Goat	Mouse antibody	1/2,500
Anti-HA	Rabbit	HA tag	1/1,000
Anti-FLAG	Mouse	FLAG tag	1/1,000

Table 4: ***Antibodies and dilutions used in western blotting***

0.8.9 Mass spectrometry

For mass spectrometry analysis, the co-immunoprecipitation protocol was performed as in methods section 1.4.5 and after the final wash all supernatant was removed. 45μl of 100mM ammonium bicarbonate and 5μl of 100mM DTT was added to the pellet and incubated at 60℃ for 15 minutes at 500rpm. 5μl of 200mM iodoacetamine was then added and samples were incubated at 25℃ for 30 minutes in the dark.

4μl of sequencing grade trypsin was added and incubated at 37℃ at 500rpm overnight. The sample was then spun through an microcentrifuge tube column for 5 minutes at 16,000g. The samples were analysed by Warwick mass spectrometry facility using the Orbitrap Fusion with UltiMate 3000 RSLCnano System (Thermo Scientific) and processed the data using proteomic software Scaffold 4 (version 4.6.2).

0.8.10 Extraction of genomic DNA

50μg of *A. thaliana* leaf tissue was cut from the plant and placed in a 1.5ml microcentrifuge tube before being flash frozen in liquid nitrogen. Two metal beads were added to tubes and samples were homogenised in a Mixer Mill tissue grinder for 2 minutes at 30 oscillations per second. 400μl of DNA extraction buffer (200M Tris-HCl pH 7.5, 250mM NaCl, 25mM EDTA, 0.5% SDS) was added and tissues were ground for a further 2 minutes. Tubes were centrifuged at

14,000rpm for 1 minute at 4℃ and the supernatant transferred to a sterile 1.5ml microcentrifuge tube. 300μl of isopropanol was added to the supernatant and chilled on ice for 20 minutes. Samples were centrifuged for a further 5 minutes at 14,000rpm at 4℃ to pellet the DNA. Supernatant was discarded and pellets were dried by leaving tube lids open for 5 minutes. Pellets were re-suspended in 50μl of sterile distilled water by gentle shaking. Extracts were stored at 4℃ for up to two days.

0.8.11 Extraction of RNA

To extract RNA from *A. thaliana* the RNeasy® Plant Mini Kit was used according to manufacturers protocol. See here for full product information and protocol:
`https://www.qiagen.com/us/shop/sample-technologies/rna/total-rna/rneasy-plant-`
Up to 100mg of sample is ground in liquid nitrogen and then lysed using the RLT lysis buffer. Samples are centrifuged through a QIAshredder homogenizer. Ethanol is added to the lysate and the sample is then centrifuged through a RNeasy Mini spin column, which binds the RNA. Once contaminants are washed away, the RNA is eluted with RNase-free water.

0.8.12 Reverse transcription PCR

DNase treatment

RNA was treated with RQ1 RNase-free DNase. 4μl of RNA, 1μl of 10x DNase buffer and 1μl of DNase was added to 4μl of sterile distilled water in a 0.2ml microcentrifuge tube. The mixture was incubated at 30℃ for 30 minutes. The reaction was stopped with 1μl of DNase Stop solution. This was then incubated at 65℃ for 10 minutes.

RT-PCR

The ReadyScript™ cDNA Synthesis kit was used according to manufacturers instructions. 4μl of 'Master Mix', 5.5μl of DNase-treated RNA (equating to approximately 2μl of RNA) and 10.5μl sterile distilled water were mixed in a 0.2ml microcentrifuge tube. The PCR cycle was as follows:

Step	Temperature	Time
Activate	25℃	5 minutes
Transcribe	42℃	30 minutes
Deactivate	85℃	5 minutes
Cool	4℃	hold

Table 5: ***Reverse transcription PCR cycles***

0.8.13 Gateway cloning

The full manual for Gateway cloning can be found here at: `https://tools.thermofisher.com/content/sfs/manuals/gatewayman.pdf`

Two step attB PCR

Primers were designed for a two-step attB primer approach. The first primer pair have template specific sequence and a half-attB sequence. The second primer pair are attB adapters. A suitable source, such as genomic DNA or cDNA was used as the DNA template. The products were created through PCR with Accuzyme™. Some of the PCR was run on a 1% agarose gel to confirm presence of bands at the correct size. The remaining PCR mixture was cleaned up with the QIAquick PCR purification kit. The basic two step PCR cycle and components can be seen below. If the basic protocol was unsuccessful, 1% DMSO could be added, or additional magnesium chloride, or an altered concentration of DNA template.

First attB PCR components
0.5μl of left (forward) primer [10μM]
0.5μl of right (reverse) primer [10μM]
0.5μl of mixed source DNA
5μl of Accuzyme™
3.5μl of dH_2O

Step	Temperature	Time	Cycles
Denature	94℃	3 minutes	1
Denature	94℃	15 seconds	11
Anneal	60℃	15 seconds	
Extend	72℃	3 minutes	

Table 6: ***attB PCR step 1 PCR cycle.***

Second attB PCR components

2μl of left primer [10μM]

2μl of right primer [10μM]

10μl of first PCR mix

25μl of Accuzyme™

10.5μl of dH_2O

Step	Temperature	Time	Cycles
Denature	94℃	3 minutes	1
Denature	94℃	15 seconds	5
Anneal	45℃	15 seconds	
Extend	72℃	3 minutes	
Denature	94℃	15 seconds	35
Anneal	52-62℃	15 seconds	
Extend	72℃	3 minutes	
Extend	72℃	5 minutes	1
Cool	4℃	Hold	1

Table 7: ***attB PCR step 2 PCR cycles.***

BP Reactions

150ng of attB-PCR product was added to 1μl of Donor vector (150ng/μl) (such as pDonorZeo or pDonor207) with up to 4μl of TE solution (10mM Tris pH 8.0, 1mM EDTA). BP Clonase™ was thawed on ice for 2 minutes and vortexed briefly. 0.5μl of BP clonase™ was added to each sample. The tubes were incubated at 25℃ for a minimum of 2 hours or overnight in a PCR machine. The entry clones were transformed into *E. coli* DH5α cells and purified, as in methods section 0.8.18.

LR reactions

1μl of entry clone 150ng/μl produced from the BP reaction was mixed with 1μl of destination vector 150ng/μl and 2.5μl of TE buffer (10mM Tris pH 8.0, 1mM EDTA). LR Clonase™ II was thawed on ice for 2 minutes and vortexed briefly. 0.5μl of LR Clonase™ II was added to each sample. The tubes were incubated at 25℃ for a minimum of 2 hours or overnight in a PCR machine. The resulting expression clone is transformed in *E. coli* DH5α cells and purified, as in methods section 0.8.18.

0.8.14 Verification of T-DNA insertion

DNA from *Arabidopsis thaliana* T-DNA insertion lines (using Col-0 as a control) was extracted using the Extract-N-Amp™ plant kit. The DNA was then stored at 4℃ for up to five days. To assess if the plants did possess the T-DNA insert the PCR protocol below was followed (table 8) and then the DNA was visualised on an agarose gel. Two PCRs were done per line, the first with left and right primers, the second with border and right primers.

T-DNA PCR components
0.5μl of left or border primer [10μM]
0.5μl of right primer [10μM]
1μl of DNA
5μl of PCR mix (as provided in the Extract-N-Amp™kit)
3μl of dH_2O

Step	Temperature	Time	Cycles
Denature	94℃	5 minutes	1
Denature Anneal Extend	94℃ 55, 60 or 63℃ 72℃	30 seconds 30 seconds 2 minutes	35
Extend	72℃	7 minutes	1
Cool	4℃	hold	1

Table 8: ***T-DNA verification PCR cycle.***

0.8.15 Visualisation of DNA using agarose gel electrophoresis

Gels were made with 1% agarose in TAE buffer (40 mM Tris, 20 mM acetic acid, 1 mM EDTA, pH 8.0) with 5μl of GelRed™ per 100ml of solution. The agarose solution was then poured into a cast and left to set at room temperature. The gel was placed into an electrophoresis tank and filled with TAE buffer. DNA samples and 1Kb plus DNA ladder were mixed with 5x Orange G loading dye and were added to the gel. The gel was run at constant voltage until the loading dye had reached the end of the gel. To visualise DNA bands the 302nm trans-illuminator on the BioDoc-IT^2® imager was used.

0.8.16 Preparation of competent *E.coli* DH5α cells

Escherichia coli DH5α cells from a glycerol stock (20mM calcium chloride, 10% glycerol) were streaked onto LB agar and incubated at 37℃ overnight. 5ml of LB

was innoculated with an overnight colony and incubated in a shaking incubator overnight at 37℃ at 250rpm. 200μl of this culture was used to innoculate 100ml of LB media, in a 250ml conical flask. Cells were grown, at 37℃ and 250rpm, to an OD600 between 0.3 and 0.4. Culture was then transferred to two pre-chilled 50ml centrifuge tubes and chilled on ice for 30 minutes. The cultures were centrifuged at 3000rpm for 20 minutes at 4℃ and the supernatant was discarded. The tubes were inverted to drain thoroughly. Cells were then re-suspended with 10ml ice-cold 0.1M calcium chloride, and chilled on ice for 10 minutes. The cultures were centrifuged at 3000rpm for 20 minutes at 4℃ and the supernatant was discarded. The tubes were inverted to drain thoroughly. The pellet was then re-suspended in 1ml ice-cold 10% glycerol in 0.1M calcium chloride. Cells were aliquoted in 50μl volumes into 1.5ml tubes and flash frozen in liquid nitrogen, then stored at -80℃.

0.8.17 Preparation of competent *A. tumefaciens* GV3101 cells

5 ml of low salt LB was inoculated with *Agrobacterium tumefaciens* GV3101 cells (in 20mM calcium chloride, 20% glycerol) and incubated overnight at 28℃ shaking at 200rpm. 2ml of this culture was used to inoculate a 100ml culture in a 250ml conical flask. Cells were grown to an OD600 between 0.5 and 1.0. The culture was then chilled on ice for 30 minutes and pelleted at 4000xg for 10 minutes at 4℃. The supernatant was discarded and pellet was gently re-suspended in 2ml of ice cold 20mM calcium chloride. Cells were aliquoted in 200l volumes into 1.5ml microcentrifuge tubes, flash frozen with liquid nitrogen and stored at -80℃.

0.8.18 Transformation of *E.coli* DH5α and DNA extraction

10μl of *E. coli* DH5α in a 1.5ml microcentrifuge tube was placed on ice for 30 minutes. 1-5μl of DNA (150ng/μl) was then added to the cells. The samples were then placed in a 42℃ waterbath for 30 seconds. The microcentrifuge tube was then chilled on ice for 2 minutes. 100μl of SOC medium (2% tryptone, 0.5% yeast extract, 10mM NaCl, 2.5mM KCl, 10mM $MgCl_2$, 10mM $MgS0_2$, 20mM glucose) was added and the samples incubated in a shaker at 37℃ for 1 hour. 100μl was then plated onto LB agar (10g/l tryptone, 5g/l yeast extract, 10g/l NaCl, 1.5%Bacto-Agar) with appropriate antibiotic selection. The plates were sealed with Parafilm and placed in a 37℃ oven overnight. The next day colonies were picked to inoculate 10ml LB (10g/l tryptone, 5g/l yeast extract, 10g/l NaCl), with appropriate antibiotic selection. The cultures were incubated overnight in a

37℃ shaking incubator. The next day the cultures were centrifuged at 4000rpm for 4 minutes at 4℃. Prior to this, 800/μl of culture would be added to 1ml sterile glycerol to create a glycerol stock, which can then be stored at -80C and used to rapidly grow new cultures. DNA was then extracted using a GeneJET Plasmid Miniprep kit as recommended by the manufacturer.

0.8.19 Transformation of *A. tumefaciens* GV3101

50μl of *A. tumefaciens* GV3101 in a 1.5ml microcentrifuge tube was placed on ice for 5 minutes. 1μl of DNA (150ng/μl) was added to the cells. The mixture was then placed in liquid nitrogen for 5 minutes, then transferred to a 37℃ water-bath for 5 minutes. The microcentrifuge tubes were removed and 100μl of low salt LB (10g/l tryptone, 5g/l yeast extract, 5g/l NaCl) was added and the microcentrifuge tubes were incubated for 2 hours in a 28℃ shaking incubator. Then 100μl was plated onto low salt LB agar (10g/l tryptone, 5g/l yeast extract, 5g/l NaCl, 1.5%Bacto-Agar) with appropriate antibiotic selection. The plates were sealed with Parafilm M ® and placed in a 28℃ oven for 2 to 3 days.

0.8.20 Transformation of *A. thaliana*

To create stable expression lines of *A. thaliana*, plants were grown for approximately 35 days under long day conditions (as in methods section 0.8.1), until approximately 50% of all flowers were open. Siliques were removed in order to enrich the transformation. 10ml of *A. tumefaciens* in low salt LB (and appropriate antibiotics) was incubated overnight at 28℃ at 180rpm. 3ml of the overnight culture was added to a 1l conical flask containing 500ml of low salt LB (and appropriate antibiotics) and then incubated overnight at 28℃. Cultures were split into two 250ml Nalgene centrifuge bottles and spun for 10 minutes at 5000rpm and 21℃. The supernatant was removed and the centrifuge bottles inverted to fully drain. The pellets were re-suspended in 20ml 5% sucrose and poured into a 1l tub along with a further 980ml of 5% sucrose. 200μl of Silwet-L77 was added to reduce surface tension. Flowers of the plant were submerged in the solution for 30 seconds. The plants were then incubated in trays sealed with plastic bags for 24 hours. The plants were then place upright and left to grow for a further week before being left to dry.

0.8.21 Confocal microscopy of leaf tissue

Leaf sections of *N. benthamiana* were infiltrated using the method from Sparkes et al. (2006). Three days post-infiltration, leaf sections were excised using a razor blade and placed, with the underside of the leaf facing up, on a glass slide with water and a coverslip was placed on top. If *A. thaliana* leaves were being imaged the same mounting process was used. Fluorescent images were acquired using a Zeiss 880 confocal microscope (1.40 63x oil objective). For GFP visualisation, excitation was at 488nm laser and emission was at 490-520nm. For YFP visualisation, excitation was at 514nm laser and emission was at 495-580nm. For RFP visualisation, excitation was at 561nm laser and emission was at 580-610nm.

0.8.22 FRET-FLIM

Genes were cloned from *A. thaliana* leaf cDNA into pGWB654 and pGWB655, using Gateway®, to produce both N- and C-terminal RFP fusions. eGFP-RTN13 and RFP-RTN3 constructs were kindly provided by Verena Kriechbaumer (Oxford Brookes). Constructs were then transformed into *A. tumefaciens*. *N. benthemiana* was co-infiltrated with both an RFP and GFP construct. Leaf samples were cut out and placed onto glass slides with water for imaging. FRET-FLIM was performed at the Central Laser Facility, Rutherford Appleton Laboratory, Harwell Oxford (Thanks to Prof. Stanley W. Botchway for help and support during the use of this facility). Data was obtained by observing a region of interest on the nuclear envelope. Calculations were made using the SPCImage 5.4 analysis software (Becker and Hickl, Berlin). The fluorescence lifetimes of the putative interactors and eGFP-RTN13 were compared to positive and negative controls. A minimum of three independent regions of interest were measured.

0.8.23 Yeast-two-Hybrid

Transformation of *S. cerevisiae* Y182 and AH109

Saccharomyces cerevisiae (Y182 and AH109) were grown in 10ml of YPDA (20g/l glucose, 20g/l peptone, 10g/l yeast extract, 100mg/l adenine) at 30℃, 200rpm overnight. 1ml of overnight culture was transferred into a 2ml microcentrifuge tube and centrifuged for 5 minutes at 2000rpm. The supernatant was removed and the pellet was re-suspended in 1ml of 0.1M lithium acetate. This resuspension in lithium acetate was repeated twice. Then the mixture was incubated at 30℃

for 1 hour. A tube of ssDNA was placed in boiling water for 10 minutes, then on ice for 5 minutes. 290μl of 50% PEG 3350, 4μl of boiled ssDNA and 3μl of plasmid DNA (500-1000ng) were combined to made the DNA mix. This was then incubated at 30℃ to equilibrate. The two vectors used were pDest22 and pDest32 with genes of interest inserted. 100μl of the AH109 yeast solution was added to the pDest22 DNA mix and 100μl of the Y182 yeast solution was added to the pDest32 DNA mix. These were incubated at 30℃ for 50 minutes. The mixtures were then transferred to a 42℃ water bath for 15 minutes and then centrifuged for 5 minutes at 3000rpm. The supernatant was removed and the pellet re-suspended in 200μl of sterile distilled water. The cultures were then spread on selective agar plates (SD-Trp for the AH109 strain and SD-Leu for the Y187 strain) and incubated at 30℃ for 2-3 days.

Yeast mating

10ml of selective liquid media (SD-Trp for the AH109 strain and SD-Leu for the Y187 strain) was inoculated with a single colony from the selective plates, and incubated overnight at 30℃ and 200rpm. A matrix to indicate mating was placed under a YPDA plate. 3μl of the pDest22 cultures were pipetted onto the appropriate area on the YPDA plate, ensuring the spots were discrete and well separated. The spots were allowed to dry by the flame. This was repeated for the pDest32 cultures, ensuring they were spotted on top of the pDest22 cultures. The plates were sealed and incubated overnight at 30℃.

Replica plating and cleaning

The overnight YPDA mating plate was replicated onto the following plates using sterile velvets: SD-Leu-Trp-His +20mM 3AT, SD-Leu-Trp-His +3mM 3AT, SD-Leu-Trp-His +1mM 3AT, SD-Leu-Trp-His, SD-Leu-Trp. Plates were sealed and incubated overnight at 30℃. The plates were then replica cleaned to ensure any cell growth was directly on the selective media, and then incubated for 2-3 days at 30℃. The plates were then assessed by eye for growth.

X-GAL assay

A circle of nylon membrane was placed on top of a YPDA plate. The SD-Leu-Trp plate (with successful growth) was used to replica plate onto the nylon membrane. The YPDA plate and nylon membrane was incubated overnight at 30℃. The

nylon membrane was then lifted off the YPDA plate with forceps and placed in liquid nitrogen for 30 seconds to lyse the cells. The membrane was then placed, colony side up, onto two pieces of filter paper soaked in X-Gal solution (10mg X-Gal in 100μl DMF, 60μl BME and 10ml Z buffer (21.5g/l $Na_2HPO_4 \bullet 12H_2O$, 5.5g/l $NaH_2PO_4 \bullet H_2O$, 0.75g/l KCl, 0.246g/l $MgSO_4 \bullet 7H_2O$, pH7.0)). Excess buffer was removed and then the petri-dish was sealed and incubated at 37℃ for 24 hours. The membrane was monitored at 2, 4, 6 and 24 hours for development of the blue colour indicating a successful protein-protein interaction.

0.8.24 Bimolecular fluorescence complementation (BiFC)

Proteins were cloned into BiFC 1 - 4 vectors using Gateway® cloning and then transformed into *A. tumefaciens*. These constructs were co-infiltrated into *N. benthamiana* so that each infiltration had both an N-terminal half of e-YFP and a C-terminal half. The pBin61 vector containing P19 was also used in some infiltrations to artificially enhance expression. Leaf sections were imaging using the Zeiss 880 confocal microscope with the 514nm Argon laser.

0.8.25 Imaging *A. thaliana* embryo germination

Imaging chamber

A. thaliana seeds were imbibed at 4℃ for 1 hour in sterile distilled water. The testa and endosperm were then removed under a dissecting microscope using fine forceps and a 0.5mm insulin needle, to reveal the embryo. MS0 (MS salts 4.4g/l, 0.5% agar) was heated in the microwave and then incubated at 65℃ for 20 minutes to remove bubbles in the solution. Under sterile conditions, 900ul of MS0 agar was added to the CoverWell™ imaging chamber. Once set, it was pushed out onto a clean microscope slide. The embryos were pipetted with minimal water into the imaging chamber. The agar was then placed back on top. The imaging chamber was affixed to a microscope slide and secured with electrical tape. A small amount of paper tissue was taped to the edge of the slide to ensure the microscope could focus on the embryos (figure 2). The imaging chamber was placed in a plant growth chamber, with long-daylight conditions (16 hours) and at 21℃. Embryos were imaged using confocal microscopy at 10 hours after artificial daybreak for up to 13 days.

Figure 2: ***Process of creating the imaging chamber. A.*** *Pour agar into imaging chamber.* ***B.*** *Push agar onto microscope slide and add embryos to imaging chamber.* ***C.*** *Affix imaging chamber to microscope slide and cut some paper tissue.* ***D.*** *Tape tissue to edges of the slide.* ***E.*** *Side on view of finished product.*

Without an imaging chamber

To asses whether the imaging chamber was causing stress to the plants, imbibed seeds were uncoated under a dissecting microscope and placed on MS0 petri-dishes (4.4g/l MS salts, 1% agar). The plate was sealed with microporus tape. The plates were placed in a plant growth chamber, with long-daylight conditions (16 hours) and at 21℃. Each day 2-3 embryos were removed from the plate and placed with water on a glass slide and a coverslip was placed on top. The embryos were imaged using confocal microscopy at 10 hours after artificial daybreak every day.

0.8.26 Extracting protein from germinating *A. thaliana* embryos

Col-0 seed were imbibed in sterile distilled water at 4℃ for 1 hour. The seeds were uncoated under a dissecting microscope using fine forceps and a 0.5mm insulin needle. Seeds were then placed on MS0 petri-dishes (4.4g/l MS salts, 1% agar). The plates were placed in a plant growth chamber, with long-daylight conditions (16 hours) and at 21℃. Each day four uncoated embryos were removed and placed in 45μl of 2x Laemmli loading dye (0.5M Tris-HCl pH 6.8, 4.4% SDS, 20% glycerol, 0.036% bromophenol blue, 2% BME). Embryos were ground with

a polypropylene microcentrifuge tube pestle, cleaned with 70% ethanol. Samples were then stored at -20℃ until all samples were collected. Samples were run on SDS-PAGE according to methods section 1.4.6.

0.8.27 Imaging *A. thaliana* embryo development

A. thaliana was grown for approximately 6 weeks, until the first siliques started to yellow. Siliques at the top of the stems were younger than those at the bottom, so by taking a selection of siliques a full range of embryo development states could be found. Siliques were removed using fine forceps, cut open using a 0.5mm needle and the developing seeds scraped out. the embryos were placed in a small droplet of sterile distilled water and the seed cases were removed using two 0.5mm insulin needles. This was all performed using a dissecting microscope. Embryos were then placed in microcentrifuge tubes containing 0.5ml sterile distilled water until imaged on the confocal microscope (maximum 1 hour).

0.8.28 Staining plant material

Rhodamine B

Rhodamine B was used to label the endoplasmic reticulum. 1.6μM rhodamine was diluted in distilled water from a stock solution dissolved in DMSO. Embryos were incubated in rhodamine B for 10 minutes. The plant tissue was removed and then placed in an microcentrifuge tube containing sterile distilled water to wash. The tissue was the placed on a glass microscope slide with water and secured with a glass coverslip.

Nile red

Nile red was used to label lipid bodies. A 0.1% solution of Nile red was diluted in distilled water from a stock solution in DMSO. Embryos or leaf sections were incubated in Nile red for 15 minutes. The plant tissue was removed and then placed in an microcentrifuge tube containing sterile distilled water to wash. The tissue was the placed on a glass microscope slide with water and secured with a glass coverslip.

0.8.29 Image analysis of plant endoplasmic reticulum

The macro created for image analysis can be seen in full in the appendix (figures 7.27 - 7.28). Images were opened using the Bio-Formats plugin in the ImageJ-based open source processing package FIJI (v1.51k) (Schindelin et al., 2012). The analysis was set up so that binary images were assumed to have black background. [*Edit ⟩Options ⟩Colours.*]

A Median filter (radius of 2 pixels) was used to reduce salt and pepper noise. [*Process Filters Median*]. To normalise the images, saturation levels were set to 0.5%. [*Process ⟩Enhance Contrast*].

The Trainable Weka Classifier (v3.2.5) was used to segment the images to create a binary image of the total ER. [*Plugins ⟩Segmentation ⟩Trainable Weka Segmentation*]. A representative image containing both tubules and sheets was loaded. By using the 'Freehand line' selection tool areas of ER and areas of background were chosen and added to either class 1 (ER) or class 2 (background) as appropriate. Once at least 5 selections for each category were made the classifier was trained (using default settings), then saved as a ".model" file. This file was then loaded as the classifier for each subsequent image and used to ' Create Result. The resulting image, titled "Classified image", was converted to a binary image. [*Process ⟩Binary ⟩Make Binary*].

The binary image image was then duplicated and to one of the images an erode function was used (iterations = 3, count = 1) to remove thinner structures in the image, such as tubules. [*Process ⟩Binary ⟩Erode*]. This image was then labelled as "Eroded" and the unaltered binary image was labelled as "Binary Total".

Both images were then converted to RBG Colour (from 8-bit), in order to utilise the "Color Pixel Counter" plugin (not included with the standard FIJI package). [*Image ⟩Type ⟩RBG Color*]. For the Binary Total image the Color Pixel Counter was run to identify 'Green' Pixels, whereas for the "Eroded" image the Color Pixel Counter was run to identify 'Red' Pixels (Cells = 20, Pixels = 0.2100, Minimum = 30). This is arbitrary, and simply allows the user to know which numbers relate to which image, as the Color Pixel Counter identifies any white pixels as coloured pixels. [*Plugins ⟩Color Pixel Counter*]. This would result in the number of white pixels in each image, from which the percentage of 'sheets' could be calculated by dividing the number of pixels in the "Eroded" image by the number of pixels in the "Binary Total" image.

0.8.30 Statistical analysis

Student T-Test

A one-tailed student T-test was performed using the Data Analysis ToolPak in Microsoft Excel 2016. Prior to this an F-Test was performed to compare whether the variance of each sample was equal or unequal. A one-tailed T-test was performed, assuming equal or unequal variance as appropriate. Significance levels were set at 0.05.

Single-factor ANOVA

Single-factor ANOVA was performed using IBM SPSS Statistics for Windows (Copyright ©IBM Corporation and its licensors 1989, 2016. Version 24.0) Armonk, NY:IBM Corp. The significance level was set to 0.05. The Levene statistic was used to assess the variance. From the ANOVA, the F critical value was compared to the F value and if smaller, the null hypothesis was rejected. If the null hypothesis was rejected, then a Tukey HSD post-hoc test was performed to assess the significance of pairwise differences.

Two-factor ANOVA

Univariate two-factor ANOVA was performed using IBM SPSS Statistics for Windows (Copyright ©IBM Corporation and its licensors 1989, 2016. Version 24.0) Armonk, NY:IBM Corp. The significance level was set to 0.05. From the ANOVA, the F critical value was compared to the F value and if smaller, the null hypothesis was rejected. If the null hypothesis was rejected, then multiple Tukey HSD post-hoc tests were performed to assess the significance of pairwise differences, both within groups and between groups.

Chapter 1

Introduction

1.1 The plant endoplasmic reticulum

Inside all eurkaryotic cells there are membrane-bound organelles that perform vital functions. The endoplasmic reticulum (ER) is the largest of these organelles (Chen et al., 2012a). It was first discovered in 1945, when a group identified "delicate lace-work" inside the cytoplasm of a fibroblast-like cell (Porter et al., 1945), although it was not given the name 'ER' until 1948 (Porter and Thompson, 1948).

The ER is the site of protein production for proteins that need to be secreted outside of the cell or for proteins that reside in membranes around the cell. Newly transcribed RNA leaves the nucleus through the nuclear pores and attaches to ribosomes for translation. For secretory and membrane proteins the ribosomes bind, via interaction of the protein's signal peptide with SRP (signal recognition particle), to the SRP receptor integrated within the ER membrane. A translocon in the ER membrane allows the newly translated protein to enter into the ER lumen, where it is folded, or inserted into the ER membrane itself Lodish et al. (2007).

Protein production and assembly are assessed by the quality control pathway. When an increase in mis-folded or unfolded proteins is detected, the UPR (unfolded protein response) is activated (Fanata et al., 2013; Wan and Jiang, 2016; Bao and Howell, 2017). The UPR helps to protect the cell from external and internal stress, such as viral infection, lack of nutrients, genetic mutations and loss of calcium (Fanata et al., 2013). The ER is also the site of the production of lipids, which are used by other membranes in the cell (Chen et al., 2012a; Stefano et al., 2014a). Moreover, the ER stores calcium, used in signalling events, and plant hormones, such as auxin and ethylene (Stefano et al., 2014a).

The ER is constantly moving and remodelling, enabling it to deliver proteins,

lipids and calcium around the cell (Chen et al., 2012a). There are fast moving areas, in which active streaming takes place, and smaller, slower movements where tubules disconnect and reconnect with other areas of the network. In mammalian cells, ER movement is linked to microtubules. In plants however, ER movement is predominately due to the actin-myosin cytoskeleton (Runions et al., 2006; Sparkes et al., 2009a). Actin monomers form polymerised chains to create actin filaments, which can grow and shrink in length. In *Arabidopsis thaliana* there are 17 myosin genes, (4 in class VIII and 13 in class XI) (Reddy and Day, 2001). Class XI myosins are implicated in organelle movement (Reddy and Day, 2001). Using ATP hydrolysis the mysosin heads can pull on the actin filament, thus moving along the filament. As the plant myosin XI is similar to mammalian myosin V Sparkes (2011), it is likely that the double-headed myosin 'walks' along the actin filament in a stepwise manner. The myosin attaches, through its tail domain, to the ER membrane via an intermediary protein Sparkes et al. (2009a); Sparkes (2011). The dependence on actin and myosin XI for ER movement was shown when actin chains were depolymerised (by the addition of lactrunculin B) and the ER stopped remodelling (Runions et al., 2006; Sparkes et al., 2009a). It has been shown however, that during mitosis, when the cells are dividing, that the ER movement is instead dependent on microtubules (Sparkes et al., 2009a).

There are also stable points of the ER (Sparkes et al., 2009a), including specific contact sites where the ER connects to the plasma membrane (PM). In mammalian and yeast cells this has been well investigated, and protein complexes at the contact sites have been discovered (Stefan et al., 2013). Though little work has been done on plant contact sites (Chen et al., 2012a), there are some proteins (such as VAPs (VAMP-associated protein, where VAMP stands for vesicle-associated membrane protein) and SYTs (synaptotagmins)) that have been implicated in ER-PM connections (Prez-Sancho et al., 2016).

Plants also have plasmodesmata, where ER (in the form of a desmotubule), PM and cytosol (as a cytoplasmic sleeve) pass through the cell walls into adjoining cells. These plasmodesmata allow the transfer of proteins, hormones and RNA molecules (William J. Lucas, 2009). The permeability of the plasmodesmata is controlled and dynamic, with three different states; the dilated state allows large molecules to pass though (subject to the size exclusion limit), the open state allows molecules smaller than 1 kDa to diffuse freely and the closed state will not allow any traffic through the plasmodesmata Sevilem et al. (2013). During the dilated state even a protein as large as GFP, at 27 kDa, has been proven to be able to pass between cells through the plasmodesmata Crawford and Zambryski (2000). Figure 1.1 highlights the organelles within a plant cell.

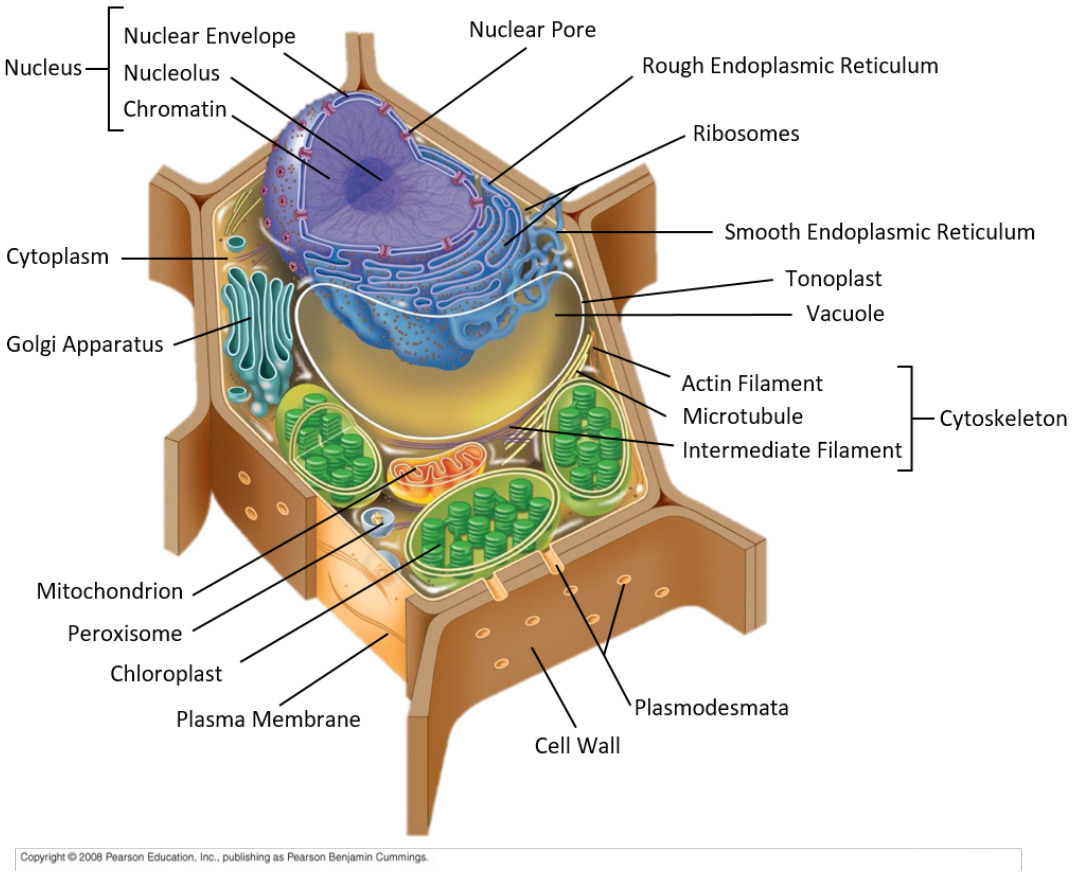

Figure 1.1: ***Plant cell with labelled organelles****. The ER is continuous with the nuclear envelope and although not depicted here forms desmotubules which pass through the plasmodesmata. In most plant cells the vacuole occupies 70-90% of the space in the cell, pushing the ER to the edges of the cell. Image from figure 6.8c of Biology 8th Edition, Campbell, published by Pearson Benjamin Cummings, Copyright (2008). Labels added by thesis author.*

1.1.1 ER-organelle contact sites

The nuclear envelope contains 'gates' through which the outer nuclear membrane and the ER membrane are continuous (Staehelin, 1997; Evans et al., 2009). These gates are constricted tubules, presumably acting as a size restriction for protein transport (Staehelin, 1997; Evans et al., 2009). In addition to these gates, it has been shown that membrane proteins made in the ER diffuse through to the inner nuclear envelope via the outer nuclear envelope (Evans et al., 2009).

Once secretory or membrane proteins are produced they are exported to the Golgi apparatus. There is evidence that the Golgi apparatus is different in plants, compared to yeast or metazoans (Nebenfhr and Staehelin, 2001; Sparkes et al., 2009c). Some of these differences are in cellular distribution; plant Golgi stacks are dispersed throughout the cell, whereas metazoans have a centralised Golgi

distribution (Nebenfhr and Staehelin, 2001). Another major difference in is their connection to the cytoskeleton; plant Golgi is associated with the acto-myosin system, whereas metazoan Golgi stacks are associated with microtubules (Nebenfhr and Staehelin, 2001). Although the existence of COPI vesicles (transporting from the cis Golgi apparatus to the ER) has been shown in plants, there is little evidence that COPII vesicles function in plants (Hawes et al., 2008). This suggests that the ER is directly connected to the Golgi apparatus. Indeed, optical trapping experiments have shown that when the Golgi bodies are pulled with the laser trap the ER follows and grows, then when released will slowly move back to its original position, with the Golgi bodies (Sparkes et al., 2009c).

The ER also connects with mitochrondria and chloroplasts, providing both with a source of calcium and lipids (Stefano et al., 2014a; Andersson et al., 2007). Although ER-mitochondria contacts are well studied in yeast and metazoans, they are poorly understood in plants. The existence of such contacts between the ER and mitochrondria is evidenced by the observation that the ER is able to to move mitochondria, and may also contribute to mitochondrial fission (Mueller and Reski, 2015; Stefano et al., 2014a). Confocal microscopy has shown that the constriction sites of mitochondria during fission events correlates with the ER network (Mueller and Reski, 2015), this has even been seen in yeast and mammalian cells (Rowland and Voeltz, 2012). There are a variety of proteins that have been found at the ER-chloroplast contact sites, though many remain unknown (Block and Jouhet, 2015). It seems likely that lipids transfer between chloroplasts and the ER since phosphatidylcholine is made in the ER, but also found in the outer-membrane of the chloroplasts (Block and Jouhet, 2015). An optical tweezer experiment showed, that as with the Golgi bodies, chloroplasts can be moved and the ER will follow (Andersson et al., 2007).

The vacuole occupies 70-90% of the space in the cell and pushes the remaining organelles to the periphery of the cell, against the plasma membrane. Depending on the developmental stage of the plant, the vacuole is filled with hydrolytic enzymes or storage proteins, both of which are supplied by the ER (Zheng and Staehelin, 2011; Viotti, 2014). These proteins can either be transported via the Golgi apparatus, or through a Golgi apparatus independent pathway (Viotti, 2014).

To date, there have been no contact sites confirmed between the vacuole and the ER, though there is some evidence to suggest that such contacts do exist (Jaquinod et al., 2007; Lang-Pauluzzi, 2000). Proteomic analysis of the tonoplast has confirmed the presence of ER proteins (Jaquinod et al., 2007). Additionally, UV imaging has shown that during plasmolysis, the vacuole shrinks under osmotic

pressure and Hechtian strands, formed from both PM and ER are formed from static points on the cell wall (Lang-Pauluzzi, 2000). This suggests that when the vacuole shrinks, it pulls the ER, which in turns pulls on ER-PM contact sites (Lang-Pauluzzi, 2000).

1.2 Morphology of the endoplasmic reticulum

Besides being highly dynamic, the ER network has a unique morphology. From early micrographs, the ER was classified as 'rough' or 'smooth', dependent on the presence or absence of ribosomes, respectively (figure 1.2)(Palade, 1956).

More recently the ER has tended to be classified into sheets and tubules. Tubules are thin cylinders of around 30nm in diameter (as measured in yeast and mammalian ER networks) (Shibata et al., 2010). These tubules connect to form three-way junctions and form the 'chicken wire' shaped network. Sheets are flat areas of the network with curved edges. Unlike mammalian cells, sheets and tubules are not in specific regions of the plant cell and are instead distributed throughout. Figure 1.3 shows a confocal image of the ER in *Nicotiana benthamiana* labelled with GFP-HDEL. HDEL is a four amino acid long tag (histidine - aspartic acid - glutamic acid - leucine) which enables the retention of proteins in the ER. By linking HDEL to GFP, the GFP is localised to the lumen of the ER (Gomord et al., 1997; Hawes et al., 2001). GFP is the Green Fluorescent Protein, which was originally discovered in a species of jellyfish (*Aequorea victoria*) (Shimomura et al., 1962). When excited with a blue light, it emits green fluorescence. By attaching GFP to proteins of interest their cellular localisation can be found (Brandizzi et al., 2004). Many other colours of fluorescent protein have either been created by mutating GFP or have been discovered in other species.

It has also been discovered that the sheets have an increased number of ribosomes compared to the tubules, this was initially suggested to be due to the small diameter of the tubules, hindering the ribosomes from attaching to the membrane (Shibata et al., 2006, 2010). More recently, in yeast, it was shown that it is not the tubule diameter than influences the distribution of ribosomes, but the presence of membrane shaping proteins, Reticulon/YOP1 (West et al., 2011). This difference in ribosome distribution gives reason to believe that the sheets and tubules have different functions. If the ribosomes localise preferentially to the sheets, then this is where the protein production will take place. The tubules might then be the site of lipid production and calcium storage.

This theory that sheets and tubules have differing functions is supported by differ-

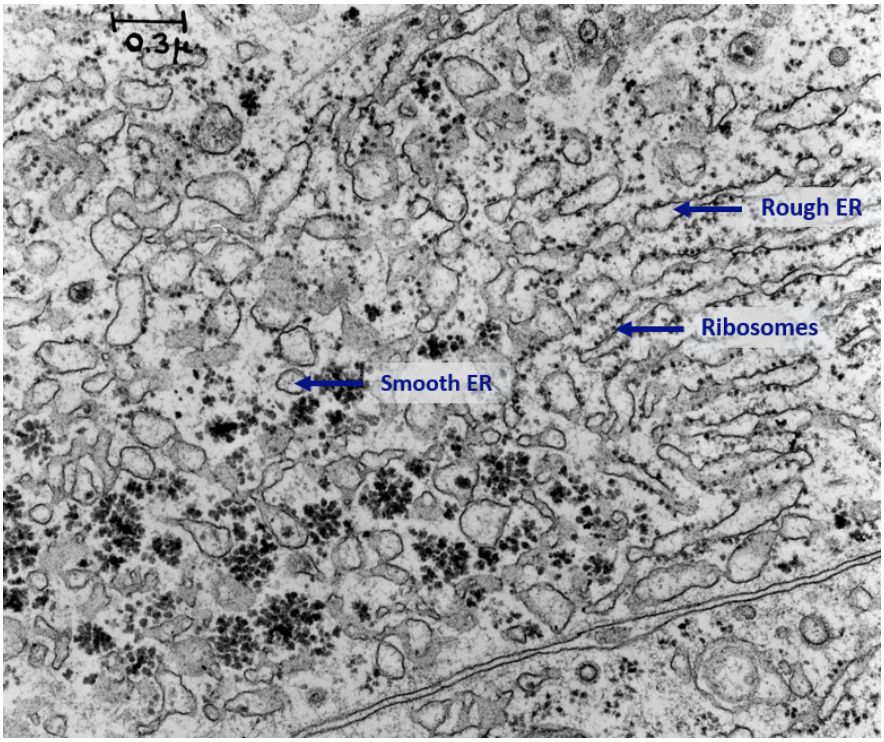

Figure 1.2: ***Electron micrograph of rat liver cells showing rough and smooth ER (Palade, 1965).*** *Ribosomes are seen as small, dark circles, some free in the cytoplasm and some attached to the surface of the ER, forming the 'rough' ER. The 'smooth' ER is defined by the lack of ribosomes. Cell Image Library accession number:37188. Labels added by thesis author. This image is licensed under a Creative Commons Attribution, Non-Commercial Share Alike License.*

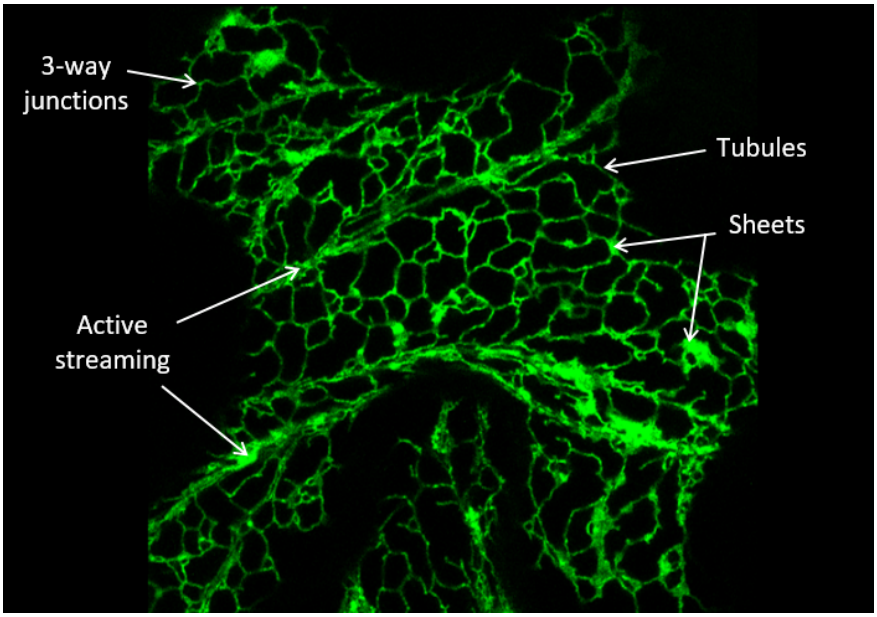

Figure 1.3: ***Confocal image of N.benthamiana lower-epidermis leaf cell ER visualised with GFP-HDEL.*** *ER tubules, 3-way-junctions and sheets are all clearly visible, as well as the bundles of tubules that are swiftly moving using the actomyosin cytoskeleton system.*

ing cell types having more of one type of morphology than another. Secretory cells such as pancreatic cells, have many more sheets (Shibata et al., 2006), whereas muscle cells and neurons have distinctly tubular ER (Zhang and Hu, 2016), relating to their reliance on calcium signalling. Cells must have a mechanism to control the proportion of sheets and tubules in the network, though the mechanisms for doing so are unknown. Advances in imaging techniques, have shown that the ER morphology is more complex than simply sheets and tubules, and that in mammalian cells there are helicoidal sheets, fenestrated sheets and tubular matrices (Nixon-Abell et al., 2016). These structures are almost certainly also found in plant cells, and so this evidence should not be ignored, however for the sake of simplicity it is easier to understand and compare morphological differences in a binary manner.

1.3 Using *Arabidopsis thaliana* to study the ER

The plant ER plays a vital role in the production of seed storage proteins, which provide some of the energy for germination. Storage proteins are also crucial to animals, including humans, since 70% of human protein consumption comes from seeds, either directly through the seeds and grains we eat, or indirectly through the animals we eat (Heldt and Piechulla, 2011). There are three main types of storage proteins; globulins, albumins and prolamins (Shewry and Halford, 2002; Ibl and Stoger, 2011). These are made in the ER and transported to protein storage vacuoles. During germination this energy resource is used up and the protein-storage vacuoles transform into lytic vacuoles.

Arabidopsis thaliana is a model organism since it has a short life cycle and requires little space. Its genome was first sequenced in 2000 (Arabidopsis Genome Initiative, 2000), though mutation studies had been published as early as the 1940s (Meyerowitz, 2001). Since *A. thaliana* is diploid (possessing two of each chromosome), it makes it a lot easier to study and manipulate its genetics compared to tetraploid or hexaploid plant species.

If the differing forms of the ER relate to varying functions (Shibata et al., 2006, 2010; West et al., 2011), then it stands to reason that the shape of the ER morphology may change in response to the needs of the cell. For example, if there is increased need for protein production (such as during germination once storage protein reserves are depleted) the cell may enable more sheet morphology to occur, allowing for increased translation. If this is true, could the reverse of this mechanism be elucidated and allow manipulation of the ER to create more sheet morphology? Could this then be exploited to increase the overall yield of

seed storage proteins and/or alter the amounts of desirable proteins - to improve the nutritional value of seeds, or for bio-pharming whereby plants are utilised as "factories" to generate high-value pharmaceutical proteins? It is not clear whether an increase in sheet morphology directly influences the protein output of the cell, neither is it the aim of this project to measure this. This project will however investigate the proteins that influence the ER morphology in *A. thaliana*.

1.4 Proteins that influence the ER morphology

To date there are a several different proteins that have been found to influence the shape of the ER network in plants (Sparkes et al., 2011; Chen et al., 2012a; Stefano et al., 2014a), metazoans and yeast (English and Voeltz, 2013a; Shibata et al., 2009; Westrate et al., 2015))

1.4.1 Reticulons

Reticulons (RTNs) were first identified in mammals (Roebroek et al., 1993; van de Velde et al., 1994), but have since been identified in yeast and plant cells. They contain a conserved 200 amino acid Reticulon Homology Domain which forms four transmembrane helices, organised into a 'W' shape (figure 1.4) (Sparkes et al., 2010). RTNs were first seen to influence membrane morphology when their presence was linked to the formation of a network of tubules from *Xenopus laevis* vesicles (Voeltz et al., 2006).

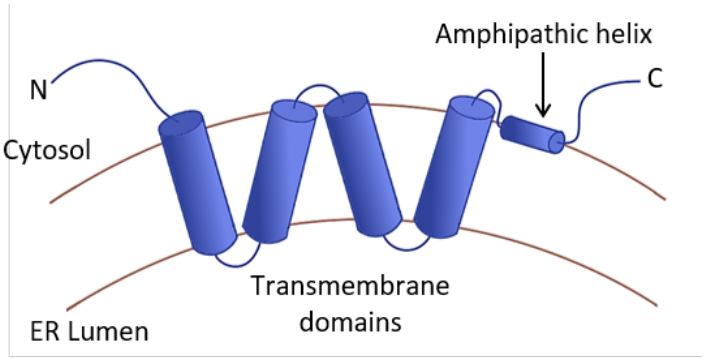

Figure 1.4: ***Diagram of the protein structure of reticulon 13.*** *The 'W' shape of the transmembrane domains allows the protein to wedge into the ER membrane and cause positive curvature. The amphiphatic helix at the C-terminal disrupts the lipid bilayer and is essential for tubule formation.*

A. thaliana contains 21 RTN genes (Nziengui et al., 2007). Some *A. thaliana* reticulons are relatively small, such as RTN15 which is only 179 amino acids long, and

others are much larger, for example RTN19 has 564 amino acids. Some of these reticulons have enzymatic domains (figure 1.5). For example, RTN20 (At2g43420) and RTN19 (AT2g26260) are 3-beta hydroxysteroid dehydrogenases.

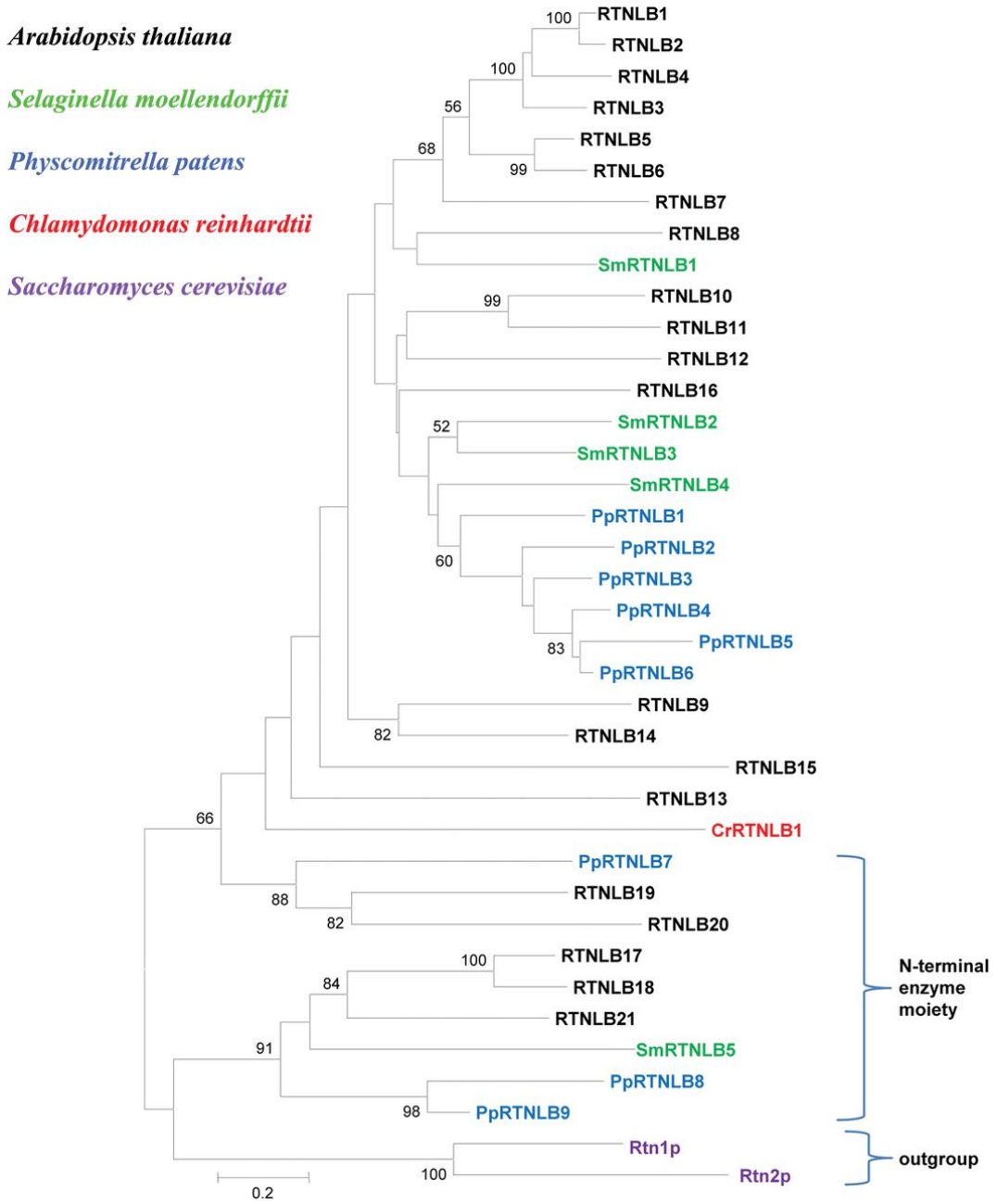

Figure 1.5: ***Evolutionary reticulon tree.*** *This shows the evolutionary relationships between plant reticulons and other species. Clearly highlighted are the reticulons with enzymatic domains. Taken from figure 3 of (Sparkes et al., 2009b), published by the Biochemical Journal, Portland Press Ltd.*

Confocal microscopy imaging of fluorescently-labelled RTNs showed that they only localise to tubules and the edges of sheets (Voeltz et al., 2006; Sparkes et al., 2010). Over-expression of RTN proteins reduces the overall proportion of ER sheets and constricts the tubules more than normal, so that when the network is

visualised with GFP-HDEL the ER appears as puncta (Voeltz et al., 2006; Tolley et al., 2008). This constriction can be measured by the reduction in lumenal flow via FRAP (Fluorescence Recovery After Photobleaching) (Tolley et al., 2008). Taken together, these results indicate that the reticulons are involved in the creation of tubules and bend the ER membrane.

It has been shown that the RTN N- and C-terminals are cytosolic, and that the two linker regions between each hairpin face into the ER lumen (Sparkes et al., 2010) (figure 1.4). The reticulon proteins are unusual in that their transmembrane domains are longer than average; they are predicted to be 22-23 amino acids long, as opposed to the 17 amino acids predicted to be required to traverse the lipid bilayer (Tolley et al., 2010). This prediction gives evidence to the theory that the helices sit at an angle in the membrane, forming a wedge shape. This wedging, along with homo and hetero oligomerisation (Shibata et al., 2008; Sparkes et al., 2010), help the proteins to bend the ER membrane in a positive curvature. In addition to this a C-terminal amphiphatic helix was found on the yeast Reticulon Homology Domain containing protein, YOP1p (Brady et al., 2014), and later confirmed present in *A. thaliana* RTN13 (Breeze et al., 2016). This amphiphatic helix is essential for tubule formation, though not sufficient (Brady et al., 2014; Breeze et al., 2016). The amphiphatic helix may aid in membrane curvature in a similar manner to BAR domains, by destabilising the lipid bilayer (Madsen et al., 2010).

1.4.2 Atlastins and RHD3

Reticulons do not work alone in shaping the ER network. In mammalian systems RTNs have been found to interact with a protein called atlastin (Hu et al., 2009). Moreover, the plant otholog of atlastin, RHD3 (Root hair defective 3) has been shown to interact with a plant RTN (Lee et al., 2013).

Atlastins were identified in mammals in 2001 from individuals with HSP (Hereditary Spastic Paraplegia) (Zhao et al., 2001). Soon after that a functional yeast homolog, Sey1p, was found (Zhang and Hu, 2013). Plants have a Sey1p sequence-related protein in the form of RHD3. RHD3 was originally discovered in 1990 as a protein that when mutated, caused the plants to grow short, wavy root hairs (named Root Hair Defective 3, RHD3) (Schiefelbein and Somerville, 1990). Deleting the RHD3 gene entirely caused a severe growth phenotype and the plants had short stems and leaves (Wang et al., 1997).

In addition to the phenotypic changes, the *rhd3* plants were found to have an altered ER network, with un-branched tubules forming bundles (Zheng et al.,

2004; Zhang et al., 2013). Over-expression of mammalian atlastin causes the network to become sheet-like, whereas over-expression of a GTP-binding mutant causes long, un-branched, tubule bundles to form (Hu et al., 2009), as in the *rhd3* mutant. This led to the theory that atlastins, including RHD3, were involved in fusion of tubules.

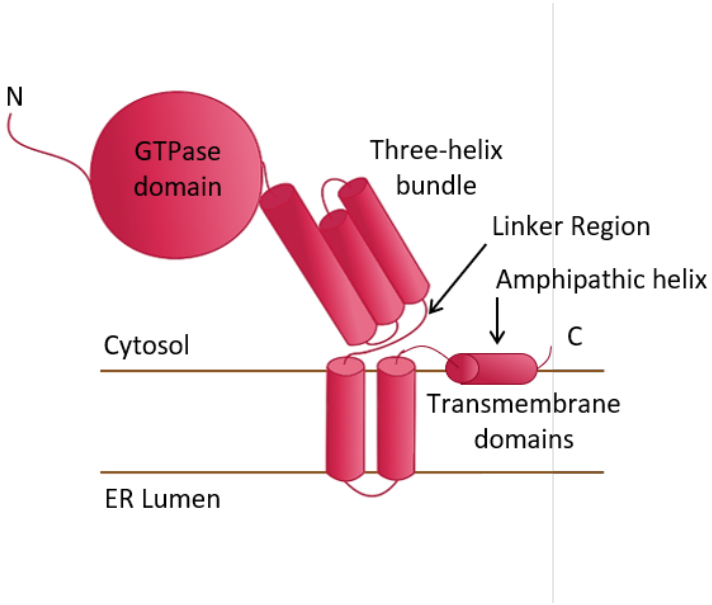

Figure 1.6: ***Diagram of the protein structure of atlastin.*** *The GTPase domains of atlastins on opposing membranes interact and the three-helix bundles change conformation relative to the transmembrane domains during membrane fusion. The amphiphatic helix helps to disrupt the lipid bilayer.*

Chemical cross-linking studies have shown that atlastins exist as oligomers (Rismanchi et al., 2008). In addition, atlastin transmembrane domains are vital to protein function; when replaced by unrelated transmembrane domains, ER tubules were seen to no longer fuse together (Liu et al., 2012) (figure 1.6). This suggests that the transmembrane domains are imperative for oligomerisation and also for their interaction with reticulons (Hu et al., 2009). Atlastin, and its orthologs in other species, have a GTP-binding domain, which functions as a GTPase (Wang et al., 1997). With this knowledge, and the crystal structures of the cytoplasmic regions of mammalian atlastin (Byrnes and Sondermann, 2010; Bian et al., 2011), several mechanisms have been proposed for how atlastins fuse tubules (Hu and Rapoport, 2016). Generally it is believed that a change in the angle of the three-helix bundle during the GTP-hydrolysis cycle allows the GTPase domains on opposing membranes to be brought together to fuse the bilayers (figure 1.7) (Hu et al., 2011). There is also some evidence that three-way junctions are simply tethered through the atlastin interaction, rather than fused completely (Hu and Rapoport, 2016).

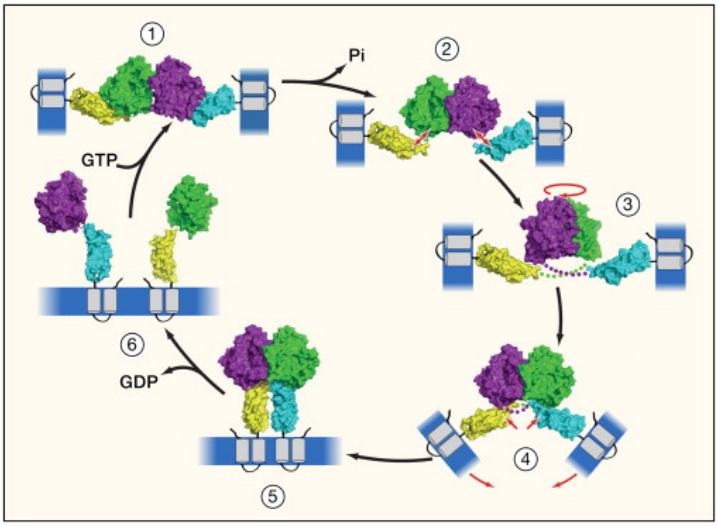

Figure 1.7: ***How atlastin may interact to fuse membranes.*** *Stage 1: Crystal structure of atlastins in the presence of GDP and inorganic phosphate (Pi) show interaction through the GTPase domains. Stages 2 - 3: Pi is released which allows the rotation of the linker region connecting the GTPase domain and the three-helix bundle. Stage 4: This rotation allows the helix bundles and the transmembrane domains to interact. Stage 5: The membranes are fused together. Stage 6: The release of GDP allows the atlastin dimers to dissociate. Reprinted from figure 2 of Hu et al., 2011, Copyright (2011), with permission from Elsevier*

In addition to the transmembrane domain and the GTPase domain, the C-terminal tail was found to be vital for membrane fusion (Moss et al., 2011). It was later discovered that the C-terminal tail contains an amphiphatic helix (Byrnes et al., 2013; Faust et al., 2015). This amphiphatic helix disrupts the bilayer, destabilising the membrane (Faust et al., 2015), which potentially enhances not only membrane fusion, but membrane curvature as well.

Figure 1.8 shows how the reticulons, atlastins and ribosomes may sit on the ER. Recently Powers et al. (2017) reported that purified Yop1p (a reticulon-like protein) and Sey1p (an atlastin-like protein) proteins from yeast, are necessary, and sufficient, to form a dynamic ER network in liposomes. Upon addition of GTP, the vesicles transformed into a dynamic network of interconnected tubules. The three-way junctions moved and fused as they would *in vivo*, which shows that a dynamic ER network can essentially be create by a handful of proteins, though does not fully explain all the morphologies seen in the cell.

Interestingly, several groups have attempted to assess the similarity of RHD3 and Sey1p/Yop1p, by carrying out complementation studies. The Chen et al. (2011) group used a A575V mutant of RHD3 (*rhd3_1*) and showed that it produced the stunted *A. thaliana* phenotype. They found that Sey1p could not complement the *rhd3_1* mutant plant line, and neither could RHD3 complement the yeast knockout *sey1p*Δ*yop1p*Δ, although both proteins localised to the ER in both cell types.

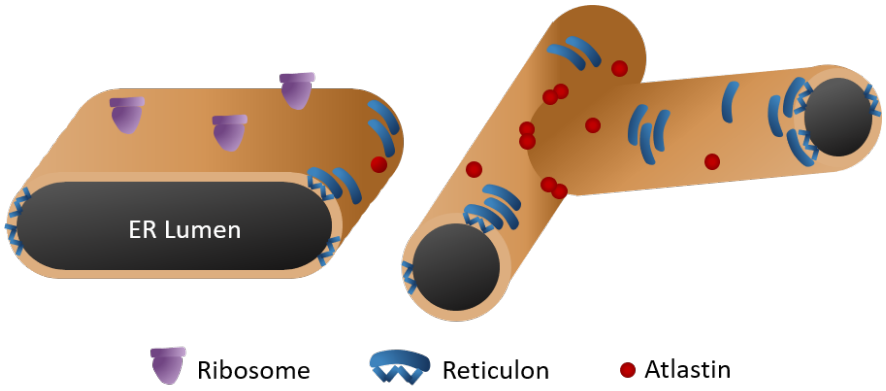

Figure 1.8: ***Diagram showing how atlastins and reticulons sit in the ER membrane.*** *Reticulons are localised to the tubules and the curved edges of the sheets. The atlastins are predominately found on curved areas as well, and pair up to fuse membranes. Ribosomes are present on the flat surfaces of sheets.*

A second group, Zhang et al. (2013) however, found that they could use RHD3 to complement the yeast knock-out *sey1p*Δ*yop1p*Δ. This difference in outcome may be due to the promoters used. Chen et al. (2011) used a Gal1 promoter, whereas Zhang et al. (2013) used the Sey1p promoter. Using the 'native' promoter of the protein you are trying to complement may enable this complementation to take place. What this shows is that there is similarity between RHD3 and Sey1p, so knowledge of one system may be transferable to another system.

1.5 Seed specific proteins

Of the 21 isoforms of reticulons and 3 atlastin homologs, *A. thaliana* has seed-specific versions of the reticulons (RTN13) and atlastins (RL2). The gene expression heat-maps in figure 1.9 show that the highest expression of RTN13 and RL2 is during seed development and in the dry seed.

RTN13 (At2g23640) is one of the smallest reticulons at only 206 amino acids long (Nziengui et al., 2007), and so is a useful 'model' protein for plant reticulons. Despite being seed-specific, RTN13 over-expression in *Nicotiana tabacum* can constrict the ER network (Tolley et al., 2008). RL2 (RHD3-like 2) (At5g45160) is the seed-specific isoform of RHD3. It is expressed in much lower levels than RHD3, and knocking the RL2 gene out does not cause any developmental defects (Chen et al., 2011; Zhang et al., 2013). Nonetheless, RL2 can complement an RHD3 knock-out, suggesting functional redundancy. Both RL2 and RTN13 interact, and when they are both over-expressed it causes severe defects in the ER morphology (Lee et al., 2013).

The presence of seed-specific proteins involved in shaping the ER could suggest that during seed development, and perhaps seed germination, there is need for greater regulation of the shape of the ER network. It has previously been shown that there are changes in the ER morphology during mung-bean germination (Harris and Chrispeels, 1980). During days 1-3 of germination, the ER was predominately tubular, and then transitioned into an ER with more sheets. In *A. thaliana* the ER has been analysed in wild-type and *rhd3* mutants (Stefano et al., 2014b). It was found that on day 3 of germination the ER was composed of large, fenestrated sheets, which broke down into a tubular network by day 12 of germination. In the *rhd3* mutant however, the ER became more disorganised and the amount of movement in the ER network decreased. This suggests that during germination the ER network undergoes major remodelling, presumably due to the changing cellular demands. However, to date the ER morphology during seed-development has not been reported.

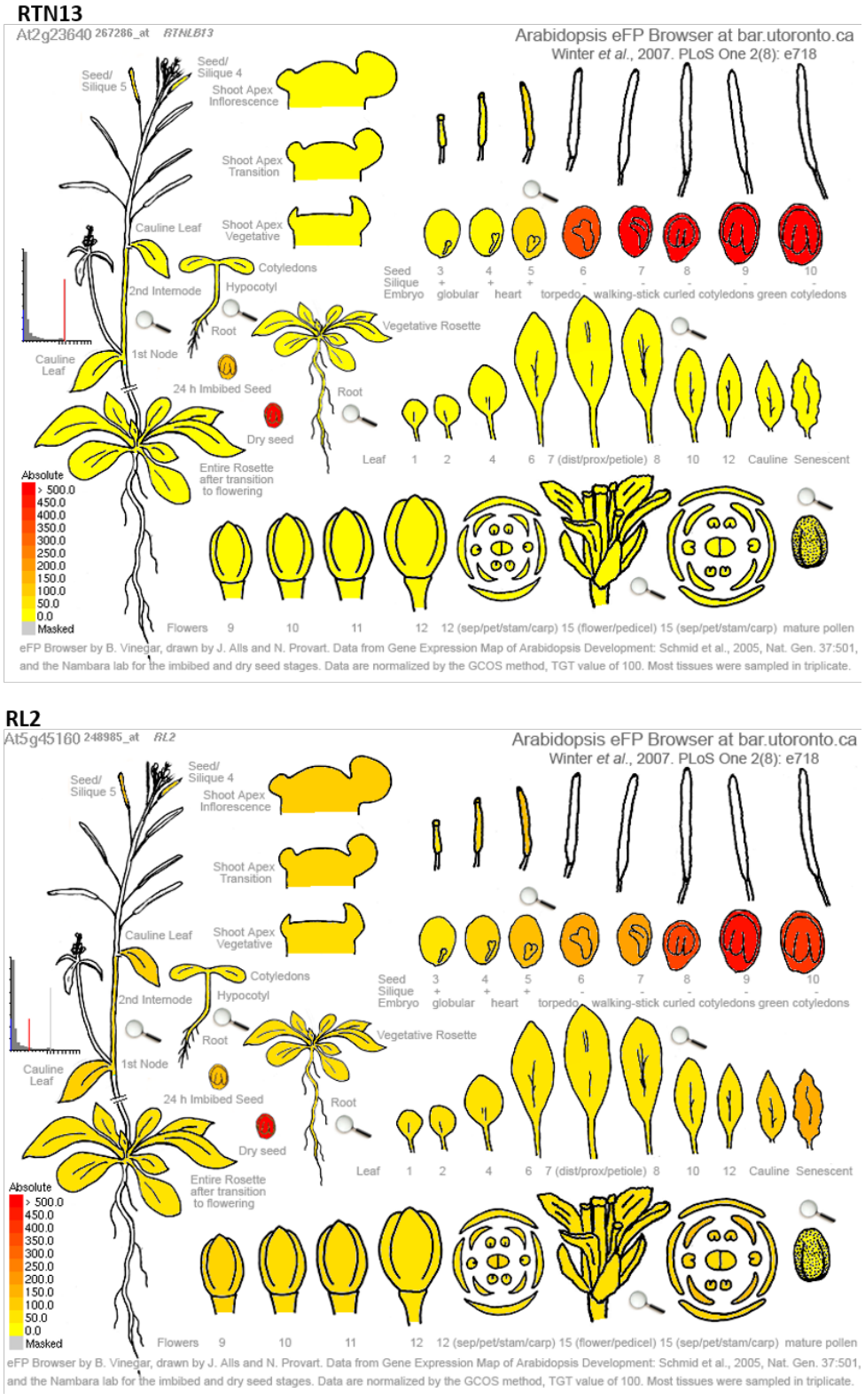

Figure 1.9: ***Gene expression maps for RTN13 and RL2,*** *seed specific reticulon and atlastin homologs. Darker colours represent higher gene expression. Both RTN13 and RL2 clearly indicate high levels of gene expression in the later stages of seed development. Created from the eFP browser (Winter et al., 2007)*

1.5.1 Other ER morphogenic proteins

Although reticulons and atlastins/RHD3 have been shown to interact *in vivo*, (Hu et al., 2009; Lee et al., 2013), there is still very little understanding about how the morphology is controlled, regulated or influenced by developmental and cellular events. It seems likely that additional, supplemental proteins are involved in creating the complex and dynamic ER morphology which differs between cell types. Kriechbaumer et al. (2015) investigated the proteins involved in the formation of plasmodesmata, which are known to specifically involve RTN3 and RTN6 (as found through proteomic analysis (Fernandez-Calvino et al., 2011)). Co-immunoprecipitation experiments with RTN3 and RTN6 identified a number of proteins including: those that could bind cytoskeleton components, those that were involved in controlling cholesterol levels and those that were present at ER-PM contact sites (Kriechbaumer et al., 2015). These experiments invite the possibility of reticulons interacting with a multitude of cellular components.

Mammalian DP1 proteins, homologs of yeast Yop1p (Voeltz et al., 2006), also contain a Reticulon Homology Domain, and localise to the curved edges of the ER membranes (Shibata et al., 2008). They also form oligomers in the ER membrane and this scaffolding may help to bend the membrane (Shibata et al., 2008). *A. thaliana* have proteins that are related to Yop1p, called HVA22. There are five HVA22 genes (a-e) (Chen et al., 2002). HVA22d was shown to label the ER network, but concentrated at the puncta (Chen et al., 2011). HVA22 co-localises with RHD3, even at puncta (Chen et al., 2011), which suggests that it may have a role in shaping the ER network, though this is yet to be verified. HVA22b is a seed specific isoform, and again, labels the ER (Lee et al., 2013). Unlike the reticulons however, HVA22 does not cause constriction of the ER network when over-expressed (Lee et al., 2013). More work is needed to fully understand the role of HVA22 (and the DP1/Yop1p proteins) in shaping the ER network.

Lunapark is another protein that has been linked to ER network formation. It was originally identified through a yeast deletion library, that caused disruption to the ER network (Chen et al., 2012c). Lunapark was found to localise to puncta at some, but not all, three-way junctions (Chen et al., 2012c), and thus may act to stabilise these regions (Chen et al., 2015; Wang et al., 2016b). Most junctions that had lunapark present, were stationary or less mobile than those without Lunpark (Chen et al., 2015). Lunapark is not necessary for the formation of three-way junctions, but a loss of lunapark reduces the number of junctions (Wang et al., 2016b). Lunapark has also been reported to interact with RTN, Yop1p and Sey1 (a yeast homolog of atlastin) (Chen et al., 2012c). Finally, lunapark may be

involved in protein quality control as it has been shown to interact with an ER-anchored ubiquitin ligase, gp78 (Zhao et al., 2016). Current work within the Frigerio lab has identified and characterised plant homologs of lunapark in *A. thaliana*, but their individual and synergistic role in plant ER network formation is not clear.

Rab proteins have long been known to provide membrane specificity for fusion and fission of membranes inside eukaryotic cells (reviewed in (Sandoval and Simmen, 2012)). In mammals Rab10 has been shown to localise to the ER and Golgi, and when depleted, or mutated caused an increase in the amount sheets in the ER (English and Voeltz, 2013b). Rab10 movement was found to be dependent on microtubules, and the authors suggested that Rab10 could help mediate membrane fusion along the microtubules, and help proteins synthesising phospholipids co-localise at the ends of tubules (English and Voeltz, 2013b). There has yet to be found a plant homolog that influences the ER shape.

A final protein of note, that also lacks a plant homolog, is CLIMP63. CLIMP63 is abundant in mammalian, professional secretory cells, which have a predominately sheet-based ER network (Shibata et al., 2010). In mammals sheets are 50nm thick, whereas in yeast they are only 30nm. It is suggested that CLIMP63 acts as a luminal spacer, creating the appropriate width for mammalian sheets. When CLIMP63 was knocked-out in mammalian cells, the width of the sheets was reduced to approximately 30nm. When over-expressed the amount of sheets was increased, but when over-expressed with RTN4 this produced a nearly normal network (Shibata et al., 2010). This shows that the membrane bending proteins work antagonistically to CLIMP63. A functional equivalent in plants has no yet been identified. It is currently unknown why mammals may need larger sheet lumens compared to yeast and plants.

There are a multitude of proteins that have been implicated in shaping the ER morphology and no doubt there are more to be discovered. Our understanding of how the ER network shape is controlled is certainly in its infancy.

1.6 Project aims and objectives

Several proteins have already been identified as influencing the shape of the ER membrane. The reticulons and atlastins have been shown to interact and are thought to be sufficient for the formation of a dynamic ER network. Nonetheless, proteins rarely work in isolation, and their activity is frequently modulated by a host of other proteins. A major aim of this research is to identify proteins that interact with the seed-specific *A. thaliana* reticulon, RTN13, and then investigate their influence on ER morphology. This will provide an increased understanding of how ER morphology is influenced.

This project will focus primarily on RTN13, rather than RL2. Although RL2 has been shown to be important in influencing ER morphology, knowing that the sheets and tubules have differing functions means that proteins that influence the ratio of these (such as reticulons) are more interesting for their impact, if any, on protein production.

Given that there are two proteins, involved in shaping the ER network, expressed predominately during seed development, this poses the question of whether there is enhanced regulation of the ER morphology at this time. Investigating the ER morphology during seed development (when RTN13 and RL2 are specifically expressed) and seed germination may increase our knowledge of how ER form relates to its function.

Aims

- Identify proteins that interact with the *Arabidopsis thaliana* seed specific isoform of the reticulon family, RTN13.
- Validate any identified interactions using a range of techniques
- Perform functional analysis of gain- and loss-of-function mutants in RTN13 interactors.
- Analyse ER morphology changes during seed development and germination in *A. thaliana*.
- Create an image analysis tool to quantify changes in ER morphology between wild type and mutant *A. thaliana*

Chapter 2

Identifying proteins that interact with RTN13

2.1 Introduction

Reticulon 13 (RTN13) is the seed specific isoform of the reticulon family in *Arabidopsis thaliana*; it is also one of the smallest isoforms. It bends the endoplasmic reticulum (ER) membrane, helping to form tubules (Tolley et al., 2008). Reticulons are currently one of the few proteins that have been shown to influence the structure of the ER (Voeltz et al., 2006; Sparkes et al., 2010). Since proteins rarely work in isolation, it would be useful to identify any proteins that interact with RTN13. Theoretically, these interactors may themselves influence the structure and morphology of the ER, or they may regulate RTN13 expression. These interactors could perhaps 'sense' the shape of the ER and relay this information, allowing the cell to modify the morphology in order to adapt to changing cellular requirements.

RTN13 has already been shown to interact with RL2 (RHD3 (Root hair defective 3)-like protein 2), the seed specific homologue of atlastin (Lee et al., 2013). Atlastins are proteins that aid membrane fusion in the ER, and form the three-way junctions with tubules (Zheng et al., 2004; Zhang et al., 2013). It was shown that when 35s:RTN13 and 35s:RL2 were co-infiltrated in *N. benthamiana* the resulting ER morphology was highly disrupted. A further experiment then showed that RL2-RFP could be co-immunoprecipitated with myc-tagged RTN13. In addition to this interaction, the BAR Arabidopsis Interactions Viewer (http://bar.utoronto.ca/interactions/cgi-bin/ arabidopsis_interactions_viewer.cgi) shows three more published interactions (Geisler-Lee et al., 2007). The first is RTN13 self-interaction, the second is RTN13 and RTN3, and finally RTN13 and RTN4 (figure 2.1). It is unsurprising that other reticulons interact with RTN13, since reticulons are known to form homo- and hetero-oligomers (Shibata et al., 2006).

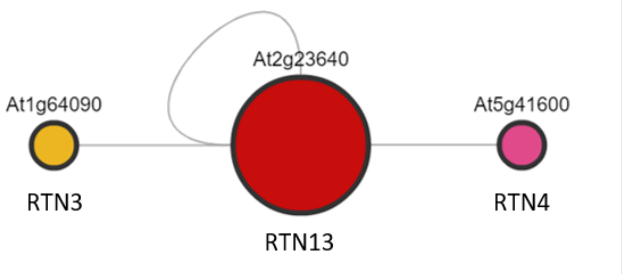

Figure 2.1: ***Published RTN13 interactions.*** *This is taken from the Arabidopsis Interactions Viewer (Geisler-Lee et al., 2007). The lines connecting the circles indicate a published interaction. The colour of the circles denotes their proposed cellular location: red = ER, pink = cytoplasm, yellow = vacuole. (Full Colour Key: Appendix figure 7.2).*

Several interactions between other reticulons have been found, figure 2.2.A, shows

the protein-protein interactions of RTN1, RTN3 and RTN13. They do not all interact with one another, and RTN1 and RTN3 only have a few other non-reticulon interactions. This is not the same for all reticulons; RTN4 for example, has interactions with many different proteins (figure 2.2.B). Some of these interactions are with other reticulons, as labelled, but otherwise there is a plethora of proteins with varying roles. There is also a large variety in the localisation of these proteins, as shown by the colour of the circles, highlighting how interconnected the ER is with other organelles (a key to the colours can be seen in appendix figure 7.2).

As shown by RTN13 interacting with RL2, there are interactions that the Arabidopsis Interactions Viewer does not contain. The database combines data from, Interolog (*in silico* interaction predictions), the BIND dataset (protein microarray data) and the MIND dataset (membrane protein interaction database from split-ubiquitin screens). That means that although this database contains "70944 predicted and 36352 confirmed Arabidopsis interacting proteins", it does not contain all published interactions. It is a good starting point to finding what interactions are out there, but does not give a fully comprehensive data series.

2.1.1 Methods that could be used to identify protein interactors

There are several methods that could be used to identify protein interactors. There are advantages and disadvantages to each technique. For this project the most important factors were: a lack of bias when finding interactors and a technique that required no prior knowledge of interactors. A brief explanation of varying methods that can be used to identify protein interactors are detailed below. Tandem affinity purification and chemical crosslinking were not used in this project, but are included to provide background on alternative techniques.

Co-immunoprecipitation

This method involves using an antibody against either the protein of interest, or a tag on the protein of interest itself. The antibody is attached to agarose beads, allowing the protein of interest, and any interactors, to be centrifuged down. The proteins that are pulled down can then be identified using mass spectroscopy. The benefits of using a tag, is that a commercial anti-tag antibody can be used, as opposed to a protein-specific and more expensive one. The disadvantage of a tag however, is that it can block interactions through steric hindrance and potentially interfere with protein expression. Examples of tags that can be used include: Fluorescent proteins (GFP, RFP), HA tag, FLAG tag or myc tag. This method does not need any prior knowledge of interactors, and can be used to find

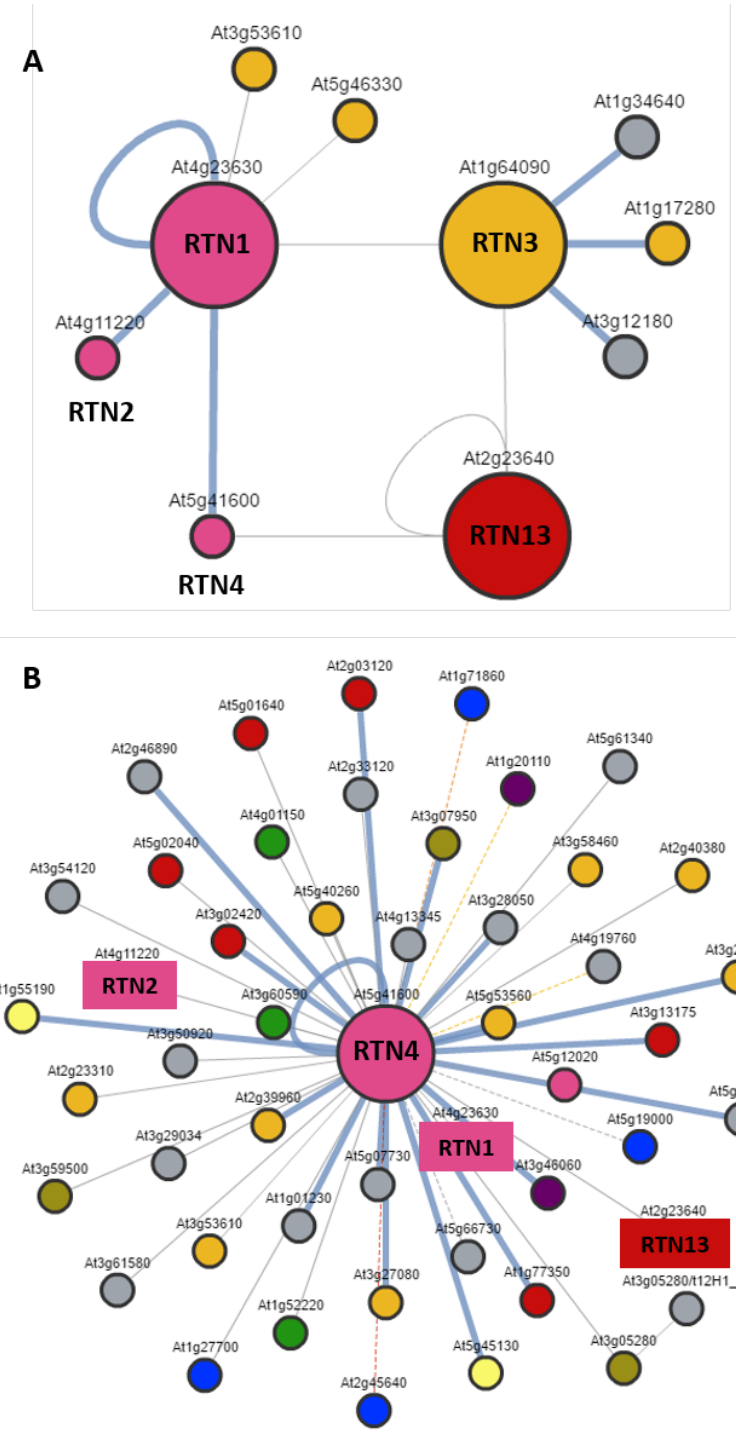

Figure 2.2: ***Network of reticulon interactions****. This highlights the interactions between RTN1, RTN3, RTN4, RTN5 and RTN13. A) RTN1 can be seen interacting with RTN2 and RTN4. RTN13 interacts with RTN4 and RTN3. B) RTN4 has 70 interactions with a plethora of different proteins. Among these are several reticulons, but also a lot of RAB proteins. The lines connecting the circles indicate a published interaction. The colour of the circles denotes their proposed cellular location: red = ER, pink = cytoplasm, yellow = vacuole, green = chloroplast, purple = peroxisome, blue = nucleus, orange = plasma membrane, brown = Golgi and grey = unknown location. (Full Colour Key: Appendix figure 7.2). This is taken from the Arabidopsis Interactions Viewer (Geisler-Lee et al., 2007).*

transient interactions, due to not needing to purify the proteins.

This was the method chosen to identify interactors with RTN13, since a stable expression line of 35S:YFP-RTN13 had previously been created. Although the protein is not expressed under a native promoter, it allowed a quick method for identifying protein interactors.

Tandem affinity purification (TAP)

TAP is similar to co-immunoprecipitation, but involves two steps of purification, it was first used for yeast proteins (Rigaut et al., 1999). The tag on the protein of interest consists of: A calmodulin binding peptide, a TEV (Tobacco etch virus) protease cleavage site and Protein A. In the first purification step IgG antibodies (attached to agarose beads) bind to Protein A. The sample is washed, to remove non-specifically bound proteins, and then a TEV protease is added. This cleaves the tag in two. A second bead, with calmodulin protein, is added and binds to the second half of the tag. The protein of interest with its interactors, can be analysed through mass spectrometry. The number of washes makes this method unsuitable for transient interactions. As with co-immunoprecipitation, the large tag can interfere with protein interactions. The tag could also be inaccessible to the binding proteins, meaning the protein of interest is not 'caught' in the first place. One group has has recently used TAP and mass spectroscopy with both *A. thaliana* seedlings and cell cultures to identify protein complexes (Van Leene et al., 2015).

Chemical crosslinking

Chemical crosslinking can be performed *in vivo* or *in vitro*, and it involves chemically binding two proteins together (reviewed in (Sinz, 2006; Bruce, 2012)). This technique has been used for a long time to find protein-protein interactions even in plants (Baird and Hammes, 1976). This technique is still being used and developed and indeed groups are cross-linking proteins *in planta* to find interactors (Zhu et al., 2016). Once the proteins are cross-linked, these proteins can be digested and the fragments analysed by mass spectrometry. There will then be fragments containing material from different proteins, which enables the user to find not only which proteins are interacting, but where they interact as well. This method can find interactors expressed at native levels. There is no risk of steric hindrance as there are no tags. It would however, be difficult to have an appropriate control as proteins nearby, but not interacting, can be cross-linked.

2.2 Aims and approach

The first aim of this project was to identify any proteins that could be found to be interacting with RTN13. A stable expression of YFP-RTN13 under an enhanced 35S promoter in *A.thaliana* was used and developing seed was collected. As shown in the gene expression heat maps in figure 1.9, this is when RTN13 is primarily expressed. By collecting 'green', or developing seed, the proteins that are interacting with RTN13 are specific to this developmental stage. The tissue was homogenised and co-immunoprecipitation was performed using an antibody against the YFP tag. This enabled RTN13, and any interacting proteins to be pulled down. The samples were sent for mass spectrometry analysis, in order to identify the proteins that were present in each sample. Controls were used to exclude any non-specific proteins.

Aims

- To find proteins that interact with RTN13, through mass spectrometry
- To clone these proteins and transiently express in *N. benthamiana* to identify protein localisation

2.3 Results

2.3.1 SDS-PAGE and Western blot analysis of co-immunoprecipitation of YFP-RTN13

To clarify whether the presence of YFP-RTN13 was detectable from developing seed, prior to mass spectrometry analysis, Coomassie staining and western blots were used. Late stage developing embryos were collected as in methods section 0.8.3. Initially three plant lines were used: wild type Columbia (Col-0), a 35S:GFP-HDEL transgenic line and a 35S:YFP-RTN13 transgenic line. Col-0 is one of the most common wild type *A.thaliana* strains, and its genome was sequenced by the year 2000 (Arabidopsis Genome Initiative, 2000). The Col-0 line was used in this experiment to identify (and subsequently eliminate from further investigation) any proteins that were promiscuous or abundant, thus were non-specific. GFP-HDEL is a protein that is often used for imaging the ER. HDEL is a ER lumen retention signal, it consists of four amino acids (histidine, aspartate, glutamate and leucine) and is found at the C-terminal end of ER-resident proteins. This signal is recognised by a receptor in the cis-Golgi membrane, and a protein containing it is then transported back to the ER, where the change in pH allows the receptor to release the protein/signal (Gomord et al., 1997; Hawes et al., 2001). Here, the GFP-HDEL line was used to identify (and eliminate from further investigation) proteins that were non-specific to RTN13, but were still associated with the ER lumen. It also allowed any proteins that were adhering to the fluorescent protein non-specifically to be identified and disregarded from further investigation.

Developing seeds were collected from all three lines and homogenised with 0.5% NP-40 (a detergent which disrupts cellular membranes) (Chinchilla et al., 2007; Liebrand et al., 2012). GFP-Trap®_A (Chromotek) was used to pull down the proteins of interest. A Coomassie stain was used to confirm that the protocol did pull down GFP-HDEL and YFP-RTN13. Figure 2.3 shows that although GFP-HDEL was successfully pulled down during the co-immunoprecipitation, YFP-RTN13 was not. This could have indicated that the GFP-Trap®_A was not effectively binding to YFP. However, given the similarity between GFP and YFP, this was unlikely. This could have suggested that YFP-RTN13 was not expressed highly enough, though confocal imaging showed expression of YFP-RTN13 (data not shown). Finally, this could have implied that YFP-RTN13 was not expressed strongly enough to be detectable through Coomassie staining.

To assess whether the protocol was ineffective, or if expression was too weak

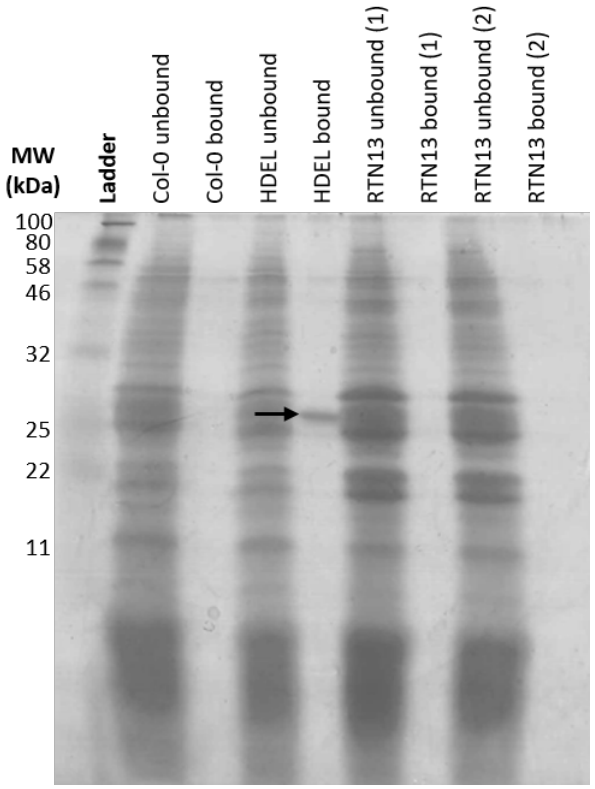

Figure 2.3: ***Coomassie staining showing both unbound and bound fractions from the initial co-immunoprecipitation of late stage developing A. thaliana embryos****. Col-0 denotes the wild-type line, HDEL denotes the GFP-HDEL overexpression line and RTN13 (1) and (2) denotes two different YFP-RTN13 overexpression lines. A anti-GFP-HRP antibody was used to pull-down the proteins. A clear band (highlighted by the arrow) can be seen in the GFP-HDEL bound fraction at aproximately 27KDa, indicating GFP-HDEL. No bands can be seen in the YFP-RTN13 bound fractions.*

for Coomassie to detect YFP-RTN13, the protocol was repeated and, alongside a Coomassie stain, a western blot was performed (using an anti-GFP-HRP antibody). As figure 2.4A shows, there are no bands in the bound lanes in the Coomassie stain. This is likely due to half the volume being loaded compared to the previous Coomassie. This is verified by the unbound lanes being fainter than in the previous gel. The western blot however, (figure 2.4B) shows strong bands in both unbound and bound lanes of GFP-HDEL and YFP-RTN13. There are three bands in the RTN13 lanes. The smallest molecular weight one is YFP on its own. The middle bands are YFP-RTN13 and the top one is YFP-RTN13 as a dimer. Reticulons are known to oligomerise. This western blot was developed using ECL and X-ray film. This confirmed that the protocol was successful and that both proteins were being pulled down and detectable through western blotting. Since mass spectrometry is far more sensitive, this was a satisfactory indication that the protocol was sufficiently optimised.

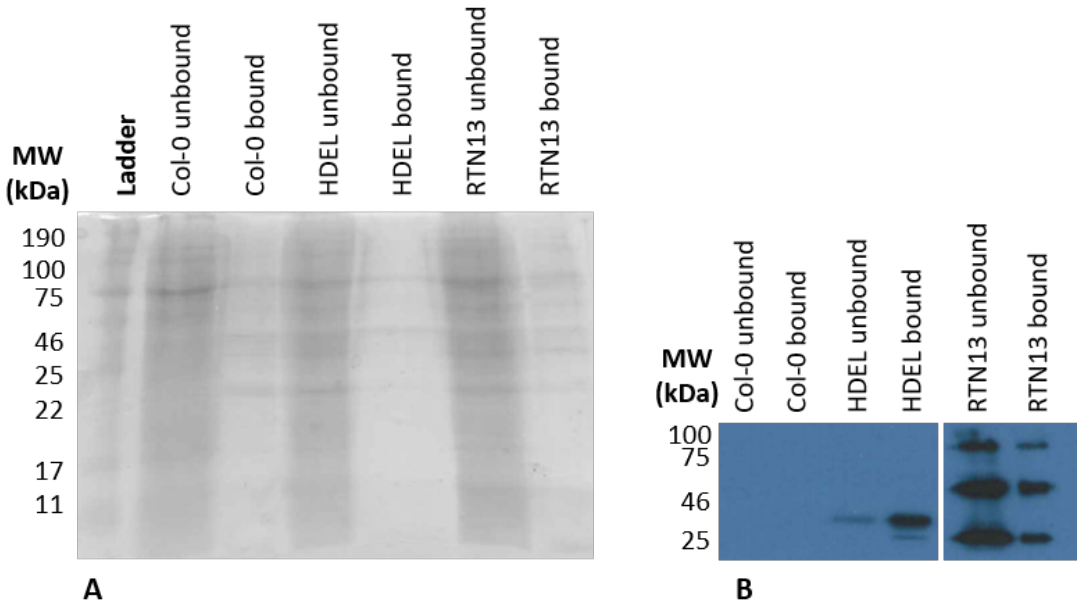

Figure 2.4: ***Coomassie stain and western from second co-immunoprecipitation of late stage developing A. thaliana embryos.*** *Col-0 denotes the wild-type line, HDEL denotes the GFP-HDEL overexpression line and RTN13 denotes the YFP-RTN13 overexpression line. A) Coomassie stain of unbound and bound fractions from the second co-immunoprecipitation. A Chromotek anti-GFP Trap-A was used for pull-down. There are no obvious bands in the bound fractions. B) Western blot of unbound and bound fractions from the second co-immunoprecipitation. A Chromotek anti-GFP Trap-A was used for pull-down and a anti-GFP-HRP antibody was used during the Western blot. Bands can be seen in both the unbound and bound fraction for GFP-HDEL. Multiple bands in the RTN13 fraction indicate (from the lowest band), free GFP, YFP-RTN13 and YFP-RTN13 oligomers.*

2.3.2 Mass spectrometry identified several protein interactors to YFP-RTN13

In order to identify proteins that were co-immunoprecipitated with YFP-RTN1, two independent co-immunoprecipitation and mass spectrometry analyses were completed with the following lines:

1. Col-0, GFP-HDEL and YFP-RTN13
2. Col-0, GFP-HDEL, YFP-RTN13 and RFP-RL2

The data from the two runs was merged using the software 'Scaffold 4 Viewer' (Proteome Software, Inc), and proteins that appeared in the Col-0 and GFP-HDEL samples were eliminated. Of the 775 proteins in the RTN13 samples, there were 83 unique proteins. Proteins that had less than three peptides were eliminated, due to lower confidence in their interaction. The function and lo-

calisation of the remaining proteins was investigated using information from: https://www.ncbi.nlm.nih.gov/ (which provides extensive information on genes and proteins), https://www.arabidopsis.org/ (which provides data on *A.thaliana* genes) and the Arabidopsis eFP Browsers from http://bar.utoronto.ca/ (which shows gene expression patterns in tissue and predicted and confirmed protein localisation in cells).

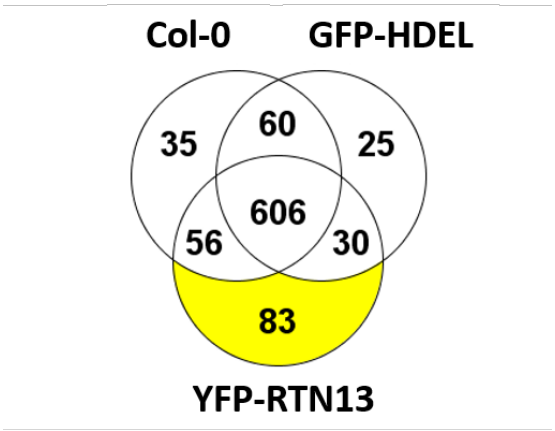

Figure 2.5: ***Venn diagram showing the number of proteins in each mass spectrometry sample.*** *Highlighted in yellow are the number of proteins (83) that were unique to the YFP-RTN13 sample. 606 proteins were common to all the samples, indicating non-specific proteins. 775 proteins were identified within the YFP-RTN13 sample, only approximately 11% were unique to that sample.*

Proteins that had functions unlikely to influence ER morphology were also disregarded, such as ribosomal proteins (for example ribosomal protein L19e - AT1G02780). Proteins that did not have predicted localisation in the ER, the cytosol or PM were also rejected (Such as AIM1 - AT4G29010, a peroxisomal protein). Although it is known that the ER connects with all organelles in the cell, to reduce the number of candidates to a manageable number for future experiments, more obvious localisations were chosen.

Eleven proteins were identified in accordance with these parameters. Three of these proteins were reticulons; RTN1 (Accession number; AT4G23630), RTN4 (AT5G41600) and RTN5 (AT2G46170). Since reticulons are known to hetero-oligomerise it is unsurprising that other reticulons were pulled down. Another protein was RL2 (the seed-specific isoform of the plant homolog), which confirmed the co-immunoprecipitation in (Lee et al., 2013). A surprising discovery was that although YFP-RTN13 co-immunoprecipitated with both RHD3 and RL2, RL2-RFP did not reciprocate. This could be due to steric hindrance by the RFP tag on the RL2 construct, thus prohibiting interaction. It could also be due to differing protein expression levels. In the YFP-RTN13 plants, RTN13 is expressed under an enhanced 35S promoter. Whereas in the RL2-RFP line, RTN13 will be

Protein Name	Abbreviation	Acession number	Predicted Location
Endomembrane protein 70 protein family	Endo70	AT5G25100	Golgi / PM
Ferulic Acid 5-Hydroxylase	FAH1	AT4G36220	ER
GTP - Binding protein 2	GB2	AT4G35860	Cytosol / Golgi / PM
Lysophopholipase 2	LPL2	AT1G52760	Cytosol / PM
NADH: Cyt B5 reductase 1	CBR1	AT5G17770	ER
Sterol Methyltransferase 2	SMT2	AT1G20330	ER
Synaptotagmin A	SYTa	AT2G20990	ER / PM

Table 2.1: ***Proteins of interest, excluding reticulons, identified from mass spectrometry data****. These proteins were identified as suitable candidates for interaction with RTN13, due to their localisation and multiple peptide units identified in the mass spectrometry analysis. Full name and accession number are given. Predicted protein location is from the cell localisation browser results (appendix figures 7.3 - 7.9). Golgi = Golgi aparatus, PM = plasma membrane, ER = endoplasmic reticulum.*

expressed under its native promoter. This lower expression level of RTN13 may not enable RL2 to interact in amounts able to be detected.

The other seven proteins that were identified as suitable candidates are listed in table 2.1. The accession number is the identification from the TAIR website (https://www.arabidopsis.org/). The predicted protein cellular and tissue localisations were derived from the BAR website (Bio-Analytic Resource for Plant Biology) (appendix figures 7.3 - 7.9). The BAR website has both an *A. thaliana* tissue gene expression browser (http://bar.utoronto.ca/efp/cgi-bin/efpWeb.cgi) and a cell localisation browser (http://bar.utoronto.ca/cell_efp/cgi-bin/cell_efp.cgi).

The reticulon genes had previously been cloned by PhD researcher, Nick Tolley (Sparkes et al., 2010). For the other seven proteins, Col-0 *A. thaliana* genomic leaf material was prepared, as described in methods section 4.10. Primers were used to attach attB sites to the genes in preparation for Gateway cloning and amplification. Unfortunately this was not achieved for Endo70 and FAH1. This was attributed to both genes being very long; the coding DNA sequence for Endo70 is 1956 nucleotides and 1563 for FAH1. Longer genes are typically harder to clone, although it was managed for SYTa whose coding DNA sequence in 1740 nucleotides long. In comparison, RTN13 has a coding DNA sequence which is 621 nucleotides long.

BP clonase™ was used to insert genes into pDonrZeo, then LR clonase™ was used to recombine the genes into pDest654 and pDest655, which tag the genes with RFP on the C- and N-terminal respectively. The predicted transmembrane regions were assessed, as were any potential signal peptides, using TOPCONS (http://topcons.cbr.su.se/pred/) and InterPro (http://www.ebi.ac.uk/interpro/). The topology diagrams from the TOPCONS predictions can be seen in appendix figures 7.10 - 7.13. InterPro gives information on predicted domains and functional analysis, the output from this is not shown. The aim of these data was

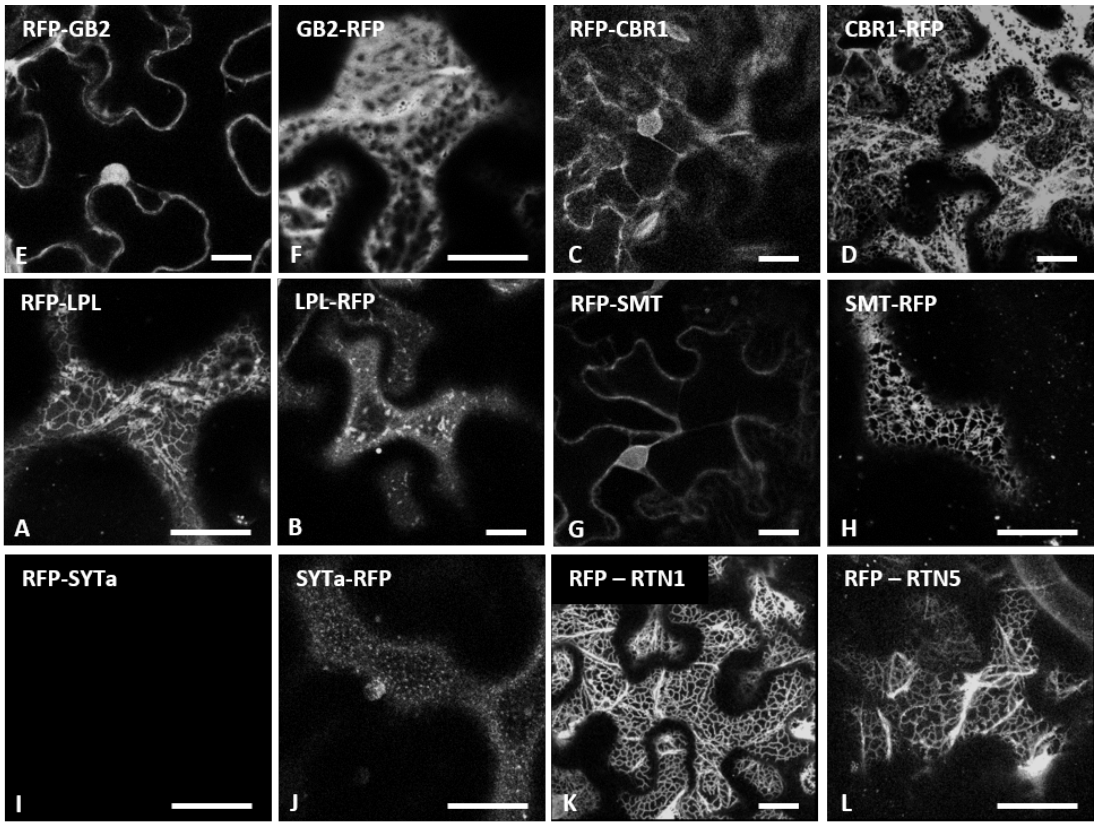

Figure 2.6: ***Localisation of interactors in N. Benthamiana transient expression.*** *Cells from the lower leaf epidermis were imaged 3 days post-infiltration. RFP-GB2 labelled nucleus and plasma membrane. GB2-RFP labelled cytosol. RFP-CBR1 had weak expression in the nucleus and plasma membrane. CBR1-RFP labelled the ER. RFP-LPL labelled the ER and Golgi. LPL-RFP labelled Golgi. RFP-SMT had weak expression in the nucleus and plasma membrane. SMT-RFP labelled the ER. RFP-SYTa gave no expression. SYTa-RFP had weak expression as puncta (on the plasma membrane). RFP-RTN1 and RFP-RTN5 labelled the ER. Scale bars = 10μm.*

to check whether the RFP tag may affect the expression or localisation of the proteins. None of the proteins had any known specified signal peptides, so both the N- and C-termini were tagged with RFP.

2.3.3 Cellular localisation of putative interactors

In order to examine the expression and localisation of the N- and C-terminal RFP tagged constructs, they were transformed into *Agrobacterium* and infiltrated into *N. benthamiana*. Figure 2.6 shows the localisations from both the N- and C-terminal tagged interactors.

RFP-GB2 and GB2-RFP had differing expression. The expression with RFP-GB2 was weak and seemed to label the nucleus and potentially the plasma membrane (figure 2.6), however it was unclear. GB2-RFP clearly labels the cytosol (figure

2.6), which is consistent with the expected localisation (see appendix figure 7.5). GB2 is a Rab protein, which participate in membrane fusion events, given that it has no predicted transmembrane domains, the cytosol is the logical localisation. The N-terminus of GB2 is more conserved with homologs in other species and though the domain prediction it is seen as more important. GB2-RFP was thus the favoured construct of the two, as the RFP-tag was less likely to interfere in future experiments.

The *A. thaliana* genome encodes 57 Rab proteins. GB2 (GTP-binding protein 2) is also classified as AtRabB1b (*Arabidopsis thaliana* Rab B1b or AtRab2c) (Moore et al., 1997). Rab proteins are small GTPases that function in membrane trafficking. They cycle between an active, GTP-bound state and inactive, GDP-bound state. Active Rab proteins are recruited to one membrane, then they are delivered to a target membrane, where conversion of GTP to GDP causes the release of the protein (Cheung et al., 2002). The two membranes can then fuse, using proteins such as SNARE complexes. It is thought that Rab proteins provide membrane specificity (Vernoud et al., 2003). The most recent classification of *A. thaliana* Rab proteins was in 2001 and was partly based on similarity to mammalian Rab proteins, their localisation and phylogenetic distance (Pereira-Leal and Seabra, 2001). The AtRabB group are most similar to HsRab2 (*Homo sapien Rab 2*), which localise to pre-Golgi intermediate compartments and are involved in ER to Golgi transport (Vernoud et al., 2003; Tisdale, 1999). A *Nicotiana tabacum* homolog, NtRab2, has also been shown to function in trafficking between ER and Golgi bodies (Cheung et al., 2002). It is likely therefore that GB2 follows these homologues and provides specificity to Golgi and ER membrane fusion events.

RFP-CBR1 and CBR1-RFP again had different expression patterns. RFP-CBR1 expression was very weak, and had similar localisation to RFP-GB2; appearing to label the nucleus, the plasma membrane and the ER (as denoted by the strands coming from the nucleus, (figure 2.6)). CBR1-RFP clearly labelled the ER, which matches the predicted cellular localisation (appendix figure 7.7). The N-terminus of CBR1 has a predicted transmembrane domain (appendix figure 7.11), the RFP tag may potentially interrupt insertion into the membrane when at the N-terminus. CBR1-RFP was the preferred construct for future experimentation.

CBR1 (NADH-Cytochrome b5 reductase 1) is localised to the ER, as it does not have the mitochondrial targeting sequence that mammalian CBRs have (Fukuchi-Mizutani et al., 1999). CBR1 transfers an electron from NADH to cytochrome b5, which in turn passes electrons onto FAD2 and FAD3 (fatty acids desaturase

2 and 3) (Fukuchi-Mizutani et al., 1999; Oh et al., 2016). This links CBR1 with linoleic acid and α-linoleic acid synthesis, two fatty acids that are integral to the function of cellular membranes (Wayne et al., 2013). A mutant form of CBR1 causes an 85% reduction in hydroxy fatty acid levels and also reduced amounts of the 18:3 fatty acid (Oh et al., 2016). Overexpression of CBR1 causes higher lvels of 18:2 and 18:3 unsaturated fatty acids. Besides being a component of lipid membranes, 18:2 and 18:3 are also common fatty acids found in seed oils (Kumar et al., 2006). This has led to the discovery that CBR1 is essential for successful seed maturation (Wayne et al., 2013).

RFP-LPL and LPL-RFP had quite different expression. RFP-LPL appeared to be localised to the ER and the Golgi, whereas LPL-RFP localised to the Golgi, though the expression was poor (figure 2.6). This is unsurprising because the C-terminal end of LPL is more conserved between homologs in different species, suggesting it is more important. Both these localisations are different to what was predicted (see figure 7.6), however given the localisation seen in recent literature (Kim et al., 2016), RFP-LPL was the favoured construct for future use.

LPL2 (Lysophopholipase 2) has been named differently by different researchers. It was initially identified as an interactor to acyl-CoA-binding protein 2, and was suggested to be involved in phospholipid repair (Gao et al., 2010; Cunnac et al., 2007). Lysophospholipases hydrolyse ester bonds on lysophospholipids to produce fatty acids and glycerolphosphate derivatives (Wang et al., 1999). In 2013 it was found that it was also a component of the ligin biosynthetic pathway. Due to its activity in converting caffeoyl shikimate to caffeate and shikimate, it was named caffeoyl shikimate esterase (CSE) (Vanholme et al., 2013). It was found that it plays a vital role in lignin biosynthesis, as when the gene was knocked-out the mutant plants were shorter, lighter and contained less lignin than wild type *A. thaliana* (Vanholme et al., 2013). More recently it has been named AtMAGL3, *Arabidopsis thaliana monoacylglycerol lipase 3*. This is in recognition to its monoacylglycerol acyltransferase activity. Unlike other 15 AtMAGL proteins, AtMAGL3 was found to not have acyl hydrolase activity (Kim et al., 2016). It has been shown to have high gene expression in roots and stems, which links well to its role in lignin biosynthesis. Alongside this, it may also be responsible for membrane lipid-remodelling (Kim et al., 2016). This makes it an interesting candidate interactor to RTN13, because membrane lipid composition is known to influence membrane fluidity and thus structure.

SMT2-RFP has stronger expression than RFP-SMT2, it clearly labels the ER (as predicted, see figure 7.8). RFP-SMT2 displays similar expression to RFP-CB5R and RFP-GB2, where the nucleus is labelled, as is the plasma membrane and

perhaps the ER. This suggests faulty localisation. The C-terminus of SMT2 is the functional domain, however the N-terminus has a predicted transmembrane domain. It is possible that the N-terminal RFP disrupts insertion into the membrane, therefore SMT2-RFP was to be used in future experiments.

SMT2 (sterol methyltransferase 2) is a key regulatory protein in the sterol biosynthetic pathway (Husselstein et al., 1996). It converts 24-methylene lophenol to 24-ethylidene lophenol. This in turn alters the ratios of campesterol and sitosterol (24-methylene lophenol is used to make campesterol, and 24-ethylidene lophenol is converted into sitosterol) (Schaeffer et al., 2001; Schaller, 2003). This is highlighted by comparing overexpression and suppression of SMT2. In SMT2 overexpression, the levels of cholesterol and campesterol are decreased, whereas the level of sitosterol is increased (Schaeffer et al., 2001). With SMT2 suppression, the amount of 24-methylene lophenol and campesterol is increased and the amount of sitosterol is decreased (Schaeffer et al., 2001). This leads to a distinct decrease in reproductive ability (Valitova et al., 2016). SMT2 could be an interesting protein with regards to ER morphology modification, as sterols influence membrane fluidity and permeability (Schaller, 2004).

There was no expression detectable for RFP-SYTa (synaptotagmin A). There were puncta type structures visible with the SYTa-RFP construct however, expression was very weak. This expression is consistent with previously published data which indicate SYTa forms puncta connecting the ER and PM (Levy et al., 2015; Perez-Sancho et al., 2015). It also matches the predicted localisation shown in appendix figure 7.9.

SYTa (or otherwise known as SYT1) is an ER resident protein, and it connects the ER to the PM (Perez-Sancho et al., 2015). It is localised on immobile nodes on the ER, can forms part of ER-PM contact sites (Levy et al., 2015). Synaptotagmin gets its name from its inital discovery in its role of neurotransmitter release from synaptic vesicles (Perin et al., 1990), though not all mammalian synaptotagmins bind calcium, despite their conserved domains, nor are they all found in neurons (Marquze et al., 2000). *A. thaliana* SYTa may act as a calcium sensor during membrane fusion events (Yamazaki et al., 2010). It has however been shown to localise with the protein VAP27-1 (Vesicle-associated membrane protein (VAMP)-associated protein 27-1) (Perez-Sancho et al., 2015; Siao et al., 2016). In mammals VAPs are part of the SNARE (soluble N-ethylmaleimidesensitive factor attachment receptor) protein complex, which helps to fuse membranes. VAP27-1 is known to localise to ER-PM contact sites (Wang et al., 2016a). VAP27-1 always co-localises with SYTa, but SYTa does not always co-localise with VAP27-1 (Siao et al., 2016). SYTa has also been shown to interact with RTN3 and RTN6 at plas-

modesmata (structures that link adjoining plant cells together) (Kriechbaumer et al., 2015). In addition to this, SYTa has been shown to regulate movement-protein trafficking of plant viruses at the plasmodesmata (Lewis and Lazarowitz, 2010). Since RTN13 is not known to localise to ER-PM contact sites, perhaps this interaction between RTN13 and SYTa is simply due to the homogenisation of the tissue. If SYTa interacts with other reticulons, then it is likely to interact with all reticulons, though perhaps not *in vivo*.

RFP-RTN1 and RFP-RTN5 can both be seen to label the ER network very well and strongly, as expected.

With these constructs created, and the localisations established, the interaction between these proteins and RTN13 could be validated.

2.4 Discussion

2.4.1 Proteins pulled down by RTN13

The proteins that were pulled down in the mass spectrometry screen are all potentially interesting, with varied functions. The Arabidopsis Interactions viewer was used to find any interactions between these proteins (excluding the reticulons). Figure 2.7 shows that the only previously known connection between these proteins is between GB2 and CBR1. The connecting protein is a polyubiquitin (AT5G03240), a protein that tags other proteins for ubiquitin degradation. None of these interactions are with any reticulons. The Arabidopsis Interactions viewer does not contain every published interaction, as it only contains data from Interolog, the BIND dataset and the MIND dataset. Firstly, Interolog is an *in silico* interaction database, so these predicted interactions may not be true. Additionally, small-scale interactions published will not have been included. Papers specific to the proteins of interest, rather than large-scale, high-throughput datasets may contain for information about interactions found.

Interestingly, a paper in published in 2002 used a TAP screen to identify interactors in the lignin pathway (Bassard et al., 2012). The baits were CYP73A5 (accession number: AT2G30490) and CYP98A3 (accession number: AT2G40890), expressed in cell suspension cultures which were either induced to enhance lignin biosynthesis or not. CYP98A3, is also known as C3H, and produces the substrate that LPL hydrolyses (caffeoyl shikimate). Among the prey that were identified were: SYTa, SMT2, RTN1/2, RTN3, RTN4, RTN5 and Cytochrome b5 isoform 1 (which is reduced by CBR1). In this paper the authors suggest that these pro-

teins are forming a metabolon (a complex of sequential metabolic enzymes). It is both fascinating and somewhat reassuring that a separate study has identified the same or similar proteins in a protein-protein interactor screen. This either gives confidence in the findings, or raises the question of are these proteins particularly 'sticky' to reticulons? The authors have not published any more work on this topic, though it is briefly mentioned in their review of metabolon assembly (Laursen et al., 2015).

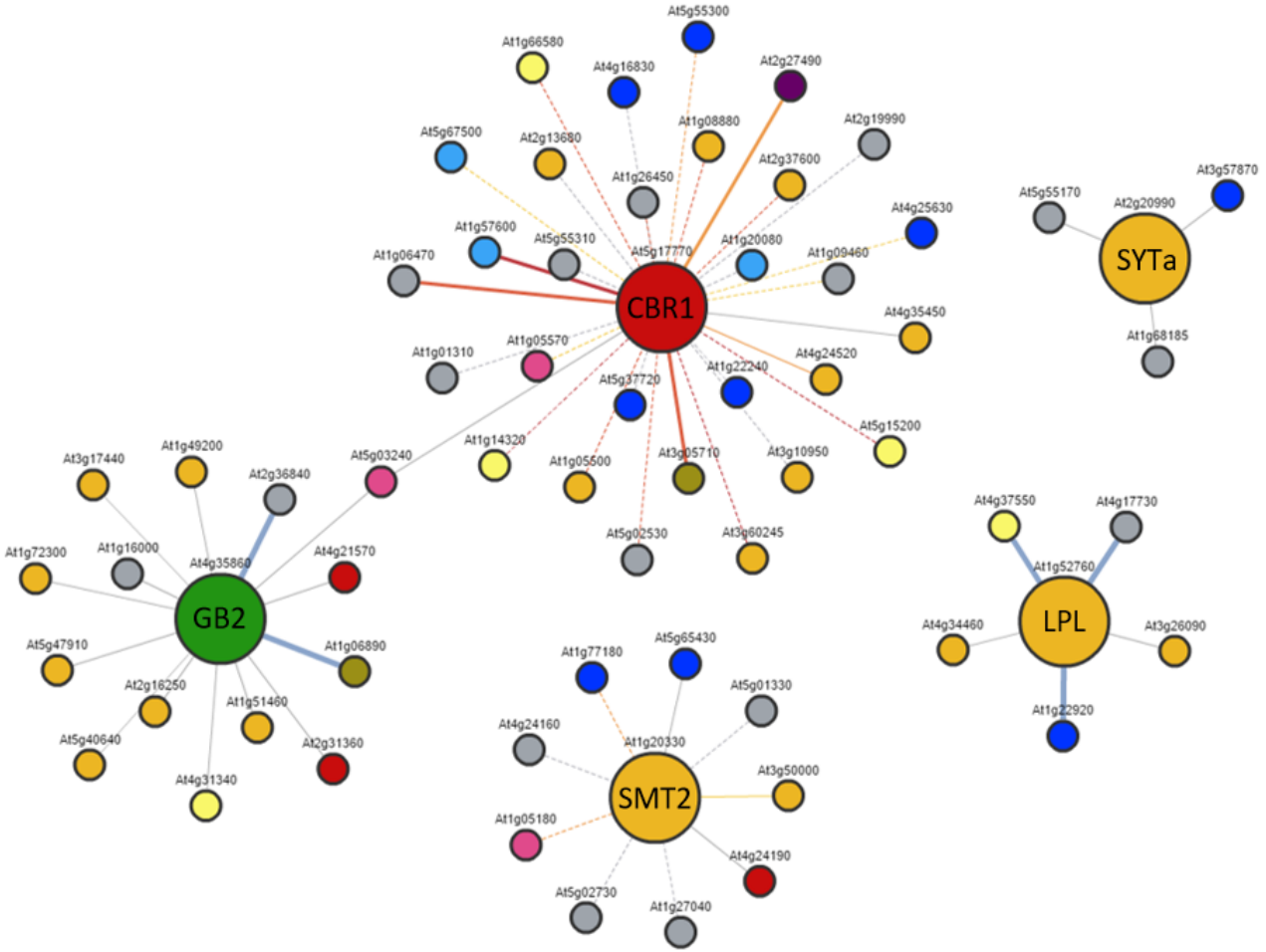

Figure 2.7: ***Published interactions of putative RTN13 interactors****, as shown by the Arabidopsis Interactions viewer. The lines connecting the circles indicate a published interaction. The colour of the circles denotes their proposed cellular location: red = ER, pink = cytoplasm, yellow = vacuole, green = chloroplast, purple = peroxisome, blue = nucleus, orange = plasma membrane, brown = Golgi and grey = unknown location. (Full Colour Key: Appendix figure 7.2). This is taken from the Arabidopsis Interactions Viewer (Geisler-Lee et al., 2007).*

All of these proteins have varied and interesting functions, with potential to be involved in membrane remodelling. Given the large number of proteins that were identified, these interactions need to be validated.

2.4.2 Protein Localisations

Protein localisation can be difficult to determine. Table 2.2 shows the predicted localisations from the Cell eFP Browser (`http://bar.utoronto.ca/cell_efp/cgi-bin/cell_efp.cgi`) and from the BAR Arabidopsis Interaction Database `https://bar.utoronto.ca/interactions/cgi-bin/arabidopsis_interactions_viewer.cgi`. Even these two data sources do not completely correlate, despite them using the same dataset, SUBA (SUBcellular location database for Arabidopsis proteins). SUBA uses information from proteome databases, prediction programmes and information about known protein families (Heazlewood et al., 2006). The Cell eFP Browser gives multiple potential localisations and its confidence in true localisation, whereas the Arabidopsis Interaction Viewer picks one that has high confidence.

Confocal imaging has been used as a way of finding the cellular localisation of a protein. This has its drawbacks as using a large fluorescent protein can cause mis-localisation, improper folding or interfering with membrane insertion. The fluorescent protein may block signals on the N- or C-terminals from being recognised by proteins for membrane insertion or trafficking, thus giving a false localisation.

As can be seen in figure 2.6, and as summarised in table 2.2 changing the position of the RFP tag on the interactors changed their localisation or expression. The constructs that were favoured were the ones that showed the clearest localisation or expression and which best matched the predicted ones. Additional experiments could be done to identify the proteins true localisations (for example, immunogold labelling in electron microscopy), though this is not an aim of the project. Since many of the techniques that will be used for validation involved confocal microscopy, it is enough to choice the most appropriate constructs, despite the potential implications when tagging with fluorescent proteins.

Protein	Predicted Cell eFP Browser	Predicted Interaction Database	Observed Confocal Imaging
CBR1	ER	ER	? / ER
GB2	Cytosol / ER / Chloroplasts	Chloroplasts	? / Cytosol
LPL	Cytosol / PM / Mitochondria	PM	ER / Golgi?
SMT2	ER	PM	? / ER
SYTa	Cytosol / ER / PM	PM	N/A / ER, PM puncta
RTN1	Cytosol / ER / PM	Cytosol	ER / N/A
RTN4	Cytosol / ER / PM	Cytosol	ER / N/A
RTN5	ER / PM	PM	ER / N/A
RTN13	Cytosol / ER	ER	ER / N/A

Table 2.2: ***Predicted versus observed cellular localisations****. ER = Endoplasmic reticulum. PM = Plasma membrane. ? = Localisation unclear. N/A = Protein not expressed.*

Chapter 3

Validating protein-protein interactions

3.1 Introduction

3.1.1 Why validating interactions is important

Having identified putative protein-interactors to RTN13, these interactions had to be verified. Although mass spectrometry is a highly sensitive technique it does have a high false positive rate, as demonstrated by the large number of proteins identified in each sample. The technique also involved homogenising the plant tissue, which may have brought proteins into contact that would not normally be able to interact within a cellular environment. Although every precaution was taken to eliminate false positives (such as having two different controls), it is possible that the interactions seen are false.

3.1.2 Methods to validate interactions

Multiple techniques can be used to to validate interactions between proteins, each with their own advantages and disadvantages. By using an assortment of techniques and being aware of their disadvantages, hopefully true interactions can be found. Some possible techniques, and their advantages and disadvantages are discussed below, to allow the reader to understand the decisions leading to the use of some techniques over others. Of the techniques discussed, co-immunoprecipiation, BiFC, FRET-FLIM and Yeast-two hybrid were used in the project; chemical crosslinking, SPR and MST were not. This of course is not a definitive list, and there are many other possible methods to validate interactions. Figure 3.1 gives a visual overview of the techniques discussed here.

Co-immunoprecipitation

In co-immunoprecipitations the proteins of interest can be tagged, either with a fluorescent tag (such as GFP) or a smaller tag such as HA, FLAG or Myc. Using fluorescent tags has the advantage that the proteins can be seen *in vivo* to ensure expression before the co-immunoprecipitation. Unfortunately these are very large and can cause steric hindrance, blocking interactions. Tags do not have to be used, as custom antibodies against the protein of interest can be made, however antibody production is both expensive and time-consuming. Using tags enables generic, cheaper antibodies to be used and allows multiple proteins to be targeted. The antibody must then be bound to agarose or sepharose beads to allow the proteins to be pulled down. This technique is not best suited to weak, or transient protein interactions, as sample washing is necessary to eliminate the 'unbound' proteins. Western blotting can then be used to identify interactions,

by using antibodies against the second protein. Again, using a tag will enable the use of generic, cheaper antibodies. Two papers that successfully used the GFP-Trap®_A with *A. thaliana* proteins were used as a reference to create the protocol that was used in this project (Chinchilla et al., 2007; Liebrand et al., 2012). The ease of this technique was a primary reason why this was chosen to validate interactions.

Chemical crosslinking

Chemical crosslinking has the advantage that no tags are needed and that information as to where the proteins are interacting is elucidated. Additionally this technique does not rely on binary interactions, and could be used for larger complexes. Because proteins are chemically bound, weak or transient interactions can be identified. One potential disadvantage is that interactions could be 'forced', and false positive results could occur. Qi and Katagiri (2009) used DSP (dithiobis(succinimidyl propionate)) to chemically crosslink *A. thaliana* proteins for mass spectrometry analysis. Klockenbusch and Kast (2010) published a paper on the optimisation of using formaldehyde to crosslink *A. thaliana* proteins. Due to the expense of this technique, and a lack of experience within the research group, this technique was not chosen for validation experiments.

BiFC

Bimolecular fluorescent complementation involves tagging two proteins of interest with the N- or C-terminal half of a monomeric fluorescent protein. If the proteins of interest interact the two halves of eYFP can reform and emit light when excited. Not only does this test interaction, but indicates where this interaction occurs *in vivo*. The large tags may of course interfere with protein expression and may cause steric hindrance. A review discussing, in detail, the advantages and disadvantages of using BiFC *in planta*, along with some large-scale studies can be read in Miller et al. (2015). Another paper of note that highlights potential pitfalls of BiFC *in planta*, is Horstman et al. (2014). It also outlines steps to follow to obtain the most reliable results. BiFC was selected for its ease of implementation, due to availability of Gateway® vectors containing the coding sequence for each of the eYFP halves.

FRET-FLIM

Fluorescence resonance energy transfer - fluorescence lifetime imaging (FRET-FLIM) relies on the transfer of light energy from a donor fluorophore to an acceptor. For example, a laser excites GFP and the emitted light then excites RFP, if the RFP is in close enough proximity (under 10nm). This would then cause emission of red light. The intensity and lifetime of the light emitted from the donor can be measured. The shorter the lifetime of the donor's emission, the

closer the two fluorescent proteins are to each other. This technique provides not only information about binary interactions, but also their strength. (Held et al., 2008) give a through discussion of a multitude of techniques suitable for imaging plant endomembrane systems, including FRET-FLIM. A more specfic review that details applications of FRET-FLIM in plant systems can be found in Bücherl et al. (2014). Although the fluorescent proteins could cause steric hindrance, this technique was chosen since the genes were already in appropriate vectors.

Yeast-two-hybrid

Yeast-two-hybrid (Y2H) is a technique traditionally used for transcription factors, as proteins have to travel into the yeast nucleus. Here, if they interact, they will bring their protein tags (a DNA binding domain (BD) and an transcription activation domain (AD)) into proximity, allowing the transcription of a set of genes. If these genes are transcribed, the yeast can grow on selective media, or will express reporter proteins, the production of which can be measured. There have been many groups that have used this technique, including the Arabidopsis Interactions Viewer, which uses data from BIND (Biomolecular Interaction Network Database) (Consortium, 2011). Despite the proteins of interest being membrane proteins, this technique was used because other reticulon proteins had been found this way (Hwang and Gelvin, 2004).

Split Ubiquitin

The split ubiquitin technique involves binding the N-terminal half of ubiquitin to one protein and the C-terminal half to the second protein of interest. If the proteins interact, the two halves of ubiqutin will be brought together, activating ubiquitin binding proteins (UBPs). These will cleave the reporter protein attached to the C-terminal ubiquitin tag. The expression of this reporter can then be measured. Detailed manuals can be found in Grefen et al. (2009) and Obrdlik et al. (2004). This technique has been successfully used for membrane proteins (Chen et al., 2012b), making it a more desirable technique than yeast-two-hybrid. Our collaborators at Oxford Brookes had endeavoured for over a year in order to apply the technique to the detection of reticulon interactors, with no success. For this reason, it was decided that split-ubiquitin was not to be used.

SPR

Surface plasmon resonance (SPR) measures the binding and dissociation of ligands. A protein (or receptor) is cross linked to a gold chip and ligands are washed over the surface of the chip. If a ligand binds, this alters the weight of the chip, resulting in a change in the light refraction angle. This change in the angle of light over time, can be translated into binding-affinity and dissociation constants. Several papers have used this technique to study *A. thaliana* protein interaction:

Lee et al. (2012); Patching (2014); Schweiger et al. (2013). Some membrane proteins have been successfully studied using SPR (Patching, 2014), however it is difficult due to needing to keep the membrane proteins either immobilised within their natural membrane, or reconstituted into a mimetic membrane, or solubilised into detergent. Maintaining the shape and activity of the membrane proteins presents a real challenge (Patching, 2014). Though interestingly SPR microscopy has been used for proteins in plasma membrane membranes (Patching, 2014). In this project both the bait and prey would be membrane proteins, which has yet to be achieved through SPR.

MST

Microscale thermophoresis (MST) is a biophysical approach that *is* suitable for membrane proteins. Jerabek-Willemsen et al. (2011) provide an excellent review on the theory of MST. There are no size limitations and the proteins are not fixed on a substrate, though the proteins have to be purified. This technique can also involve the use of fluorescent tags. By heating an area of liquid, containing the proteins of interest, with an infra-red (IR) laser,the proteins will move away from that area as the temperature increases. If proteins are bound together, they will move slower than if not interacting. The amount of fluorescence in the area surrounding the IR laser can be measured, indicating how quickly the proteins are moving. The Schweiger et al. (2013) paper highlights the advantages of combining MST with SPR to clarify protein-protein interactions. Not having focused on techniques to purify proteins, this technique was not chosen.

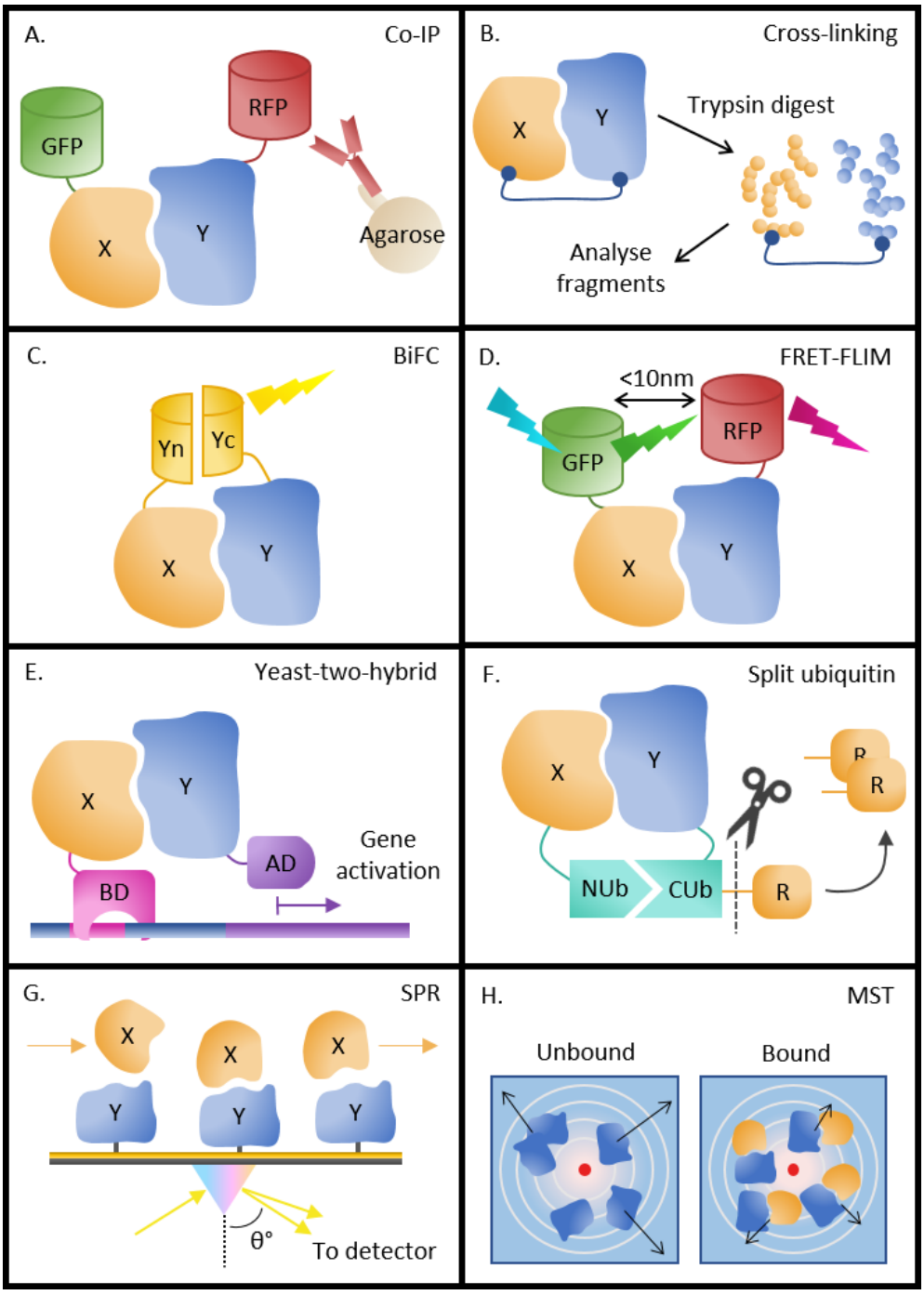

Figure 3.1: ***Methods to validate protein interactions****. X and Y are proteins that are interacting. A) Co-immunoprecipitation with fluorescent protein tags, GFP and RFP. B) Cross linking and mass spectrometry analysis. C) Bimolecular fluorescence complementation, where Yn is the N-terminal half of YFP and Yc is the C-terminal half of YFP. D) FRET-FLIM with GFP as donor fluorophore and RFP as the acceptor. E) Yeast-two-Hybrid. AD = activation domain, BD = Binding domain. F) Split ubiquitin. NUb = N-terminal domain of ubiquitin. CUb = C-terminal domain of Ubiquitin. R = Reporter protein. G) Surface plasma resonance. θ° is the angle of refracted light. H) Microscale thermophoresis.*

3.2 Aims and approach

Several proteins were identified, through co-immunoprecipitation and mass spectrometry, as interacting with YFP-RTN13 in developing *Arabidopsis thaliana* seed. Having successfully cloned some of these putative interactors, their interaction with RTN13 had to be validated. By using a variety of approaches, true interactors can be found, whilst remaining aware of the limitations of each technique.

Aims

- To use co-immunoprecipitation and western blotting to assess whether RTN13 and the potential interactors can pull each other down. Both fluorescent tags, GFP and RFP, were targeted as well as smaller HA and FLAG tags.
- To use FRET-FLIM to investigate binary interaction between RTN13 and the potential interactors that reside on the ER network.
- To use bimolecular fluorescence complementation to test binary interaction between RTN13 and potential interactors.
- To use yeast-2-hybrid to test binary interaction between RTN13 and the putative interactors.

3.3 Results

3.3.1 Reverse co-immunoprecipitation with fluorescent tags

To confirm interaction between RTN13 and the proteins identified through mass spectrometry, reverse co-immunoprecipitation using fluorescent tags was initially employed. RTN13 was cloned into pGWB606, which carried an eGFP tag at the N-terminus. This construct, along with the RFP tagged interactors was transformed into *Agrobacterium tumefaciens* and subsequently infiltrated into *Nicotiana benthamiana*. All infiltrations were done with an OD_{600} of 0.25 for each construct. RFP-Trap®_A was used to pull down the interactors. A western blot with anti-GFP-HRP was used show whether or not eGFP-RTN13 was co-immunoprecipitated.

A mock infiltration, consisting of an infiltration without *A. tumefaciens*, was used as a negative contol. This would show if there was any contamination, or if any *N. benthamiana* proteins were detectable through the western blot. RFP-RTN3 was infiltrated on its own as another negative control. Although it would be pulled down by the RFP-Trap®_A, nothing should be detected on the blot. eGFP-RTN13 was also infiltrated alone, as it would not be pulled down by the RFP-Trap®_A, but should be detected in the 'Unbound' and 'Homogenate' blots. A co-infiltration of RFP-RTN3 and eGFP-RTN13 was used as a positive control. They had previously been shown to interact by collaborators at Oxford Brookes. Based on the localisation and expression (figure 2.6) the following interactor constructs were used: CBR1-RFP, GB2-RFP, RFP-LPL, SMT2-RFP, SYTa-RFP and RFP-RTN1/4/5. These were co-infiltrated alongside eGFP-RTN13.

A Coomassie stain of the 'Homogenate' sample was used to show equal loading of protein. This of course does not indicate how much infiltrated protein was expressed in the leaf sample. Despite having equal OD_{600} for each construct, it is not guaranteed that all the proteins are expressed exactly the same amount across all infiltrations, despite being under the same promoter. Figure 3.2 shows the 'Homogenate' Coomassie stain. All the lanes look equal by eye, except for the RFP-RTN1 lane, which looks slightly weaker.

eGFP-RTN13 should run at approximately 51 kDa (24 kDa for RTN13 and 27 kDa for eGFP). Figure 3.3 shows the western blots for the first reverse co-immunoprecip-itation. There are no bands in any of the three blots in the mock or RFP-RTN3 only lanes. This indicates that there was no contamination of the samples and that the anti-GFP-HRP antibody did not bind to RFP. The eGFP-RTN13 only sample has bands at the correct size in the 'Unbound' and

'Homogenate' blots. This shows that although it was present in the sample, it did not bind to the RFP-Trap®_A. All three blots have strong bands, at just over 46kDa, for the RFP-RTN3 and eGFP-RTN13 co-infiltration indicating that they are interacting. The 'Homogenate' blot does show some fainter bands at approximately 25kDa. This is likely to be 'free' GFP, which was formed when the tissue was homogenised.

As can be seen in the 'Bound' lanes in figure 3.3, RFP-LPL, CBR1-RFP, SYTa-RFP, RFP-RTN5 and RFP-RTN1 all successfully pulled down eGFP-RTN13, with varying strength. GB2-RFP, SMT2-RFP and RFP-RTN4 did not. RFP-RTN5 and RFP-RTN1 have noticeably weaker bands in the 'Unbound' and 'Homogenate' blots, however this does not seem to affect the 'Bound' blot. This could suggest that although there was poor expression of eGFP-RTN13 in the leaf tissue, the interactions of RTN5, RTN1 with RTN13 are very strong, hence the enrichment seen in the 'Bound' lanes.

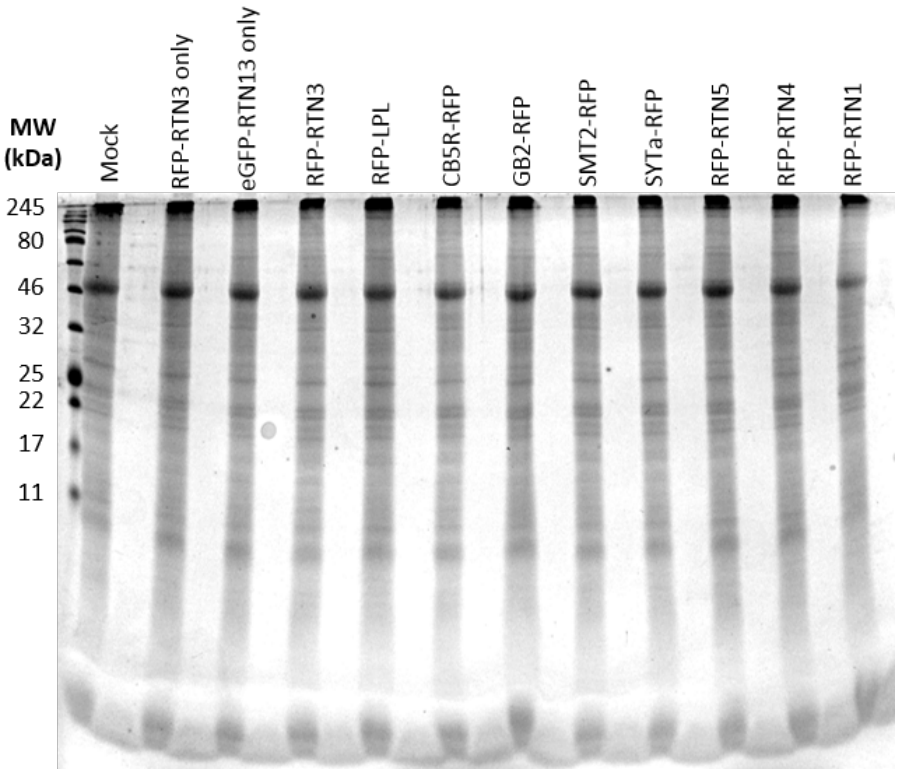

Figure 3.2: ***Reverse co-immunoprecipitation total protein Coomassie from N. benthamiana leaf infiltrations.*** *Total protein sample was taken from supernatant of the homogenate prior to antibody addition. Lanes to the right of and including RFP-RTN3 are co-infiltrations in N. benthamiana of eGFP-RTN13 and the labelled construct. The mock sample was an infiltration without A.tumefaciens. A lane was left blank in-between each sample. This shows approximately equal loading of total protein for each sample.*

This reverse co-immunoprecipitation experiment was repeated, and the results

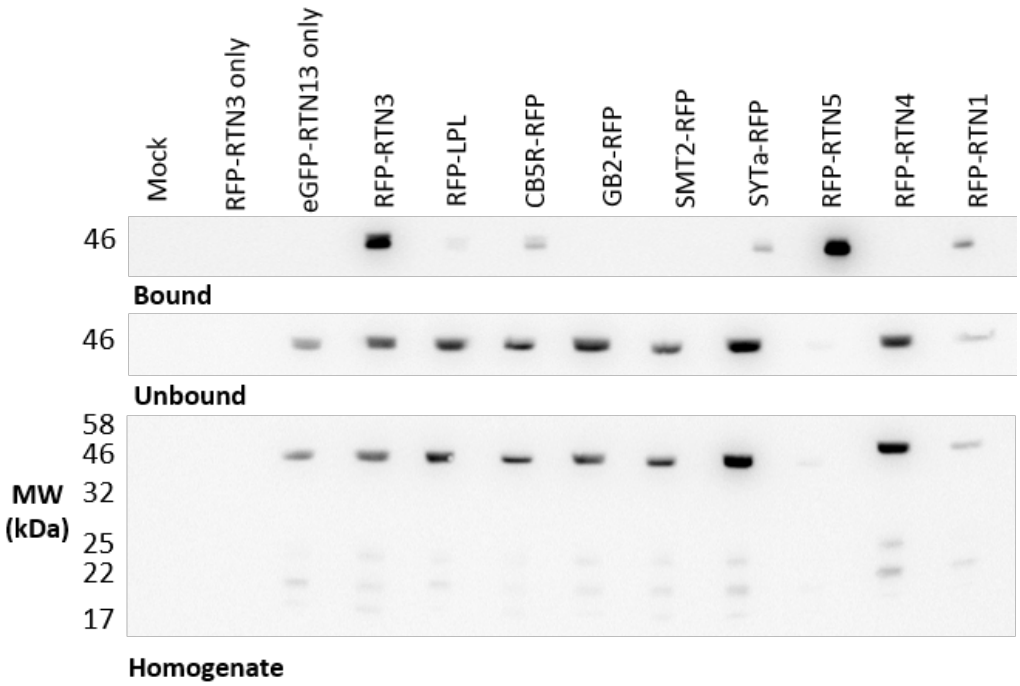

Figure 3.3: ***Reverse co-immunoprecipitation western blots from N. benthamiana infiltrations****. Co-immunoprecipitation used anti-RFP Trap_A. Bands were visualised with an anti-GFP antibody. The mock sample was an infiltration without A.tumefaciens. Lanes to the right of and including RFP-RTN3 are eGFP-RTN13 co-infiltrated with the labelled construct. The 'Bound' samples are from the RFP-Trap_A pull down and show bands at approximately 46 kDa. The 'Unbound' samples are from the supernatant of the pull down showing bands at approximately 46 kDa. The 'Homogenate' samples are aliquots taken prior to the RFP-Trap_A being added. Bands at approximately 46 kDa indicate YFP-RTN13. Lower bands indicate free YFP.*

from the second set of western blots can be seen in figure 3.4. The repeat shows very similar results to the initial reverse co-immunoprecipitation. The mock and the RFP-RTN3 only samples have no bands in the 'Bound' or 'Unbound' blots. The eGFP-RTN13 only lane has a strong band at approximately 46 kDa in the 'Unbound' blot, and no bands in the 'Bound' blot. This shows that the negative controls worked in this repeat. There are faint bands at approximately 25 kDa in the 'Unbound' blot, these are likely to be free GFP, as seen in the 'Homogenate' blot in figure 3.3. RFP-RTN3 does pull down eGFP-RTN13 again, as shown by the strong band in the 'Bound' blot in figure 3.4.

CBR1-RFP, SYTa-RFP, RFP-RTN5 and RFP-RTN1 all successfully pulled down eGFP-RTN13. The bands in the reticulon lanes were stronger than the others, suggesting a stronger interaction with eGFP-RTN13. In this experiment RFP-LPL does not appear to pull down eGFP-RTN13, unlike in the other blot. This could simply be due to lower protein expression. In the first co-immunoprecipiation, the band in the RFP-LPL lane was weak, which could indicate that although RFP-LPL and eGFP-RTN13 interact, they do so weakly. Generally the bands in the 'Unbound' blot are uniform in strength, however the RFP-RTN5 and RFP-RTN1 lane both have weaker bands, as in the previous experiment. This could indicate a high affinity for binding to eGFP-RTN13 (therefore leaving little protein left in the 'Unbound' supernatant), but RFP-RTN3 does not follow this trend.

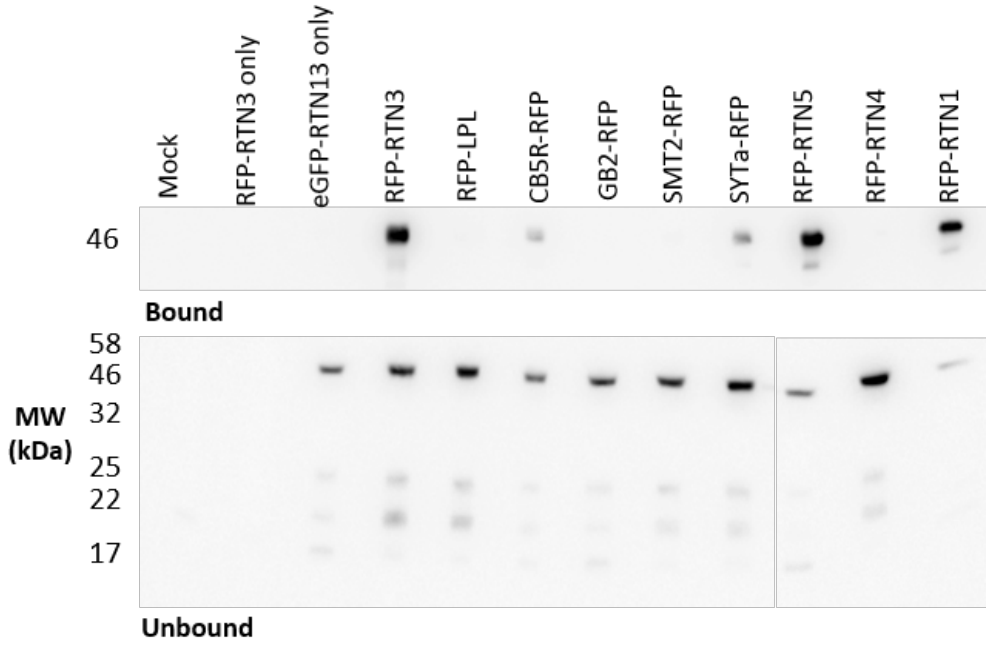

Figure 3.4: ***Reverse co-immunoprecipitation western blots from N. benthamiana infiltrations repeat****. Co-immunoprecipitation used anti-RFP Trap_A. Bands were visualised with an anti-GFP antibody. The mock sample was an infiltration without A.tumefaciens. Lanes to the right of and including RFP-RTN3 are eGFP-RTN13 co-infiltrated with the labelled construct. The 'Bound' samples are from the RFP-Trap_A pull down and show bands at approximately 46 kDa. The 'Unbound' samples are from the supernatant of the pull down showing bands at approximately 46 kDa. The 'Homogenate' samples are aliquots taken prior to the RFP-Trap_A being added. Bands at approximately 46 kDa indicate YFP-RTN13. Lower bands indicate free YFP.*

3.3.2 Forward co-immunoprecipitation with fluorescent tags

To confirm that the proteins could pull each other down in both directions, a co-immunoprecipitation that targeted eGFP-RTN13 and western blots identifying the RFP-tagged interactors was performed. *N. benthamiana* was co-infiltrated with eGFP-RTN13 and the RFP-tagged proteins, as in the previous co-immunoprecipitations. GFP-Trap®_A was used to pull down eGFP-RTN13, and a primary anti-RFP antibody (with a secondary anti-mouse-HRP antibody) was used to identify any interactors that were pulled down. The expected weights of the proteins can be seen in table 3.1. The same controls were used as previously. A mock infiltration, with no *A. tumefaciens*, was used to indicate any contamination. RFP-RTN3 was infiltrated alone to show that the GFP-Trap®_A was specific to GFP and eGFP-RTN13 was also infiltrated alone to show that the anti-RFP and anti-mouse-HRP antibodies were specific. RFP-RTN3 and eGFP-RTN13 were co-infiltrated as a positive control.

Protein	**kDa**	**Protein**	**kDa**
eGFP- RTN13	51	RFP-LPL	64
RFP-RTN1	58	CBR1-RFP	59
RFP-RTN3	58	GB2-RFP	50
RFP-RTN4	56	SMT2-RFP	67
RFP-RTN5	56	SYTa-RFP	93

Table 3.1: ***Weight of proteins with a GFP or RFP tag in kDa****. GFP and RFP weigh approximately 27 kDa.*

Figure 3.5 shows the 'Bound' and 'Unbound' blots for this co-immunoprecipitation, figure 3.6 shows the 'Homogenate' blot. There are no bands in the mock or eGFP-RTN13 only lanes in any of the three blots. This indicates that the negative controls have worked, and that the antibodies used in blotting were specific. There is a faint band in the RFP-RTN3 only lane between 46 and 80 kDa in the 'Bound' blot. Given that there was no GFP present to be interacting with the GFP-Trap®_A, there should be no bands in this lane. This could indicate that the GFP-Trap®_A is not highly specific, and can bind RFP. It could indicate that the samples were not washed enough, and some unbound RFP-RTN3 was present. Additionally it could mean that the anti-RFP antibody is more sensitive than the anti-GFP-HRP used in previous western blots. In the 'Unbound' and 'Homogenate' blots for the RFP-RTN3 only lane there are several bands. The band at 46 kDa is likely to be RFP-RTN3, the upper band, could be RFP-RTN3 self-interaction. The band at approximately 25 kDa is likely to be free RFP.

As in the previous co-immunoprecipitation, eGFP-RTN13 and RFP-RTN3 in-

teract, as shown by the bands in the 'Bound' blot. The upper band in the 'Bound' blot is potentially RFP-RTN3 self-interaction, whereas the lower blot is the correct size for RFP-RTN3 alone. The lowest band in the 'Unbound' and 'Homogenate' blots, at 25 kDa, is likely free RFP.

There are clear bands in the CBR1-RFP, GB2-RFP, RFP-RTN5 and RFP-RTN1 lanes, at the appropriate sizes, in the 'Bound blot'. This indicates that eGFP-RTN13 has successfully interacted with these proteins. As with the RFP-RTN3 sample, there appear to be multiple bands in the RFP-RTN5 and RFP-RTN1 lanes, perhaps due to self interaction. In the 'Unbound' and 'Homogenate' blots, every lane has additional bands at approximately 25 kDa, indicative of free RFP.

There are no bands for RFP-LPL, SMT2-RFP, SYTa-RFP and RFP-RTN4 in the 'Bound' blot. RFP-LPL is present in both the 'Unbound' or 'Homogenate' blots, proving that it is not interacting with eGFP-RTN13. For SYTa-RFP and RFP-RTN4 however, there are no bands in the 'Unbound' or 'Homogenate' blots, suggesting that those proteins are not actually present in the samples. Therefore one cannot say whether they are interacting or not with eGFP-RTN13. There are bands for SMT2-RFP in the 'Unbound' and 'Homogenate' blots, however they are faint, suggesting poor protein expression. The reduced amount of protein may be why nothing is seen in the 'Bound' blot, or it could indicate there was no interaction with eGFP-RTN13.

3.3.3 Co-immunoprecipitation with HA and FLAG tags

To ascertain whether the RFP and GFP tags were interfering with protein-protein interaction through steric hindrance, a third co-immunoprecipitation was done. Proteins were tagged with an HA tag (hemagglutinin, from human influenza virus HA protein) or a FLAG® tag (a specifically designed, short, hydrophilic 8-amino acid peptide). This was done by inserting the genes of interest into pEarleyGate201 and pEarleyGate202 respectively. *N.benthamiana* was co-infiltrated with FLAG-RTN13 and HA-tagged interactors. All infiltrations were done with an OD_{600} of 0.25. The co-immunoprecipitation was performed with an anti-HA antibody. Protein A Sepharose was then added to bind the anti-HA antibody, and enable the proteins of interest to be pulled down. To detect FLAG-RTN13 western blots were performed with an primary anti-FLAG antibody and a secondary anti-mouse-HRP antibody. As with the previous co-immunoprecipitations, a mock infiltration was used to indicate any contamination. FLAG-RTN13 was infiltrated alone to assess the specificity of the anti-HA antibody and the Protein A

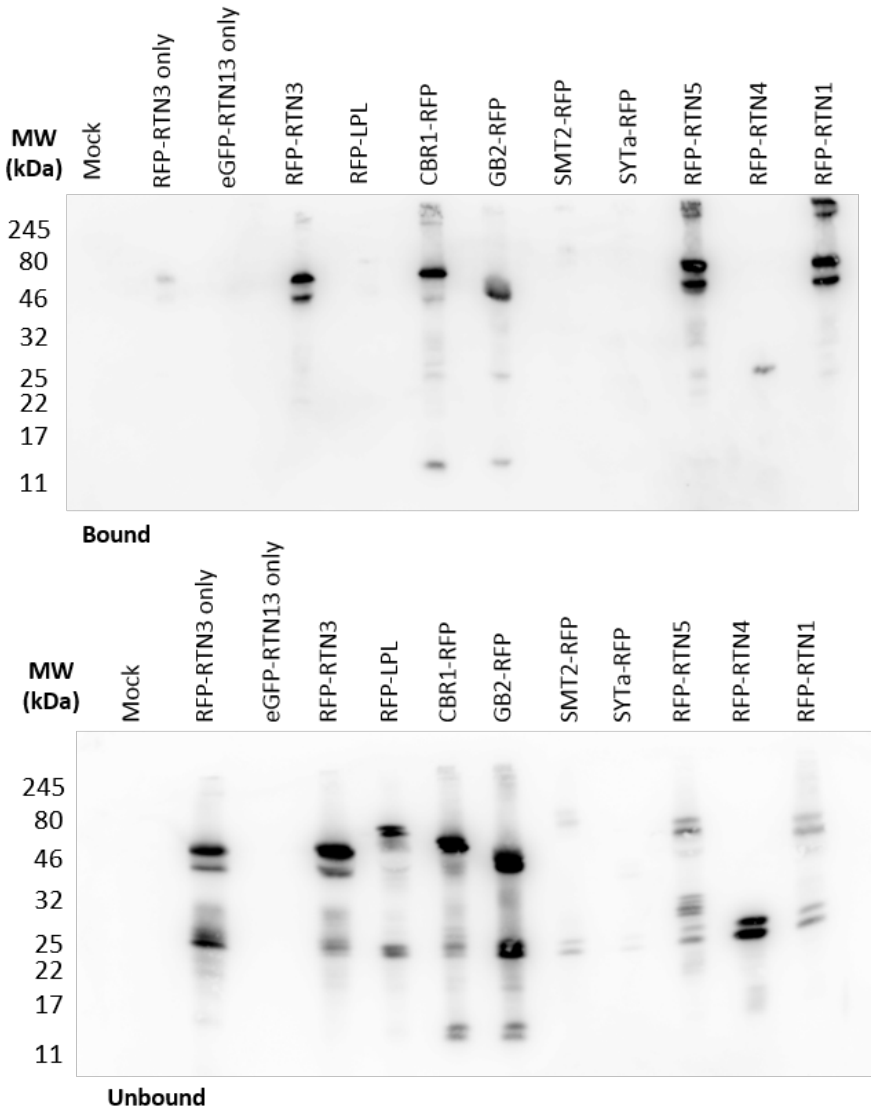

Figure 3.5: ***Forward co-immunoprecipitation western blots from N. benthamiana leaf infiltrations****. GFP-Trap_A was used to pull down eGFP-RTN13 and a primary anti-RFP antibody and secondary anti-mouse-HRP antibody were used in the western blot to identify any interactors that were successfully pulled down. The mock sample was an infiltration without A.tumefaciens. The 'Bound' samples are from the bead pull down. The 'Unbound' samples are from the supernatant of the pull down. Predicted protein weights can be found in table 3.1. Bands at 27 kDa are free-RFP. The bands from the 'Bound' blot suggest that RTN13 interacted with RTN3, CBR1, GB2, RTN5 and RTN1. Given the weakness of the SMT2, SYTa and RTN4 bands in the 'Unbound' blot it may be possible that they interacted with RTN13 but the protein concentration was too low to be detected in the 'Bound' fraction.*

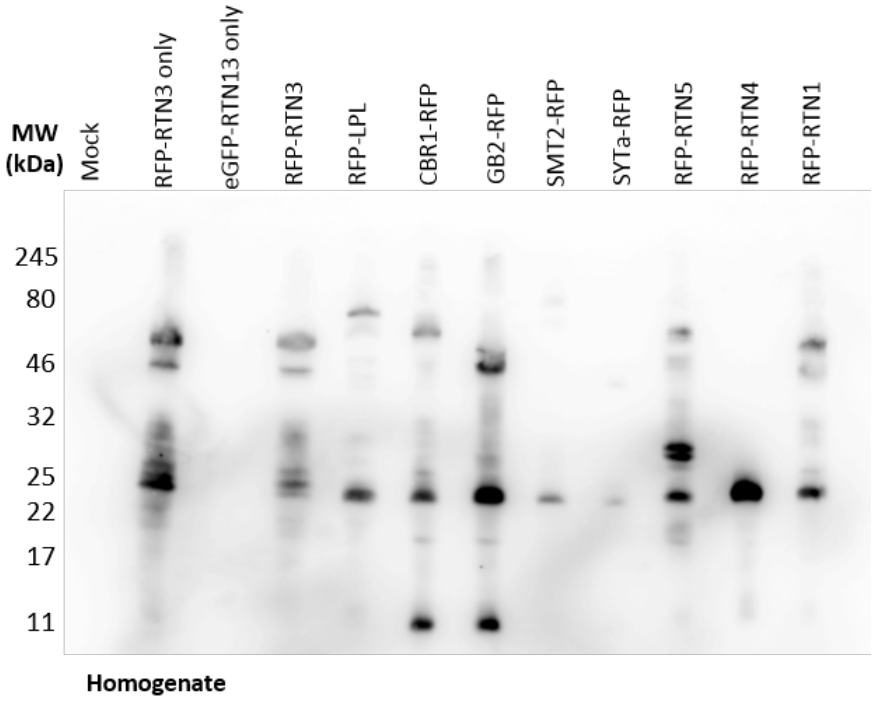

Figure 3.6: ***Forward co-immunoprecipitation 'Homogenate' western blot from N. benthamiana leaf infiltrations.*** *A GFP-Trap_A was used to pull down eGFP-RTN13 and a primary anti-RFP antibody and secondary anti-mouse-HRP antibody were used in the western blot to identify any interactors that were successfully pulled down. The 'Homogenate' samples are aliquots taken prior to antibody being added. The mock sample was an infiltration without A.tumefaciens. The lack of banks in the eGFP-RTN13 only lane suggest the antibodies were specific to RFP. The lack of appropriate sized bands in the SMT2, SYTa and RTN4 samples suggest that these proteins were not present in the samples.*

sepharose. HA-RTN13 was infiltrated alone to assess the specificity of the anti-FLAG and anti-mouse-HRP antibodies. The positive control was a co-infiltration of HA-RTN13 and FLAG-RTN13. RTN3 was not used as the positive control, because the gene was not in an entry vector or available as an attB product.

A Coomassie stain of the 'Homogenate' samples show approximately equal loading of total protein (figure 3.7), though this does not indicate that the level of protein expression was equal in all samples.

Figure 3.8 shows the 'Bound', 'Unbound' and 'Homogenate' western blots for this co-immunoprecipitation. The bands in the 'Homogenate' and 'Unbound' blots are between 17 and 22 kDa. This is smaller than expected, as FLAG-RTN13 should run at approximately 24 kDa. Since there is only 1 band in the 'Homogenate' and 'Unbound' blots, and there are no bands in the mock and HA-RTN13 lanes, this indicates that the bands are indeed FLAG-RTN13. The double bands that appear towards the right of the blot, are likely due to movement of the PVDF

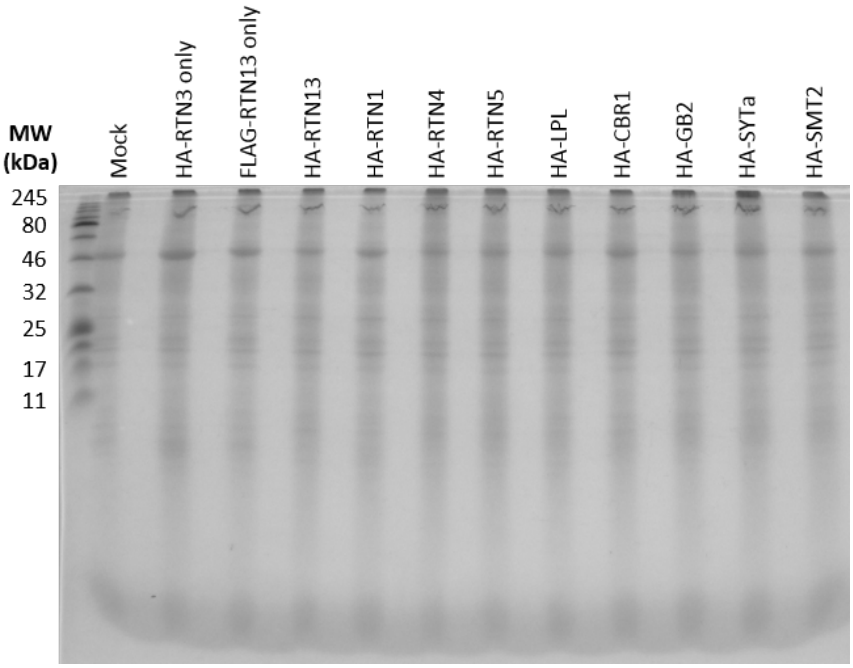

Figure 3.7: ***HA/FLAG co-immunoprecipitation total protein Coomassie from N. benthamiana leaf infiltrations****. Aliquots of the homogenate were taken prior to antibody addition. The mock sample was an infiltration without A.tumefaciens. This gel indicates that the loading of total protein in each sample was similar.*

membrane during transfer. The breaks in the 'Unbound' blot are due to samples being loaded in a different order. The original 'Bound' and 'Unbound' blots, with the ladders can be found in appendix figures 7.15 and 7.14.

In the 'Bound' blot, the mock lane contains no bands, which suggests there was no contamination. However, there are multiple bands in all the other lanes. The three (perhaps four) bands that are present in the HA-RTN13 lane, are also present in the majority of the other lanes. One possible explanation could be that the anti-mouse antibody is binding to Protein A. Protein A (a 42 kDa protein) will bind any IgG antibodies. The anti-mouse-HRP antibody is an IgG antibody from goat. The varying weights could be Protein A bound to the anti-mouse-HRP antibody, which may or may not be bound to the anti-FLAG which may or may not be bound to the FLAG-tagged protein. Given the weight of the bands in the 'Homogenate' and 'Unbound' blots, and the bands that appear in the HA-RTN3 only lane in the 'Bound' plot, it is likely that the lower band (between 17 and 22 kDa) is FLAG-RTN13. This would then suggest that all proteins, except HA-CBR1, pulled down FLAG-RTN13.

Table 3.2 summarises the outcomes of the western blotting experiments, in order to clarify which proteins were seen to interact with RTN13 constructs. RTN1, RTN3 and RTN5 were repeatedly seen to interact with RTN13, which is un-

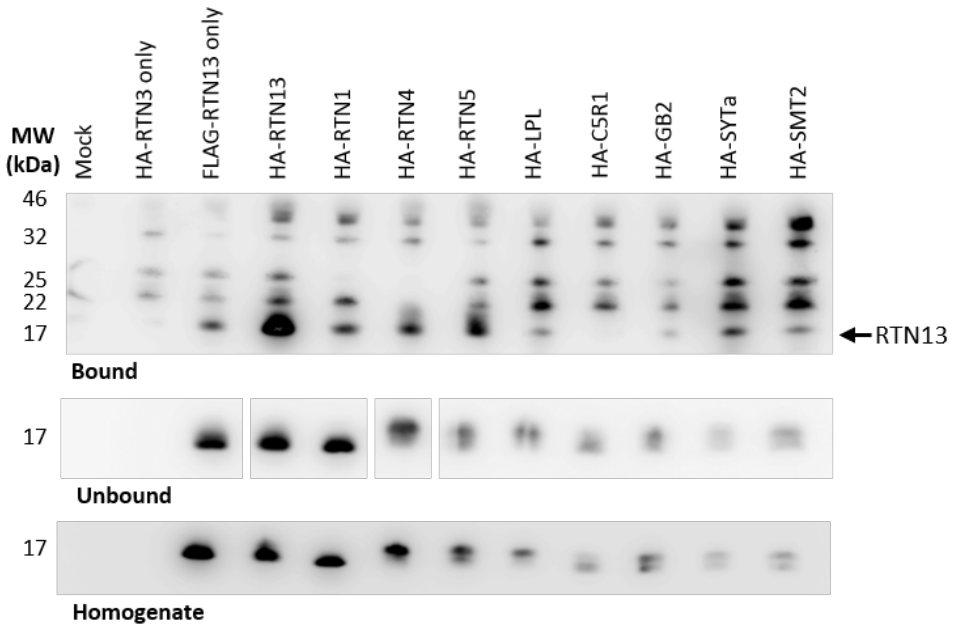

Figure 3.8: ***HA/FLAG co-immunoprecipitation western blots from N. benthamiana leaf infiltrations****. The co-immunoprecipitation was performed with an anti-HA antibody, and the western blots were developed with a primary anti-FLAG antibody and a secondary anti-mouse-HRP antibody. The mock sample was an infiltration without A.tumefaciens. Lanes to the right of and including HA-RTN3 are FLAG-RTN13 co-infiltrated with the labelled construct. The 'Bound' samples are from the bead pull down. The 'Unbound' samples are from the supernatant of the pull down. The 'Homogenate' samples are aliquots taken prior to antibody being added. Based on the size of the bands present in the 'Unbound' and 'Homogenate' blots (approximately 17 kDa), the lowest band in the 'Bound' blot (as indicated by the arrow) is FLAG-RTN13. The 'Bound' and 'Unbound' blots next to the ladder can be seen in the appendix (figure 7.14)*

surprising given the known oligomerisation of reticulons. Interestingly, RTN4 was only seen to interact with RTN13 in the HA/FLAG co-immunoprecipitation. There are no obvious reason why these two may not interact, though it could be that the fluorescent tags were somehow inhibiting interaction. Of the non-reticulon proteins, there was not a single one that interacted in all co-immunoprecipitation experiments.

Interactors	Reverse Co-IP 1	Reverse Co-IP 2	Forward Co-IP	HA/FLAG Co-IP
RTN1	✓	✓	✓	✓
RTN3	✓	✓	✓	N/A
RTN4	x	x	N/A	✓
RTN5	✓	✓	✓	✓
LPL	✓	?	x	✓
CBR1	✓	✓	✓	x
GB2	x	x	✓	✓
SYTa	✓	✓	N/A	✓
SMT2	x	x	?	✓

Table 3.2: ***Summary of western blotting validation experiments.*** *'N/A' = Not applicable. The interaction either wasn't tested, or the data does not allow interpretation of interaction. 'Tick' = Interaction between RTN13 and the protein listed was seen. 'Cross' = Interaction between RTN13 and the protein listed was not seen. 'Question mark' = Unsure of outcome.*

3.3.4 FRET-FLIM

A different method that was used to analyse the interaction between RTN13 and the other proteins was fluorescence resonance energy transfer with fluorescence lifetime imaging (FRET-FLIM). *N. benthamiana* was infiltrated with eGFP-RTN13 (the donor) and RFP-tagged interactors (the acceptors). Each construct was infiltrated at an OD_{600} of 0.25. Not all the constructs were used, since measurements had to be taken from the nuclear envelope. The ER network is continuous with the nuclear envelope, and with over-expression of constructs (such those driven by a 35S promoter) there is a clear signal from the nuclear membrane. The ER network itself is too dynamic to enable measurements to be taken over the required 100 seconds. Since, the network is too dynamic, and GB2 and SYTa do not express on the nuclear envelope, these two constructs were not included in this experiment.

As a negative control, eGFP-RTN13 was infiltrated alone. This enabled a measurement of eGFP lifetime, with no acceptor fluorophore present, which set a baseline for no interaction. RFP-RTN3 and eGFP-RTN13 were co-infiltrated to provide a positive control. The co-immunoprecipitation had already shown that they interacted, and previous FRET-FLIM measurements taken by collaborators at Oxford Brookes had shown that these two proteins interacted. The data presented here were taken over two sessions and a minimum of four cells per construct were imaged, except for RFP-RTN4 where only one cell was measured (which had poor expression).

Figure 3.9 shows an example of the output from the FRET-FLIM experimen-

tation. The upper panel (A-E) depicts an eGFP-RTN13 and RFP-RTN3 co-infiltration. The lower panel (F-J) shows the negative control: eGFP-RTN13 infiltrated alone. In the merged channel confocal images (A and F) it is clear to see that the eGFP-RTN13 and RFP-RTN3 image has significantly more yellow pseudo-colouring than the negative control, indicating co-localisation. The region of interest was chosen, as can be seen by the blue lines intersecting in images B and G. The heat-map FLIM images (C and H) show a clear difference in fluorescence lifetime, with the co-infiltration producing a darker blue than the single infiltration (indicating a shorter fluorescence lifetime). This is verified by the lifetime distributions (E and J), where the lifetime in pico-seconds is on the x-axis and the number of pixels is on the y-axis. The fluorescence lifetime for the chosen pixel is displayed in the top-left corner of these lifetime distributions. This value was taken as the fluorescence lifetime for the cell. The data was adjusted so that the Chi-squared residual (χ_r^2) value (as seen in D and I) was close to 1.

Figure 3.10 visually shows the results from the FRET-FLIM data. Comparing the fluorescence lifetime of eGFP-RTN13 and RFP-RTN3 to just eGFP-RTN13, the difference is striking; there is a reduction in lifetime of approximately 0.2 nanoseconds. This is indicative of an interaction. For the other proteins the difference in fluorescent lifetimes is less defined, which perhaps indicates that no interaction was occuring. The numerical data for each pairing can be seen in table 3.3.

To statistically assess whether the other infiltrations did have a shorter fluorescence lifetime than eGFP-RTN13 alone a Student T-Test was performed. Prior to this a F-Test was performed to compare whether the variance of each sample was equal or unequal to eGFP-RTN13 alone (results not shown). Then a one-tailed T-test was performed, assuming equal or unequal variance as appropriate. A one-tailed test was used to assess whether the co-infiltrations had smaller fluorescence lifetimes than the single infiltration. To assess if the fluorescence lifetimes were smaller or larger, a two-tailed test could have been performed. The test statistic, the Critical t value and the p value for each sample can be seen in table 3.4. According to the t-test the following samples did have a significantly smaller fluorescence lifetime compared to the negative control: RFP-RTN3 ($p = 0.000$), RFP-RTN1 ($p < 0.006$), RFP-RTN5 ($p = 0.000$) and CBR1-RFP ($p < 0.026$).

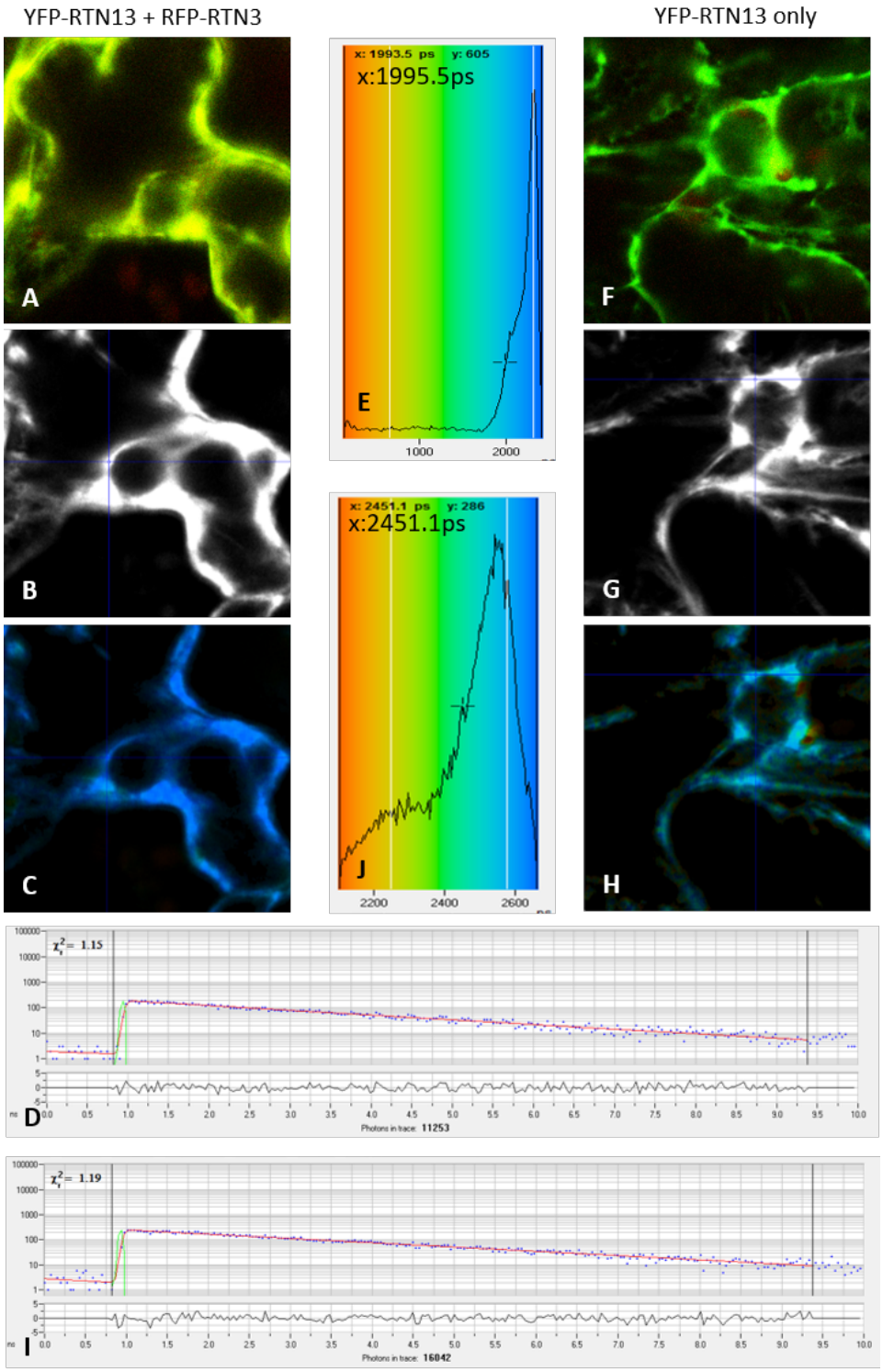

Figure 3.9: ***FRET-FLIM confocal images and output from the FRET-FLIM software****. Images A-E show data from eGFP-RTN13 and RFP-RTN3 infiltration, a successful interaction. Images F-J show the negative control infiltration of eGFP-RTN13 only. A & F) Red and green channel merged confocal images. B & G) Overall fluorescence captured on the confocal over 100 seconds. C & H) Heat map showing fluorescence lifetime measured across the image. D & I) Number of photons and the residuals against time (in nanoseconds). Also shows the* χ_r^2 *value for the data collection. E & J) Distribution of number of pixels against fluorescence lifetime. The shift from right to left between images E and J, shows the difference between the two samples. The value is the top left corner of these images was used as the numerical output.*

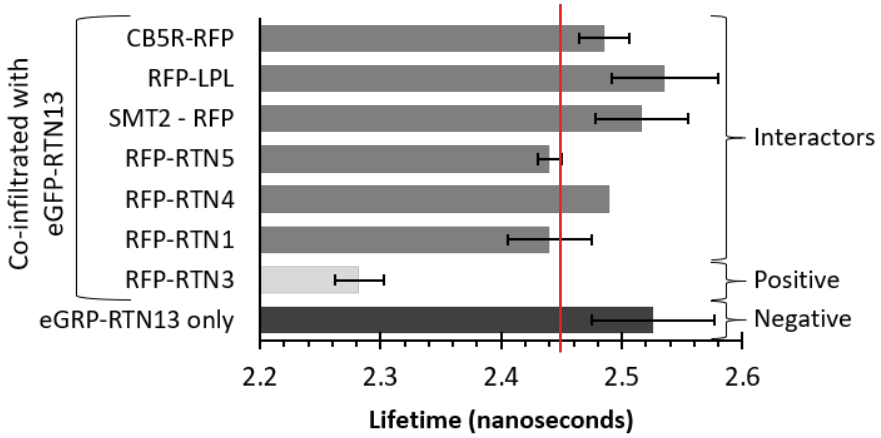

Figure 3.10: ***FRET-FLIM results****. All N. benthamiana leaf samples were infiltrated with eGFP-RTN13 and the construct labelled on the graph. The negative control was eGFP-RTN13 only, setting a benchmark for non-interaction (the red line indicates the minimum value seen from the control, lifetimes below this could be considered as positive interactions). RFP-RTN3 and eGFP-RTN13 show strong interaction, as indicated by the shorter fluorescence lifetime. The error bars show the standard deviation of the sample. A minimum of 4 repeats was performed for all samples, except RFP-RTN4 in which poor expression enabled only 1 sample to be imaged.*

Donor	Acceptor	N	Range	Mean	SD
eGFP-RTN13	-	9	2.45 - 2.60	2.53	0.051
eGFP-RTN13	RFP-RTN3	8	2.26 - 2.30	2.28	0.020
eGFP-RTN13	RFP-RTN1	4	2.39 - 2.47	2.44	0.035
eGFP-RTN13	RFP-RTN4	1	2.49 - 2.49	2.49	-
eGFP-RTN13	RFP-RTN5	4	2.43 - 2.45	2.44	0.008
eGFP-RTN13	SMT2-RFP	8	2.45 - 2.58	2.52	0.039
eGFP-RTN13	RFP-LPL	9	2.48 - 2.60	2.54	0.044
eGFP-RTN13	CBR1-RFP	9	2.44 - 2.50	2.49	0.021

Table 3.3: ***FRET-FLIM results****. N = number of cells imaged. Range = minimum and maximum values obtained from each infiltration. SD = The standard deviation of the sample population.*

	t Stat	t Critical	p Value	Variance?
RFP-RTN3	13.21	1.80	2.15E-08	Unequal
RFP-RTN1	3.02	1.80	0.0058	Equal
RFP-RTN5	4.89	1.83	0.0004	Unqual
SMT2-RFP	0.42	1.75	0.3403	Equal
RFP-LPL	-0.44	1.75	0.3313	Equal
CBR1-RFP	2.18	1.80	0.0259	Unequal

Table 3.4: ***Statistical outcomes of F-test and t-test for FRET-FLIM data****. If the t-critical value was larger than the t-stat value, failed to accept the null hypothesis (the fluorescence lifetimes of the sample was the same as the negative control). The variance was determined equal or unequal through an F-test.*

3.3.5 Bimolecular fluorescence complementation (BiFC)

In BiFC, if the proteins come in close enough contact, the two halves of eYFP will come together, enabling them to be excited and then emit fluorescence. Both halves of eYFP (Yn and Yc) can be tagged on both the N- and C-terminus of the proteins of interest. *N. benthamiana* was co-infiltrated with a construct containing the Yn half, and a second construct containing the Yc half.

Initially Yn-RTN13 and Yc-RTN13 were co-expressed, however no expression was seen, even when the OD_{600} was increased from 0.5 to 1. The BiFC was repeated with the inclusion of the pBin61-P19 vector. The P19 protein is a viral-encoded suppressor of gene silencing (Voinnet et al., 2003), this artificially increases protein expression. Even with the increased OD_{600} and suppression of gene silencing, there was no detectable expression from the Yn-RTN13 and Yc-RTN13 co-infiltration.

Yn-RTN1 and Yc-RTN1 were also co-expressed, and some expression was seen, however it was very weak. Figure 3.11 shows the best images taken of Yn-RTN1 and Yc-RTN1. The expression did not improve with an increased OD_{600}, nor upon addition of P19. The ER network is visible, verifying that RTN1 is self-interaction on the ER network, but it is not clearly defined.

This shows that although the system itself worked, this was not a useful tool with the proteins in question. Since RTN13 could not be shown to self-interact, it was deemed unnecessary to test RTN13 interaction with any other proteins. RTN13 and RTN1 co-infiltrations were tested, but despite an OD_{600} of 1 and presence of P19, no expression was visible.

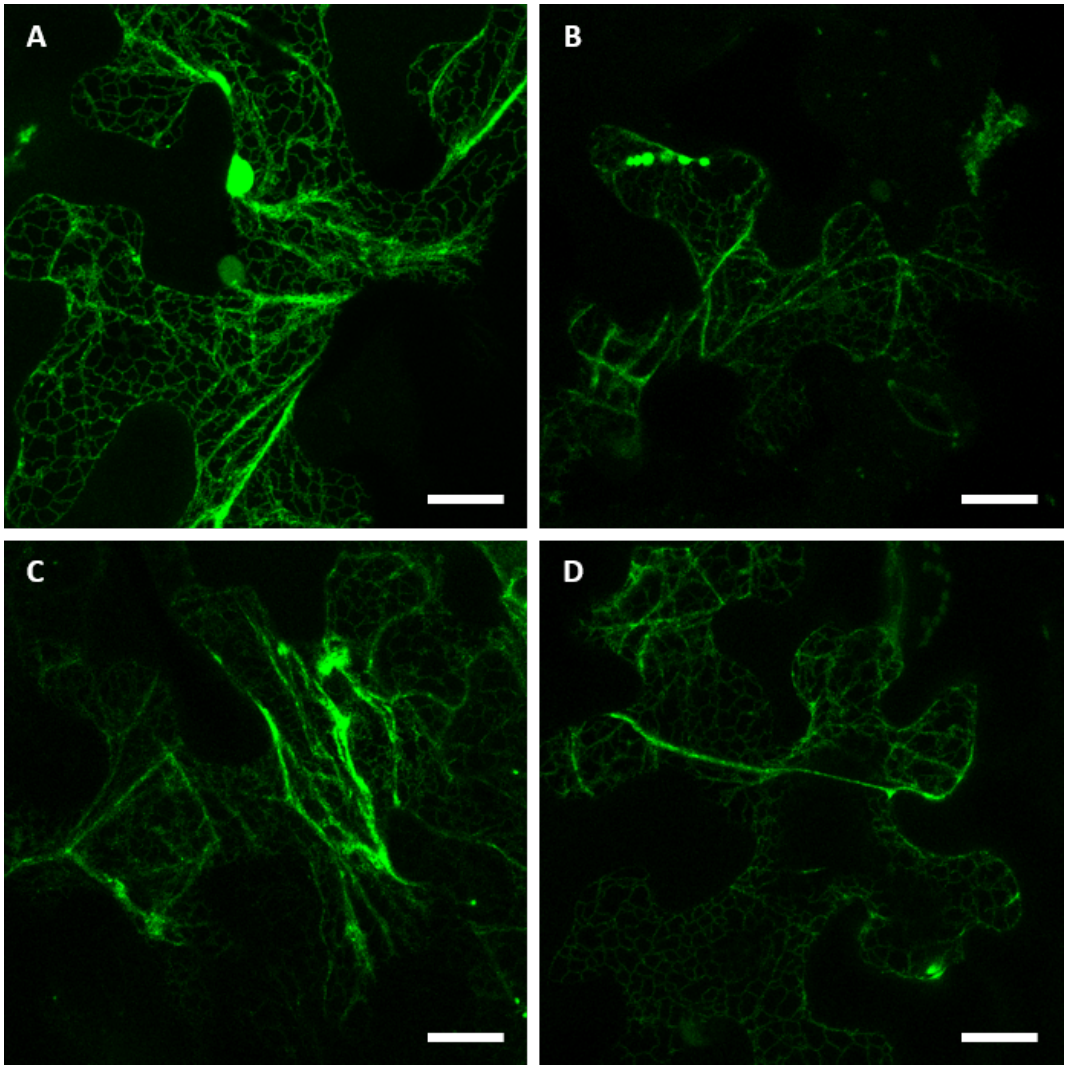

Figure 3.11: ***Bimolecular fluorescence complementation of RTN1 in infiltrated N. benthamiana****. Expression of Yn-RTN1 and Yc-RTN1 in infiltrated lower-epidermis leaf cells of N. benthamiana. The ER network is visible, indicating that RTN1 is self-interacting, despite the low expression. Scale bars are 20µm.*

3.3.6 Yeast-2-hybrid (Y2H)

Y2H is typically used for soluble proteins, as the protein interactions must occur within the nucleus. The first protein is tagged at the N-terminal with a binding domain (BD), and the second protein is tagged with an activation domain (AD). If the proteins interact, the BD and AD will be in sufficiently close contact to enable transcription of reporter genes. In this assay the reporter genes were for the production of histidine and β-galactosidase. Whether the proteins interacted, and the strength of the interaction, could then be measured by yeast-growth on media lacking histidine and production of blue colour in an X-Gal assay.

A YPDA plate was used to allow yeast to mate without any selection pressure. These colonies were then replica plated onto, SD-Leu-Trp, which indicated if mating was successful. The YPDA plate was also replica plated on SD-Leu-Trp-His (with varying concentrations of 3AT). This showed if the proteins encoded in each yeast strain were interacting. Increasing concentrations of 3AT showed any auto-activation of the the reporter genes was occurring

Two transcription factors were used as positive and negative controls: NF-YB9 and NF-YC2. *A. thaliana* has 30 NF-Y (Nuclear Factor-Y) proteins (Calvenzani et al., 2012). These transcription factors form heterotrimers, consisting of an NF-YA, an NF-YB and an NF-YC. NF-YB9 and NF-YC2 in entry vectors were kindly given by Emily Breeze (University of Warwick). These proteins interact with each other, but will not self-interact.

Table 3.5 shows the matrix of protein interactions, as determined by growth on media lacking histidine. In order to obtain clear, distinct colonies, multiple sets of plates were used to complete the matrix. Appendix figures 7.16 - 7.19 show the outcome of each set of plates. The only interactions seen were between AD-RTN4 and BD-RTN1, BD-RTN4 and BD-RTN13. The interaction between AD-RTN4 and BD-RTN1 was weaker than the other two interactions. If these were true interactions, it would be expected to see interaction between AD-RTN1 with BD-RTN4 and AD-RTN13 with BD-RTN4. This suggests that the interactions are false positives, or that the structure of RTN4 enabled the binding domain and activation domain to be in the correct configuration.

Table 3.6 shows the matrix of proteins tested against each other in the X-Gal assay. The plates after 24 hours of incubation can be seen in figures 7.20 and 7.21 in the appendix. Generally any colour development seen was weak. Also the interactions are not reciprocated in both directions, suggesting that they are false positive interactions.

AD → BD ↓	RTN1	RTN4	RTN5	RTN13	RL2	LPL	CB5R	GB2	SMT2	SYTa
RTN1	-	+	-	-	-	-	-	-	-	-
RTN4	-	++	-	-	-	-	-	-	-	-
RTN5	-	-	-	-	-	-	-	-	-	-
RTN13	-	++	-	-	-	-	-	-	-	-
RL2	-	-	-	-	-	-	-	-	-	-
LPL	-	-	-	-	-	-	-	-	-	-
CB5R	-	-	-	-	-	-	-	-	-	-
GB2	-	-	-	-	-	-	-	-	-	-
SMT2	-	-	-	-	-	-	-	-	-	-
SYTa	-	-	-	-	-	-	-	-	-	-

Table 3.5: ***Yeast-two-hybrid interaction matrix one****. The top row indicates the proteins tagged with an activation domain and the first column indicates proteins tagged with a binding domain. - denotes no interaction, as no colony growth on media lacking histidine. + and ++ denotes interactions of increasing strength, measured by colony growth on media lacking histine. Only AD-RTN4 interacted with BD-RTN1, BD-RTN4 and BD-RTN13. Since reciprocal interactions were not seen, these interactions are likely to be false-positives. AD = Activation domain. BD = Binding domain. .*

AD → BD ↓	RTN1	RTN4	RTN5	RTN13	RL2	LPL	CB5R	GB2	SMT2	SYTa
RTN1	-	-	-	-	-	-	+	+	-	+
RTN4	-	-	-	-	-	-	-	-	-	-
RTN5	-	-	-	-	-	-	-	-	-	-
RTN13	-	-	-	-	-	-	-	-	-	-
RL2	+	-	-	-	+	+	-	-	-	-
LPL	-	-	-	-	-	+	+	-	-	-
CB5R	-	-	-	-	-	-	-	-	-	-
GB2	-	-	-	-	-	-	-	-	-	-
SMT2	+	-	-	-	-	+	-	-	-	-
SYTa	-	-	-	-	-	-	-	-	-	-

Table 3.6: ***Yeast-two-hybrid X-Gal assay matrix two****. The top row indicates the proteins tagged with an activation domain and the first column indicates proteins tagged with a binding domain. - denotes no interaction, as seen by no blue colouring, indicating no β-galactosidase production. + and ++ denotes interactions of increasing strength, shown by blue colouring indicating β-galactosidase production. Since reciprocal interactions were not seen, these interactions are likely to be false-positives. AD = Activation domain. BD = Binding domain.*

3.4 Discussion

The various methods used to validate the interactions between RTN13 and the proteins identified by co-immunoprecipitation and mass spectrometry have not provided a clear, definitive answer on whether the putative interactors truly associate with RTN13. Table 3.7 gives an overview of the results from each method, not including the yeast-two-hybrid and BiFC.

From the reverse co-immunoprecipitations, RFP-RTN1, RFP-RTN3, RFP-RTN5, CBR1-RFP and SYTa-RFP were shown to be interacting with eGFP-RTN13. RFP-LPL was shown to be interacting in the first reverse co-immunoprecipiation, but not the second. Given the weak band that was present in the first experiment, it is suspected that the interaction was not detected in the second blot, potentially due to weaker protein expression.

It is interesting that the reverse and the forward co-immunoprecipitation techniques did not produce the same outcome. This could be due to variations in the affinity of the antibodies used, or the protein expression levels in each infiltration. In the forward co-immunoprecipitation RFP-RTN1, RFP-RTN3, RFP-RTN5, CBR1-RFP and GB2-RFP were shown to be interacting with eGFP-RTN13. RFP-RTN4 and SYTa-RFP may have been interacting with eGFP-RTN13, however they were not detected in the 'Homogenate' blot. SMT2-RFP may have been interacting, as there is a very faint band in the 'Bound' blot, however it's also very faint in the 'Homogenate' blot. Since there was an equally faint band in one of the negative controls, it leaves the question as to whether there was enough washing, to be able ascertain whether this was a true interaction, or simply contamination.

The HA/FLAG co-immunoprecipitation is difficult to interpret, due to the multiple bands that were present in the 'Bound' blot. Based on the assumption that the bands in the negative control were contamination, it appears that every protein except HA-CBR1 interacted with FLAG-RTN13. This is at odds with the results of the forward and reverse co-immunoprecipitations; where CBR1 consistently appeared to be associating with RTN13 and RTN4, for example, was not. This could be due to steric hindrance of the fluorescent proteins preventing interactions. Using HA and FLAG tags was meant to reduce this steric hindrance, and indeed, more proteins appear to interact with FLAG-RTN13.

It would have been interesting to test the interactors against each other and themselves in the co-immunoprecipitation experiments. Perhaps then the formation of a potential metabolon could be elucidated. The existence of a metabolon

Interactors	Reverse Co-IP 1	Reverse Co-IP 2	Forward Co-IP	HA/FLAG Co-IP	FRET-FLIM
RTN1	✓	✓	✓	✓	✓
RTN3	✓	✓	✓	N/A	✓
RTN4	x	x	N/A	✓	N/A
RTN5	✓	✓	✓	✓	✓
LPL	✓	?	x	✓	x
CBR1	✓	✓	✓	x	?
GB2	x	x	✓	✓	N/A
SYTa	✓	✓	N/A	✓	N/A
SMT2	x	x	?	✓	x

Table 3.7: ***Overall results of validation experiments****. 'N/A' = Not applicable. The interaction either wasn't tested, or the data does not allow interpretation of interaction. 'Tick' = Interaction between RTN13 and the protein listed was seen. 'Cross' = Interaction between RTN13 and the protein listed was not seen.*

may be something to examine in future, however the number of combinations to test is large. If the non-reticulon interactors were investigated, this would still be 25 separate co-immunoprecipitations, not including positive and negative controls. If RTN1, RTN4 and RTN5 were included this would result in 64 individual co-immunoprecipiations. Besides the feasibility of running all the samples at the same time, the cost would be large, due to the amount of antibody needed. Despite this, it is certainly a consideration for the future.

With first interpretation, the FRET-FLIM experiment seemed to suggest that only RFP-RTN3 was successfully interacting with eGFP-RTN13 (t stat = 13.2, t-crit = 1.8, p = 0.000). Multiple t-tests were used to investigate the hypothesis that the fluorescence lifetimes were the same of all interactors. This statistical analysis suggests that the fluorescence lifetime values for RFP-RTN1 (t stat = 11.0, t-crit = 1.8, p = 0.006), RFP-RTN5 (t stat = 4.9, t-crit = 1.8, p = 0.000) and CBR1-RFP (t stat = 2.2, t-crit = 1.8, p = 0.026) are smaller than the negative control. This could indicate that these proteins at the nuclear membrane are interacting with eGFP-RTN13, though weakly. The main disadvantage with this technique, was that due to the dynamic nature of the ER, the measurements had to be taken on the nuclear membrane. Although the nuclear membrane is continuous with the ER network, this is probably not the native localisation of the proteins of interest. They appeared to be present on the nuclear membrane, perhaps due to the high expression levels induced by the 35S promoter. Chemicals such as latrunculin B could be used to inhibit ER network movement (Runions et al., 2006; Sparkes et al., 2009b), however they are toxic to cells and create an unnatural environment. Finally with this technique the measurement of interaction is simply binary. If these proteins are forming a metabolon, then the other components may be needed to enable interaction, or the presence of

the other members of the complex cause the fluorescent probes to not be close enough contact to transfer fluorescence energy.

The BiFC was not as successful as initially hoped. It is unclear why RTN13 failed to show expression, or why the expression with RTN1 was so poor, even with the presence of P19. It has been noted that RTN13 expresses best with the pVKH vector, which confers higher expression than a normal 35S promoter. Perhaps the BiFC vectors do not provide high enough expression to enable detection. This does not explain however, why RTN1 exhibited poor expression, not only in individual cells, but throughout the infiltrated leaf section.

Yeast-two-hybrid also produced underwhelming results, even taking into account the caveat that it is not usually used for membrane proteins. The histidine selection results were inconsistent, with proteins only showing an interaction in one direction. For example, AD-RTN4 interacted with BD-RTN1, but AD-RTN1 did not interact with BD-RTN4. The X-Gal assay presented similar inconsistencies; interactions were only seen in one direction and none of them were the same as in the previous assay. The colour development was weak, if any, even after 24 hours.

Split-ubiquitin may have been a more appropriate technique, as it is designed for membrane proteins. Future work could include optimising this technique. Given that collaborators at Oxford Brookes failed to achieve results with this method, it was deemed inefficient to have multiple groups working to optimise the same technique.

Another method that would have been interesting to try is microscale thermophoresis. This is a technique that can be investigated, though it is unclear as to whether this is suitable for non-binary interactions. The proteins would also have to be purified, which is a process that would probably need significant development.

It is possible that the proteins considered here are forming a metabolon, as implied in Bassard et al. (2012). The majority of the techniques used here were simply looking at binary interactions. With the co-immunoprecipitation, if *N. benthamiana* has homologues to the other interactors, then it is possible that they will allow the formation of the multi-protein-complex and give a positive outcome.

Despite the mixed results there is evidence from the co-immunoprecipitation experiments that all of these proteins are interacting with RTN13. They are strong candidates, and so are worth investigating further. Do these proteins affect the ER architecture when over-expressed or knocked-out? If so, how? Can the outcomes of such investigation clarify any roles these proteins may have in maintaining or altering ER morphology?

Chapter 4

Investigating the biological function of RTN13 interactors

4.1 Introduction

Despite having no clear answer from the interaction validation experiments, all of the proteins discussed in chapter 3 were assumed to be interactors, as they all interacted with RTN13 in at least one experiment. If these proteins are interacting with RTN13, then it stands to reason that they may influence the shape of the ER.

Over-expressing a protein is one method that can be used to identify whether the protein influences the morphology of the ER. Transient over-expression of YFP-RTN13 and GFP-HDEL in *N.benthamiana* showed that RTN13 caused constrictions in the ER network, seen as pucatate expression of GFP-HDEL in pockets of constricted ER tubules (Tolley et al., 2010) and (Breeze et al., 2016). By over-expressing the proteins of interest with GFP-HDEL, both transiently in *N.benthamiana* and stably in *A. thaliana*, any resulting changes in the ER network may be seen.

Both RTN13 and RL2 have been mutated to identify any changes that occurred in ER morphology with inactive or defective versions of these proteins (Tolley et al., 2010; Lee et al., 2013; Breeze et al., 2016). A mutant line of SMT2 has been studied and it was found that the plants had a shorter stature and smaller siliques (Carland et al., 1999, 2010), though the ER morphology was not investigated. Mutating proteins can be labour intensive and requires knowledge of the protein's structure, or its domains. Information about key amino-acid residues and domains can be found by identifying conserved regions in protein homologs, though knowledge of *how* the proteins function is still needed. Instead of mutating a protein, the gene could be knocked-out. This may also provide information about the functional role of the protein, depending on the level of redundancy in the system.

One method that can be used to create gene knockouts is T-DNA (Transfer-DNA) insertion. DNA is transferred from *Agrobacterium tumefaciens* into a host's genome. This method inserts a non-coding DNA sequence into the gene (or upstream, disrupting promoters). This either blocks the gene from being transcribed, or creates a partial transcript. Unlike transposons, T-DNA will not move within the genome after insertion and is stable for multiple generations. A good review of T-DNA insertion can be found in Radhamony et al. (2004). A T-DNA insertion line of lysophospholipase (LPL2/CSE2) has been previously studied. It was found that the stems were 37% shorter due to the collapsed vessels inside (Vanholme et al., 2013). With such dramatic phenotypic changes, it will be interesting to analyse whether the ER network is also altered. Several of

the proteins of interest have multiple variants, which could mean that functional redundancy causes no changes to occur to the ER network.

By using these over-expression and knockout systems for the proteins of interest, their role in the architecture of the ER may be established through any changes in morphology. This would lead the way into investigating how these proteins function in the regulation of ER morphology.

4.2 Aims and approach

To assess whether the proteins that were found to interact with RTN13 influence the ER morphology, they will be over-expressed and down-regulated in plants co-expressing GFP-HDEL as an ER marker. The over-expression will be achieved using the 35S promoter. If a conformational change is seen in the ER network, then these proteins definitely have a role in influencing the architecture of the ER. The genes will be knocked-out using T-DNA insertion lines. If a conformational change is seen, then these proteins have vital roles in maintaining or influencing the ER network. If no conformational change is seen, then perhaps there is redundancy and other proteins are supporting the role or that they play no role.

4.2.1 Aims

- Image the ER network with transient over-expression of the potential RTN13 interactors in *N. benthamiana*
- Image the ER network with stable over-expression of the potential RTN13 interactors in *A. thaliana*
- Image the ER network of knockouts of the potential interactions using in stable T-DNA insertion *A. thaliana* lines

4.3 Results

4.3.1 Transient over-expression in *N.benthamiana*

To begin to understand whether the proteins that interacted with RTN13 influenced the ER morphology themselves, they were initially transiently over-expressed with GFP-HDEL in *N.benthamiana*. The co-expression with GFP-HDEL would show any alternations in the ER network morphology. RTN1, RTN4 and RTN5 were not shown here as their effect on the ER network is well known and documented (Sparkes et al., 2010). Figures 4.1 and 4.2 show the remaining RFP tagged proteins co-expressed with GFP-HDEL. Although the localisation of these proteins was discussed, one paper that shows comparative confocal images of plant organelles is (Mathur, 2007). This led to the creation of a web-based resource, showcasing confocal images of plant organelles, The Illuminated Cell, which at the time of writing was unfortunately under maintenance (http://illuminatedcell.com/).

CBR1-RFP predominately co-localised with GFP-HDEL, and did not produce any changes in the network. One thing that was noticeable was that CBR1-RFP labelled additional oval structures that were associated with the network, but not labelled by GFP-HDEL. A time-series showing how these ovals interacted with the network can be seen in appendix figure 7.22. They were often found nestled in the gaps of the network and were moved around by the tubules. These structures could have been endosomes or mitochondria. They were unlikely to be Golgi as they were more ovoid than circular. The network structure suggested that CBR1-RFP over-expression did not influence the morphology of the ER.

GB2-RFP overlapped with the GFP-HDEL expression, but was very diffuse. The ER network looked normal, so over-expression of GB2-RFP was unlikely to be affecting the morphology of the ER.

SMT2-RFP over-expression produced an interesting network. SMT2-RFP seemed to label the ER as a continuous network, however it appeared disorganised, with tubules closely bundled together. GFP-HDEL was not longer expressed as a continuous network, but was 'dotted'. This change in the network and distribution of GFP-HDEL was due to the over-expression of SMT2-RFP as in the lower right-hand corner a normal GFP-HDEL network can be seen in a cell not expressing SMT2-RFP.

SYTa-RFP was difficult to image as the puncta were not bright and quite diffuse across the plasma membrane. The images seen in figure 4.2 show that the

ER network labelled by GFP-HDEL was normal and the SYTa-RFP puncta co-localised with the network. There were some large areas of over-saturation in the red channel, which appear to be sites of protein aggregated, perhaps due to over-expression, but these did not appear to co-localise with the network, or disrupt the network.

RFP-LPL was expected to label the ER network (figure 2.6) however, its expression was much more similar to that seen with LPL-RFP. Comparatively LPL-RFP in figure 4.2 here looks more similar to what was expected with RFP-LPL. In each case, no change in GFP-HDEL expression nor in the ER morphology was seen.

Overall, except from SMT2 over-expression, the over-expression of these proteins did not affect the morphology of the ER. SMT2 obviously does play a role in shaping the ER network, though from these images it is unclear what precisely that is. The dotted appearance of the GFP-HDEL, suggests the tubules are constricted, and so the lumen is smaller. The other may not affect the network alone, as in the Lee et al. (2013) paper where RL2 over-expression did not affect a change in the network until co-expressed with RTN13.

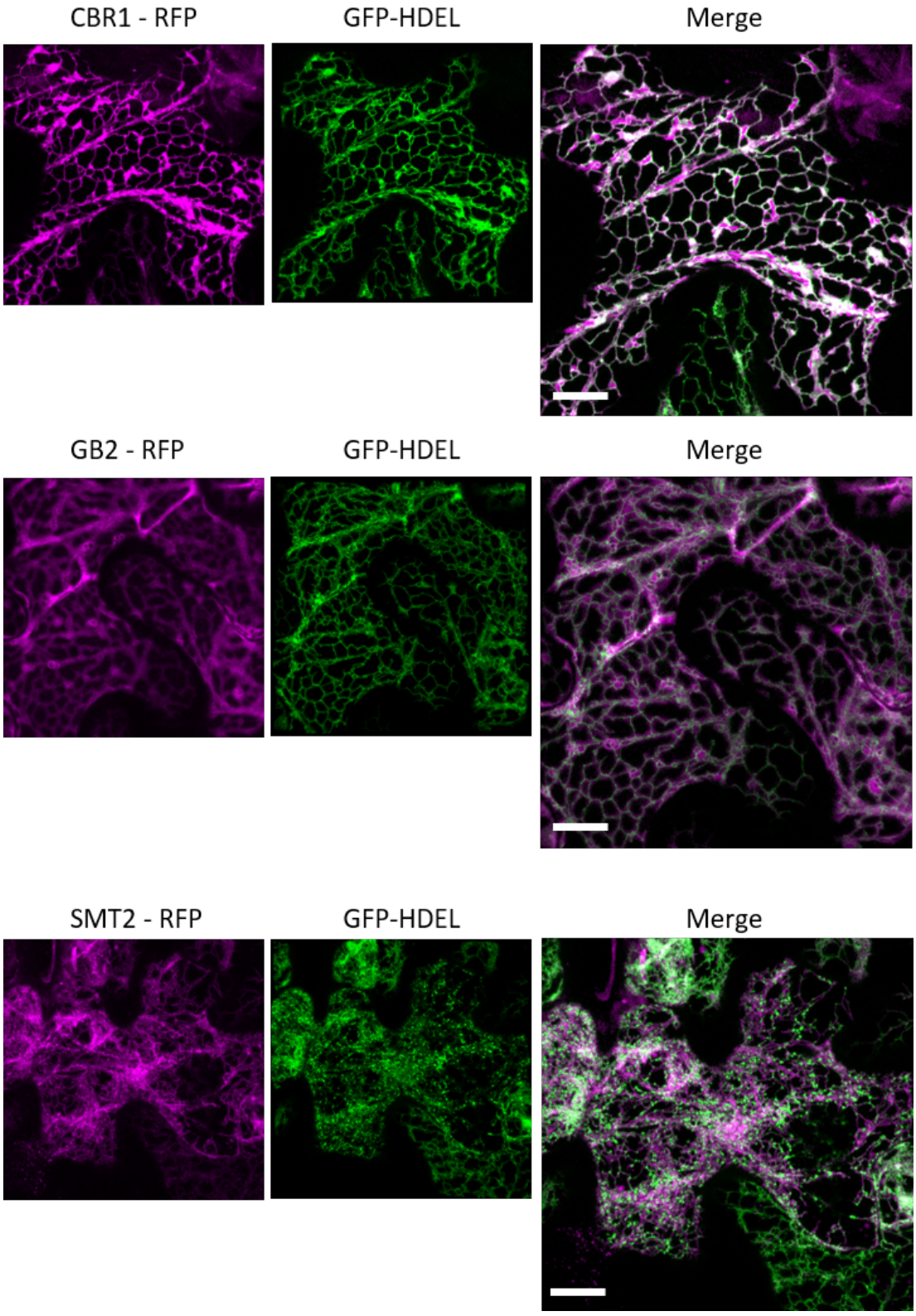

Figure 4.1: ***Transient over-expression of CBR1-RFP, GB2-RFP and SMT2-RFP with GFP-HDEL.*** *N. benthamiana was infilitrated and cells in the lower leaf epidermis were imaged. CBR1-RFP colocalises at the ER with GFP-HDEL. GB2-RFP localises to the cytoplasm though overlays the GFP-HDEL labelled ER. SMT2-RFP appears to label a disturbed ER network and GFP-HDEL appears as puncta, suggesting ER tubule construction. Scale bars = 10µm.*

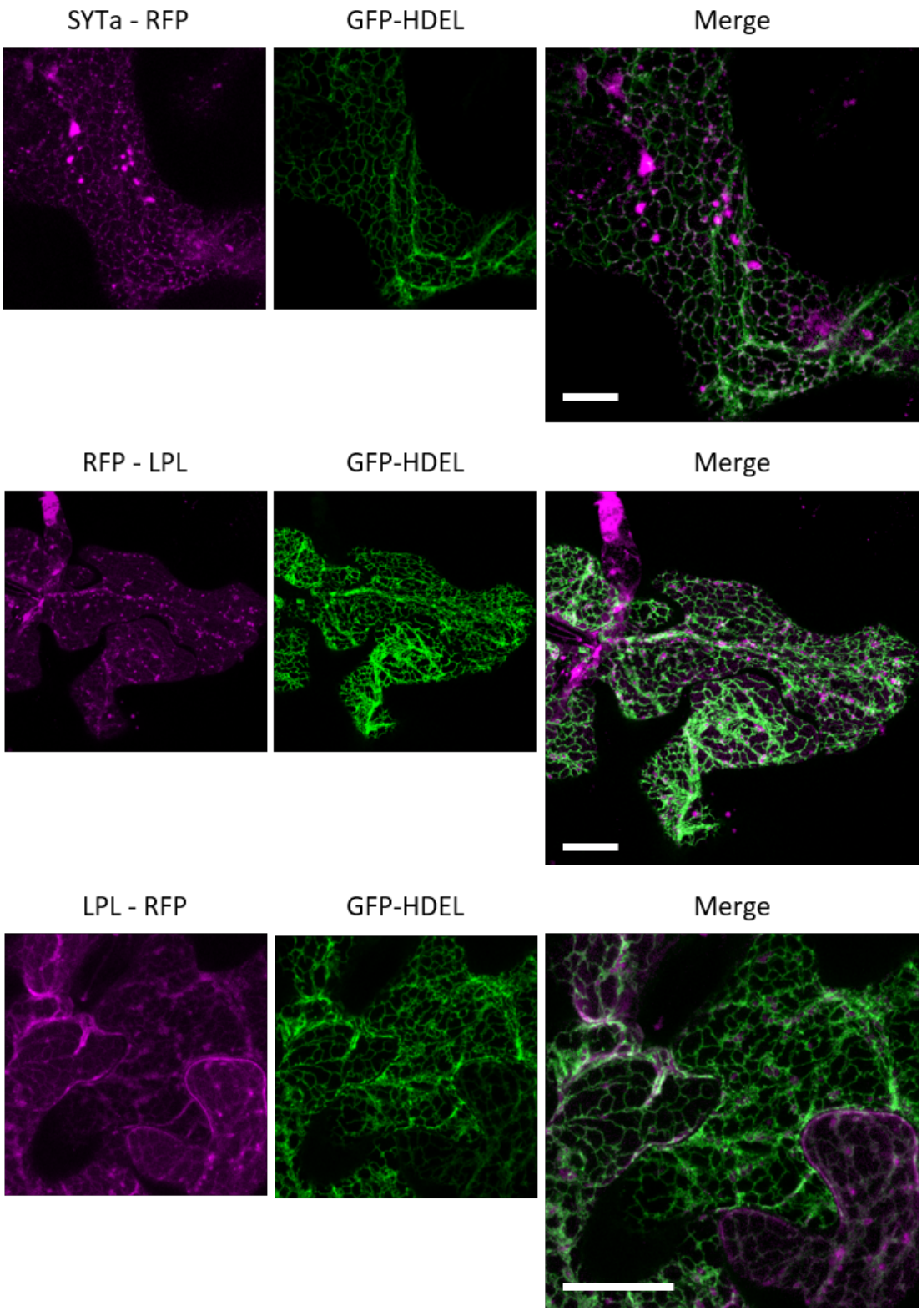

Figure 4.2: ***Transient over-expression of SYTa-RFP, RFP-LPL and LPL-RFP with GFP-HDEL.*** *N. benthamiana was infilitrated and cells in the lower leaf epidermis were imaged. SYTa-RFP labels puncta that overlays the GFP-HDEL labelled ER, though there are some protein aggregates. Both RFP-LPL and LPL-RFP appear to label the Golgi and ER network, though the latter weakly. Scale bars = 10μm.*

4.3.2 Stable over-expression in *A.thaliana*

In addition to the transient over-expression in *N. benthamiana*, the 35S-RFP constructs were dipped into *A. thaliana* Col-0 and *A. thaliana* 35S-GFP to create stable expression lines. This was to confirm any changes occurring to the ER network within the proteins' native environment.

The RFP-LPL construct was never visualised in the stable lines. In addition to this, the weakness of the SYTa-RFP expression was therefore difficult to image. Of the remaining constructs, only GB2-RFP was successfully transformed into the 35S:GFP-HDEL line (figure 4.3). Although stable expression lines of CBR1-RFP and SMT2-RFP were found, plants expressing these and GFP-HDEL were not found within the time limit of the project.

GB2-RFP was still expressed as over-lapping the ER, but far more diffusely (suggesting cytoplasmic localisation) and, as in the transient over-expression, the ER network looked normal. This confirms that over-expression of GB2 only did not influence the ER morphology.

CBR1-RFP was again expressed in the ER, and the ER network looked normal, as in the transient over-expression. Due to lack of GFP-HDEL expression, it cannot be confirmed if the additional oval-shaped organelles are also labelled in *A. thaliana*.

SMT2-RFP did localise to the ER, though the expression was very poor and there was a lot of fluorescence background (figure 4.3). The ER network looked normal, and did not appear to be disorganised in the way observed during transient expression. It is possible that the poor expression led to a more normal ER morphology, or that SMT2 has a greater affect in *N. benthamiana* than in *A. thaliana*. It would be useful to image this stable expression with GFP-HDEL expressed to assess whether the GFP-HDEL expression is altered as it was in the transient expression.

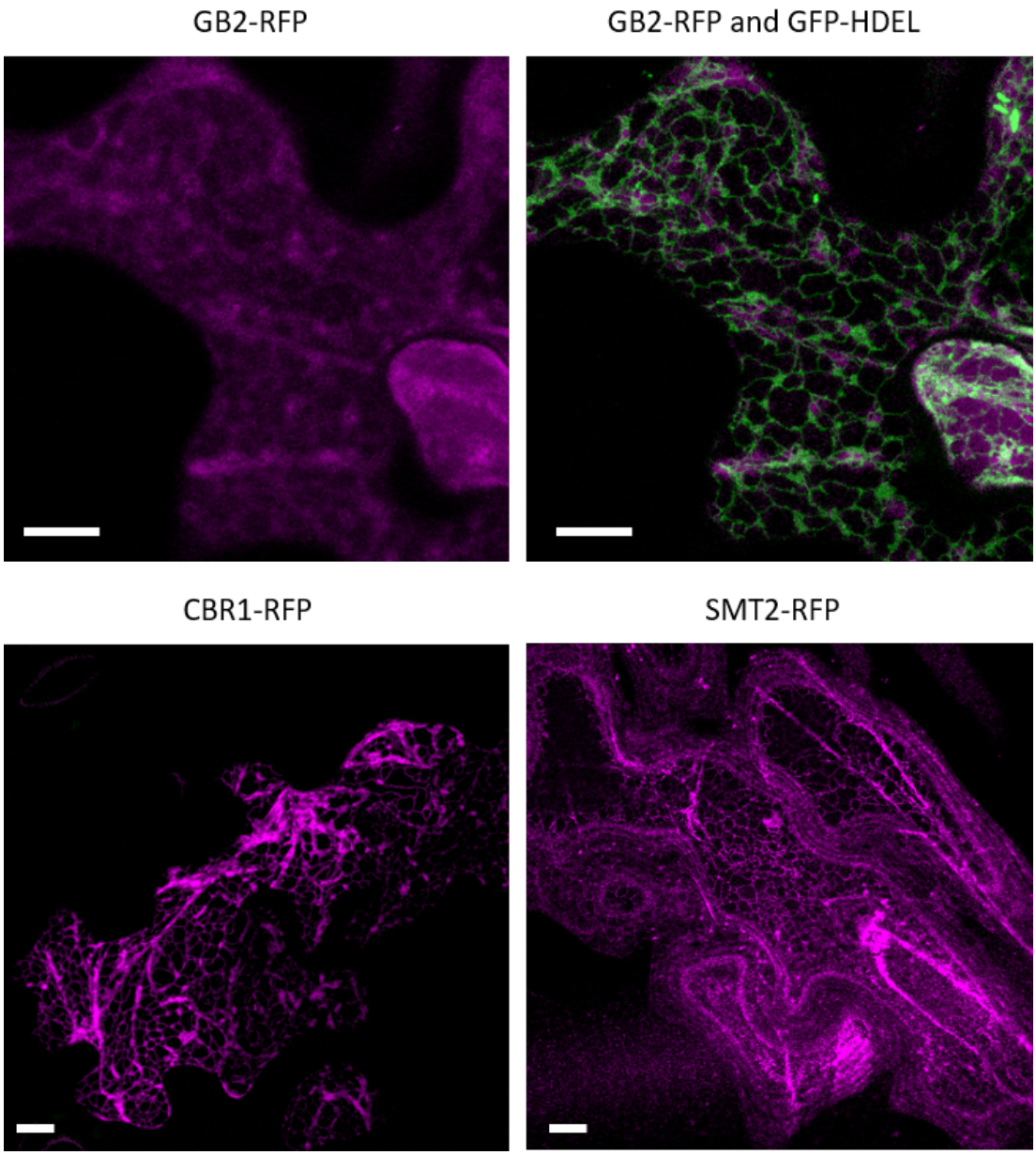

Figure 4.3: ***Stable over-expression of CBR1-RFP, GB2-RFP and SMT2-RFP.*** *Over-expression lines created using A. thaliana and the lower-epidermal leaf cells were imaged. GB2-RFP appears to label the cytoplasm, and does not alter the ER morphology. CBR1-RFP labels the ER and does not produce aberrant morphology. SMT2-RFP also labels the ER, though the expression was very poor. Scale bars are 10μm.*

4.3.3 Gene knockouts through T-DNA insertions

T-DNA insertions are one method of stopping the protein of interest from being expressed. Transfer-DNA is inserted either upstream of the coding region, or within the introns and exons of the gene. Many T-DNA insertion lines have been created and can be bought, for a nominal fee, from www.arabidopsis.info. To find the appropriate T-DNA insertion lines for each of the genes, two different websites were used:

- signal.salk.edu/cgi-bin/tdnaexpress
- seqviewer.arabidopsis.org/servlets/sv

Both sites allow available T-DNA insertion lines to be found by entering the gene accession number. Where the T-DNA insertions are in relation to the introns/exons and promoter regions is much clearer on the second website.

Several T-DNA insertion lines were chosen for each gene. Preference was given to lines that were labelled as homozygous, or shown to have produced a phenotype, or a loss of function. The position of the T-DNA insertion was varied so that some were in the exons and some were in the region upstream of the gene. The T-DNA lines chosen and their insertion sites can be seen in table 4.1.

Gene name	T-DNA insertion line	Site of insertion
CBR1	SALK 129878	5' UTR
CBR1	SAIL 371 A08	Intron
GB2	SAIL 445 H01	Exon
GB2	SALK 083103	Intron
LPL	GK 368 D11	Exon
LPL	SALK 008202	5' UTR
SMT2	GK 399 A09	5' UTR
SMT2	SALK 044472	Upstream intergenic
SYTa	SAIL 775 A08	Exon
SYTa	SALK 088781	5' UTR
RTN5	SALK 129950	Upstream intergenic

Table 4.1: ***T-DNA insertion lines and the genes that they disrupt.*** *5' UTR are the 5' untranslated regions which contain sequences that allow ribosomes to bind and initiate translation. Introns are non-coding regions of genes that influence splicing and disrupting these introns may produce nonsense translations. Upstream intergenic regions are non-coding regions between genes, disrupting these may disrupt promoter regions.*

To assess whether the lines truly were homozygous for the T-DNA insertion, a PCR test was completed. Samples from four plants of each line were taken and two PCRs with three primers were performed for each plant. Primers to check whether the T-DNA insertion were present, and whether the lines were

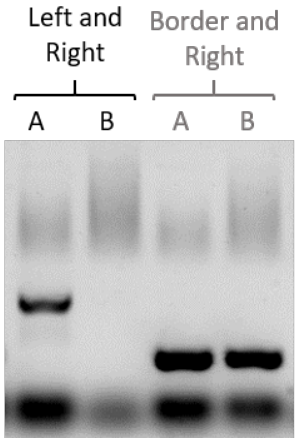

Figure 4.4: ***DNA gel electrophoresis showing a homozygous and heterozygous T-DNA insertion lines of GK 371 A08 (A CBR1 T-DNA Insertion line).*** *Lanes B show a plant that was homozygous for the T-DNA insertion, as only one band was seen and with the border and right primer. Lanes A show a plant that was heterozygous for the T-DNA insertion as a band is seen with both sets of primers. The bands at the bottom in all lanes are primer-dimers.*

homozygous were designed using signal.salk.edu/tdnaprimers.2.html. A right and left primer showed if the gene was there, without a T-DNA insertion sequence. The border and left primer showed if the T-DNA insertions sequence was present. Therefore if two bands were seen the plant was heterozygous (figure 4.4). Plants that were homozygous were chosen for growing to seed. Heterozygous plants were grown to seed, then re-grown and tested again until a homozygous plant was found.

Once the homozygous lines were found, they were transformed via floral dipping with GFP-HDEL. This was to enable the visualisation of the ER network. The rate of transformation is, at best, 1 in 100. Therefore within the time-frame of this project, a successfully transformed mutant was not found for some lines. Those without a successful transformation were imaged using rhodamine B. This is a fluorescent lipophilic dye that is not specific to the ER (it is also known to label lipid bodies and mitochondria) (Grabski et al., 1993). Rhodamine B also produces a high fluorescence background which makes imaging difficult. The ER network for each of these T-DNA insertion lines can be seen in figures 4.5 and 4.6.

Of all the T-DNA lines, only GK 368 D11 produced a phenotype. These plants were shorter in stature (data not shown), as seen by Vanholme et al. (2013). The only line that produced a noticeable change in the ER network was SALK 088781, a SYTa knockout (figure 4.6 H). The network here looks broken and intermittent. This suggests that SYTa may indeed influence the architecture of the ER.

For the other T-DNA insertion lines, there might be no change in the ER because of functional redundancy in the absence of the knocked-out protein. Table 4.2 shows the number of proteins that may allow functional redundancy when the protein interactors were down-regulated. For example, there are many *A. thaliana* RAB proteins, but ATRAB2A-2C are closely related and are localised to the same regions, (Rutherford and Moore, 2002; Vernoud et al., 2003). In the case of LPL, it is part of the family of MAGL (Monoacylglycerol lipases) however, of the 16 members, only 9 are localised to the ER and Golgi (Kim et al., 2016). This potentially means that there are 8 other MAGLs that could fulfil the function of LPL2, if knocked-out. The same is true for SMT2 and SYTa, where there are multiple members of the family. It would be interesting to assess the ER network in multiple knock-out lines, for example: SMT2 and SMT3 knocked-out together.

Protein Name	**Other names**	**Number in the family**	**Family names**
CBR1		2	CBR2
GB2	ATRAB2C / ATRABB1b	3	ATRAB2A,ATRAB2B
LPL2	CSE / ATMAGL3	16	ATMAGL1 - 16
SMT2		3	SMT1, SMT3
SYTA		5	SYTB - E
RTN		21	RTN 1 - 21

Table 4.2: ***Numbers of proteins directly related to the protein interactors.*** *GB2 - (Rutherford and Moore, 2002; Vernoud et al., 2003). LPL2 - (Kim et al., 2016). SMT2 - (Carland et al., 2010). SYTa - (Uchiyama et al., 2014). RTN - (Nziengui et al., 2007).*

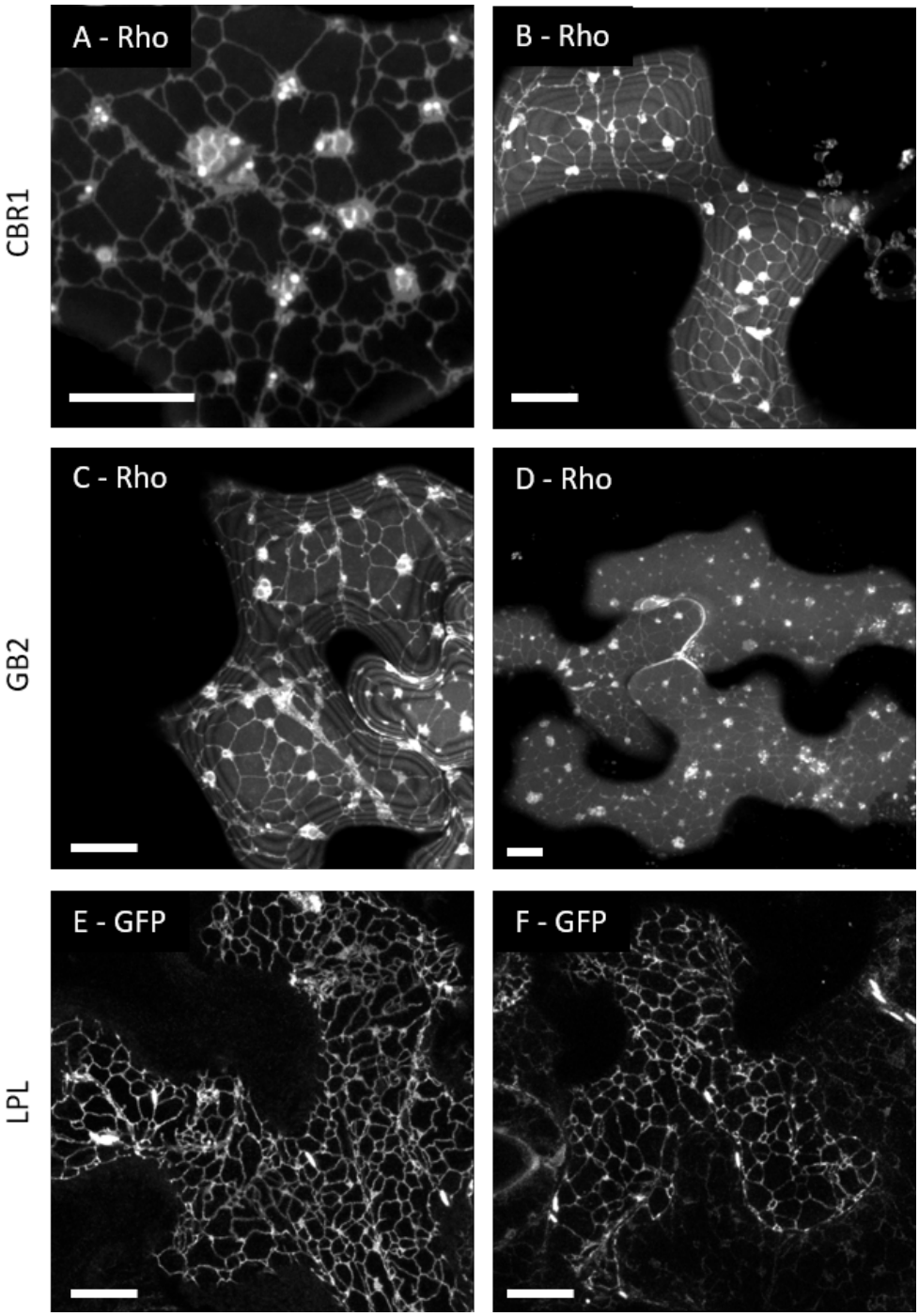

Figure 4.5: ***The ER network in A. thaliana T-DNA lines for CBR1, GB2 and LPL.*** *Those imaged using rhodamine B are indicated with (Rho) and those imaged with GFP-HDEL and indicated with (GFP). The lower-epidermic leaf cells were imaged.* ***A*** *= SALK 129878 (Rho).* ***B*** *= SAIL 371 A08 (Rho).* ***C*** *= SAIL 445 H01 (Rho).* ***D*** *= SALK 083103 (Rho).* ***E*** *= SALK 008202 (GFP).* ***F*** *= GK 368 D11 (GFP). Scale bar = 10nm*

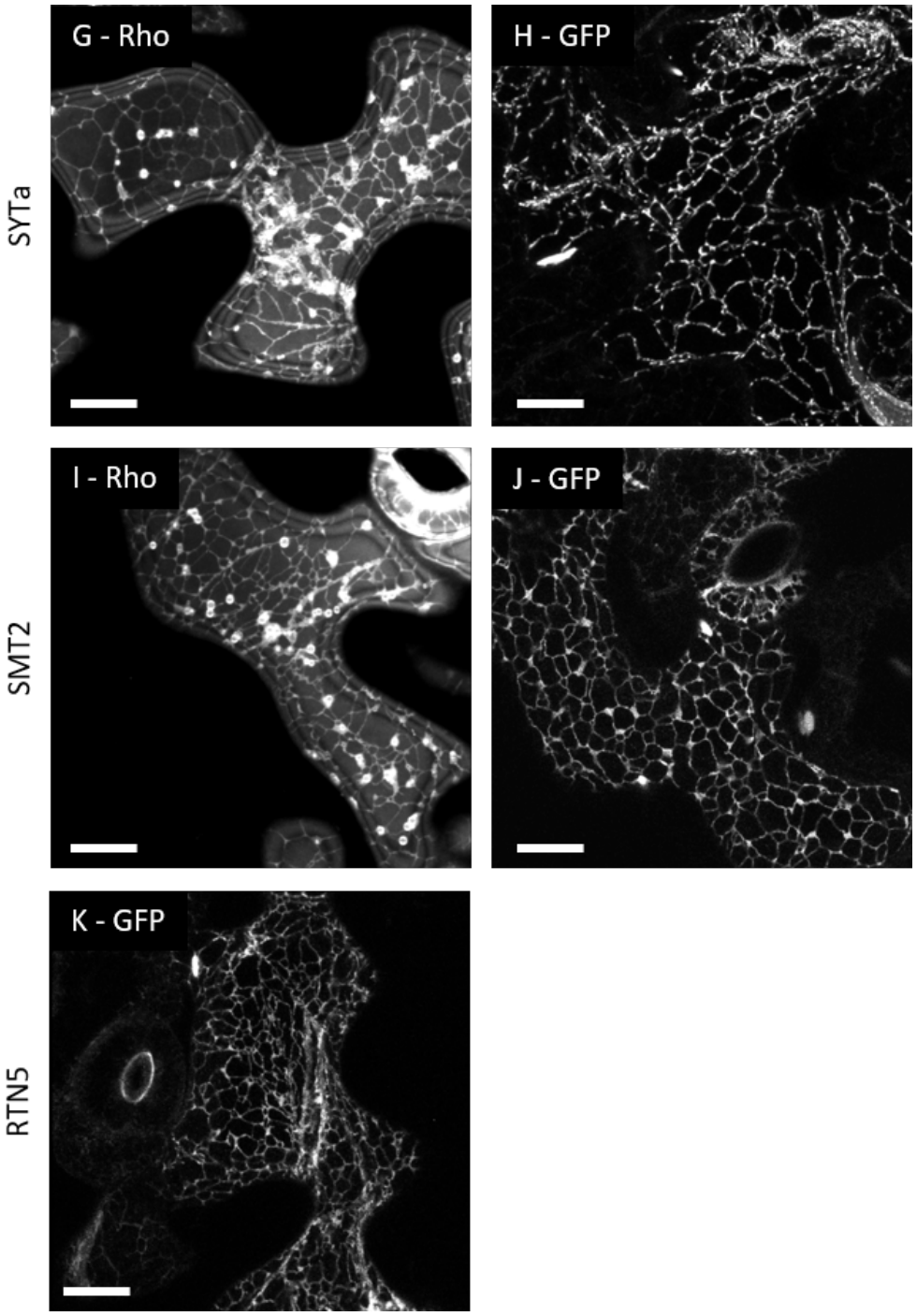

Figure 4.6: ***The ER in A. thaliana T-DNA lines for SYTa, SMT2 and RTN5****. Those imaged using rhodamine B are indicated with (Rho) and those imaged with GFP-HDEL and indicated with (GFP). The lower-epidermic leaf cells were imaged.* ***G*** *= SAIL 775 A08 (Rho).* ***H*** *= SALK 088781 (GFP).* ***I*** *= GK 399 A09 (Rho).* ***J*** *= SALK 044472 (GFP).* ***K*** *= SALK 129950 (GFP). Scale bar = 10nm*

4.4 Discussion

Of all of the RTN13-interacting proteins transiently over-expressed in *N. bethamiana*, only SMT2 produced any changes to the ER morphology. It appears to have constricted the tubules, but also caused the tubules to bundle together and the network to become disorganised. SMT2 over-expression causes level of sitosterol to increase and levels of cholesterol and campesterol to decrease. This suggests that the levels of these sterols are vital for the proper form of the ER network. It is known that sterols can increase the fluidity of the lipid membranes (Hartmann, 1998; Valitova et al., 2016), and this suggests that membrane fluidity is a vital part to the formation of the ER network.

None of the other transient protein over-expressions influenced the shape of the ER network. This does not mean that they do not influence the ER morphology. RL2 over-expression does not cause alterations to the ER network, despite its importance in the formation of the network (Lee et al., 2013).

Stable over-expression in *A. thaliana* did not produce any abnormal ER morphologies. SYTa-RFP has poor expression even in transient systems, and could not be imaged. GB2-RFP was successfully transformed in *A. thaliana*. It labelled the cytoplasm as expected, and as in the transient system, it did not produce any ER alterations. CBR1-RFP labelled the ER, which appeared to have normal morphology. SMT2-RFP, contrary to the transient expression, did not produce any abnormal ER morphology, though without GFP-HDEL expression it is difficult to confirm that.

Overall, the stable expression of the RFP-tagged interactors needs to be repeated, with true homozygous lines found before transformation with GFP-HDEL. As with the transient over-expression, the lack of abnormal morphology does not mean that these proteins are not influencing the morphology of the ER.

For future work it would be useful to assess the ER morphology with the over-expression of the RFP-interactors with over-expression of RTN13. There was an increase in the abnormality when RTN13 was co-expressed with RL2, indicating their interaction, as described by Lee et al. (2013). If RTN13 and the interactors truly interact, and influence the shape of the network, further aberrations may be seen.

Other mutant or knockout lines of key proteins could also be used with the over-expression of the RFP-tagged interactors. This again may provide further insight into how these interactors influence the architecture of the ER, if at all.

It may also be that the ER network shows no abnormal morphology, though the function of the ER may be impaired. By studying the levels of secretion of the ER in the over-expression lines, or the T-DNA insertions lines, a change in secretion compared to normal may be measured. Another key function of the ER network that has not been explored here is the unfolded protein response (UPR). The UPR is activated when an accumulation of unfolded proteins leads to ER stress. The induction of the UPR could be measured by changes in gene expression. Many genes have been found to be up-regulated in the UPR in *A. thaliana* (Martnez and Chrispeels, 2003). Groups, such as Lu and Christopher (2008), have use gene expression as a molecular marker for UPR. By looking for the presence of these molecular markers in the over-expression and T-DNA insertion lines, it could be found if the UPR was indeed activated.

Only one of the SYTa T-DNA insertion lines have an effect on the ER morphology. This suggests that SYTa is important in shaping the ER network. The network appeared to be disjointed, suggesting that the tubules were constricted. There were also no sheets present in the network.

There are several reasons why the other lines may not have shown a change in ER morphology. The first being that there is redundancy in the genes, and other proteins are replacing the one that was knocked-out. The second is that although the PCR test stated whether the lines are homozygous or not, this does not directly relate to whether the protein is completely absent. Sometimes T-DNA insertion lines can produce knockdowns instead of knockouts; the level of protein expression is greatly reduced as opposed to completely gone. This would be something to test in the lines that did not affect the ER morphology.

Chapter 5

ER morphology during embryo development and germination

5.1 Introduction

5.1.1 ER morphology

The ER has two main distinguishing morphologies: cisternal sheets and tubules. It has recently been debated whether or not the sheets are actually sheets, or simply bundles of tubules densely packed together. The Lippincott-Schwartz lab used super-resolution imaging to study ER morphology in mammalian cells and suggested that the peripheral sheets were actually a dense, tubular network (Nixon-Abell et al., 2016), though this has yet to be ascertained in plant models.

In mammalian cells, it has been seen that the ER morphology changes during mitosis; during interphase the ER is predominately tubule, with interconnected cisternae, whereas between prometaphase and telophase the ER morphology is predominantly cisternal (Lu et al., 2009; Puhka et al., 2012). Different cell types in mammals also have differing ER morphologies. For example: pancreatic cells (whose main function is to secrete proteins) have more sheets, whereas muscle cells (which need to store and release calcium) have more tubules (Shibata et al., 2010; Voeltz et al., 2002; Schwarz and Blower, 2015). This all adds to the theory that differing ER forms relate to the differing functions of the ER. The tubules are thought to be too highly curved to easily accommodate ribosomes, and so are more likely to be the site of lipid production and calcium storage. Whereas the sheets, on which the ribosomes sit, are where secretory protein production occurs (Shibata et al., 2006; Chen et al., 2012a; West et al., 2011). Knowing this it would be interesting to discover whether plant cells show the same ER morphological changes during their life cycle.

Reticulons and atlastins are known to influence ER morphology. Both protein families have a seed-specific isoform, which suggests that influencing the ER morphology is particularly important during seed development. Although a lot of work has been done on the transcriptomics of seed development and germination, ER morphology at these times has not been studied since the 1980s (Harris and Chrispeels, 1980).

5.1.2 Seed development

A. thaliana is a dicotyledonous plant, a member of the *Brassicaceae* family. This means that its embryos contain two cotyledons, which make up the bulk of the seed, and later develop into leaf-like organs. The endosperm and the testa

(the hard outer coat) are much thinner layers, which together made the seed coat.

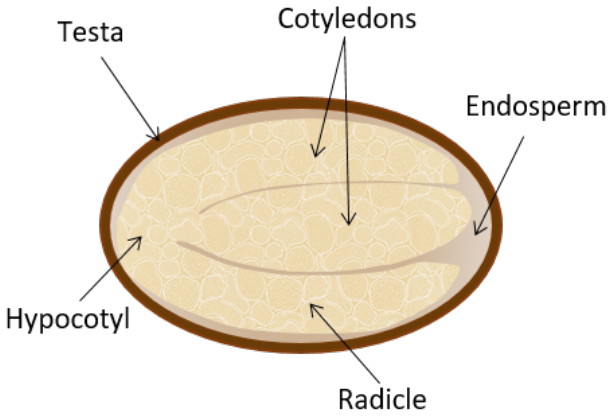

Figure 5.1: ***A mature Arabidopsis thaliana seed.*** *The testa is a hard, brown coat which softens upon water uptake. The testa is broken by the radicle during germination. The root develops from the radicle. In order to image the embryo using confocal microscopy the testa and the endosperm must first be removed.*

Seed development is characterised by four main stages. The first stage is fertilization. In angiosperms (flowering plants, such as *A. thaliana*), there is the fertilization of the egg to create the embryo and the fertilization of the central cells to produce a triploid endosperm (Goldberg et al., 1994). The second stage of seed development is the growth of the endosperm and the testa (together forming the seed coat). Next the embryo grows by means of cell division (embryogenesis). During embroygenesis, the embryo grows from 1 to around 200 cells, which is the heart stage embryo (Goldberg et al., 1994; Capron et al., 2009). Then in the fourth and final stage, the embryo grows by means of cell expansion (maturation). The embyro from heart stage to maturity can see in seen in figure 5.2. A lot of research has gone into understanding how the body plan is established, prior to the heart stage and an excellent review can be found in Capron et al. (2009).

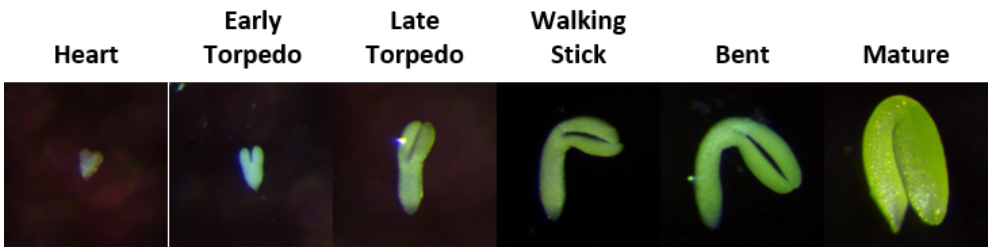

Figure 5.2: ***Seed development in A.thaliana****. These are the later stages of embryo development seen without the testa and endosperm. Although seed development is a continuous process, these six stages can be defined. All images were taken at the same magnification.*

During this transition to a mature embryo, the cells (both in the embryo and the endosperm) produce storage proteins and lipids. Figure 5.3, taken from Baud et al. (2002), highlights when lipids, proteins and even starch are produced during seed development in terms of 'days after flowering'. Day 5/6 after flowering is approximately the heart stage embryo and by day 10-12 the embryos are mature. From then on the seed becomes metabolically inactive and starts to dessicate, until by day 20 it is fully developed and dormant (Baud et al., 2002).

Once the seed has desiccated it can go into a dormancy state. Dormancy is a hard term to define, particularly as different plant species exhibit different types of dormancy. A dormant seed is generally defined as not having "the capacity to germinate in a specified period of time, under any combination or normal physical factors that are otherwise favourable for germination" (Baskin and Baskin, 2004). Simply put: dormancy is an absence of germination.

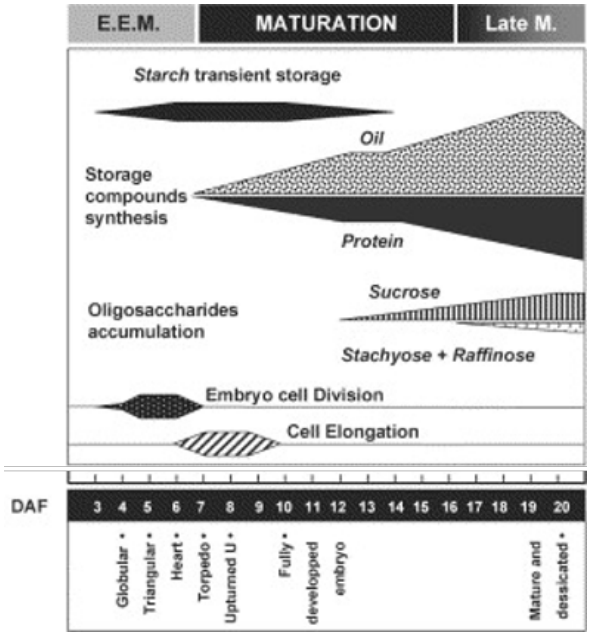

Figure 5.3: ***Major events during A.thaliana seed development****. From the torpedo stage the embryo starts to mature and a large increase in oil and protein production occurs. There is also a transient production and storage of starch from the globular stage and prior to late maturation. Adapted from figure 6 of (Baud et al., 2002). DAF = Days after flowering.*

5.1.3 Seed germination

Despite the large differences between seeds from different families, germination is defined as the process beginning with a seed absorbing water, and ending with elongation of the embryonic axis (Bewley, 1997). In the case of *A. thaliana*, this ends in testa rupture by the radicle (figure 5.4). An excellent review which covers both germination and dormancy can be found in Bentsink and Koornneef (2008).

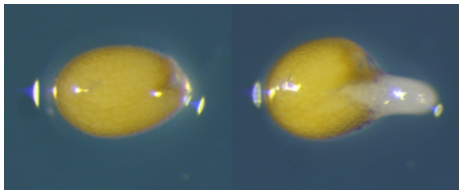

Figure 5.4: ***Germination of an A. thaliana seed.*** *Germination is defined as rupture of the testa by the radicle. The first image was taken 24 hours after imbibition and second was at 48 hours.*

There are various external factors that influence the onset of germination. ABA (abscisic acid) has been found to block the seed from germinating, whereas GA (gibberellic acid) is crucial for initiating germination (Koornneef et al., 2002; Finch-Savage and Leubner-Metzger, 2006). Temperature also affects germination. 'Stratification' is a method by which seeds are placed in water and then into a cold environment. This is known to break dormancy and ensure that all the seeds will germinate at the same time when transferred to a higher temperature. A final signal that may regulate germination is the absence or presence of light (Finch-Savage and Leubner-Metzger, 2006).

The testa is a dead layer of cells (keeping the endosperm layer intact), and when removed the seeds will not germinate (Bethke et al., 2007). This shows that the endosperm is the primary tissue responsible for maintaining dormancy. Removing the testa and endosperm causes the seeds to grow and become green (Bethke et al., 2007). This is fortunate because the seed coat needs to be removed to enable imaging of the embryonic ER by confocal microscopy.

In order to germinate, the seed must have access to water. Phase one of germination is the absorption of water, which can damage organelles, membranes, proteins and DNA after the period of dessication (Han and Yang, 2015). Therefore it is important that enzyme activity is resumed upon imbibtion, the absorption of water. It is currently believed that essential mRNAs are stored in the dessicated seed, so that upon imbibtion, transcription is not required. This has been corroborated by data that shows *de novo* protein synthesis starts only eight hours

after imbibtion (Han and Yang, 2015). After the first uptake of water, phase two is a plateau stage, where organelles (such as the mitochondria) are repaired and replenished (Bewley, 1997).

In phase three a second uptake of water occurs which results in the elongation of the radicle, subsequently piercing the testa. During this phase proteins and lipids stored in the endosperm are transferred to the tip of the radicle (Holdsworth et al., 2008; Bethke et al., 2007). In cereal crops (such as barley), it is well known that cells in the endosperm secrete enzymes (such as β-glucosidase) to digest the cell walls of seed coat, and there is some microscopy evidence that this also occurs in *A. thaliana* (Bethke et al., 2007; Han and Yang, 2015).

These events show that major metabolic and transcriptomic events take place during seed development and germination. Since the ER is the site of secretory protein production (including storage proteins) and lipid production, it is of interest to analyse how ER morphology changes in response to these events.

5.1.4 Image Analysis

Quantifying images has always been a desire of microscopists. In 1980, one group used grids and rulers to analyse the number of times cisternal (sheet) or tubular ER crossed the grid-lines in electron microscopy images (Harris and Chrispeels, 1980). They found that the amount of cisternal ER increased 48 hours after mung-bean imbibition. Technology has moved on significantly since then, and now computational analysis is becoming the norm.

Some groups have used mathematical modelling to try and explain the various morphologies seen in the ER network (Shibata et al., 2010; Shemesh et al., 2014). They vary the amount of tubule-creating proteins, and by minimising the energy of the network, they are able to mathematically recreate the different morphologies (such as sheets, tubules and three-way junctions). However, not only do these techniques need a lot of specialist knowledge, they are not analysing real systems.

Other groups have used electron microscopy to assess the ER network. They take multiple images of the network (through tomography or serial electron microscopy) and then recreate a 3D network (West et al., 2011; Terasaki et al., 2013). The volume of the network can be calculated, as can the diameter of the tubules and sheets. The disadvantage of using electron microscopy is, firstly, that the network is fixed; one of the key features of the ER network is how dynamic it is. Secondly, electron microscopy is time consuming to prepare the samples and

to analyse, requiring huge computational power; this limits the number of cells that can be imaged.

Confocal microscopy has the advantage that one can image living cells, thus capturing the dynamic nature of the ER. It is also quick, with little sample preparation. It is less technically challenging and the size of the dataset created is much smaller (which means less computational power is needed). One group in 2009 took advantage of this and used series of confocal images to create 3D models, from which the volume of the network could be calculated (Bouchekhima et al., 2009). They also 'skeletonised' the network, allowing them to make calculations about the number of three-way junctions, their inter-connectivity and the length of the tubules (Bouchekhima et al., 2009). At the time, they were only able to analyse chosen sections of the network, due to a lack of computational power, which is no longer a problem today. This selection process however, introduced user bias, and allowed 'difficult' areas of the network (such as large sheets) to be excluded from analysis.

Based on this method of skeletonisation, another group created a more comprehensive network analysis, differentiating between stable and un-stable three-way junctions (Lin et al., 2014). They also looked at the geometry of the junctions and compared the networks of wild-type cells and cells treated with an actin inhibitor (latrunculin B), which dramatically reduces the remodelling of the network. Again however, they were only looking at selected areas of the network, not the whole network.

In 2013 one group used Renyi-Entropy thresholding to create a binary image of the ER network (English and Voeltz, 2013b). This method categorises pixels in background or foreground, based on their intensity values and splits the image histogram into two. They were then able to remove low-frequency structures, such as the tubules by changing the factor in the thresholding. This method is easily done in the open-source software ImageJ (Schindelin et al., 2012), and requires very little computational power. As with the other methods, the authors selected areas of the network to analyse instead of analysing the whole network. In addition to this technique, there are many ImageJ plugins that can be utilised to analyse confocal images such as MorphoLibJ (Legland and Arganda-Carreras, 2014) and MiToBo (Möller et al., 2016), though they are not specific to ER network analysis.

More recently a MatLab (The MathWorks, 2017) package has been created that allows various measurements to be taken of the ER network, including the width and length of tubules, the size and shape of sheets and the size and shape of

polygonal regions (Fricker, 2016). It is a very comprehensive package that uses an intensity independent approach, which is beneficial for confocal images. It was used recently to show that reticulon proteins require an amphiphatic helix to constrict ER tubules (Breeze et al., 2016). It is an amazing package that can produce an enormous amount of information about ER networks. The only potential issue is that it requires the MatLab R2016a programme, which though often available through academic institutions, is not open source.

The aim of this final section of the project was to create an image analysis tool that was easy to use, accessible, that used little computational power and analysed the whole network, eliminating user bias. This tool was then used to analyse the ER network during seed development and germination.

5.2 Aims and approach

Seed development and germination are points in the plants life cycle where dramatic cellular changes take place. As yet, no one has studied the morphology of the ER during these situations. Given the importance that the ER has on the cellular function, and that it is the area of production of storage proteins (which make up a vast proportion of the seed), it will be interesting to understand how the morphology changes in response to these life-cycle events. By studying ER morphology, the link between form and function may be made clearer. In addition to this, studying mutants that are known to influence the ER morphology, may help to elucidate the mechanisms by which the morphology changes. Furthermore, in this age of computing, it is important to use all the tools that we can. By creating an image analysis tool, subtler changes between wild-type and mutant plants may be discovered than would be by eye alone.

Aims

- To image the ER during seed development and germination to compare the normal morphology to a variety of mutants including: a *lnp1lnp2* knockdown, a *pah1pah2* knockout, a triple reticulon knockout (*RTN1/2/13*) and an over-expression of YFP-RTN13.
- To create a simple and easy to use image analysis tool, in order to compare the ER morphology of mutant plants to wild-type

5.3 Results

5.3.1 Seed development

In order to image the ER during seed development, the seed had to be removed from the siliques (seed pods) and each seed coat then removed. The seed coat in each stage was green and soft. When seeds begin to desiccate, at the mature stage, the embryo becomes whiter and the seed coat turns brown and both become harder. Each stage of seed development can be found by collecting variously aged siliques along the stem. The higher up the stem (and closer to the flowers), the younger the seed. It can be difficult to categorise each embryo extracted, because the development is a continuous process.

GFP-HDEL during seed development

To begin with, a 35S:GFP-HDEL line was used to identify 'normal' ER morphology at each stage of development. HDEL is a retention signal for ER resident proteins. If a protein has this tag on its C-terminal, it will be captured and transported into the ER lumen (Gomord et al., 1997).

The heart and early torpedo stage embryos were very difficult to image. The embryos were very small and delicate and placing the cover-slip on top of the embryos often damaged them so that they could not be imaged. The earliest stage that could be routinely imaged was the late torpedo stage. At each stage of development, a minimum of three embryos were imaged. The images seen in figure 5.5 are representative of the ER morphology seen using the GFP-HDEL line. All images were taken from the developing cotyledons, rather than the hypocotyl or radicle.

In the late torpedo stage, there appeared to be no distinct ER morphology (figure 5.5). The nuclear envelope could be seen in most cells, which showed that GFP-HDEL was being expressed. Besides that, there was no clear network. It is unlikely that there was no ER, given that these cells are dividing and differentiating (requiring protein expression and lipid production). This may be due to the 35S promoter not being active at this stage. Repetition of this experiment with the latest Airyscan module will be necessary to improve resolution, in addition to using a promoter that is active during the torpedo stage of development.

The walking stick stage showed an interesting, dual morphology. The outer edges of the cells appeared to have distinct circles in a sheet-like network, whereas the inner section of the cell contained a tubular network. It is possible that the circles

were formed by the presence of lipid bodies. The dual morphology may be caused by the presence of vacuoles, which pushed the lipid bodies to the edges of the cells.

The ER morphology was completely altered in the bent cotyledon stage. The network appeared to consist of regions of tubules and regions of sheets. Though the inconsistent fluorescence of the sheets suggests they may instead have been bundles of tubules. Without higher resolution microscopy this cannot be confirmed.

The mature stage ER had a bright outer section made of sheets or densely packed tubules. The inner section was either made of sheets or a tubular network, with some cells possessing both features. The combination of morphologies suggests that the ER network was rapidly altering so the transitions were visible. The increase in the amount of sheet morphology suggests that the cells were undergoing increased protein production. Potentially producing storage proteins.

The post-mature stage generally appeared more tubular, though there were still areas of sheets similar to the bent embryo stage. The vacuoles were also visible, outlined by brighter areas of fluorescence.

The variation in ER morphology was unexpected and it is evident that huge changes are occurring over a short time-scale. (Referring back to figure 5.3, torpedo embryos are found approximately 7 days after flowering and transitions to the mature stage 3 to 5 days after.) There does not seem to be any obvious transitions between each of the morphologies shown; imaging more embryos may help to identify the changes that occur.

Col-0 during seed development

To assess whether the over-expression of GFP-HDEL was altering the ER morphology wild-type Col-0 *A. thaliana* was also imaged. In order to image the ER in Col-0 embryos, rhodamine B (a lipophilic probe) was used as a stain. Rhodamine B is not specific to the ER, and at low concentrations it is known to label lipid bodies and mitochondria (Grabski et al., 1993). The embryos were stained for 10 minutes, to allow time for the rhodamine B to pass through the cell wall and plasma membrane and get transported to the ER. It was clear that rhodamine B labelled more structures than GFP-HDEL (highlighted in appendix figure 7.24). rhodamine B also formed a large fluorescence background, making it difficult to obtain clear images. In addition to these issues, torpedo stage embryos could not be imaged as they could not be stained. Figure 5.6 shows the rhodamine B

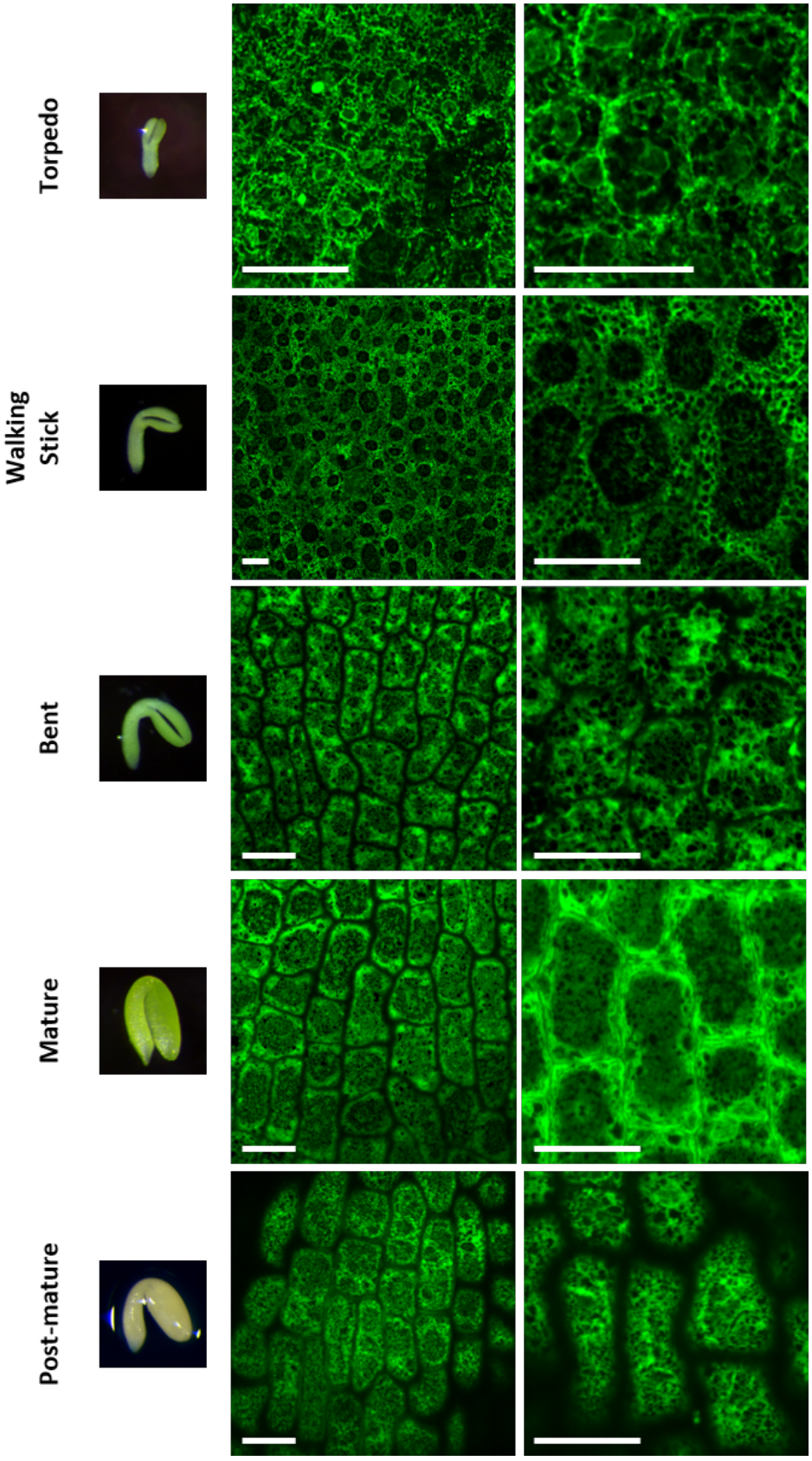

Figure 5.5: ***ER morphology during A. thaliana seed development in a GFP-HDEL line.*** *Cells imaged are from the centre of the cotyledons. Scale bars = 10μm.*

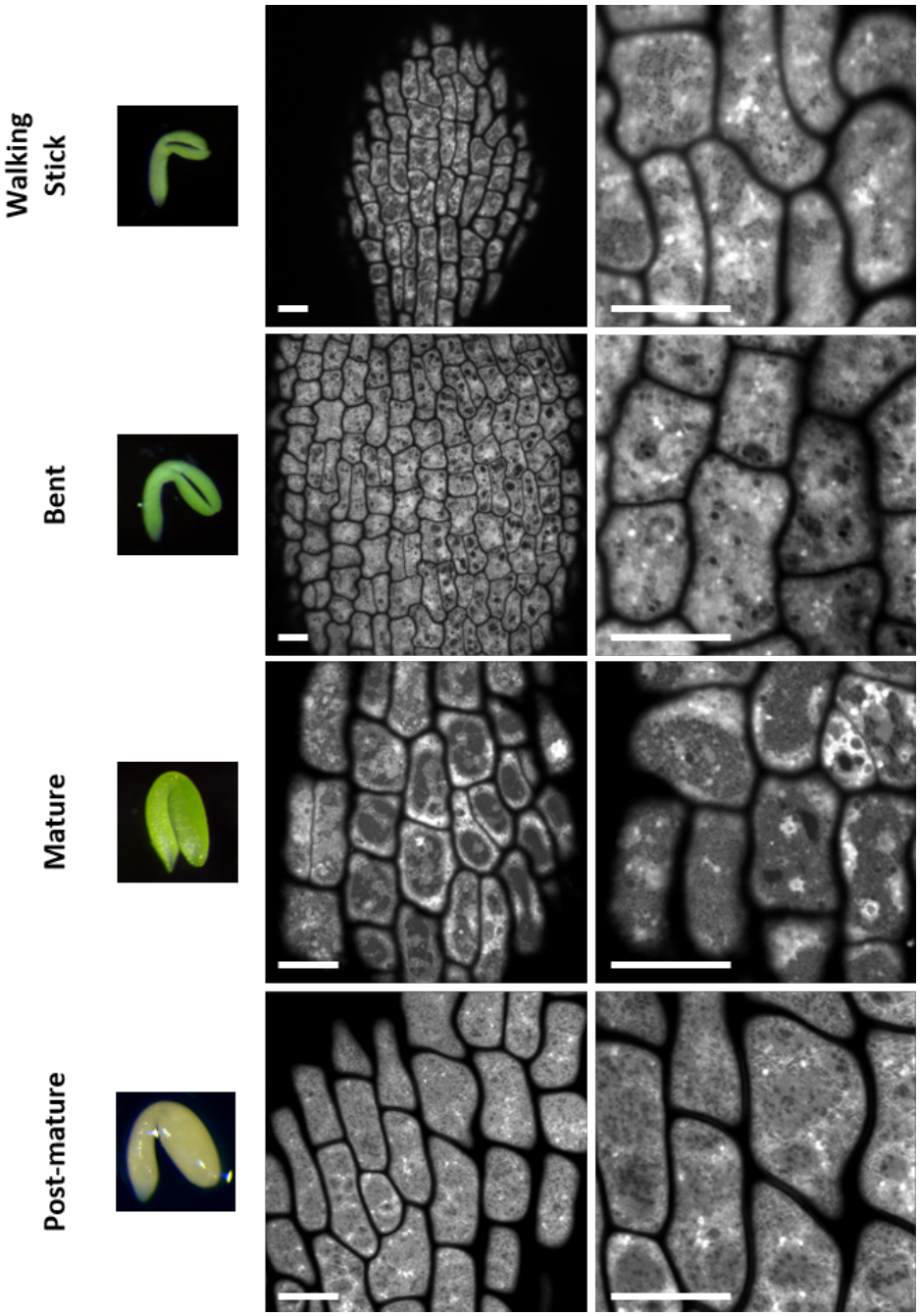

Figure 5.6: ***ER morphology during A. thaliana seed development in a Col-0 line.*** *Cells imaged are from the centre of the cotyledons. Scale bars = 10μm.*

stained ER at each stage of development.

The ER morphology of Col-0 at the walking stick stage was different to what was seen with GFP-HDEL. Col-0 had a mixture of sheets and tubules. Unlike the GFP-HDEL, there were not defined 'inner' or 'outer' sections, and it was more comparable to the GFP-HDEL bent stage morphology. This could have been due to difficulties in precisely defining each stage. The Col-0 walking stick embryos imaged may have been slightly older than the GFP-HDEL walking stick embryos. Perhaps the morphology seen with the GFP-HDEL walking stick stage in figure 5.5 is short-lived, and occurs in 'early' walking stick embryos.

The Col-0 bent stage (figure 5.6) appeared to have a predominately sheet-based morphology, though the sheets were not uniform, with some areas brighter than others. Perhaps the high fluorescence background was reducing the clarity of the images. This again differed to the morphology seen with GFP-HDEL. The bright circles may have been lipid bodies, and indicates that rhodamine B is labelling additional organelles. The high fluorescence background may also have been caused by rhodamine B labelling the plasma membrane or the tonoplast, as it is a lipophillic dye.

The Col-0 mature stage appeared similar to GFP-HDEL, as the outer sections of the cells contained bright sheet-like ER, and the inner sections had a mixture of sheets and tubules. There were more differences between the individual cells in the Col-0, and the morphology of the ER did not look as regular as with GFP-HDEL.

The Col-0 post-mature embryos presented an ER that was mainly composed of sheets, but appeared to be divided into multiple segments within each cell. These segments look similar to protein storage vacuoles, which is similar to what was seen in the GFP-HDEL line, though appeared to have more sheets. This again may be due to the high fluorescence background caused by the rhodamine B.

Despite the differences between the Col-0 development series and the GFP-HDEL development series, it likely that the GFP-HDEL over-expression is not dramatically influencing the ER morphology. Since rhodamine B did stain more organelles than just the ER, it was harder to determine what the ER structure was. The background fluorescence was very high, again making it difficult to determine the morphology. As seed development is a continuous process, then slightly younger or older embryos may have differing morphology, despite being classified as the same stage. More embryos would have to be imaged across each stage in order to get a complete time-line of morphology transitions.

Study of ER mutants during seed development

ER morphology mutants were analysed to elucidate the mechanisms behind the morphology changes seen during seed development. A YFP-RTN13 over-expression line in a RTN13-knockout background was used to evaluate the ER with higher levels of tubulation. Over-expression of YFP-RTN13 with GFP-HDEL in *N. benthamiana* shows the lumen of the ER is more constricted (Breeze et al., 2016). A triple-reticulon knockout (RTN1, RTN2 and RTN13), co-expressed with GFP-HDEL, was used to assess how the ER morphology changes with fewer membrane-constricting proteins. A double lunapark amiRNA knockdown (*lnp1lnp2*) was investigated, because this knockout has been shown to decrease the stability of the three-way junctions (Chen et al., 2015; Shemesh et al., 2014). Finally, the *pah1pah2* mutant, co-expressed with GFP-HDEL was imaged. The *pah1pah2* mutants contains T-DNA insertions in both the PAH1 and PAH2 genes (phosphatidic acid phosphohydrolase 1 and 2). This mutant decreases phosphatidic acid hydrolysis and increases sheets in the ER network (Nakamura et al., 2009; Eastmond et al., 2010). Figures 5.7 and 5.8 show the results from analysing the ER morphology of these various mutants at different stages of seed development.

In the YFP-RTN13 over-expression line there were large, bright fluorescent bodies throughout the embryo, as can be seen in the torpedo stage in figure 5.7. These aggregates did not appear to interfere with the ER network. Besides the aggregates, the late torpedo stage embryo had a tubular network, though this could not be compared to the the GFP-HDEL line, due to the inactive 35S promoter used for the GFP-HDEL construct. The walking stick network appeared to be a mixture of tubules and sheets, though the sheets had irregular fluorescence, suggesting that they could have be bundles of tubules. This again is different to the GFP-HDEL line and appeared to be more similar to the bent stage ER morphology. This could have be due to the walking stick stage embryos of YFP-RTN13 being more mature than those of the GFP-HDEL line. Both the bent and mature stage in the YFP-RTN13 line had tubular networks. The bent stage network had irregularly sized holes, with some much larger than others. The mature stage network looked disorganised, though not very different to the network seen in the GFP-HDEL line. Except from the walking stick stage, no sheets were seen in the network, suggesting that the over-expression of RTN13 was causing more constrictions.

In the triple reticulon knockout there was no ER network visible in the torpedo stage embryo, there were only dim, fluorescent spots in each cell. These may have

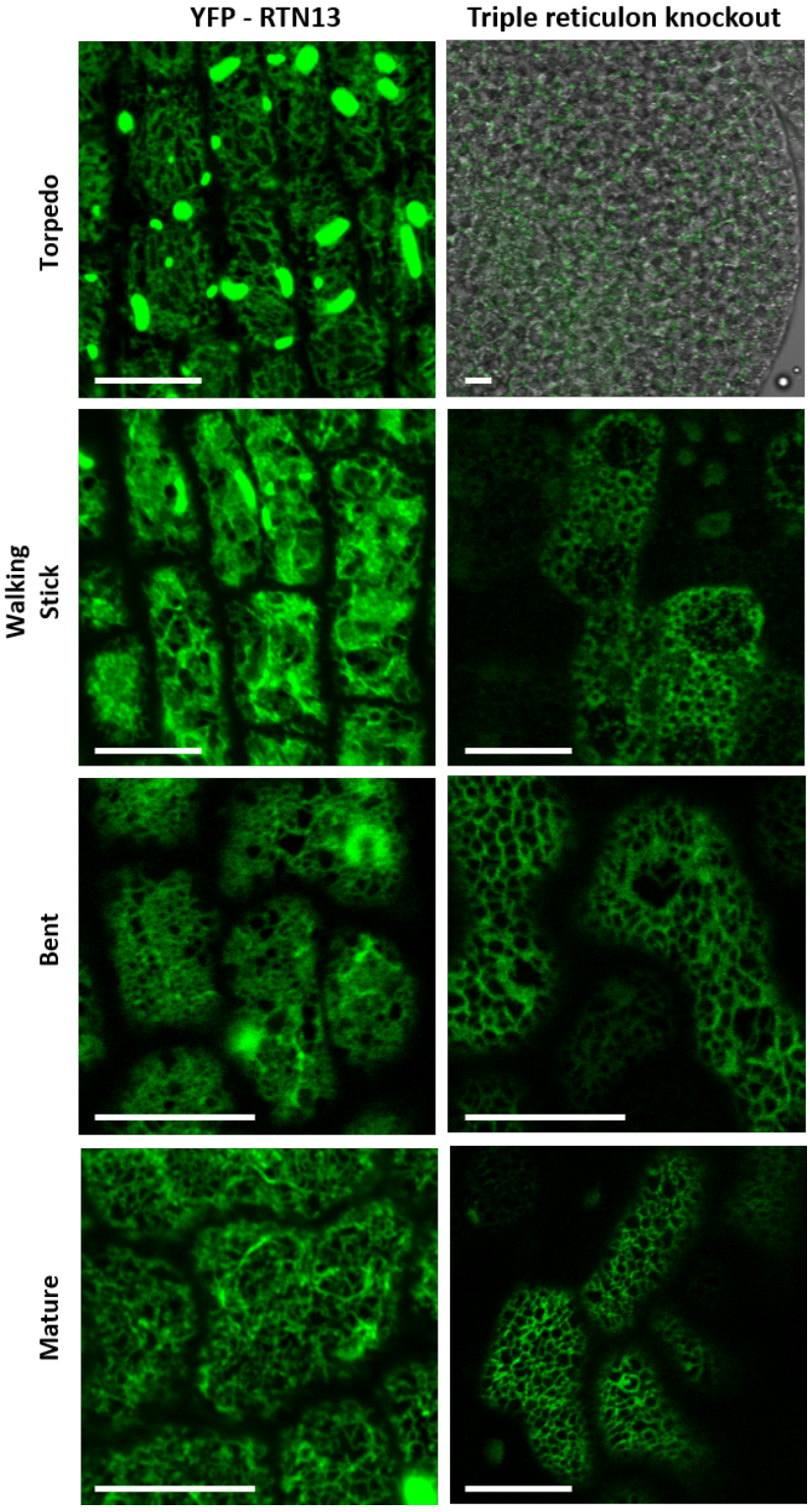

Figure 5.7: ***ER morphology through A. thaliana seed development*** *of the YFP-RTN13 over-expression line and the triple reticulon knockout mutant with GFP-HDEL. Cells imaged were from the centre of the cotyledons. Scale bars = 10μm.*

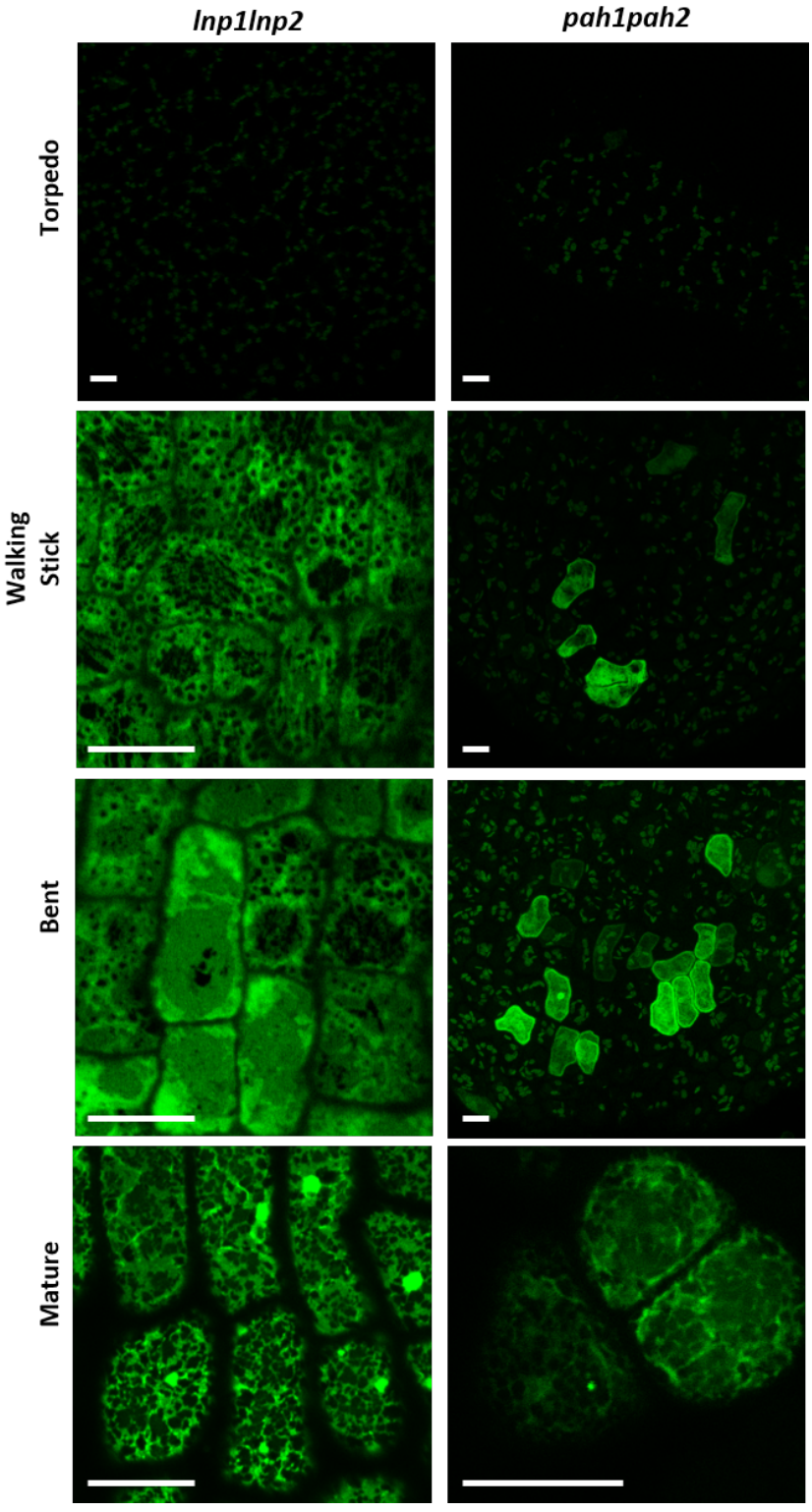

Figure 5.8: ***ER morphology through A. thaliana seed development*** *of lnp1lnp2 and pah1pah2 mutants each expressing GFP-HDEL. Cells imaged were from the centre of the cotyledons. Scale bars = 10µm.*

been caused by auto-fluorescence of chloroplasts. The network in the walking stick embryo looked similar to the GFP-HDEL line, except there were two inner sections per cell rather than one. The bent stage embryo had a predominately tubular network, though there were a few small sheets. The mature stage had a tubular network similar to that seen in the GFP-HDEL line, but the holes in the network were larger and more angular. At no development stage was there a network with a large amount of sheets as seen in the GFP-HDEL line, which is contradictory to what might be expected with a knockout of three reticulon proteins. Given that there are 21 reticulons however, perhaps others are fulfilling the role and therefore over-compensating.

In the *lnp1lnp2* line, again there were only dim fluorescent spots in the torpedo stage embryo. The walking stick network looked somewhat similar to the GFP-HDEL line, with circular holes in the network in the outer section and tubular network on the inner section. The outer section appeared more sheet-like however, and the inner sections appeared more linear and less honeycomb-like. The bent embryo had a mix of morphologies, with some of the same morphology as seen in the walking stick, whereas other cells had networks almost completely made of sheets. This was probably showing the transition between the two types of morphologies seen in the GFP-HDEL line. The mature stage embryos again seemed to be in a transition stage between tubules and sheets. This could suggest that the *lnp1lnp2* line is slightly slower to change ER morphology or develop.

The *pah1pah2* torpedo stage embryo again only had dim fluorescent spots and this continued into the walking stick and bent stages. There are a few cells where the ER was visible and the network in these appeared to be continuous sheets. By the mature stage, the spots were no longer present, suggesting that they were chloroplast auto-fluorescence, as by the mature stage the embryos were less green. The ER network appeared more tubular, though there was still evidence of sheets. These seeds, and the plant they came from, were highly abnormal. The plant was short, pale and had produced few siliques. There were very few viable seeds (most aborted) and within each silique there was a wide developmental range of embryos (both heart and mature stage present in the same silique).

The mutants all produce different morphologies at each stage and do differ from the network seen in the GFP-HDEL line. This suggests that these proteins do contribute to maintaining normal ER morphology during seed development.

5.3.2 Seed germination

Imaging Chamber

Although germination is defined as when the radicle emerges through the testa, the germinating embryos were imaged until vegetative ER morphology was observed. In order to image the ER network, the seed coat had to be removed. Initially, to determine how the ER changed over time, an imaging chamber was created, so that the same embryos could be imaged whilst they germinate. Inspiration for this was taken from Peterson and Torii (2012). The imaging chamber was created as in methods section 0.8.25. A 35s:GFP-HDEL line was used to visualise the ER network.

Figures 5.9 and 5.10 show the ER morphology of two different embryos, from two separate imaging chambers, over ten days. Although there are multiple embryos in the images shown, it clear to see that some of the embryos grew and became green, and others did not. The MS0 agar contained kanamycin, the selective antibiotic for the GFP-HDEL line, preventing the growth of any seed that did not express GFP-HDEL. This also inhibited bacterial and fungal growth, which was an issue when this experiment was first attempted.

The cotyledons were preferentially imaged as opposed to the hypocotyl or the radicle. This is partly because the hypocotyl cells develop at a very fast rate and, the cells become very large, very quickly. Secondly, the radicle develops into the root and these cells become very thin and elongated, and with a highly curved organ is more difficult to image the ER network. Although these data are not shown here, the hypocotyl and radicle cells, do undergo the same ER morphology changes, but at a faster rate than cells of the cotyledons. The images shown in figures 5.9 and 5.10 show cotyledon cells, except for day 2 of embryo A, which show cells from the radicle.

The images here were taken on a Leica SP5 confocal microscope, an older machine, with poorer resolution compared to the Zeiss 880. At the beginning of this project, the Zeiss 880 was not present in the department. The images contain significant background fluorescence, and there is some distortion around the cells. In addition to this, the cover-slip of the imaging chamber was made from plastic, as opposed to than glass, which further reduced the image quality.

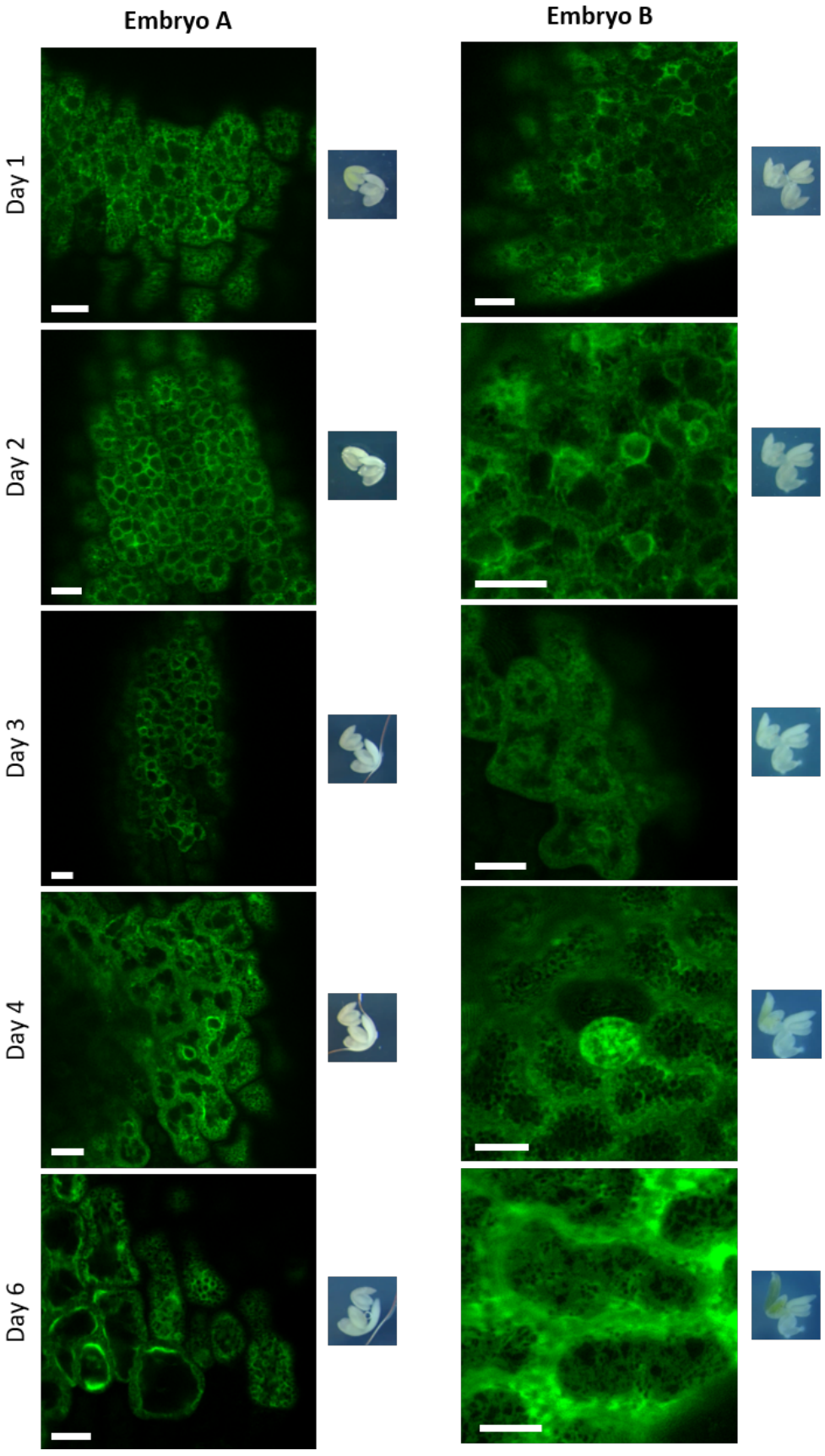

Figure 5.9: ***GFP-HDEL A. thaliana seed during germination in an imaging chamber, days 1- 6.*** *Confocal images of the cotyledon cells with respective image of the embryo. Embryo A is the lower one in the image and embryo B is the embryo in the top left. Scale bars = 10µm.*

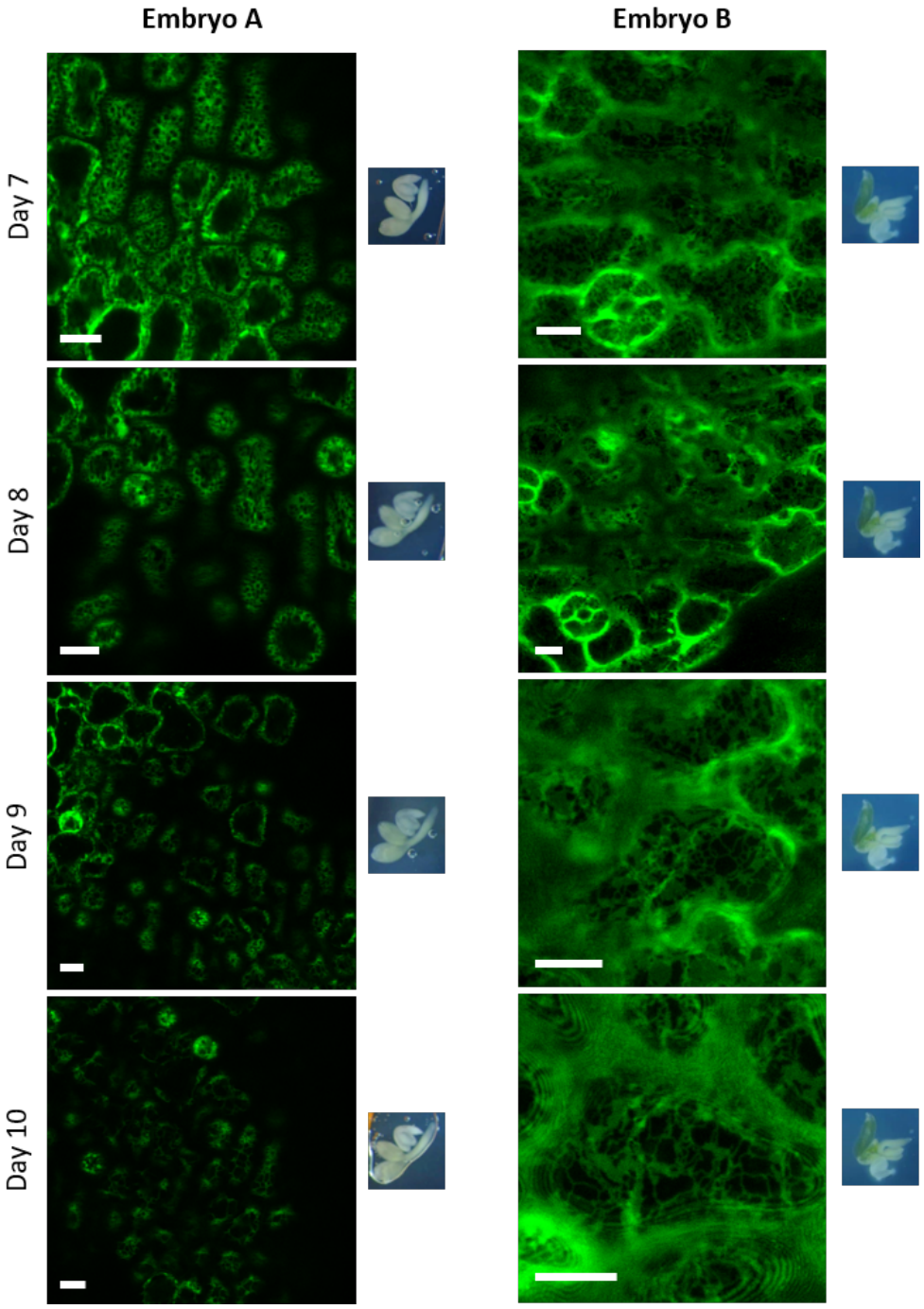

Figure 5.10: ***GFP-HDEL A. thaliana seed during germination in an imaging chamber, days 7 - 10.*** *Confocal images of the cotyledon cells with respective image of the embryo. Embryo A is the lower one in the image and embryo B is the embryo in the top left. Scale bars = 10µm.*

As seen in figures 5.9 and 5.10, the ER in embryos A and B looked very similar during days 1-3. The protein storage vacuoles and the nuclei were distinguishable by the negative space created by the ER. This shows that other organelles can impact on the morphology of the ER. Around this, a tubular ER network was visible. These images were taken predominately through the mid-section of the cells. The images that were taken at the top of the cells (where the ER network is mainly present) had such high background fluorescence that the network was indistinguishable.

On day 4 there was a change to both the ER morphology and the morphology of the vacuoles. In embryo A the vacuoles appeared less prominent, whereas the nuclei appeared more so. The ER of embryo B appeared to have thicker tubules and the holes in the network were more circular. This is perhaps indicative of lipid bodies. It was also evident that there was chlorophyll production in embryo B, by the green pigmentation that developed.

By day 6, the vacuoles in embryo A had become one large vacuole. This suggests that the protein storage vacuoles had transitioned into a lytic vacuole. The visible portion of ER network had distinct circles, as embryo B did on day 4. The ER network in embryo B on the other hand, was an almost continuous sheet, with very few tubules. The amount of chlorophyll in the embryo had also increased. If the form of the ER is related to its function, the increase in the number of sheets may be indicative of an increase in protein production.

By day 10 the network in both embryos had transitioned to vegetative ER, with a reduced amount of sheets. It is worth noting that embryo A did not produce as much chlorophyll as embryo B suggesting that it did not develop as well. This is supported by each change in ER morphology occurring later in embryo A.

The changes shown were seen repeatedly in many embryos and multiple imaging chambers. The dramatically different morphologies suggest that the ER network is changing in response to the needs of the cell and the presence of other organelles (such as lipid bodies).

Daily imaging

In order to assess whether the embryos were becoming stressed by being inside the imaging chamber, the time-course was repeated but, once uncoated the embryos were placed onto an MS0 agar petri dish. Embryos were then imaged using a traditional glass cover-slip and slide, with water. The embryos could not be re-used after imaging as they were often damaged in the process. A minimum of

three embryos were imaged each day, and the images shown in figures 5.11 and 5.12 are representative of those embryos.

On day 1 (figure 5.11) the network appeared to be an irregularly shaped, tubular network. The protein storage vacuoles and the nuclei were visible as in the previous experiment. On day 2 there was a subtle change in the network. Although still tubular, the holes in the network appeared more circular. This looked very similar to the network as seen in the imaging chamber embryos.

By day 3 however, the network had become a continuous sheet in most cells, though the occasional ones were a mixture of sheets and circular holes. The protein storage vacuoles had turned into lytic vacuoles and the cells had significantly increased in size. Although the same morphology occurred as when using the imaging chamber, the change occurred much sooner. This increase in sheets could indicate a point of increased protein production.

On day 4 all the embryos had a ER network formed predominantly of sheets. What is interesting is that the sheets are not uniform; there appear to be areas that are brighter than others. Perhaps the brighter sheets were thicker, or there were multiple sheets layered on top of one another.

By day 5 (figure 5.12) the proportion of sheets were reduced, and a more tubular network started to appear. The number and the size of the sheets continued to reduce, where by day 7 the network appeared to be similar to a vegetative network.

The transition to vegetative ER network occurred three days faster in this experiment compared to the imaging chamber experiment. This suggests that although the embryos were stressed inside the imaging chamber, this did not impact the ER network morphology, simply the rate of change.

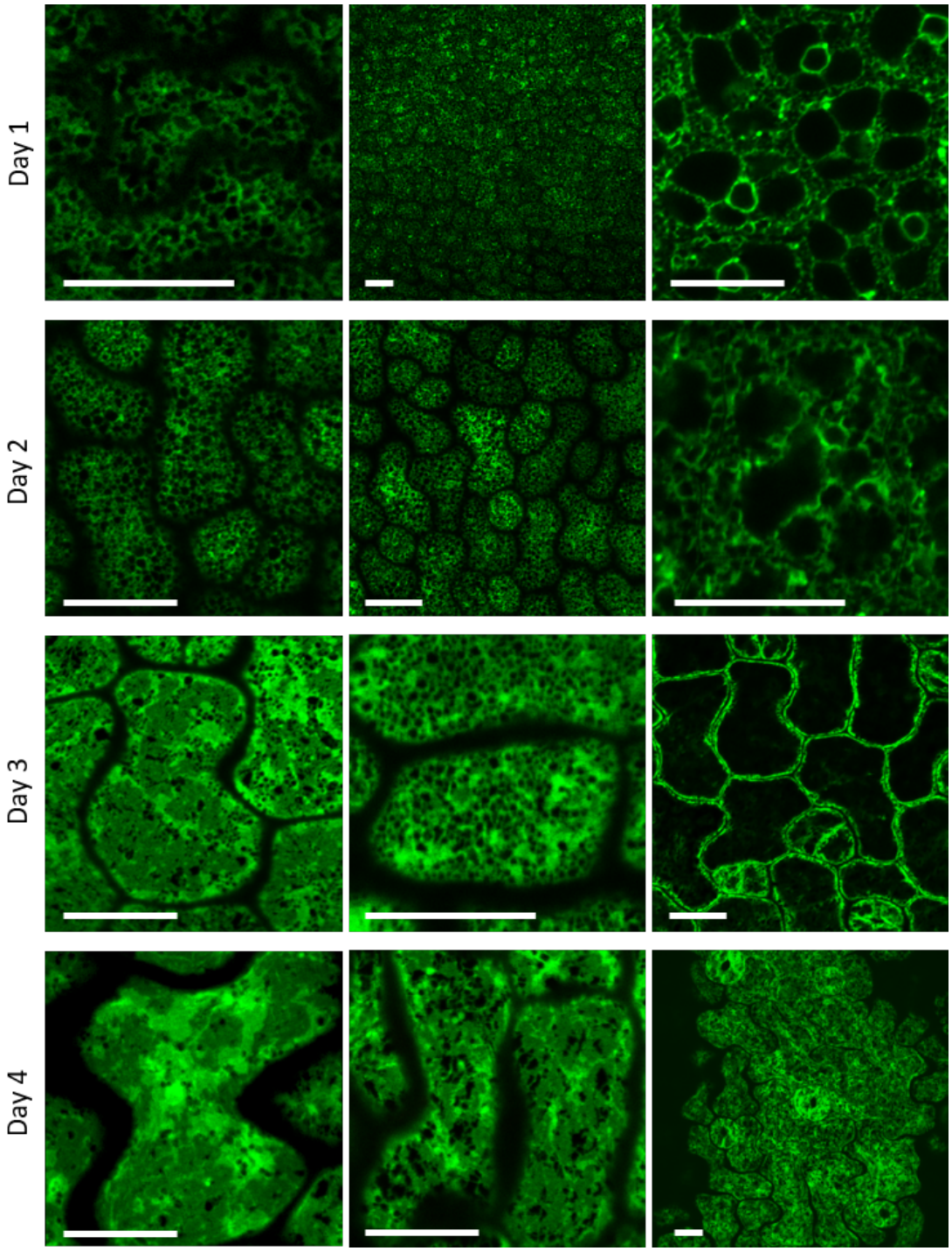

Figure 5.11: ***GFP-HDEL A. thaliana seed during germination, days 1 - 6.*** *These images show cells from the cotyledon, all from individual embryos. The transition from tubular to sheet morphology can be seen as can the transition from protein-storage vacuoles to lytic vacuole. Scale bars = 10µm.*

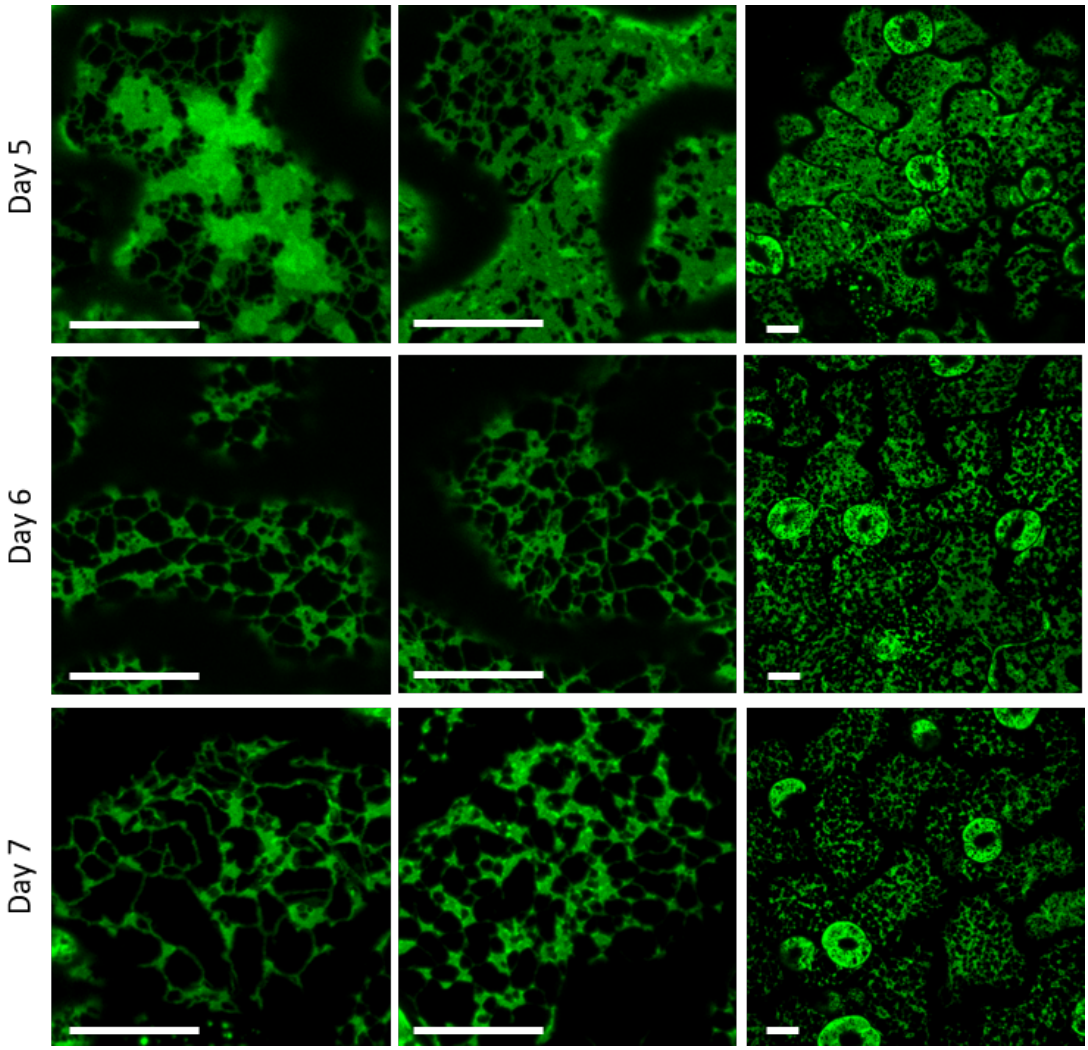

Figure 5.12: ***GFP-HDEL A. thaliana seed during germination, days 5 - 7.*** *These images show cells from the cotyledon, all from individual embryos. The transition from sheet morphology to predominately tubular, vegetative morphology can be seen. Scale bars = 10μm.*

Total protein during germination

In addition to imaging the ER during germination, the total protein content of the seed was also analysed. Forty Col-0 *A.thaliana* seeds were uncoated, and then placed on an MS0-agar plate. Four embryos were homogenised in SDS-sample buffer every day, and the proteins visualised using Coomassie staining of SDS-PAGE. There was a shift in the amount and mixture of proteins present from day two to day five (figure 5.13). The bands around 25 kDa disappeared by day four and the bands below 17 kDa disappeared by day five. These may be storage proteins, such as 2S Albumin, being broken down for energy. From day five there was a strong band at around 46kDa, not present earlier. This may have been proteins that are part of photosynthesis, such as the light-harvesting complexes or Ribulose Bisphosphate Carboxylase (RuBisCO). There may also be an increase in the number of ribosomes, or heat shock proteins or even ATP Synthases, as the plant increases it metabolic activity. The bands from day five to day ten do increase in strength, and this is due to the growth of the seedlings and thus a overall increase in the amount of protein.

The change in protein composition links to the appearance of sheets in the ER morphology (figure 5.17). This suggests that the cells are becoming metabolically active again, after dormancy, and that the increase in the amount of sheets in the ER network coincides with an increase in protein production.

Differences in germination with or without a seed coat

To obtain a time-line of how the plants developed during the germination experiment, uncoated and whole seeds were placed on MS0-agar, and photographed every day. Figure 5.14 shows how the embryos grew over ten days. One day 3 both the uncoated and whole seeds turned green, indicating that the plants were producing chlorophyll. This shows a correlation in the change of protein composition of the seeds and the increase in sheets in the ER network. The increase in sheet morphology may be in response to increased translation pressure.

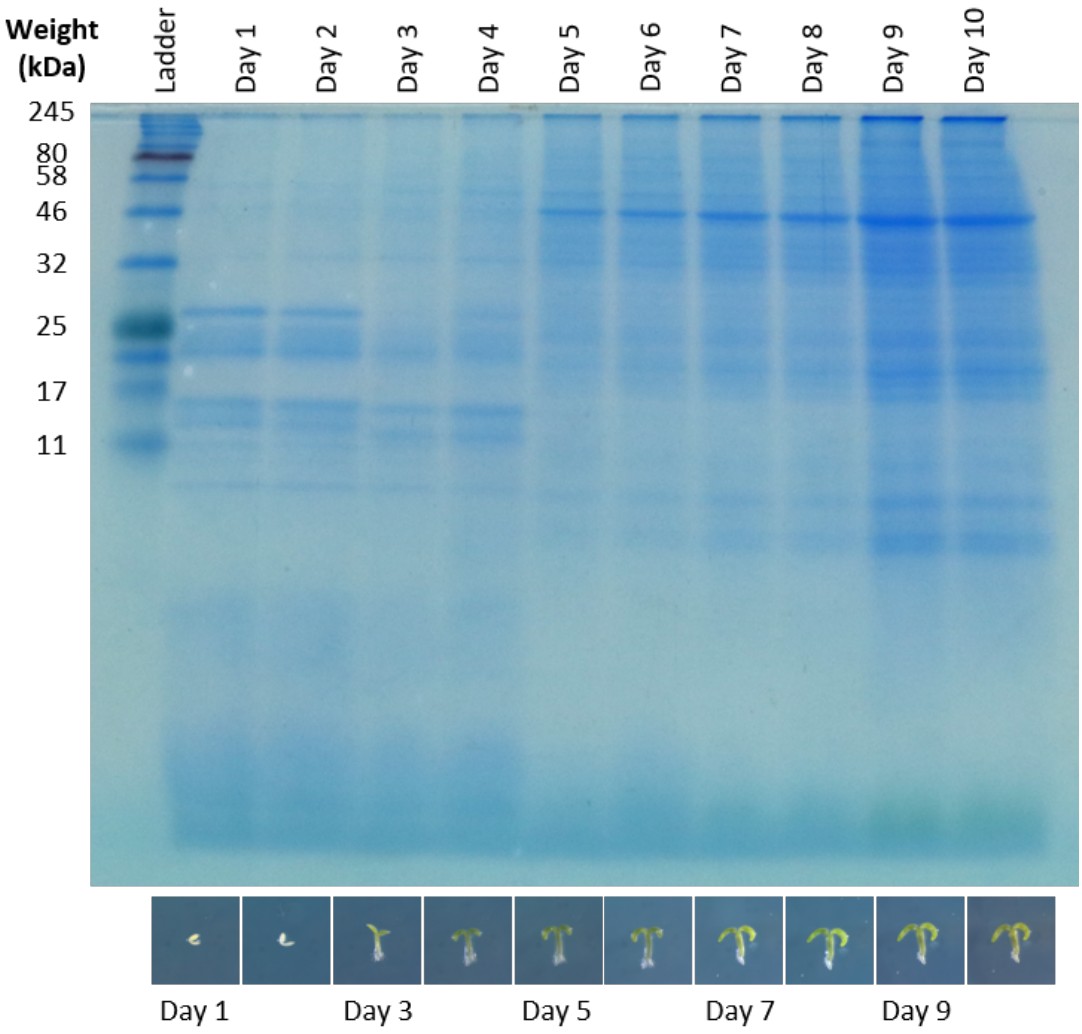

Figure 5.13: ***Total protein change in A. thaliana seeds throughout germination.*** *Images at the bottom correlate the protein change to morphological changes during seed germination and growth. Bands around 25 kDa in days 1-4 may be storage proteins, which are used up during initial germination. Bands appearing at day 4 at approximately 46 kDa may be proteins relating to photosynthesis.*

Interestingly the whole seeds grew bigger and became more developed than the uncoated seeds. By day 10, the whole seeds had four leaves, whereas the uncoated seeds remained at a similar size as on day 5. Appendix figure 7.25 shows the uncoated and whole seeds on day 28. The uncoated embryos had either died or not developed any further than on day 10. The whole seeds had grown and developed as would be expected. For future work, it would be worth investigating what the ER morphology is for the whole seeds. Perhaps the ER morphology is different, or the changes occur on a different time-scale.

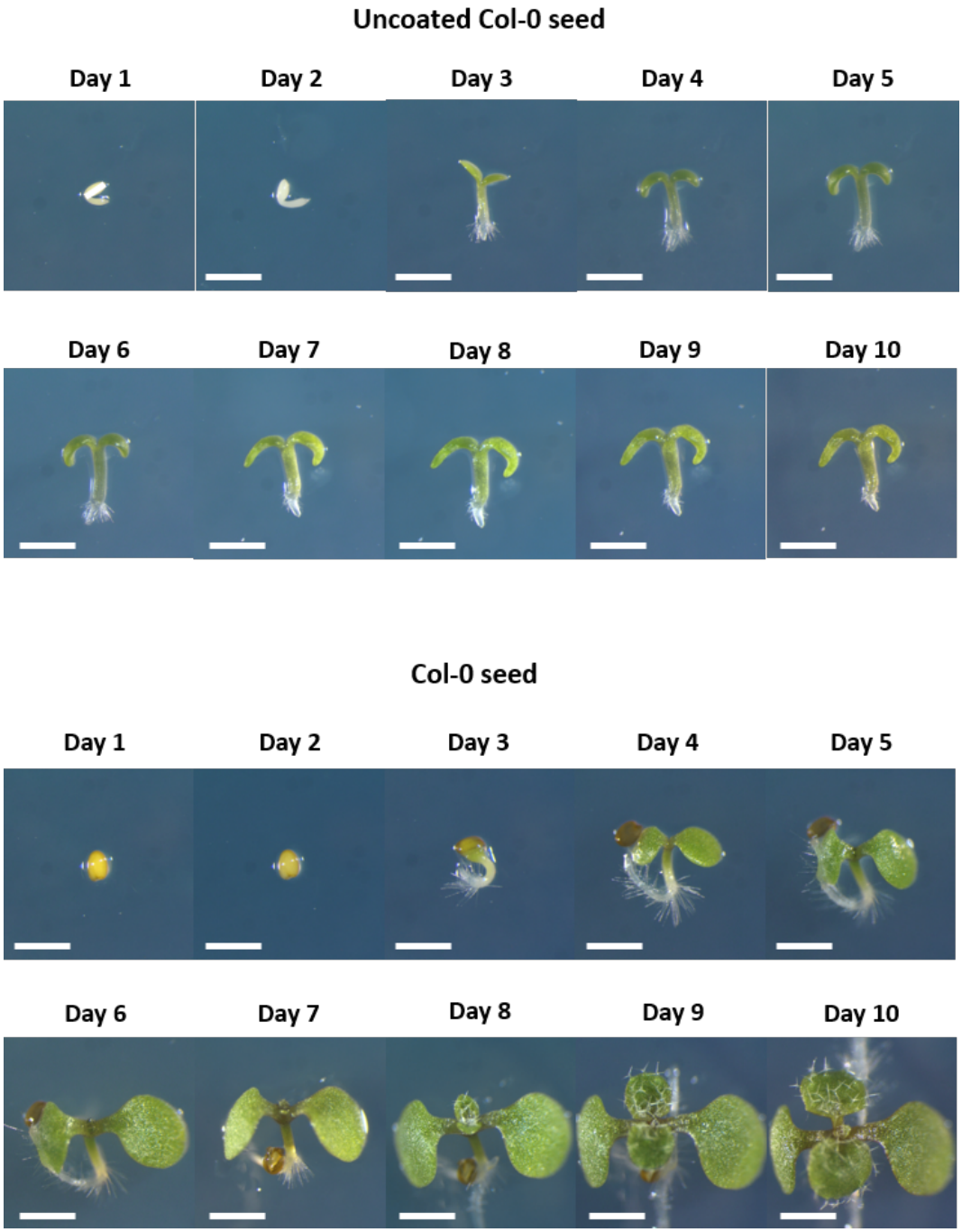

Figure 5.14: ***Col-0 A. thaliana seed during germination and seedling development.*** *The upper panel shows how the plant develops over ten days if the seed is uncoated (removal of testa and endosperm) on day one. The lower panel show how the plants develop if the seed is not uncoated. Removing the endosperm and testa severely stunts and inhibits growth and development. Scale bar = 1mm.*

Rhodamine B staining

To ascertain whether the over-expression of GFP-HDEL was causing changes to ER morphology, Col-0 embryos were stained with rhodamine B (figure 5.15). Alongside this, a calnexin-GFP line was also stained with rhodamine B, to test whether rhodamine B labels other membranes than the ER. Calnexin is an ER-resident chaperone, that assists in protein folding. Unlike GFP-HDEL it labels the membrane of the ER, as opposed to the lumen. The results from the calnexin-GFP germination can be seen in figure 5.16.

Day 2 of Col-0 germination appeared very similar to day 2 of GFP-HDEL germination. The network was tubular with circular holes, however there were a few bright spots distributed throughout and some of the cells had sheets. Day 1 and 2 of rhodamine stained calnexin-GFP highlights that the bright spots were not part of the ER network, and what appeared to be sheets with rhodamine B were closely situated tubules.

On day 3, for both the Col-0 and the calnexin lines, the network was predominately sheets, as in the GFP-HDEL line. The rhodamine B clearly stained additional spots, which are likely to be lipid bodies (figures 5.15 and 5.16).

By day 4 the sheets in both the Col-0 and calnexin lines had begun to disperse, and tubules were visible. The bright spots identified with rhodamine B were localised to the holes in the sheets.

By day 6 the ER was a predominately tubular, vegetative network. The spots labelled by rhodamine B were still present, and again localised to the sheets.

Overall there were a few differences between the network visualised with GFP-HDEL compared with rhodamine B. However, by using calnexin-GFP most differences could be attributed to the rhodamine B either staining additional structures, or the increased fluorescence background created poorer resolution.

Nile red staining

To determine whether the circles that had been previously been seen with rhodamine B were caused by lipid bodies, Nile red was used to stain the lipid bodies. Figures 5.17 and 5.18 show the results from day 1 to day 7 of germination.

On day 1 and 2 it was clear that there were large numbers of lipid bodies in the seed. These lipid bodies also fit very well into the circles formed in the network. These lipid bodies are larger however, than the bright spots seen with rhodamine

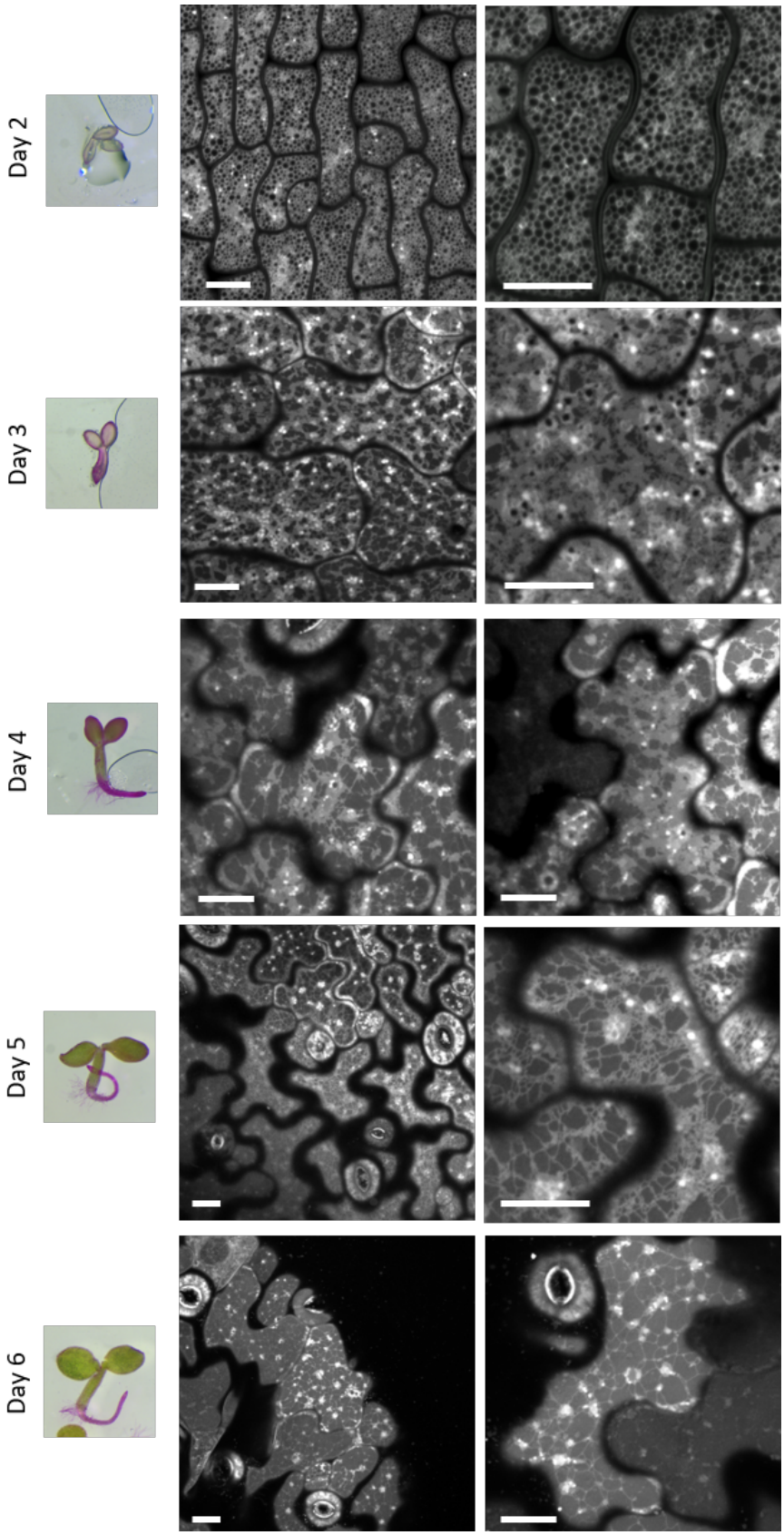

Figure 5.15: ***Rhodamine B stained Col-0 A. thaliana embryos during germination.*** *Cells imaged are from the cotyledons. Rhodamine B stains additional organelles to the ER, though the changes in morphology from tubular, to predominately sheet and finally to vegetative tubular can still be seen, indicating that this change is not due to the over-expression of GFP-HDEL. Scale bar = 10 μm.*

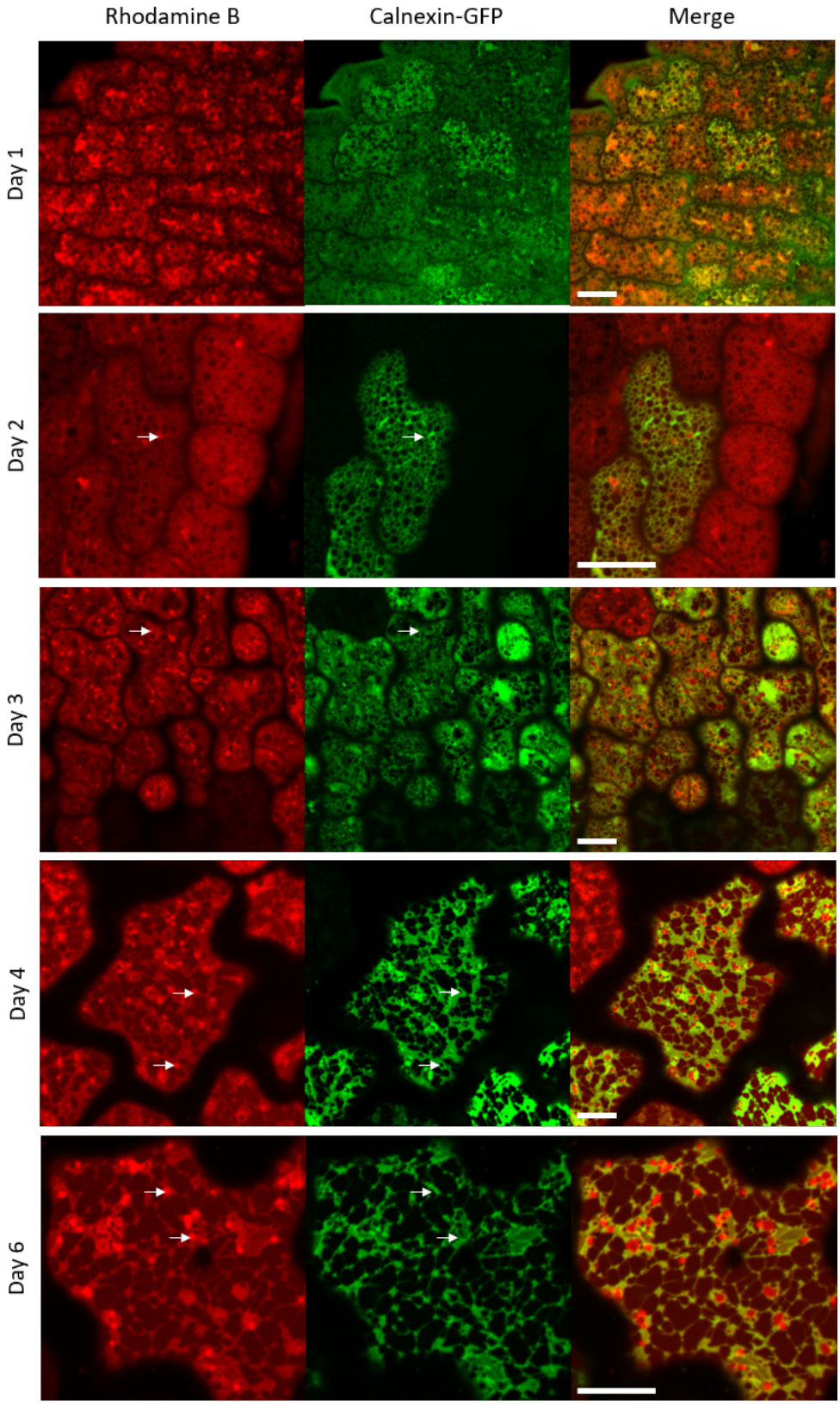

Figure 5.16: ***Rhodamine staining of a calnexin-GFP A. thaliana line during germination.*** *Cells imaged are from the cotyledons. Rhodamine B stains additional organelles to the ER, though the changes in morphology from tubular, to predominately sheet and finally to vegetative tubular can still be seen. Arrows indicate organelles and structures stained by rhodamine B which are not present in the calnexin-GFP images. Scale bar = 10 μm.*

B. Perhaps there are multiple types of lipid bodies. On day 2 the lipid bodies are present except in ER cisternal sheets, which suggests that the lipid bodies influence the shape of the ER network and conversely.

On day 3 there were fewer lipid bodies than on day 1 and 2. They are present in the holes of both the tubule and sheets. There were however a few holes in the network that did not appear to have any lipid bodies inside. This suggests that although the lipid bodies may be influencing the shape of the network, the network is capable of forming these shapes itself.

By day 4, when the network was predominately made of sheets and the number of lipid bodies had greatly reduced. The image shown is maximum projection of a series of images. It shows that some of the lipid bodies are larger than the holes that they appear to make in the network, and only the top part of the spheres are intruding into the sheet.

On day 5, which had a reduced amount of sheets, it is interesting to note that the lipid bodies that were present were associated with sheets. None of them were next to tubules. This could be because the tubules are more dynamic, and so the sheets provide a more stable area for the lipid bodies to associate with the ER.

By day 6, the particular embryos imaged had a vegetative ER with few lipid bodies. On day 7 the embryos imaged had more sheets than those imaged on day 6. This shows that although the time-line of ER morphology changes is fairly reliable, there will always be individual differences.

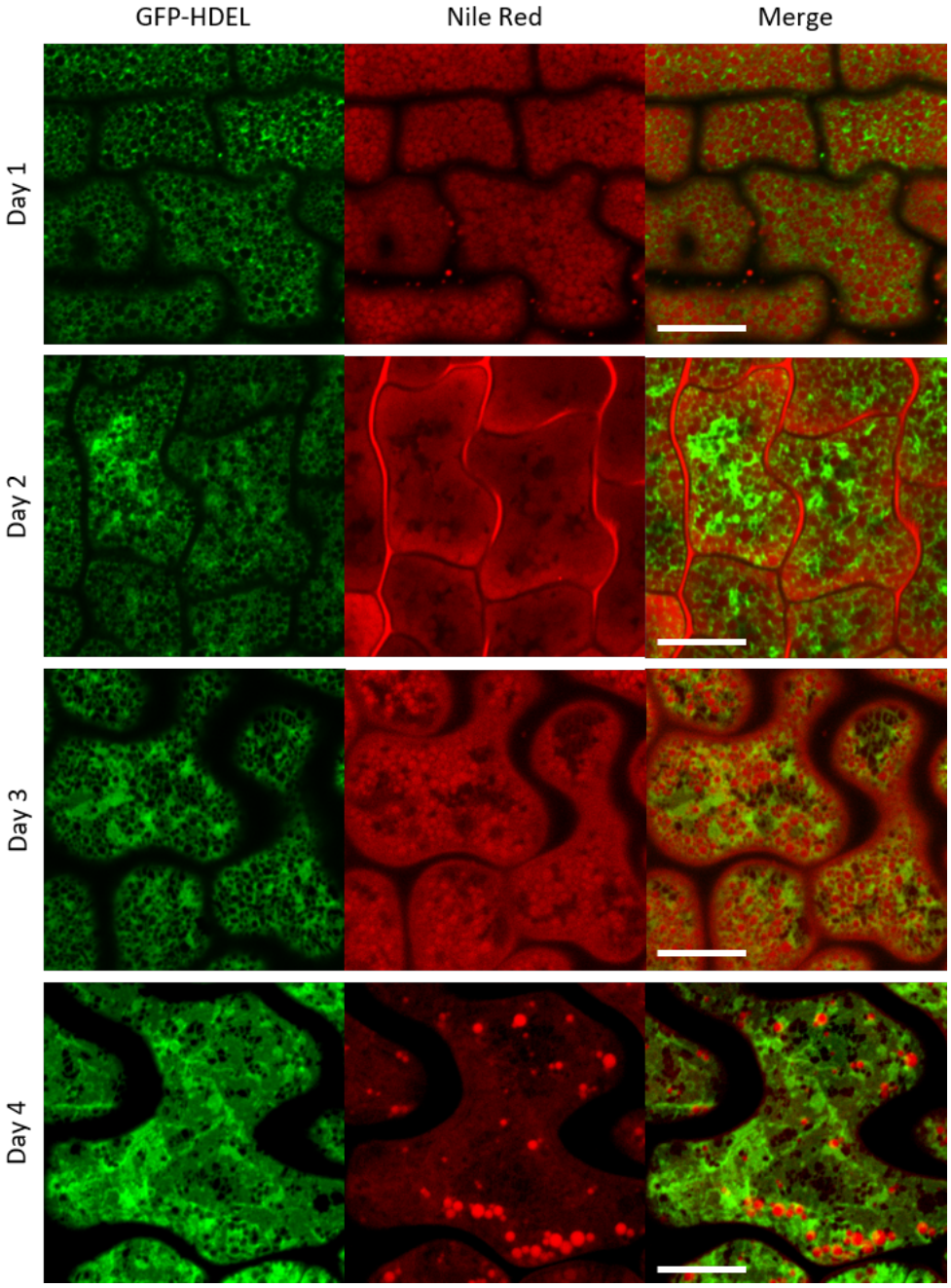

Figure 5.17: ***Nile red staining of GFP-HDEL A. thaliana embryos during days 1 - 4 of germination.*** *Nile red stains the lipid bodies in the cell. On day 1 the many lipid bodies sit within the holes of the ER network. By day 4 the number of lipid bodies has reduced, but they still sit within holes of the ER network. Scale bar = 10 μm.*

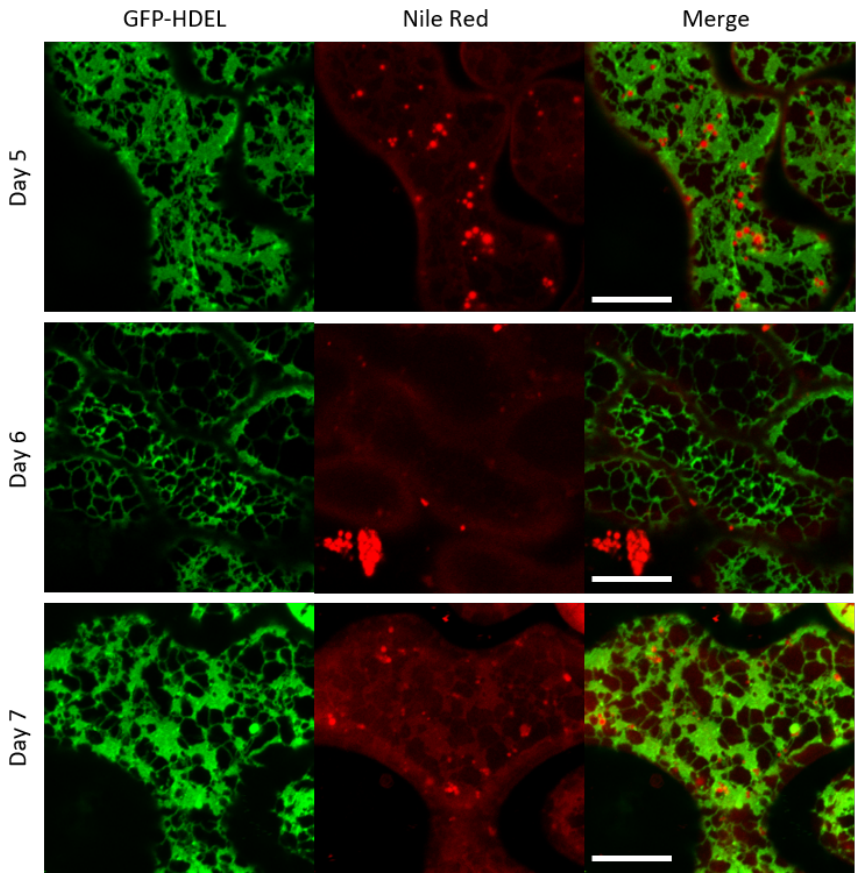

Figure 5.18: ***Nile red staining of GFP-HDEL A. thaliana embryos during days 5 - 7 of germination.*** *Nile red stains the lipid bodies in the cell. The lipid bodies have dramatically reduced in number from day 1, though they still remain within the holes of the sheets in the ER. The lipid bodies are always in contact with the ER. Scale bar = 10 μm.*

Mutants during germination

To understand more about how the morphology of the ER is controlled, analysing the ER network in mutant plant lines may provide some answers. The same mutants used in the seed development experiment were employed: the YFP-RTN13 over-expresison, the triple-reticulon knockout (RTN1/RTN2/RTN13), the *pah1pah2* knockout and the *lnp1lnp2* knockout. The germination series for mutants can be found in figures 5.19 and 5.8.

As with the YFP-RTN13 development series there were large fluorescent aggregates present in most cells. On day 1 and day 2, the network was still tubular, though there appeared to be smaller, more numerous holes in the network. On day 3, unlike the GFP-HDEL line, there were no sheets in the network. By day 4 some sheets had developed, though not to the same degree as in the GFP-HDEL line, and these continued into day 5. On day 6 the network was entirely tubular and looked like vegetative ER. All of this shows that the over-expression of YFP-RTN13 creates a more tubular network, through increased constriction.

Day 1 and 2 of the triple-reticulon knockout produced a tubular network, very similar to the GFP-HDEL line. On day 3, although not shown, there were significant differences between the different embryos imaged. One embryo had an ER network similar to day 1 and 2, another embryo had a network that was predominately made of sheets and the one shown here was mixture of the two others. On days 4 and 5 the network was generally made of sheets. By day 6 the amount of sheet morphology had reduced, though there were more than in the GFP-HDEL line. Knockout of those three reticulons may have lead to an increase the number of sheets, though this is difficult to quantify by eye.

The *lnp1lnp2* mutant had tubular network, similar to the GFP-HDEL line on days 1 and 2. Day 3 and 4 produced networks predominately consisting of sheets, though the holes within the sheets are bigger than those in the GFP-HDEL line. On day 5 the number of sheets has reduced, though again, there appear to be more larger holes and fewer smaller ones, as compared to the GFP-HDEL line. By day 6 the network is mainly tubular and looks like normal, vegetative ER. The *lnp1lnp2* mutant appears to have increased the size of the holes in the sheets, though it is unclear as to how this links to more unstable junctions Chen et al. (2015); Shemesh et al. (2014).

The *pah1pah2* mutant had a tubular morphology on day 1 and 2, like the GFP-HDEL line, which was surprising given that it is known to create sheets in the network. On day 3 however, the network was predominately sheet-like, though

there were patches which had circular holes. These circular holes were smaller and more clustered than in the GFP-HDEL line. By day 4 there were no holes in the network, and it was one large sheet. There were irregularities in the fluorescence, suggesting there were tubules or sheets laying on top of one another. On day 5 the cells still had large sheets, though darker areas of fluorescence suggested there were holes within the layers of cisternal sheets. By day 6 there were more tubules present, though there were still more sheets than with the GFP-HDEL lines. The *pah1pah2* mutant not only increases the percentage of sheets in the cell, but how early they appear and how long they last.

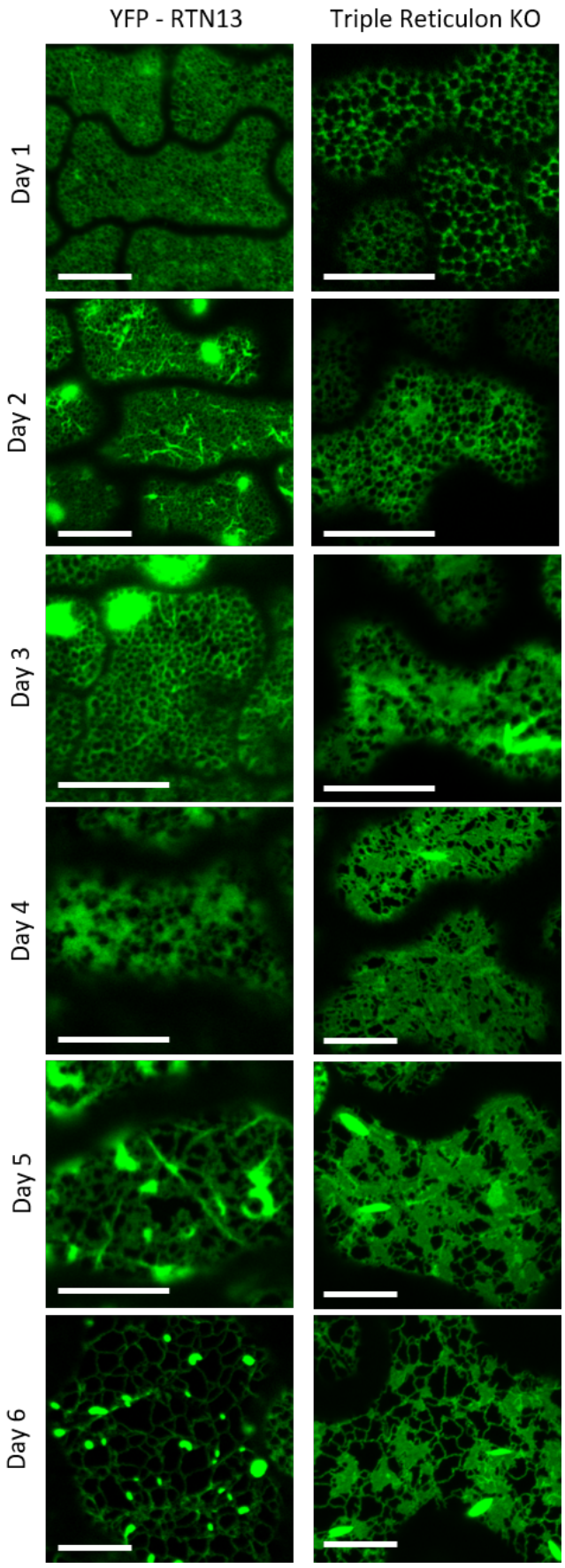

Figure 5.19: ***ER morphology through A. thaliana seed germination of YFP-RTN13 over-expression and triple-reticulon knockout mutants.*** *The cells imaged were from the embryo cotyledons. The ER of the triple-reticulon knockout was visualised with GFP-HDEL. Large protein aggregates were present in the YFP-RTN13 sample, due to the high over-expression. Scale bars = 10µm*

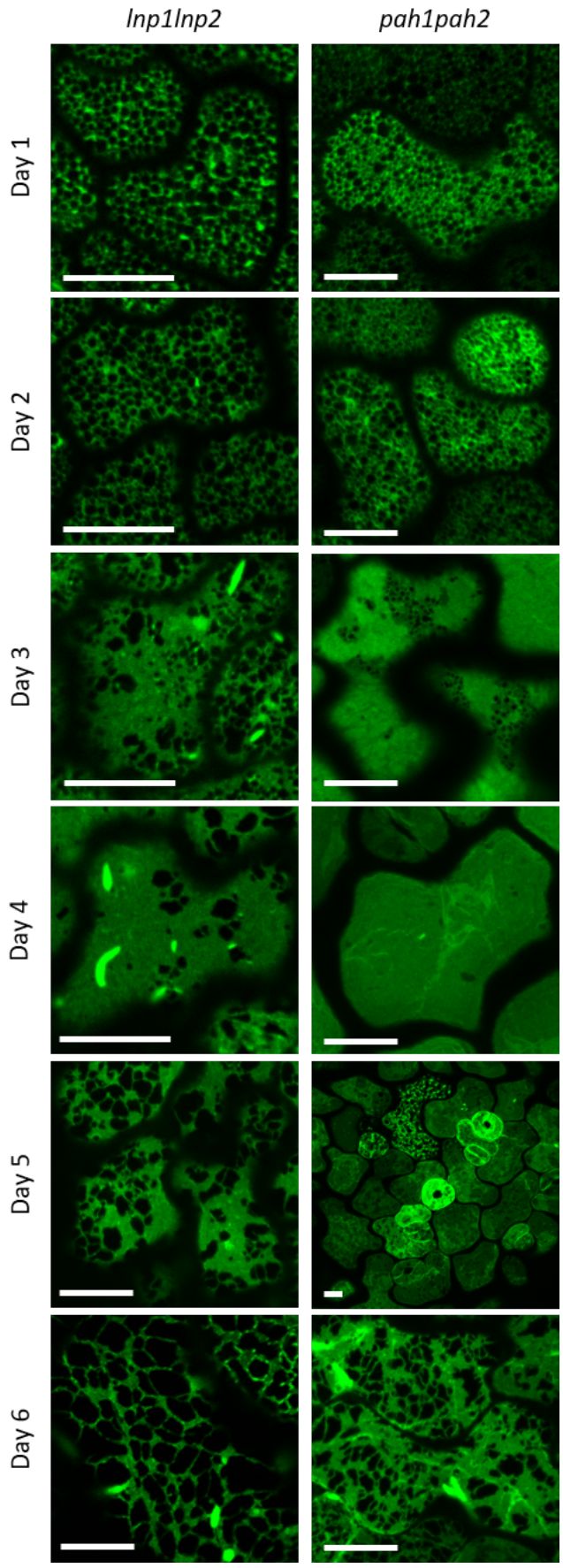

Figure 5.20: ***ER morphology through A. thaliana seed germination of lnp1lnp2 and pah1pah2 mutants.*** *The cells imaged were from the embryo cotyledons. The ER in both lines was visualised with GFP-HDEL. Scale bars = 10µm*

5.3.3 Image analysis of seeds from the GFP-HDEL line

Having acquired many hundreds of images of the ER during germination and development, it is clear that there are large differences in the morphology between different stages and different plant lines. In this age it is important to quantitatively analyse images. Smaller, or more subtle differences might then be identifiable.

The aim of this final section of the project was to create a simple, easy to use tool that could compare mutant ER morphology to wild-type morphology. Many image analysis tools can be computationally difficult, requiring a lot of time to analyse each image, or require specialist knowledge about a programme or a coding language. ImageJ, or FIJI (Schindelin et al., 2012), is an open-source programme, making it accessible to everyone, as opposed to commercial programmes such as MATLAB. FIJI (a version of ImageJ that contains commonly used plugins) also allows actions to be recorded and stored as a macro. This again makes it more accessible to those who do not have extensive (or any) coding knowledge. One of the simplest features that could be used to compare ER morphologies is the ratio of sheets to tubules in the network. For example the *pah1pah2* mutant is known to create networks with an increased proportion of sheets.

Initially Renyi-Entropy thresholding and Otsu thresholding were performed with varying factors to create two binary images. One which showed the whole ER and one which showed just the sheets of the ER, similar to the method used in English and Voeltz (2013b). Both these methods work by mathematically fitting the histogram values (which show the number of pixels at each intensity from 0 to 255) into two categories: black (background) or white (foreground). This method did not produce biologically relevant results for every morphology. Other methods that were tested in order to create an image with just sheets, included Fourier Transform and Gaussian Blur, though neither were used as segmentation proved to create better binary images.

A COST (European Cooperation in Science and Technology) training school on 'Image Analysis in Phenotyping', presented a different method of creating binary images. The Trainable Weka Segmentation (v3.2.5) (Arganda-Carreras et al., 2016) can be trained to identify background or foreground pixels from a user image. It combines multiple learning algorithms and filters to identify different classes within an image.

In addition to the segmentation tool, the images were pre-processed using a Median filter, which reduced the amount of noise in the image, particularly 'salt

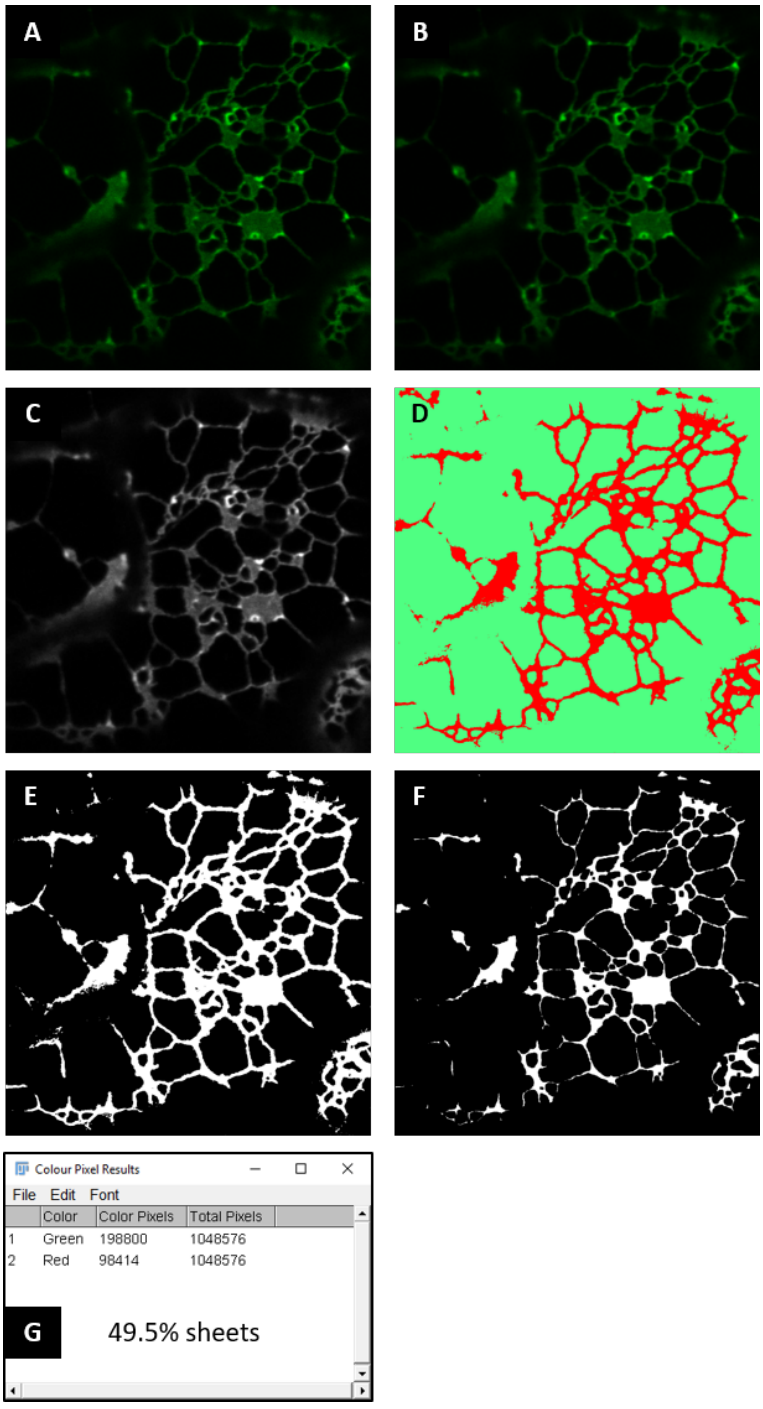

Figure 5.21: ***Example output from the image analysis macro.*** *A) The original image. B) The image after the Gaussian Blur filter has been applied. The ER looks more uniform. C) The image after the histogram normalisation has occured. D) The output from the Trainable Weka Segmentation. E) The binary image showing the total ER network. F) The binary image after the Erode function was applied, this simulates the sheets of the ER. G) The results from the Color Pixel Counter, where Green signifies the pixels in the total ER and Red signifies the pixels in the sheets.*

and pepper' noise (where pixels have intensity values of 0 or 255 at random). Secondly the saturation levels were set to 0.5% (the percentage of pixels with intensity values of 225), to normalise the histogram.

The 'Erode' function used on a binary image was found to create the most suitable images. The Erode function starts from a black pixel (background) and identifies any white pixels adjacent to it. The function then turns the adjacent white pixels black. This can be repeated until the low frequency structures, such as tubules are removed from the image. The edges of the sheets will also be removed and made smaller.

Once the two binary images had been created (one showing the complete network and the other showing the sheets), the percentage of sheets could be calculated using the 'Color Pixel Counter' (Pichette, 2010). By converting the 8-bit binary images into RGB colour images, the plugin would count the white pixels as coloured pixels. By taking the square root of the number of pixels in an image, dividing by the image resolution and then squaring the answer, the area in microns could be calculated. This was implemented as without it, the zoom level of the images would affect the outcome. By dividing the area of the sheets by the area of the whole network, the percentage of sheets could be found. The full macro code can be found in appendix figures 7.27 and 7.28. An example of the output from each step can be found in figure 5.21.

Figures 5.22 and 5.23 show some examples for the processed confocal image and the two binary images for days 1 - 7 of germination. These images were created using GFP-HDEL. Col-0 plants were not imaged because the background fluorescence that was produced by the rhodamine B staining made it impossible to obtain good results. Likewise the resolution of the network from the seed development series made it difficult.

The macro does slightly over-estimate the size of the tubules, which sometimes results in them not being fully eroded. However, as mentioned previously, the erode function will also affect the sheets, making them smaller, which is why the number of erode cycles has been purposely made lower than necessary to entirely remove the tubules (the reduction in sheets will compensate for the remaining tubules). The macro also cannot distinguish between the bundles of tubules and the sheets, occasionally making it appear as though there are more sheets than we would label. Appendix figure 7.26 shows this more clearly.

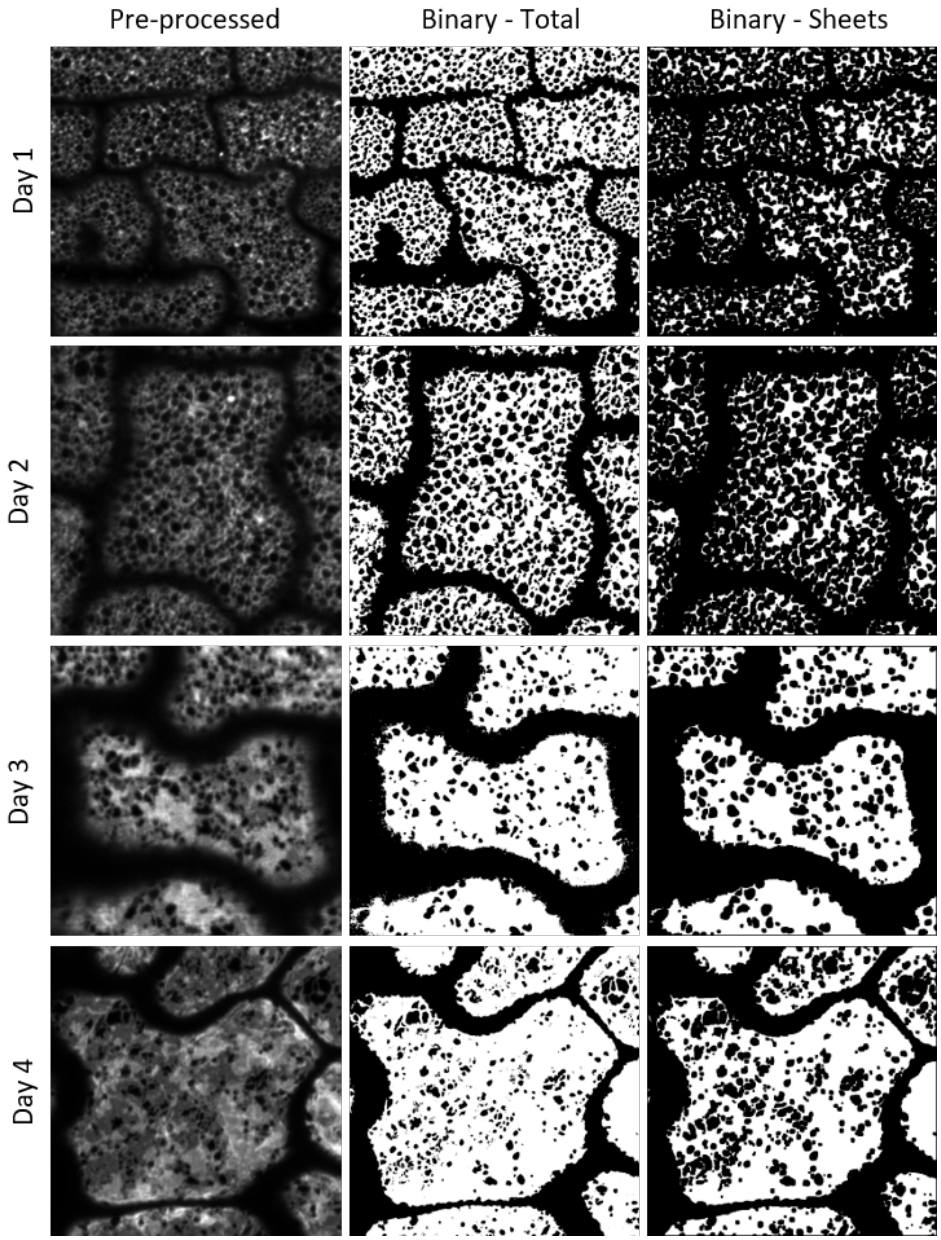

Figure 5.22: ***Image Analysis germination of GFP-HDEL line, days 1 - 4.*** *Pre-processed images had a median filter and a saturation level applied. The Binary - Total imagers were the result of the Trainable Weka Segmentation. The Binary - Sheets images were after the Erode function had been applied.*

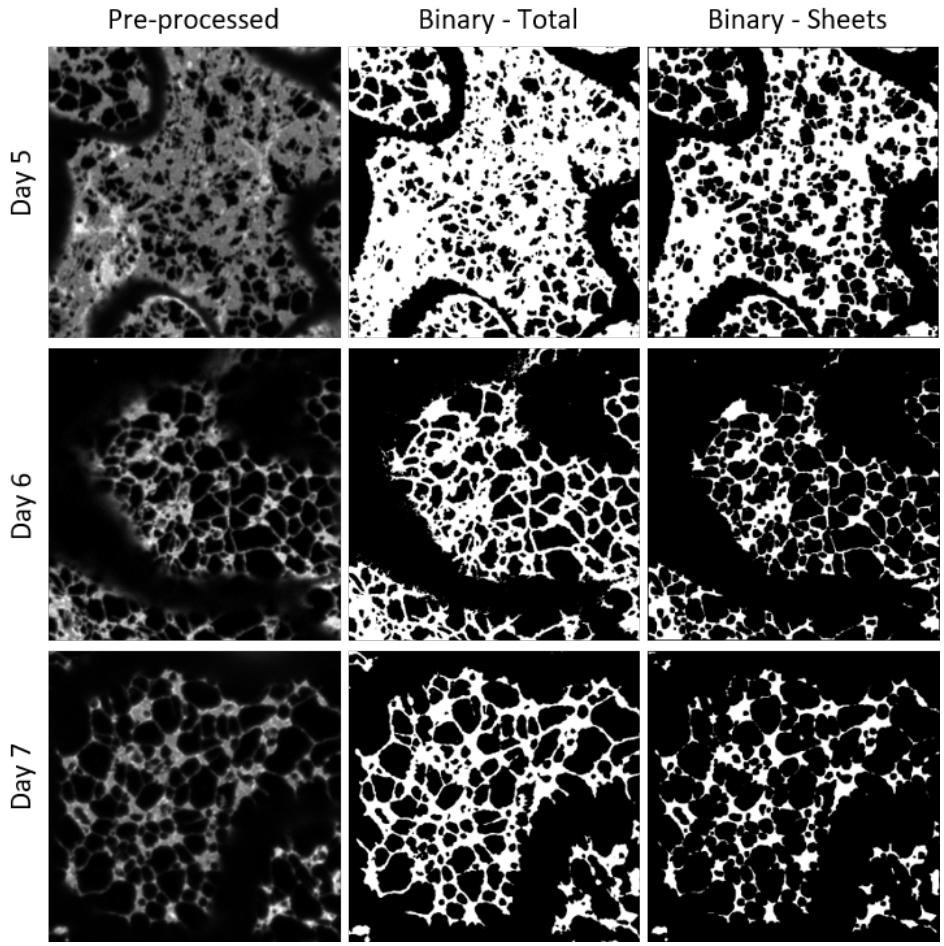

Figure 5.23: ***Image Analysis germination of GFP-HDEL line, days 5 - 7.*** *Pre-processed images had a median filter and a saturation level applied. The Binary - Total imagers were the result of the Trainable Weka Segmentation. The Binary - Sheets images were after the Erode function had been applied.*

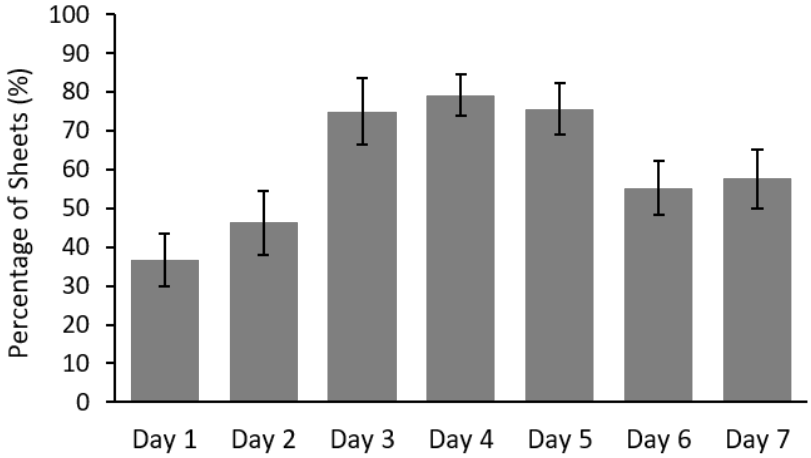

Figure 5.24: ***Average percentage of sheet morphology in cells during germination.*** *Error bars show the standard deviation (+ and -). Minimum number of samples (N) = 11. A clear increase in the percentage of sheet morphology can be seen between days 3 and 5. The percentage of sheet morphology remains higher in days 6 and 7 then it was in days 1 and 2.*

Figure 5.24 and table 5.1 show the percentage of sheet morphology from day 1 to day 7 of germination. A one-way ANOVA was conducted to evaluate the null hypothesis that each day has the same mean; the variance within each day was equal to between days (n=97). The assumption of homogeneity of variances was tested and found tenable using Levene's test ($F(6,90) = 0.635$, $p = 0.702$). The ANOVA was found significant (appendix figure 7.29) ($F = 72.992$, F-Crit = 2.201, $p = 0.000$ (1.9×10^{-32})) and therefore failed to accept the null hypothesis, suggesting that there is a difference in the percentage of sheet morphology between one or more of the days.

Post-hoc Tukey analysis was conducted to compare the difference in means between days (table 5.2 and appendix figure 7.30 for full output). Day 3 (mean = 74.9, sd = 8.5), day 4 (mean = 79.2, sd = 5.3) and day 5 (mean = 75.6, sd = 6.6) were identified as having the most sheet morphology. Days 3, 4 and 5 did not indicate a difference in the mean percentage of sheet morphology compared to each other ($p < 0.6$), however days 3, 4 and 5 has significantly more sheet morphology compared to days 6 and 7 ($p < 0.000$). The macro also identified a small increase in the amount of sheet morphology from day 1 (mean = 36.7, sd = 6.8) to day 2 (mean = 46.3, sd = 8.3) ($p = 0.022$). Whether these are actual sheets, or slightly dense regions of tubules is debatable, but does perhaps hint at the seed beginning to increase the number of sheets. Day 1 had significantly less sheet morphology than all other days ($p < 0.000$). Day 2 had significantly less sheet morphology than other days, except compared to day 6 ($p = 0.057$). The number of sheets also appears to increase between day 6 (mean = 55.2, sd = 7.0) and day 7 (mean = 57.6, sd = 7.6), though this is not statistically significant ($p = 0.980$) indicating that there was a similar amount of sheet morphology. It can only be assumed that some of the seedlings imaged on that day where slightly slower to develop, this can be corroborated by the increased standard deviation.

	Day 1	Day 2	Day 3	Day 4	Day 5	Day 6	Day 7
Mean (%)	36.7	46.3	74.9	79.1	75.6	55.1	57.6
Standard Deviation	6.8	8.3	8.5	5.3	6.6	6.9	7.6
Number of cells analysed	14	11	16	14	18	12	12

Table 5.1: ***Percentage of sheet morphology in the ER from image analysis results of the GFP-HDEL line.*** *Mean percentage of sheet morphology and the standard deviation shown for each set of images analysed from each day. The percentage of sheet morphology clearly peaks at day 4, with day 1 exhibiting the lowest percentage compared to the other days.*

	Day 2	Day 3	Day 4	Day 5	Day 6	Day 7
Day 1	-9.595 (p = 0.022)	-38.239 (p = 0.000)	-42.481 (p = 0.000)	-38.933 (p = 0.000)	-18.483 (p = 0.000)	-20.946 (p = 0.000)
Day 2		-28.644 (p = 0.000)	-32.886 (p = 0.000)	-29.338 (p = 0.000)	-8.888 (p = 0.057)	-11.351 (p = 0.000)
Day 3			-4.241 (p = 0.674)	-0.693 (p = 1.000)	19.756 (p = 0.000)	17.293 (p = 0.000)
Day 4				3.547 (p = 0.808)	23.998 (p = 0.000)	21.535 (p = 0.000)
Day 5					20.45 (p = 0.000)	17.987 (p = 0.000)
Day 6						-2.463 (p = 0.980)

Table 5.2: ***Difference in means of percentage of sheet morphology between days for GFP-HDEL A. thaliana germination.*** *Post-hoc Tukey one-way ANOVA test conducted between the two days. p-values smaller than 0.05 suggests sufficient evidence for significant difference in means. The majority of the days have significantly different percentage of sheet morphology, except days 3, 4 and 5 compared to each other and days 6 and 7 compared to one another. Days 2 and 6 also have similar percentages of sheet morphology.*

5.3.4 Image analysis of mutants

In addition to this, some of the mutants imaged thoughout germination were also subjected to image analysis (pages 162 and 163). The lunapark double knockout (*lnp1lnp2*), the *pah1pah2* mutant and the triple reticulon knockout lines were all analysed. The YFP-RTN13 over-expression line was not analysed as the large fluorescent aggregates in the majority of images interfered with the image analysis.

Figure 5.25 and table 5.3 show the percentage of sheets from day 1 to day 7 of germination for each of the lines, including GFP-HDEL only. A two-way ANOVA was conducted to evaluate three null hypotheses: firstly that the mean percentage of sheet morphology is the same for each day, secondly that the mean percentage of sheet morphology is the same in each line and finally that there is no significant interaction between which day and which line.

The ANOVA was found significant for all three hypothesis (appendix figure 7.31). Firstly, the mean percentage of sheet morphology was significantly different between some days (F(5,283) = 103.343, F-crit = 2.249, p = 0.000 (1.24×10^{-59})). Secondly, the mean percentage of sheet morphology was significantly different between some lines (F(3,283) = 29.721, F-crit = 2.639, p = 0.000((1.52×10^{-16})). Finally, there was an interaction between the lines and the days (F(15,283) = 6.635, F-crit = 1.705, p = 0.000((4.29×10^{-12})). To further analyse the specific differences between each of these variables post-hoc Tukey analysis was performed

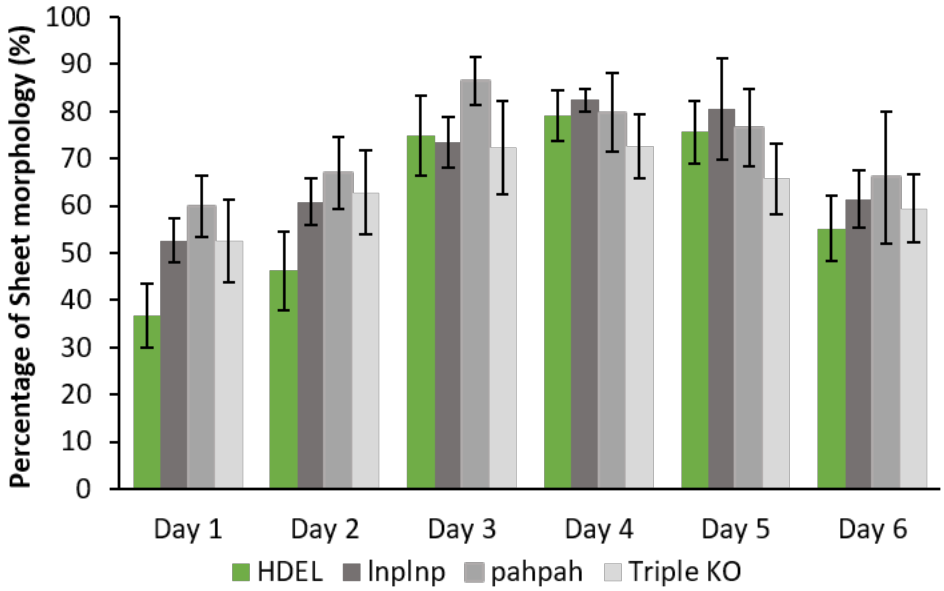

Figure 5.25: ***Percentage of sheet morphology in the ER from image analysis of GFP-HDEL only and mutant A. thaliana lines.****. Error bars show the standard deviation of each sample (+ and -). Minimum number of cells imaged in each sample (N) = 8. All of the mutant lines appear to have more sheets than the GFP-HDEL only line*

(appendix figure 7.32).

The Tukey analysis showed that as with the GFP-HDEL only analysis, day 3 (mean = 76.84 sd = 9.06), day 4 (mean = 78.4, sd = 6.7) and day 5 (mean = 74.1, sd = 9.5) were identified as having the most sheet morphology (appendix figure 7.33). Days 3, 4 and 5 did not indicate a difference in the mean percentage of sheet morphology compared to each other (day 3 v day 4, p = 0.944; day 3 v day 5, p = 0.365; day 4 v day 5, p = 0.052). The macro also identified an in the amount of sheets from day 1 (mean = 49.2, sd = 11.6) to day 2 (mean = 58.9, sd = 10.6) (p = 0.000). Day 1 had significantly less sheet morphology than all other days (p <0.000). As previously day 2 had significantly less sheet morphology than other days, except compared to day 6 (difference = -1.42, p = 0.949).

To investigate the differences between lines a post-hoc Tukey was conducted. There was an overall significant difference between the GFP-HDEL line and the *lnp1lnp2* mutant (mean difference = -5.47, p = 0.000 (6.65×10^{-5})) and an overall significant difference between the GFP-HDEL line and the *pah1pah2* mutant (mean difference = -10.05, p = 0.000 (5.63×10^{-13})). There was not a significant difference in the overall percentage of sheet morphology between the GFP-HDEL only line and the triple reticulon knockout mutant (mean difference = -1.67, p = 0.518) (appendix figure 7.33).

		Mean percentage of sheets (%)	Standard deviation	Count
Day 1	HDEL	36.7	6.8	14
	lnp1lnp2	52.7	4.7	12
	pah1pah2	60.0	6.4	10
	Triple KO	52.5	8.8	8
Day 2	HDEL	46.3	8.3	11
	lnp1lnp2	60.9	4.9	12
	pah1pah2	67.0	7.6	8
	Triple KO	62.8	8.9	13
Day 3	HDEL	74.9	8.5	16
	lnp1lnp2	73.5	5.3	12
	pah1pah2	86.5	5.0	12
	Triple KO	65.2	9.8	9
Day 4	HDEL	79.1	5.3	14
	lnp1lnp2	82.4	2.4	12
	pah1pah2	79.82	8.3	7
	Triple KO	72.6	6.8	12
Day 5	HDEL	75.6	6.6	18
	lnp1lnp2	80.5	10.8	10
	pah1pah2	76.5	8.2	13
	Triple KO	65.8	7.5	15
Day 6	HDEL	55.1	6.9	12
	lnp1lnp2	61.4	6.1	10
	pah1pah2	66.0	14.0	11
	Triple KO	59.5	7.2	12

Table 5.3: ***Descriptive statistics of percentage of sheet morphology in the ER from image analysis of GFP-HDEL only and mutant A. thaliana lines.*** *Statistics provided from the output of a two-factor ANOVA. HDEL = GFP-HDEL line. Triple KO = Triple reticulon knockout.*

To further analyse the interaction between the lines on each day an appropriate post-hoc Tukey test was conducted (table 5.4). The *lnp1lnp2* mutant had significantly more sheet morphology than the HDEL-only line for days 1 and 2 (day 1, difference = 16.01, p = 0.000; day 2 difference = 14.62, p = 0.000). For days 3 - 6 however there was no significant difference in percentage of sheet morphology between the *lnp1lnp2* line and the GFP-HDEL line. Overall there was no significant difference between the *lnp1lnp2* mutant and GFP-HDEL. The main morphological difference that was seen by eye, the increased size of holes in the sheets, could not be measured with this macro. The post-hoc Tukey analysis comparing days within each line was also conducted, though will not be discussed in detail here (appendix tables 7.1 - 7.3).

The *pah1pah2* mutant had significantly more sheets than the GFP-HDEL line on days 1 and 2 (day 1, difference = 23.29, p = 0.000; day 2 difference = 20.73, p =

	Day 1	Day 2	Day 3	Day 4	Day 5	Day 6
HDEL vs *lnplnp*	-16.01 (p = 0.000)	-14.62 (p = 0.000)	1.36 (p = 0.962)	-3.27 (p = 0.477)	-4.93 (p = 0.414)	-6.22 (p = 0.391)
HDEL vs *pahpah*	-23.29 (p = 0.000)	-20.73 (p = 0.000)	-11.64 (p = 0.001)	-0.68 (p = 0.994)	-0.91 (p = 0.989)	-10.84 (p = 0.033)
HDEL vs Triple KO	-15.85 (p = 0.000)	-16.57 (p = 0.000)	2.55 (p = 0.840)	6.59 (p = 0.028)	9.80 (p = 0.006)	-4.31 (p = 0.655)

Table 5.4: ***Difference in percentage of sheet morphology means between wild type and mutant germination*** *Highlights the difference in means, and significance of the difference for each day between the HDEL-only line and the mutants, lnplnp, pahpah and the triple-reticulon knockout, calculated through a two-factor ANOVA and a post-hoc Tukey test (appendix figures 7.34 and 7.35)*

0.000) and also day 3 (difference = 11.64, p = 0.001) and day 6 (difference = 10.84, p = 0.033). For day 4 and 5 there is no significant difference in the percentage of sheet morphology (day 4 difference = 0.68, p = 0.994, day 5 difference = 0.91, p = 0.989), despite the *pah1pah2* mutant visually seen to have an ER network consisting of one continuous sheet. This is because the macro did not always process the sheets very well; the irregularities in the sheet fluorescence were sometimes processed as 'holes' in the network (appendix figure 7.36). The image analysis macro would determine the percentage of sheet morphology to be less than 70%, whereas human analysis would determine it as almost 100%, which shows there is some dependence on fluorescence intensity when analysing the network. Due to this, the macro should not be used on the *pah1pah2* mutant, particularly in comparison to other lines.

The triple reticulon knockout had significantly more sheets than the GFP-HDEL only line for days 1, 2, 4 and 5. For day 3 the triple-reticulon knockout did not have significantly less sheet morphology than the GFP-HDEL only line (difference in means = 2.55, p = 0.840), however the triple reticulon knockout did have a larger standard deviation (sd = 9.77), which was due to the wider range of morphologies seen on this day (some of the cells had networks more similar to days 1 and 2, whereas others had networks with large proportions of sheet morphology). Finally there was no significant difference between the triple reticulon knockout and the GFP-HDEL only line for day 6 (difference in means = 4.31, p = 0.655).

Overall the macro was successful in identifying the percentage of sheets in a cell, though perhaps generally over-estimated the percentage. The *pah1pah2* mutant showed that it was important to have consistent intensity in a structure, despite the macro being an intensity-independent approach. With the *lnp1lnp2* and triple reticulon knockout the macro agreed with the initial analysis, and quantified the differences.

5.4 Discussion

There were large changes seen in the ER morphology during seed development. Some of these changes were perhaps influenced by other organelles present in the cell, such as the vacuoles or lipid bodies. The walking stick stage had an unusual morphology which was possibly created by other cellular structures. The increase in the amount of sheet morphology correlated to an increase in protein production. The mature stage of seed development is known to be a stage where storage proteins are produced.

There is no clear picture as to the morphology during the torpedo stage, though the recent addition of the Airyscan module to the Zeiss 880 confocal microscope, may be able to help resolve the network. Additionally the transitions between each of the stages are not yet obvious. Further investigation into this, with more plants and more embryos images at each stage, may help make the transitions clearer.

The rhodamine B stain with the Col-0 line did not make these transitions clearer. The stain produces larger fluorescence background and evidently labels additional structures than just the ER. The morphology at each developmental stage in Col-0 did not always correspond with what was seen in the GFP-HDEL line. The mutant lines did affect the ER morphology during seed development, though apart from the *pah1pah2* mutants, some of these changes were subtle.

Given that as of now, the ER morphology has never been studied during seed development, this is new information about how the cell develops and changes during this maturation event.

There were more changes, with clearly defined transitions during seed germination. Using the imaging chamber to first identify these changes worked well as a starting point, though the image quality of using a traditional imaging set-up was far better. Although the plants were stressed in the imaging chamber, this did not affect the ER morphology, apart from from the time it took to transition between the various stages. The rhodamine B stained Col-0 and calnexin-GFP showed the same changes in the network during germination, showing that these changes are part of the process of germination, not a factor of GFP-HDEL over-expression.

Day 3 and 4 of germination are important time points. The amount of sheet morphology in the ER network increased dramatically, and this correlates to a change in protein composition of the plants and also the production of chlorophyll. This shows that the function of the ER, a site of secretory protein production, is intrinsically associated with the shape of the network.

With the exception of the work reported in Harris and Chrispeels (1980) and Stefano et al. (2014b), the ER morphology during germination has not been studied, and certainly not in as much detail. Interestingly in the mung-bean it has been seen that on day 4 there was a "smaller number of large cisternae" and that there is a reduction in the amount of tubular ER prior to protein mobilisation. The mung-bean is also a dicot, which may offer some similarities in how the seeds germinate. In *A. thaliana* it has also been previously shown that by day 3 of germination there is an increase in sheet morphology, which subsequently changes to a predominately tubular morphology (Stefano et al., 2014b). This project identified more granular changes in the morphology and brought an insight into how other organelles may influence the ER structure.

The mutants affected the morphology of the ER in a greater way during germination than they did during seed development. Although the over-expression of RTN13 did create more tubules, interestingly the reticulon knockout did not seem to have a great effect. This shows that although RTN13 is a major contributor to influencing the ER network, it is not the only protein that can have an effect.

Quantifying the percentage of sheets in the cell is one way of comparing morphologies and different lines, though there are evidently more changes than simply that. The macro did work, and correctly identified the days that had the highest percentage of sheets. There are some problems with the macro over-estimating the amount of sheet morphology when faced with tubules that are closely bundled together, and as shown with the *pah1pah2* mutant, can have trouble correctly identifying sheets when the fluorescence intensity varies across the sheet.

The macro could be developed further. Investigating the various properties of the Trainable Weka Segmentation may produce more optimised binary images. More importantly though the networks produced could be 'skeletonised', which means creating a network consisting of lines 1 pixel wide (as in the Bouchekhima et al. (2009) and Lin et al. (2014) papers). This could provide information about the connectivity of the network, how many tubules there are, or how many three-way junctions. Potentially, the edges of the binary image could be found and analysed, which may provide information about the size of the sheets, the size of the holes

in the network and how many there are. In this respect, the Fricker (2016) software is far more advanced and can produce much more information about the network. The disadvantage of this, is that access to MatLab is needed, whereas the macro created here is used on FIJI, and open source platform. Currently, until a new gold standard in ER image analysis is developed, users must decide what information they want to gather from their images, and decide what method would be most appropriately and useful for them.

Chapter 6

General discussion and future outlooks

Our limited understanding of how ER morphology is influenced is increasing. It has been shown that the form of the ER relates to its multiple functions Shibata et al. (2006, 2010); West et al. (2011). ER tubules are predominately the site of lipid production and calcium storage, whereas the sheets are the site of secretory protein production, marked by the presence of ribosomes. Reticulons and atlastins have so far been the fundamental proteins implicated in shaping the ER network Voeltz et al. (2006); Sparkes et al. (2010); Chen et al. (2011); Zhang et al. (2013). Since proteins rarely work in isolation, it has been the focus of this project to identify which other proteins reticulons might interact with.

This project has identified five non-reticulon interactors and three reticulon interactors to RTN13, the seed-specific isoform in *A. thaliana*. Through co-immunoprecipitation, using developing seeds and mass spectrometry, CBR1, GB2, LPL, SYTa, SMT2 and RTN1/4/5 were found as protein interactors to RTN13. GB2 is part of the RAB family, which is typically thought to provide membrane specificity in membrane fusion events (Cheung et al., 2002; Vernoud et al., 2003). SYTa may act as a calcium sensor during membrane fusion (Perez-Sancho et al., 2015; Siao et al., 2016), and has been shown to localise with VAP27-1, part of the SNARE complex (Yamazaki et al., 2010). CBR1, links to linoleic acid synthesis (Wayne et al., 2013), and SMT2 is involved in sterol biosynthesis (Husselstein et al., 1996; Schaller, 2003); both of which may influence membrane fluidity and other characteristics. Finally, LPL, also known as CSE or AtMAGL3, has been linked to lignin biosynthesis, and may be involved in membrane remodelling (Vanholme et al., 2013; Kim et al., 2016). The large variation in these roles suggests that ER morphology may be linked to more pathways than previously known. It is not the first time that these proteins have been identified as interactors (Bassard et al., 2012), future work could involve collaboration with the first group to have identified these interactions.

These interactions with RTN13 were validated through co-immunoprecipitation,

using a variety of tags and antibodies. Although there was no clear consensus, each putative interactor exhibited an interaction with RTN13 at least once during the validation experiments. The HA/FLAG co-immunoprecipitation experiment should be repeated with the tags on alternate N- or C-terminals. Alternative validation experiments were not as successful. Firstly, FRET-FLIM indicated that these proteins were not interacting with RTN13, though this could have been due to steric hindrance, preventing the florescent tags transferring energy. Secondly, the yeast-2-hybrid experiments were unsuccessful in even validating the homo-oligomerisation of reticulons. Yeast-2-hybrid is not typically advised for membrane proteins, and although using split-ubiqutin would have been preferable. Finally, bimolecular fluorescence complementation (BiFC) was also unable to verify even RTN13 self-interaction, though this may have been due to weak protein expression. For future work, other methods of validation, such as SPR (surface plasmon resonance) or MST (microscale thermophoresis) may be considered (Schweiger et al., 2013; Patching, 2014), though optimising protein expression may be highly time-consuming given the difficulties of expressing membrane proteins.

Additionally, it is advisable to try to determine the true localisations os the proteins, particularly given the differences in expression, as shown with N- and C-terminal RFP tags (figure 2.6), and the uncertainty in localisation provided by the Cell eFP browser (appendix figures 7.5 - 7.9). One potential method to determine these localisations could be to use immunogold labelling with electron microscopy. Future work should also test the proteins for interactions with each other (e.g. LPL interacting with SYTa). If previous publications are correct, in that these proteins form a metabolon (Bassard et al., 2012), then conducting pairwise co-immunoprecipitations may help to elucidate this metabolon.

The interactor proteins were over-expressed and down-regulated to try to asses whether they may have roles in shaping the network. Through transient expression in *N. benthamiana*, SMT2-RFP appeared to alter the ER network, however when over-expressed in *A. thaliana*, this change in ER morphology did not occur. For future experiments it would be recommended to re-transform these constructs, and to ensure that the resulting plants are homozygous. In addition to studying the over-expression of these proteins on their own, RTN13 and RL2 should each be co-expressed with each interactor. This may show more aberrant morphologies, as in Lee et al. (2013). Perhaps each interactor should also be over-expressed in reticulon knock-out lines (such as the triple RTN1/2/13 knock-out), or other mutants such as *lnp1lnp2* or *pah1pah2* to see whether any ER morphology changes are exacerbated.

Of the T-DNA insertion lines, only one line (SALK 088781), a SYTa T-DNA insertion, showed any change in morphology. This suggests that SYTa is influencing the ER morphology, though in order to truly assess whether a gene has been down-regulated or knocked-out, quantitative PCR should be used to measure how many RNA transcripts are being produced from the gene in question. Gene redundancy may hide the gene down-regulation, and several of the proteins investigated are part of a larger family, in which other members may be able to compensate for the loss of function. It is therefore suggested that multiple T-DNA insertion lines should be crossed to create multiple knock-outs, such as SMT1, 2 and 3. If the plants are viable, then resulting changes to the ER morphology may be seen.

It is well known that different mammalian cells have differing ER morphologies (Shibata et al., 2010; Voeltz et al., 2002; Schwarz and Blower, 2015). Imaging of the ER during seed germination has been briefly assessed in the past Harris and Chrispeels (1980); Stefano et al. (2014b), but this project gives the first in-depth, granular insight into how the ER morphology changes during *A. thaliana* seed germination. The amount of sheet morphology increases between day 3 and 5 of germination, which correlates well to a change in the composition of protein within the plant. This suggests that the ER morphology alters as the amount of protein production increases. Further investigation could include multi-colour confocal imaging to analyse what impact other organelles have on the ER morphology. Labelling the tonoplast may give an insight into how the change from protein storage vacuoles to lytic vacuoles influences the ER, if at all. Future experiments should also more thoroughly assess what proteins there are present at each stage of germination, this could be through analysis of protein or gene expression. This may also lead to the discovery of more proteins involved in influencing the ER morphology changes, or perhaps show the involvement of the protein interactors discovered during this project. Light sheet microscopy is technique that could be used to continually assess the changes in ER morphology throughout germination, though the technique is relatively simply, difficulties are presented in keeping the specimen alive and un-stressed, and particularly in processing the large quantity of data produced. Perhaps imaging at more regular intervals, may provide more information, without incurring the difficulties in data processing.

Finally, this project also provides a novel investigation into ER morphology during seed development, which was only possible due to the enhanced resolution of the Zeiss 880 confocal microscope. This project showed that there are dramatic changes to the ER morphology as the embryo develops and this could correlate

with the major biochemical events occurring within the embryo (Baud et al., 2002). This work however, should be repeated with the use of the new AiryScan module, which will provide even better resolution. The increased resolution is important for resolving the ER structure in the early stages of seed development, when the cells are particularly small. It would also be advisable to carefully assess the number of days after flowering, rather than assessing the seed development stages visually. This could provide a more robust way of differentiating the development stages. A wide range of ER morphologies were seen, which can be partially linked to known biochemical and cellular events during seed development. Gene and protein expression analysis would be interesting to see whether changes in expression link to the varying morphologies seen. A rapid experiment would be to do the SDS-PAGE analysis that was performed for the germination experiment, however as discussed the stages are difficult to define, and although this would provide information about the change in protein composition, it would not provide insight into what the proteins are.

There are still many questions that need answering with regards to how the ER morphology is maintained, or controlled. It is still unknown what signals are needed (or given) in order for an increase or decrease in the amount of sheets morphology to occur? Do cells 'recognise' that they have more sheets than tubules, or is this ratio only controlled by the expression of reticulons? Different mammalian cell types have clearly different ER morphologies. Do different plant cells? Would this even be possible to assess by confocal imaging, since only the top layer of cells can be clearly imaged? It is still not known whether there are more morphologies than simply tubules and sheets, though the improvement of imaging techniques and computer analysis has begun to enable investigation into this. Answering these questions and continuing investigations into proteins that are implicated in influencing the ER morphology will help to increase our understanding of the dynamic and complex ER.

Chapter 7

Appendix

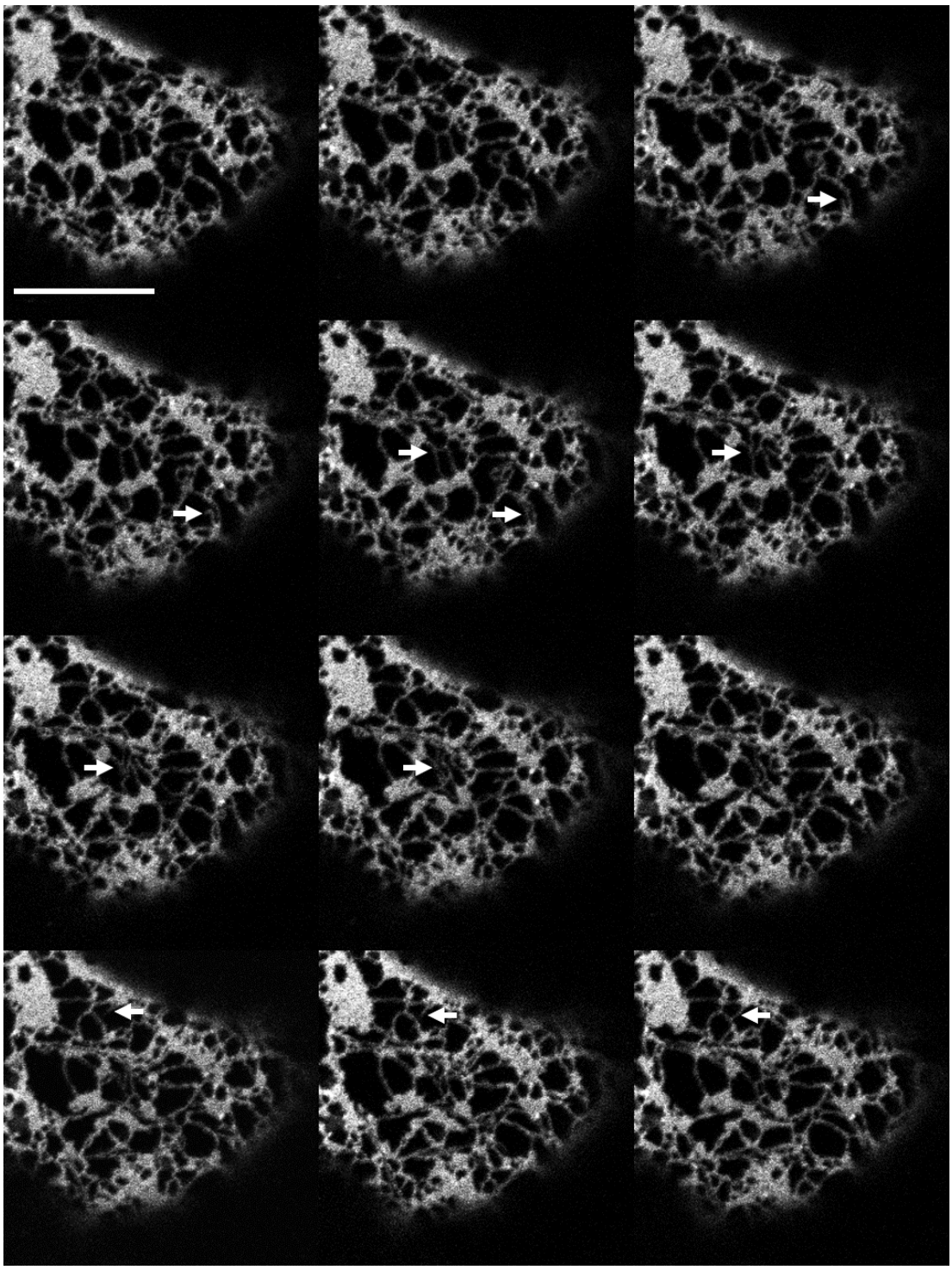

Figure 7.1: ***A series of confocal images showing the dynamic nature of the ER in N. benthamaina leaf cells.*** *The ER is labelled using GFP-HDEL. The arrows show areas of interest, where tubules are moving or breaking apart and joining together. Scale bar in top left = 10 μm.*

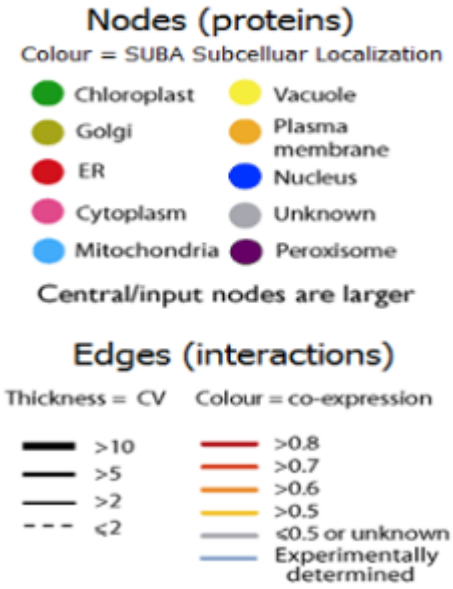

Figure 7.2: ***Key to colours and line thickness in interaction maps.*** *Taken from www.arabiodpsisinteractionsviewer.com.*

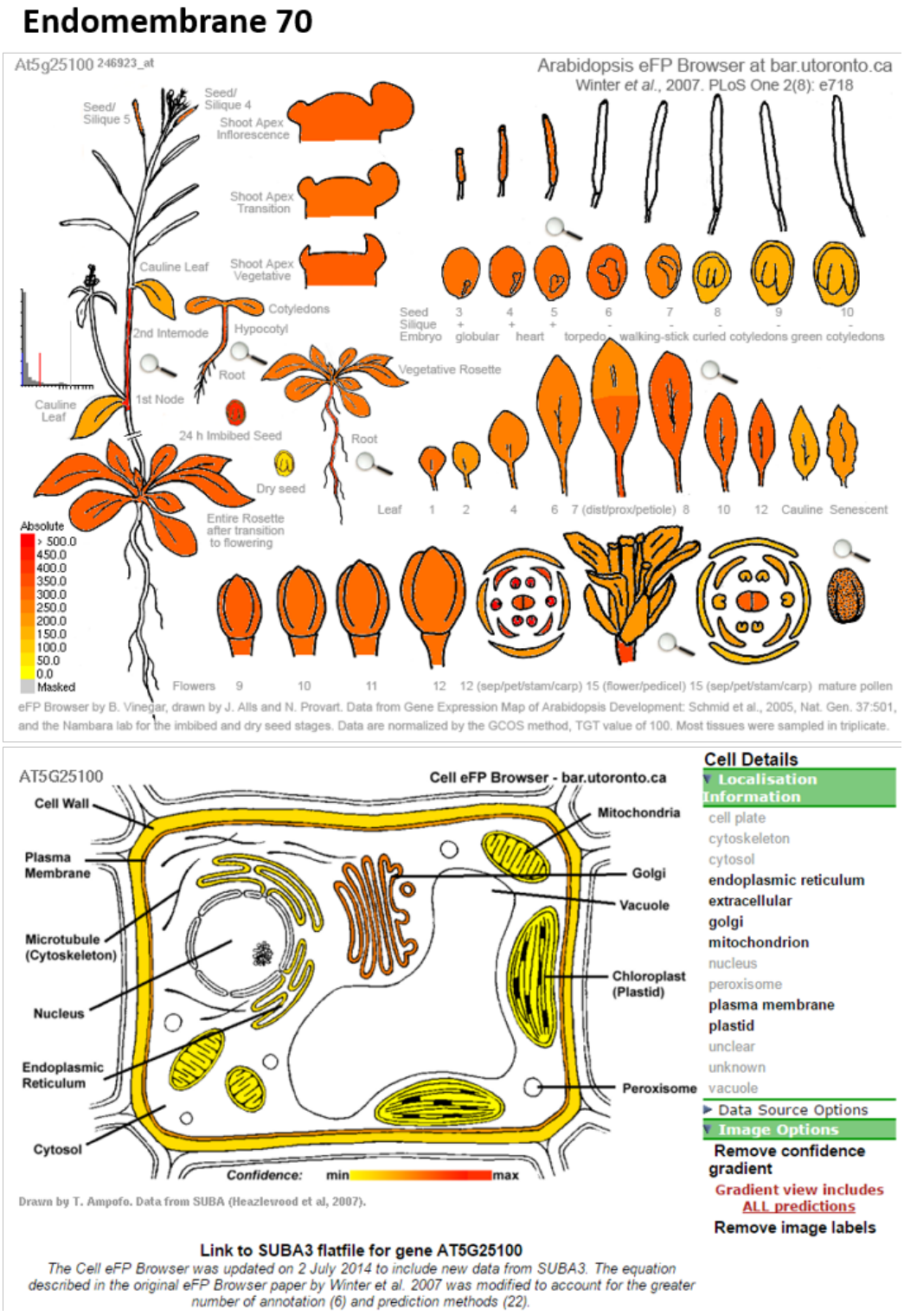

Figure 7.3: ***Endo70 tissue and cellular localisation in A. thaliana.*** *Upper panel - Gene expression map of tissues in A. thaliana shows high expression level in most tissues, with slightly lower expression in later seed development. Lower panel - Cellular localisation suggests predominately localisation in the Golgi membrane and plasma membrane. Created from the eFP browser (Winter et al., 2007)*

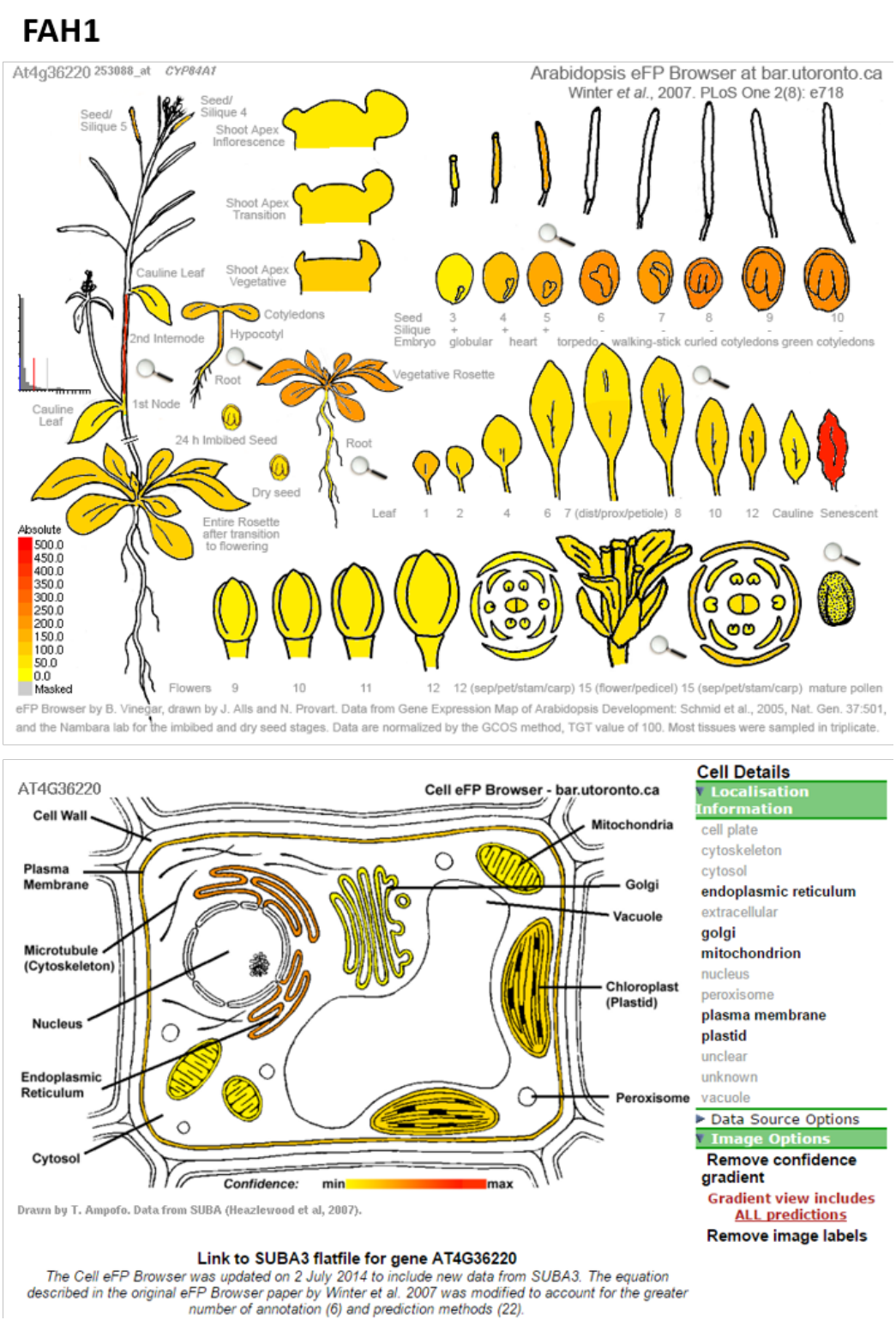

Figure 7.4: ***FAH1 tissue and cellular localisation in A. thaliana.*** *Upper panel - Gene expression map of tissues in A. thaliana shows highest expression in late seed development, senescent leaves and vegetative rosette . Lower panel - Cellular localisation suggests FAH1 localises to the ER membrane. Created from the eFP browser (Winter et al., 2007)*

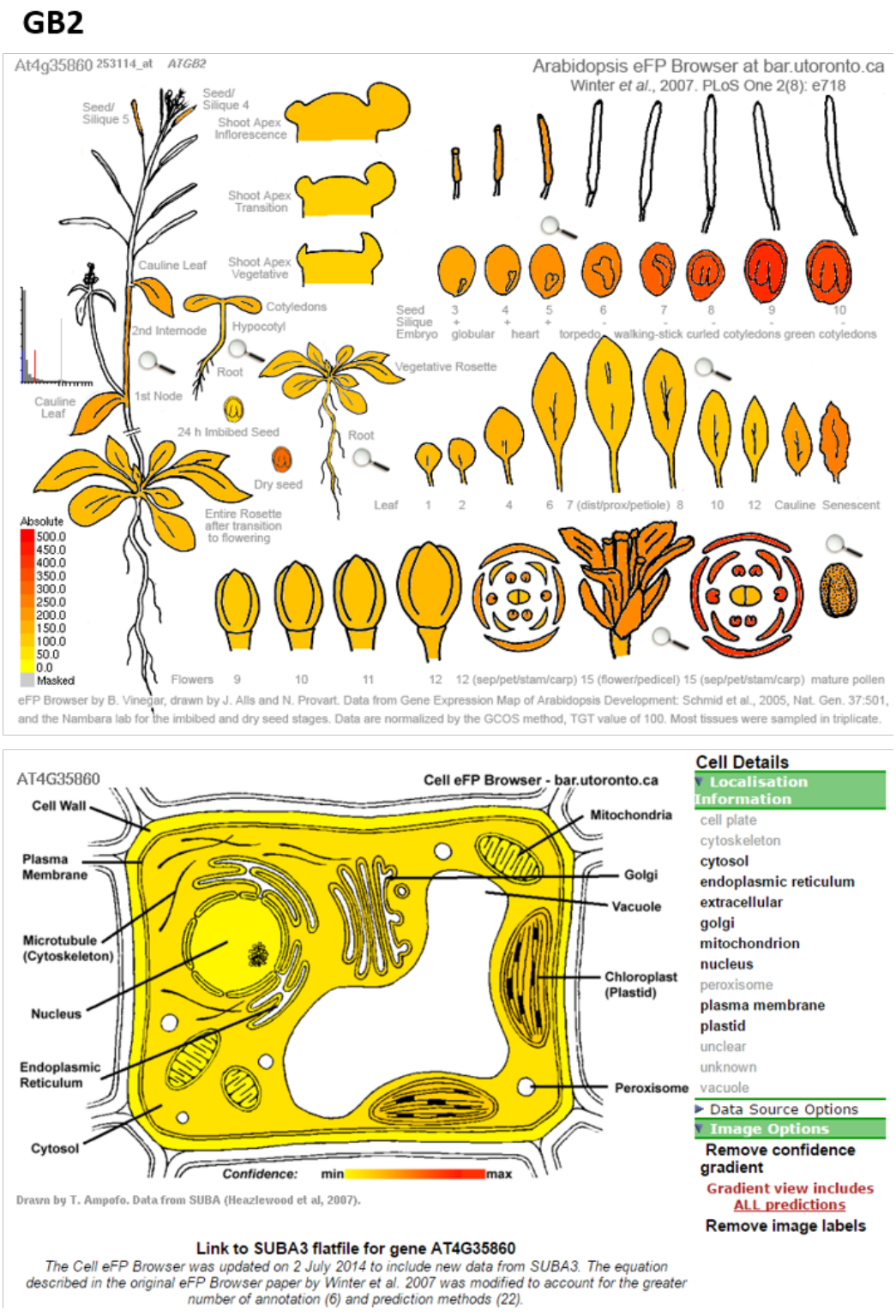

Figure 7.5: ***GB2 tissue and cellular localisation in A. thaliana.*** *Upper panel - Gene expression map of tissues in A. thaliana suggests highest gene expression in late seed development. Lower panel - Cellular localisation images suggests ubiquitous localisation. Created from the eFP browser (Winter et al., 2007)*

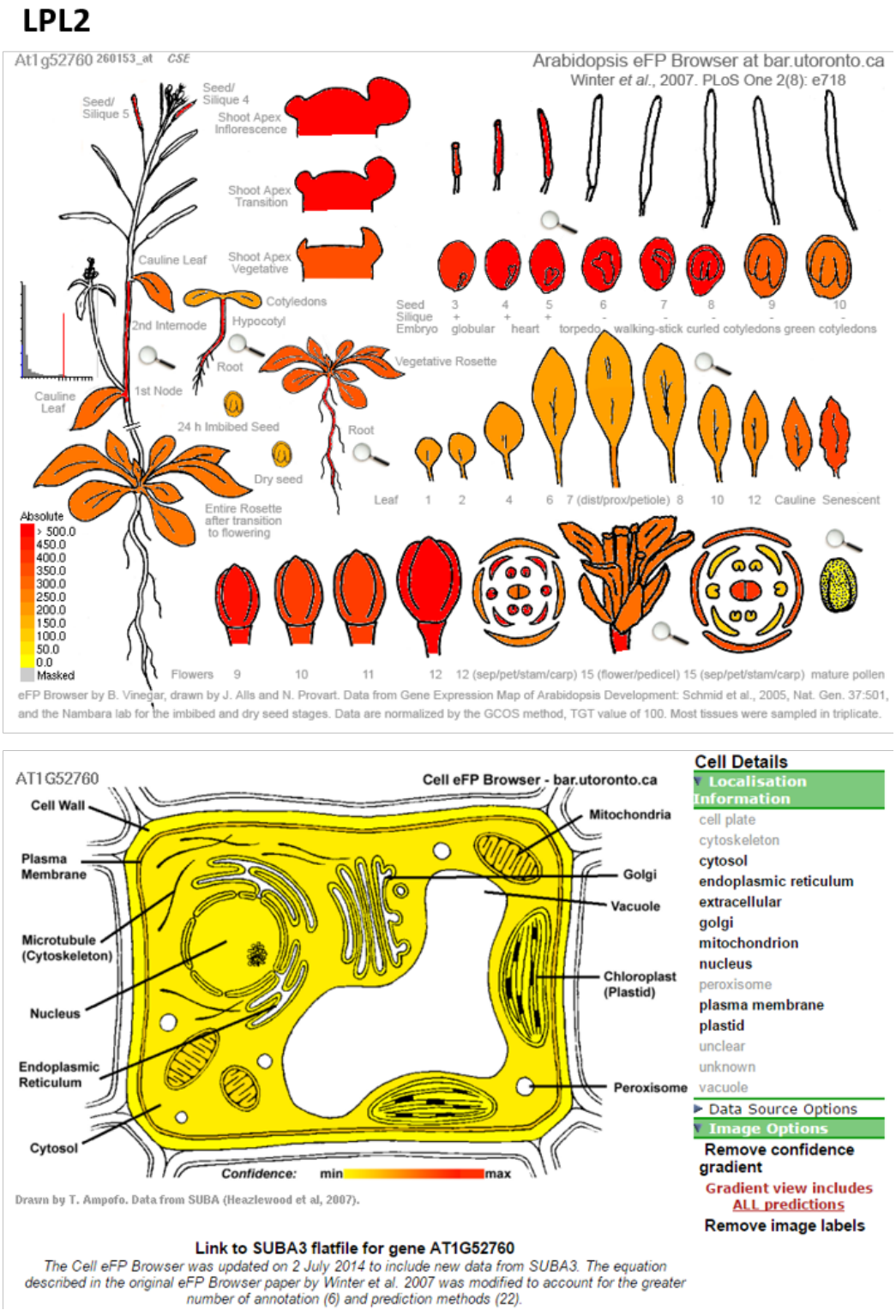

Figure 7.6: ***LPL2 tissue and cellular localisation in A. thaliana****. Upper panel - Gene expression map of tissues in A. thaliana shows high gene expression in the majority of tissues. Lower panel - Cellular localisation images suggests ubiquitous localisation. Created from the eFP browser (Winter et al., 2007)*

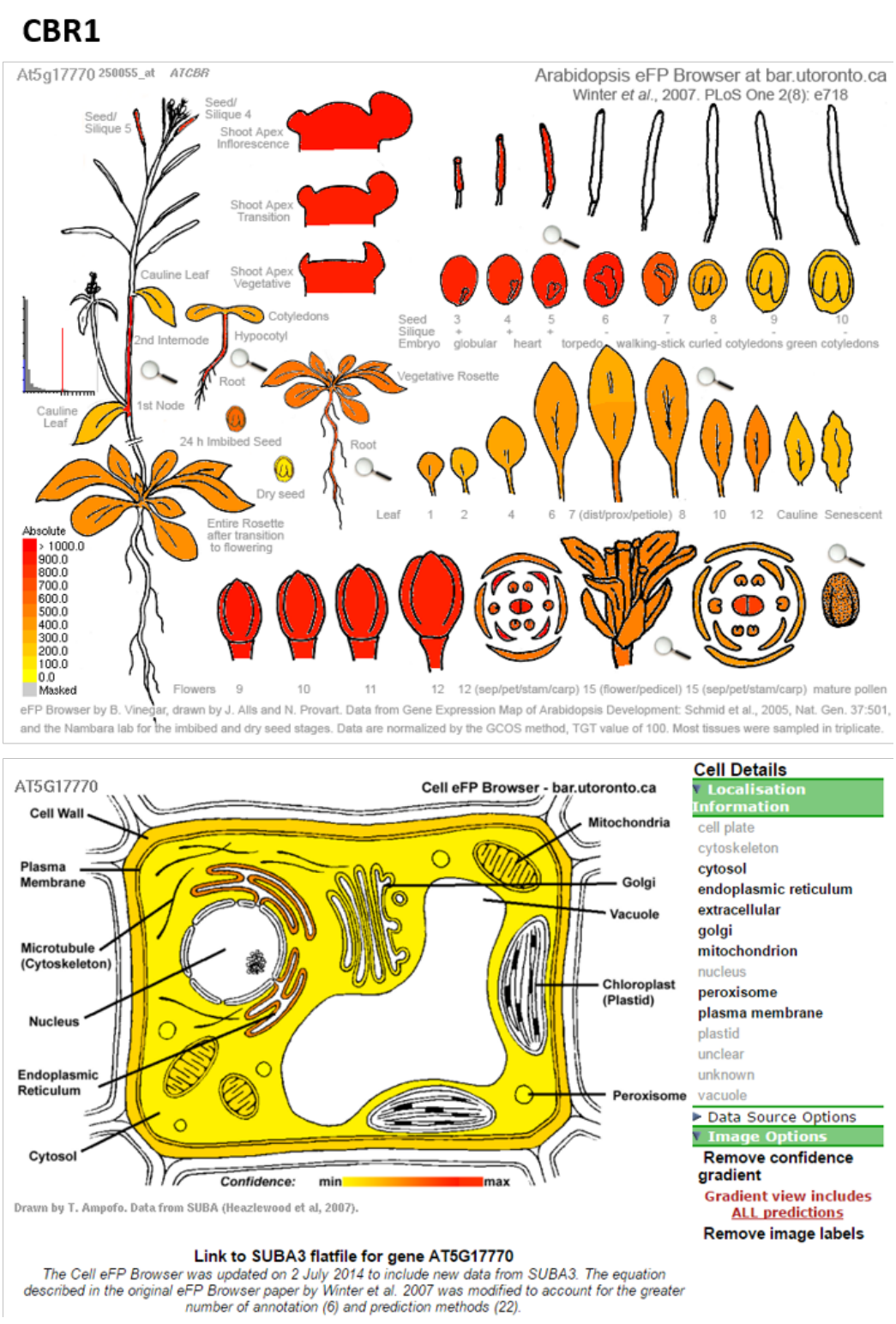

Figure 7.7: ***NADH: CBR1 tissue and cellular localisation in A. thaliana****. Upper panel - Gene expression map of tissues in A. thaliana suggests high gene expression in earl seed development, with slightly lower expression in late seed development. Lower panel - Cellular localisation images suggest ER membrane localisation. Created from the eFP browser (Winter et al., 2007)*

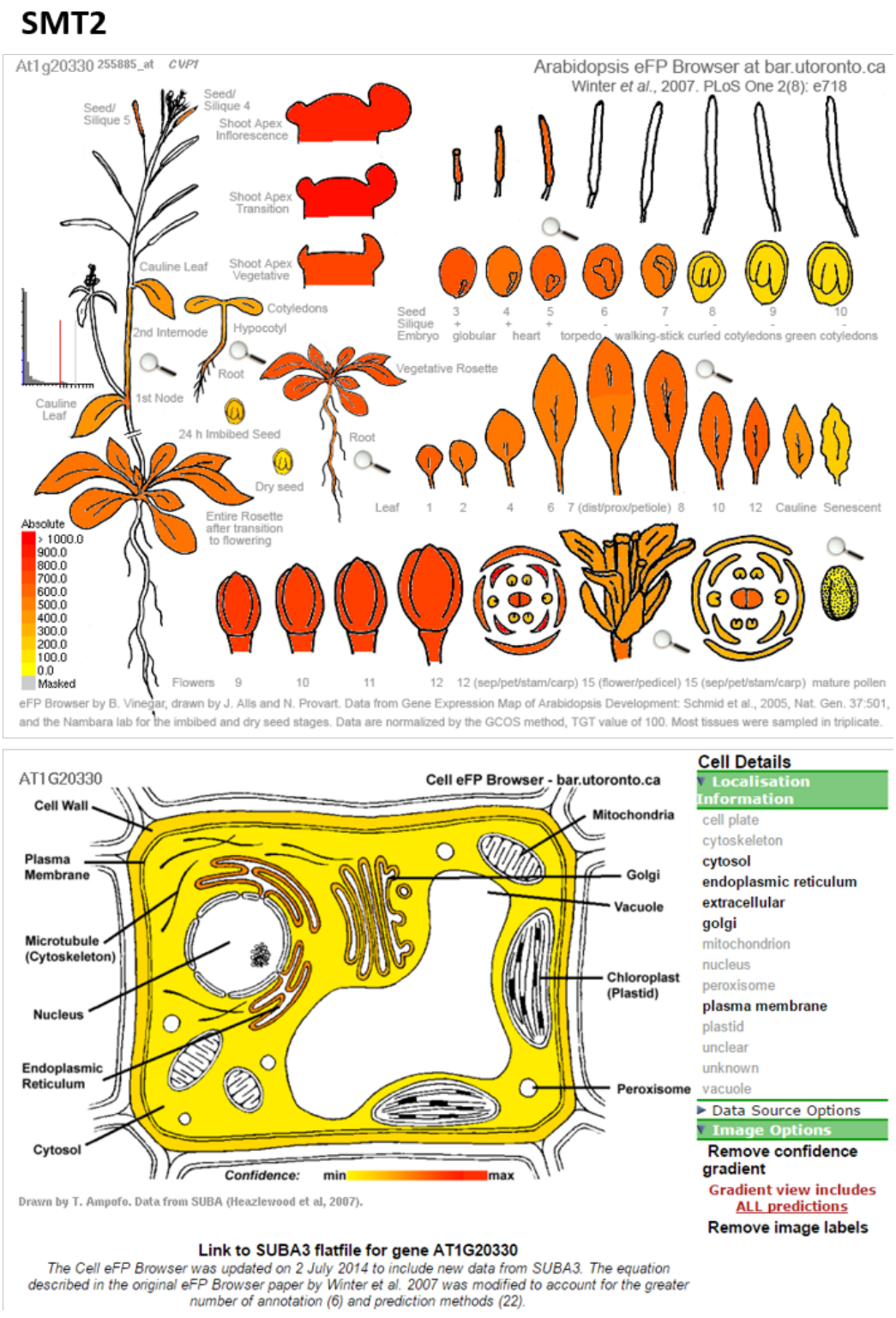

Figure 7.8: ***SMT2 tissue and cellular localisation in A. thaliana.*** *Upper panel - Gene expression map of tissues in A. thaliana suggests high gene expression in earl seed development. Lower panel - Cellular localisation image suggests ER membrane localisation. Created from the eFP browser (Winter et al., 2007)*

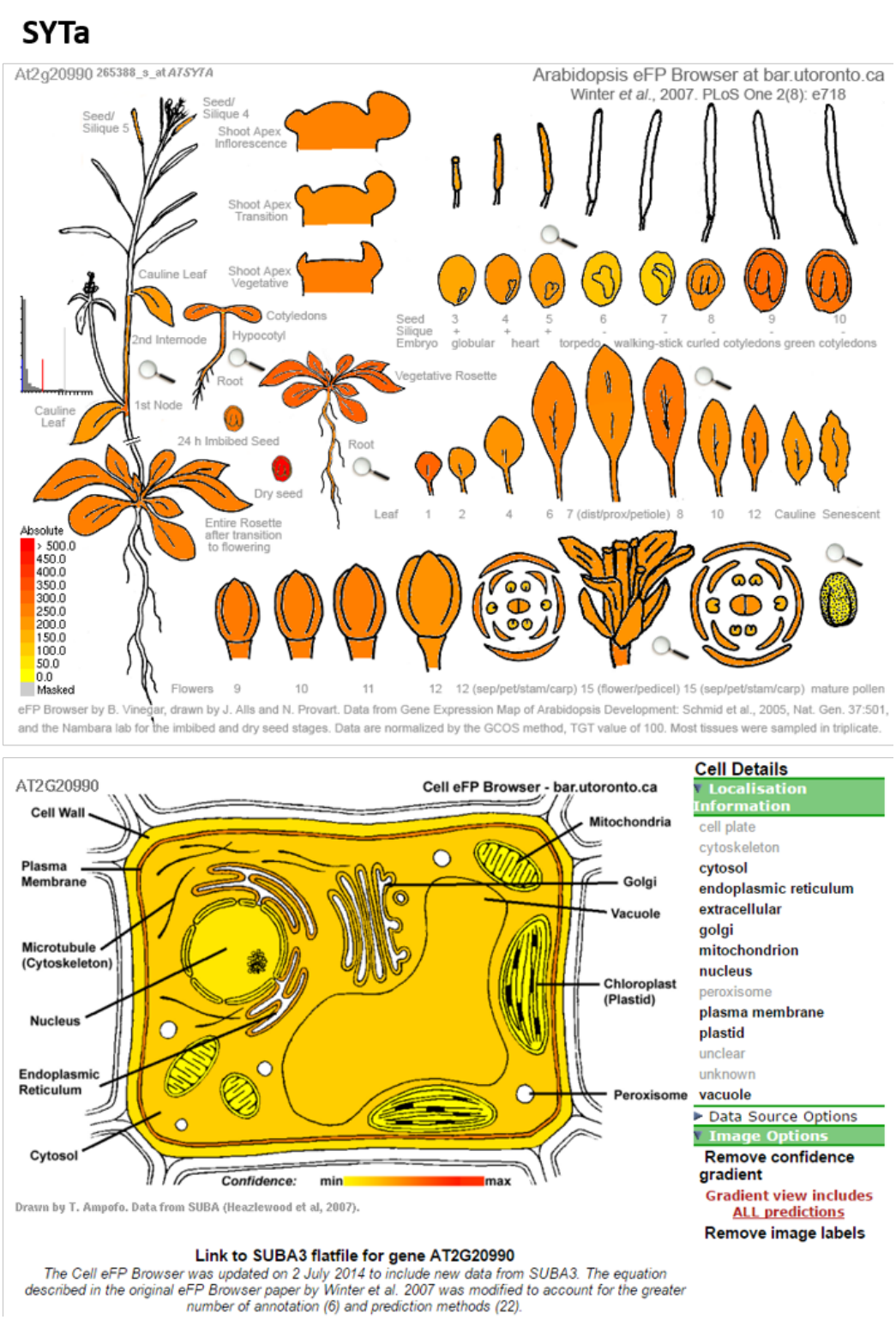

Figure 7.9: ***SYTa tissue and cellular localisation in A. thaliana.*** *Upper panel - Gene expression map of tissues in A. thaliana suggests higher gene expression in late seed development compared to earlier stages. Lower panel - Cellular localisation image suggests localisation in the plasma membrane and the ER membrane. Created from the eFP browser (Winter et al., 2007)*

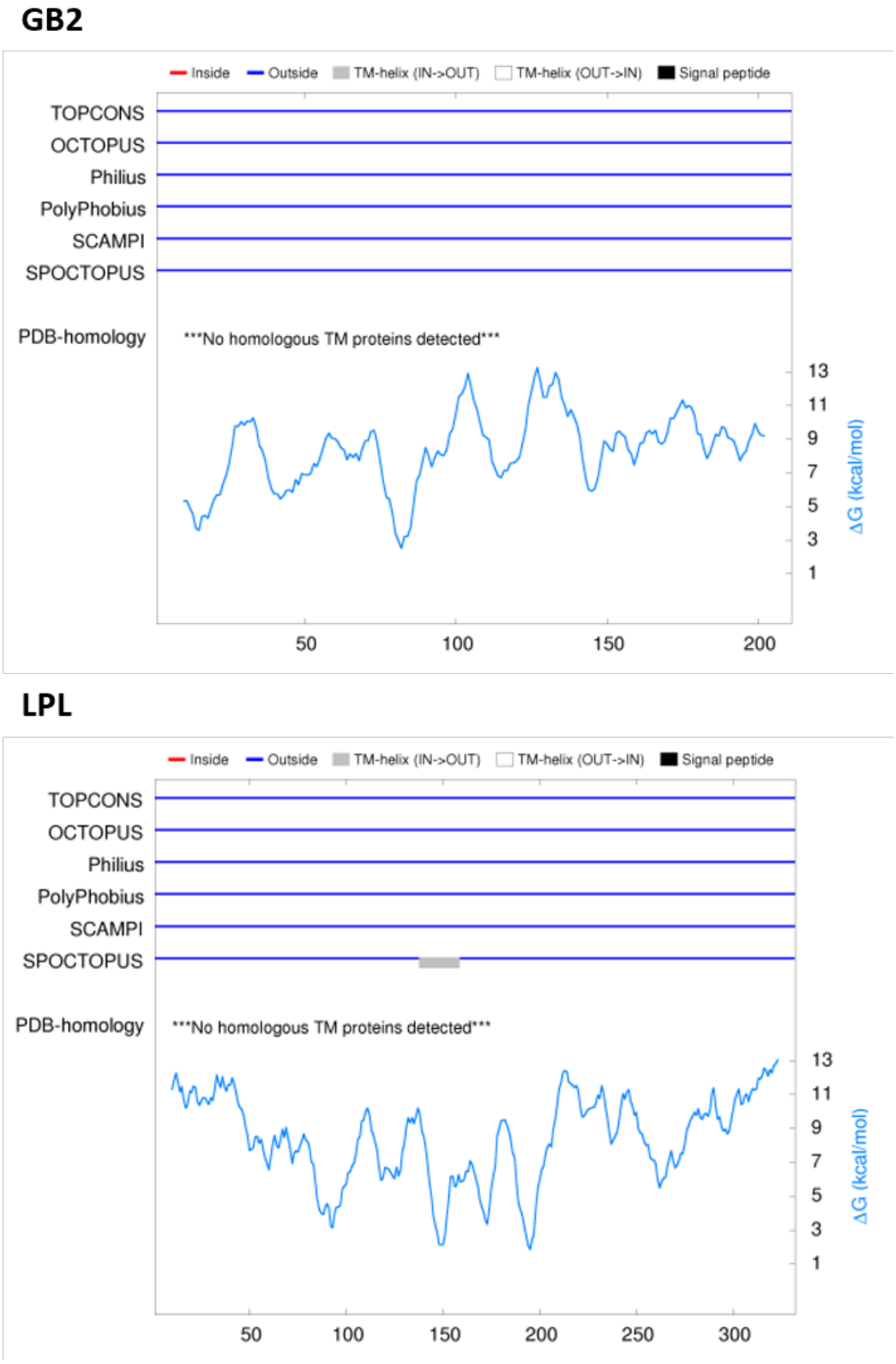

Figure 7.10: ***Protein topology of GB2 and LPL2.*** *The predicted transmembrane regions were assessed, as were any potential signal peptides, using TOPCONS (http://topcons.cbr.su.se/pred/). There were no predicted transmembrane domains for either GB2 or LPL2.*

CBR1

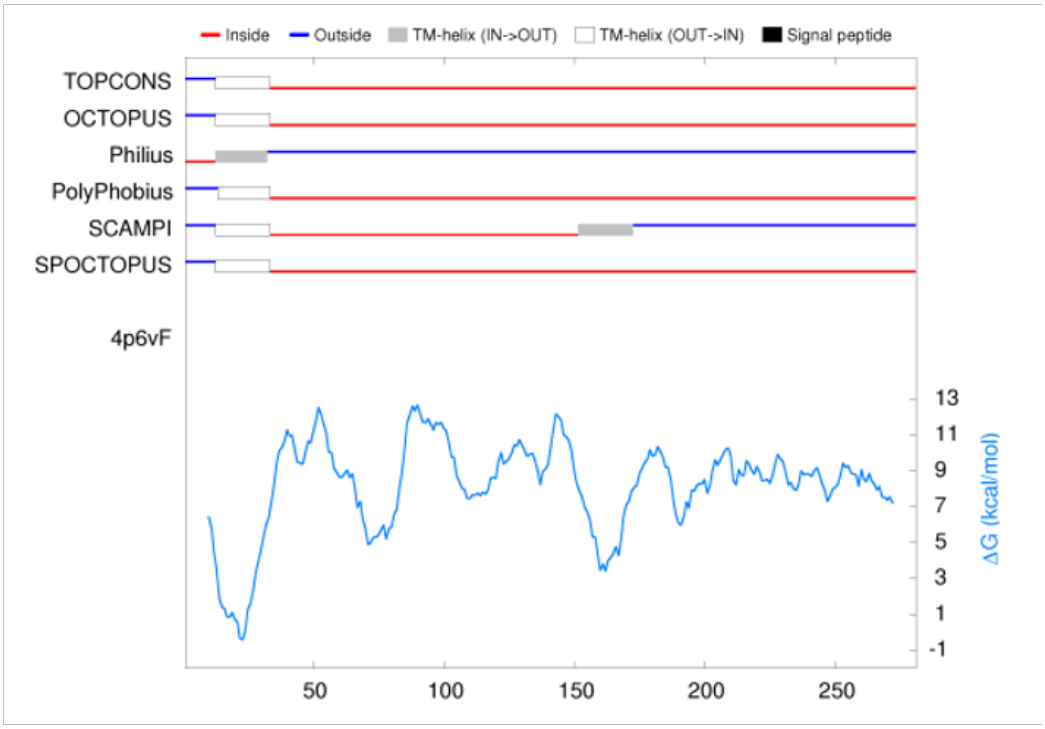

RTN1

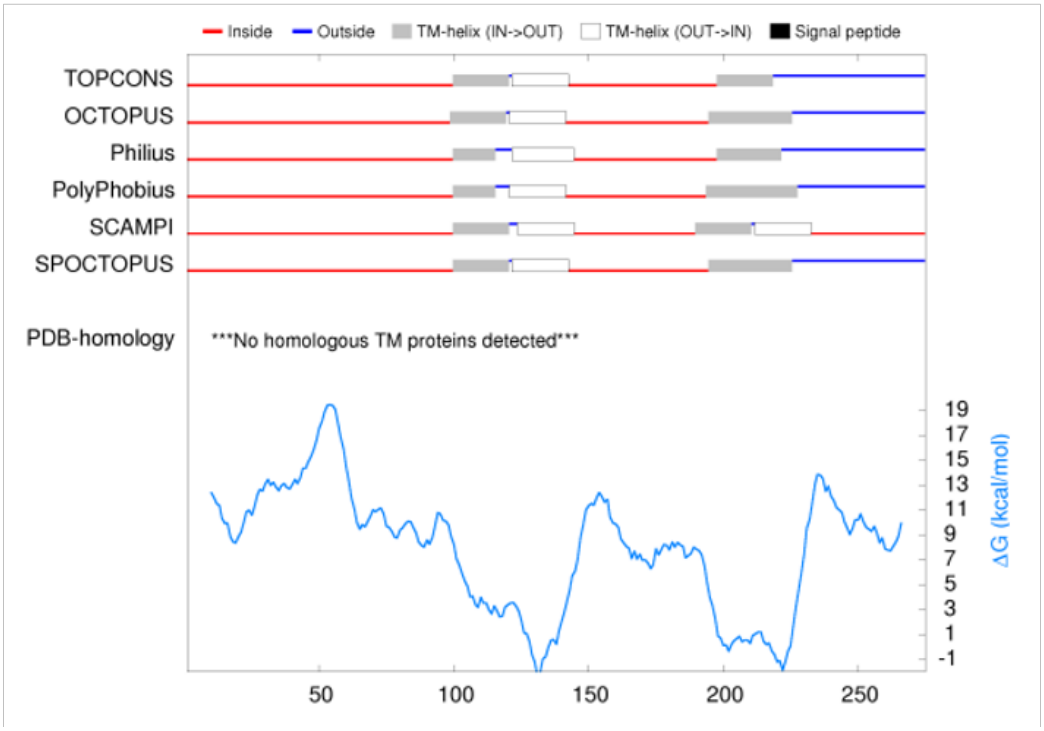

Figure 7.11: ***Protein topology of CBR1 and RTN1.*** *The predicted transmembrane regions were assessed, as were any potential signal peptides, using TOPCONS (http://topcons.cbr.su.se/pred/). There was one predicted transmembrane domain for CBR1 and 4 transmembrane domains for RTN1.*

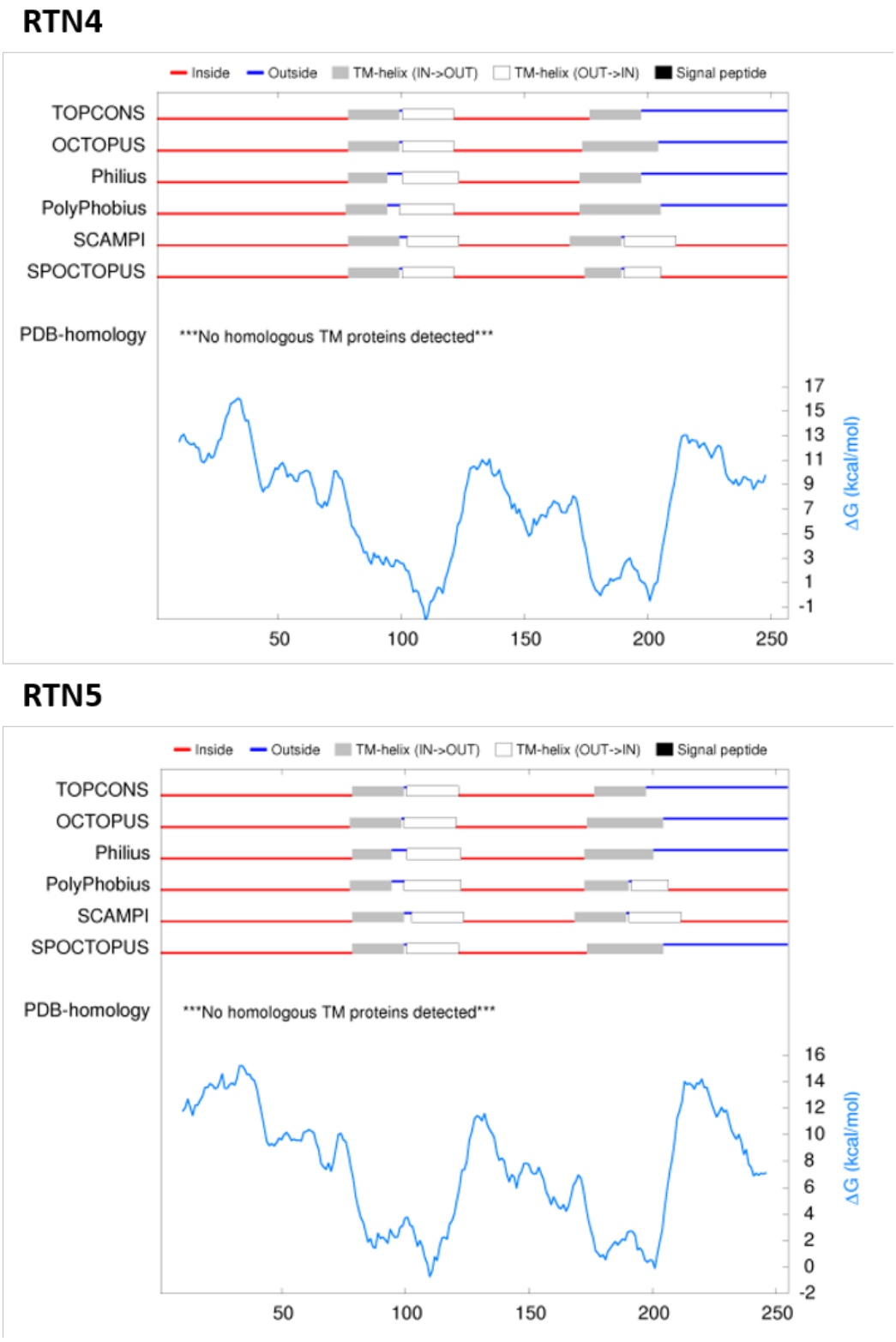

Figure 7.12: ***Protein topology of RTN4 and RTN5.*** *The predicted transmembrane regions were assessed, as were any potential signal peptides, using TOPCONS (http://topcons.cbr.su.se/pred/). Each protein has 4 predicted transmembrane domains.*

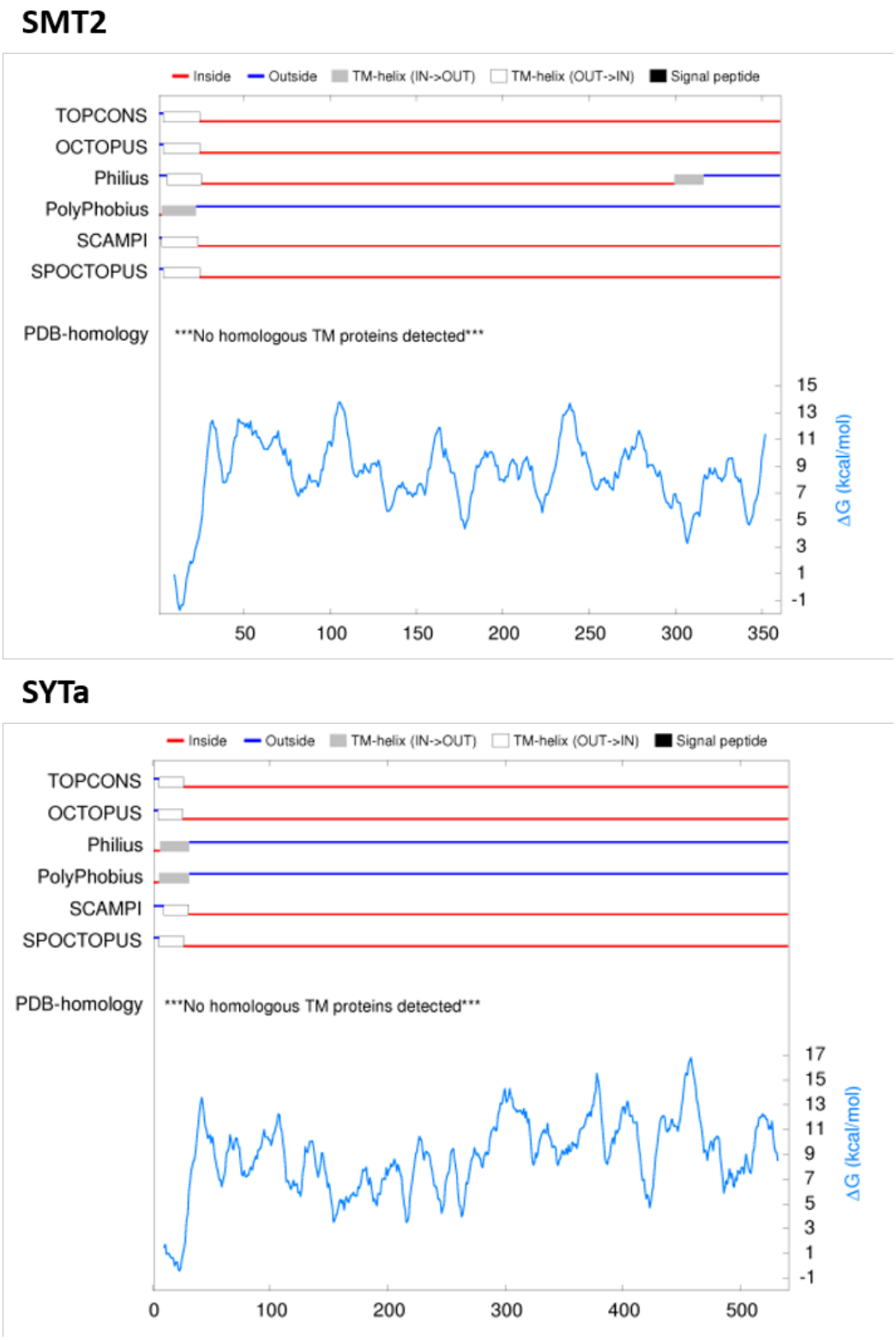

Figure 7.13: ***Protein topology of SMT2 and SYTa.*** *The predicted transmembrane regions were assessed, as were any potential signal peptides, using TOPCONS (http://topcons.cbr.su.se/pred/). Eas protein, SYTa and SMT2, had one transmembrane domain predicted.*

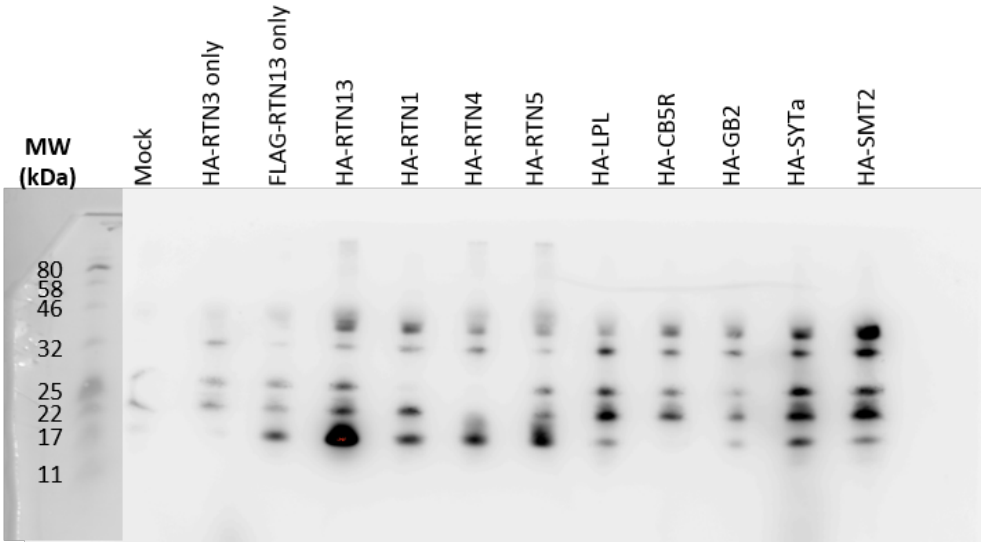

Figure 7.14: ***HA/FLAG 'Bound' western blot with ladder.*** *The ladder indicates that the band absent in the mock and HA-RTN13 only lanes compared to the other lands is FLAG-RTN13, which is running at between 17-22 kDa, which is lower than expected (FLAG-RTN13 = approx 24 kDa).*

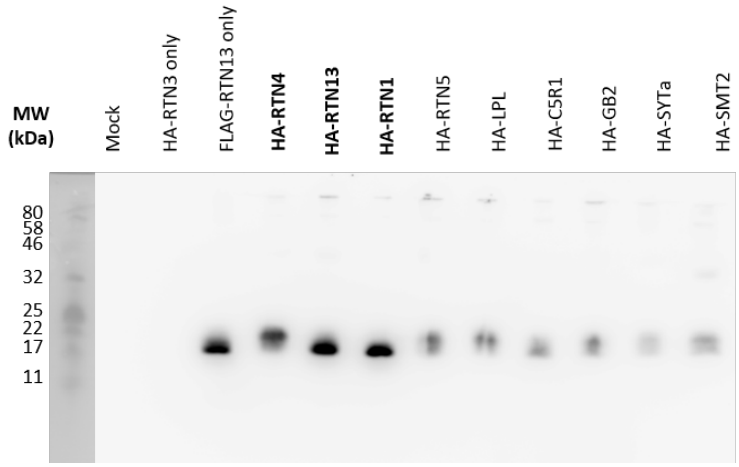

Figure 7.15: ***HA/FLAG 'Unbound' western blot in full with ladder.*** *The ladder shows that the bands are between 17 and 22 kDa which suggests that FLAG-RTN13 is running lower than expected (FLAG-RTN13 = approx 24 kDa) The labels in bold indicate the lanes that were in a different order to the other HA/FLAG co-immunoprecipitation blots.*

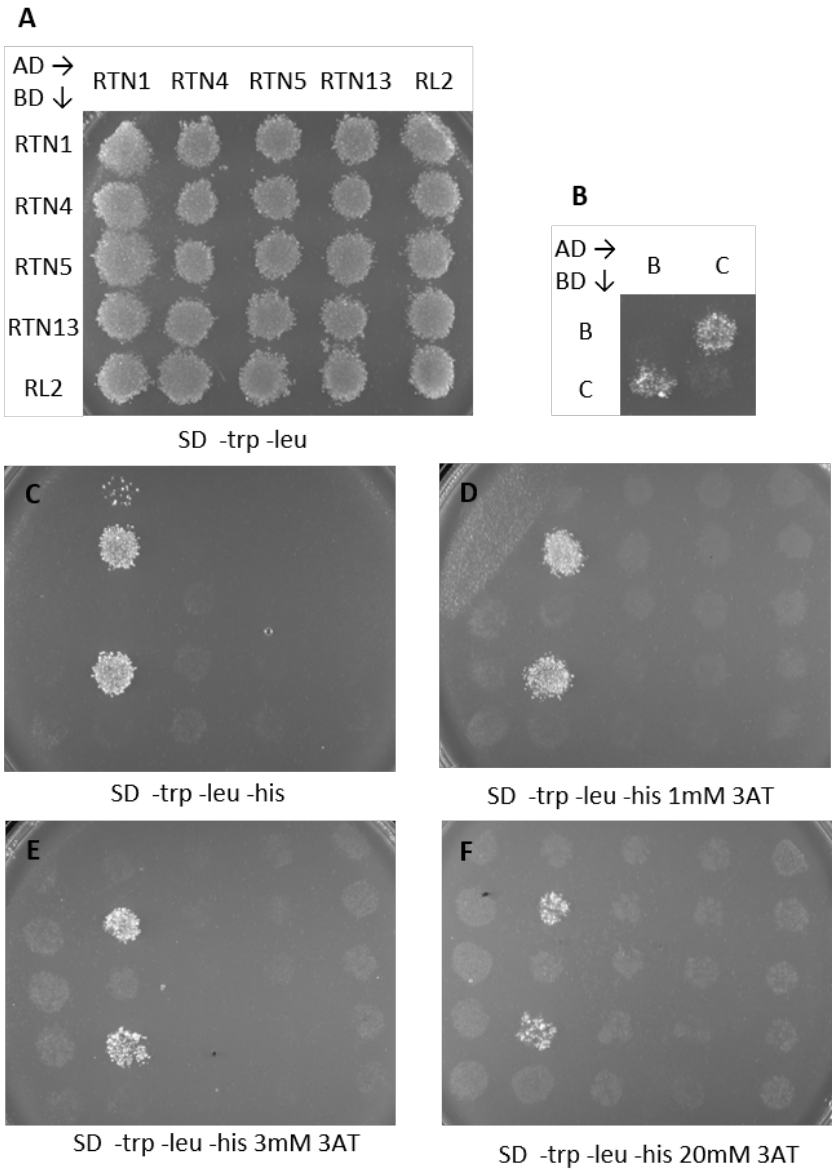

Figure 7.16: ***Yeast-two-hybrid screen 1****. AD = Activation domain. BD = Binding domain. A) SD-Leu-Trp plate; indicates successful mating of the two yeast strains. B) Positive and negative controls on SD-Leu-Trp-His plate. B = NFY-B2 and C = NFY-C9. These proteins form heterodimers. C) SD-Leu-Trp-His plate; indicates successful protein-protein interactions D-E) SD-Leu-Trp-His plates with increasing concentrations of 3AT. This indicates the strength of the interactions and inhibits any auto-activation.*

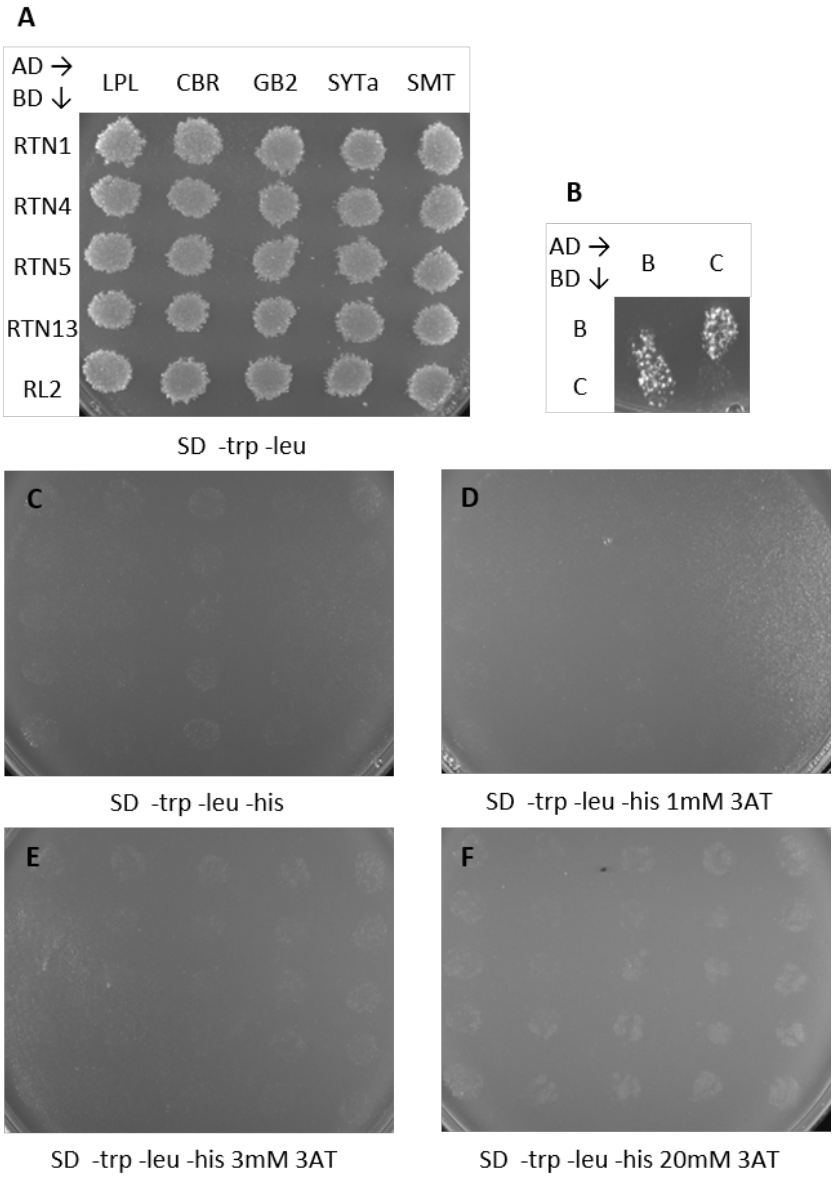

Figure 7.17: ***Yeast-two-hybrid screen 2****.AD = Activation domain. BD = Binding domain. A) SD-Leu-Trp plate; indicates successful mating of the two yeast strains. B) Positive and negative controls on SD-Leu-Trp-His plate. B = NFY-B2 and C = NFY-C9. These proteins form heterodimers. C) SD-Leu-Trp-His plate; indicates successful protein-protein interactions D-E) SD-Leu-Trp-His plates with increasing concentrations of 3AT. This indicates the strength of the interactions and inhibits any auto-activation.*

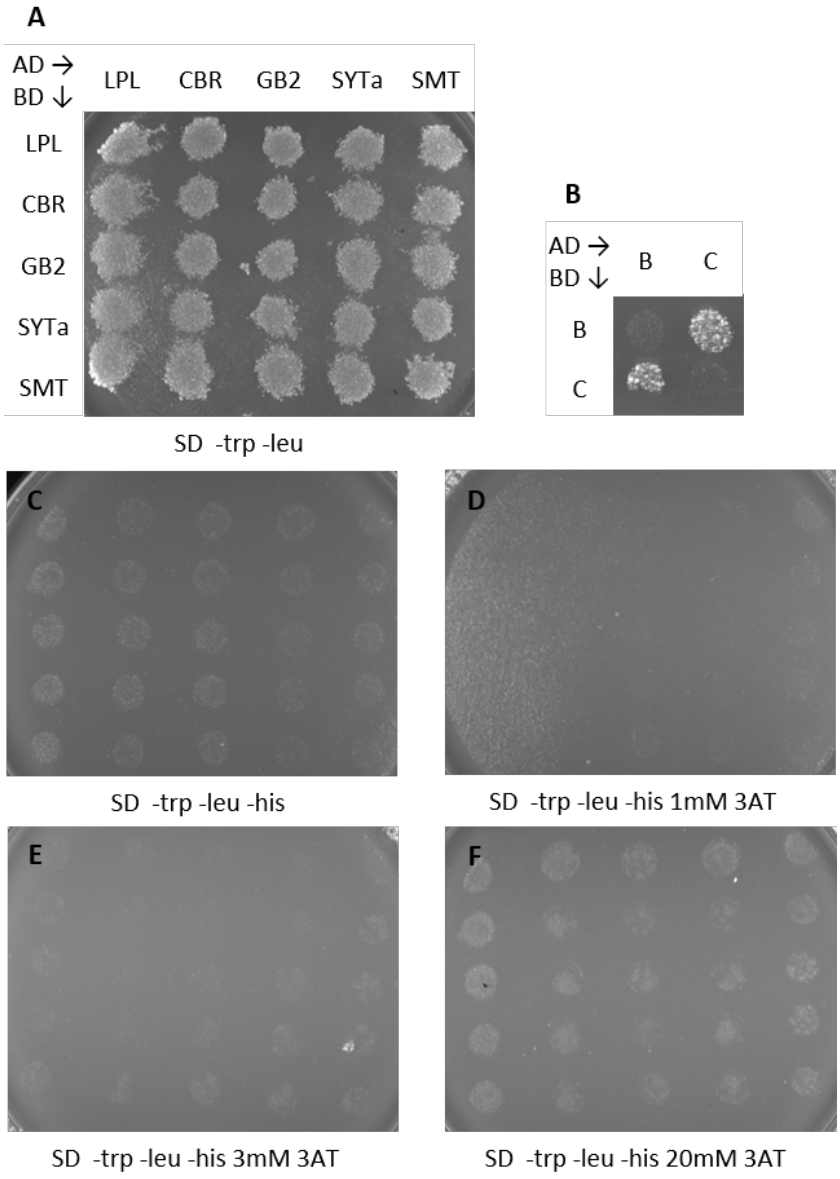

Figure 7.18: ***Yeast-two-hybrid screen 3****. AD = Activation domain. BD = Binding domain. A) SD-Leu-Trp plate; indicates successful mating of the two yeast strains. B) Positive and negative controls on SD-Leu-Trp-His plate. B = NFY-B2 and C = NFY-C9. These proteins form heterodimers. C) SD-Leu-Trp-His plate; indicates successful protein-protein interactions D-E) SD-Leu-Trp-His plates with increasing concentrations of 3AT. This indicates the strength of the interactions and inhibits any auto-activation.*

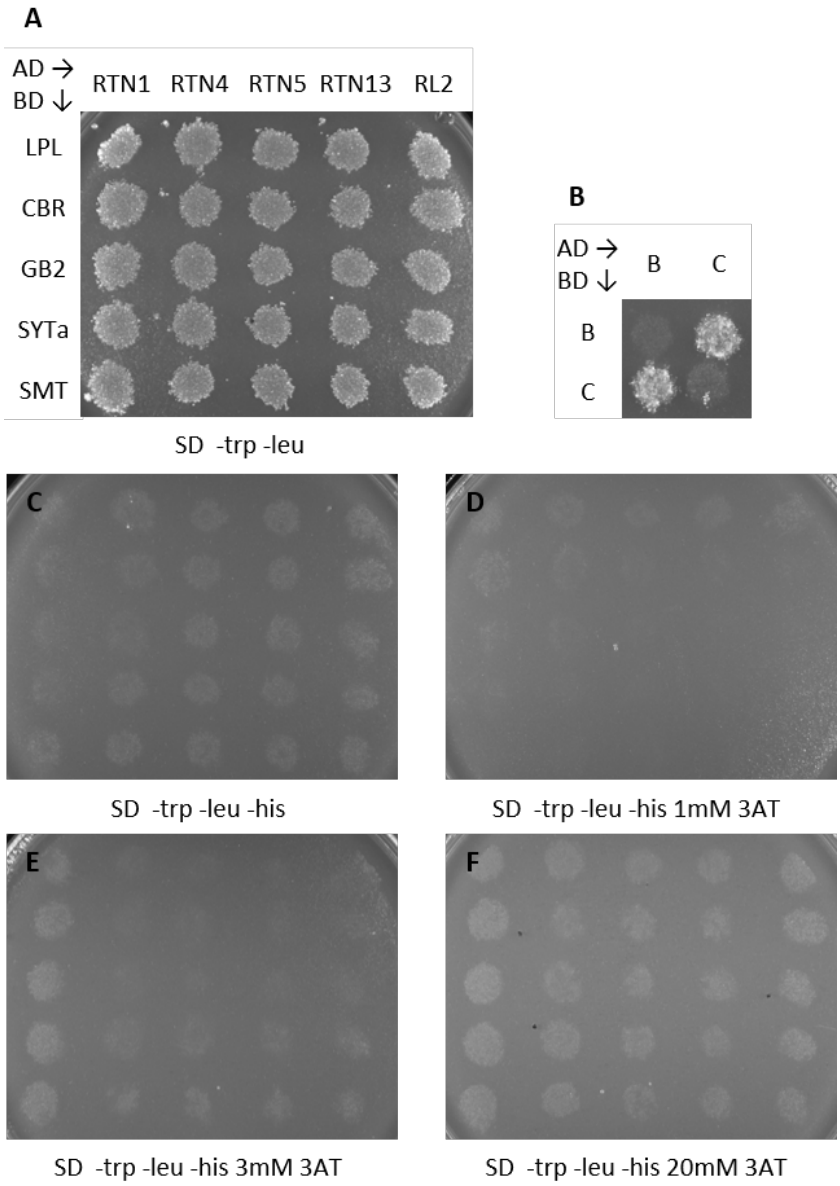

Figure 7.19: ***Yeast-two-hybrid screen 4****. AD = Activation domain. BD = Binding domain. A) SD-Leu-Trp plate; indicates successful mating of the two yeast strains. B) Positive and negative controls on SD-Leu-Trp-His plate. B = NFY-B2 and C = NFY-C9. These proteins form heterodimers. C) SD-Leu-Trp-His plate; indicates successful protein-protein interactions D-E) SD-Leu-Trp-His plates with increasing concentrations of 3AT. This indicates the strength of the interactions and inhibits any auto-activation.*

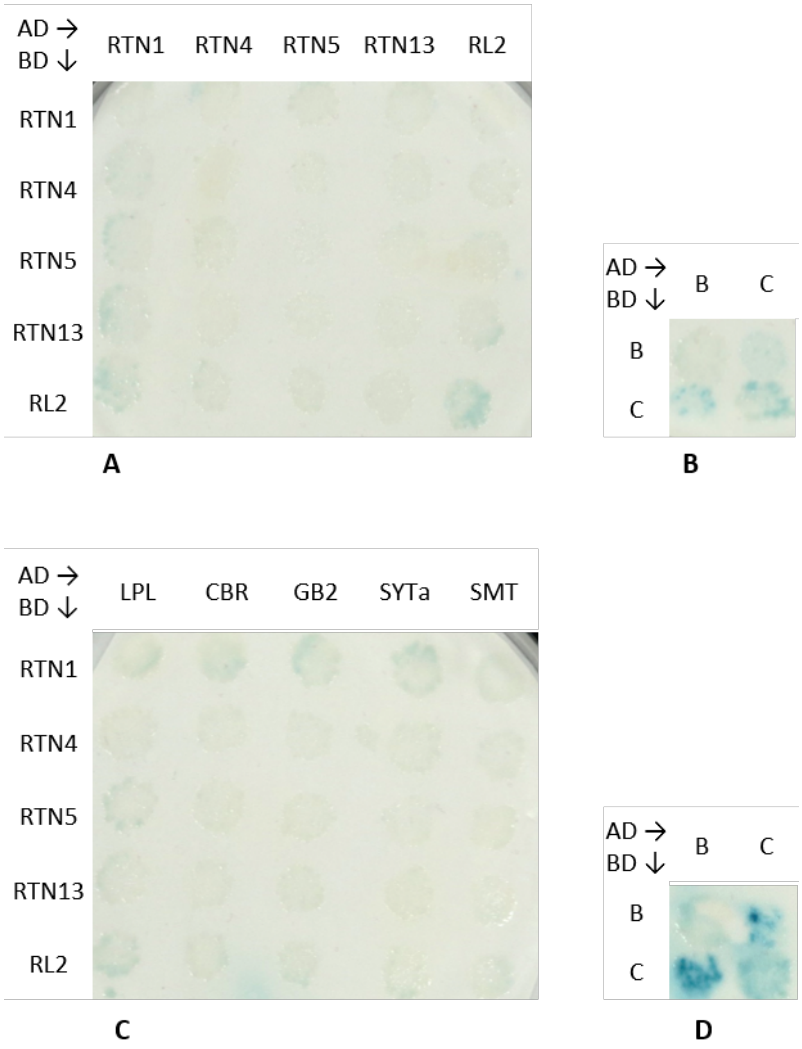

Figure 7.20: ***X-Gal assay 1 and 2****. AD = Activation domain. BD = Binding domain A) Results of assay 1. B) Positive and negative controls of assay 1. B = NFY-B2 and C = NFY-C9. C) Results of assay 2. D) Positive and negative controls of assay 2. B = NFY-B2 and C = NFY-C9.*

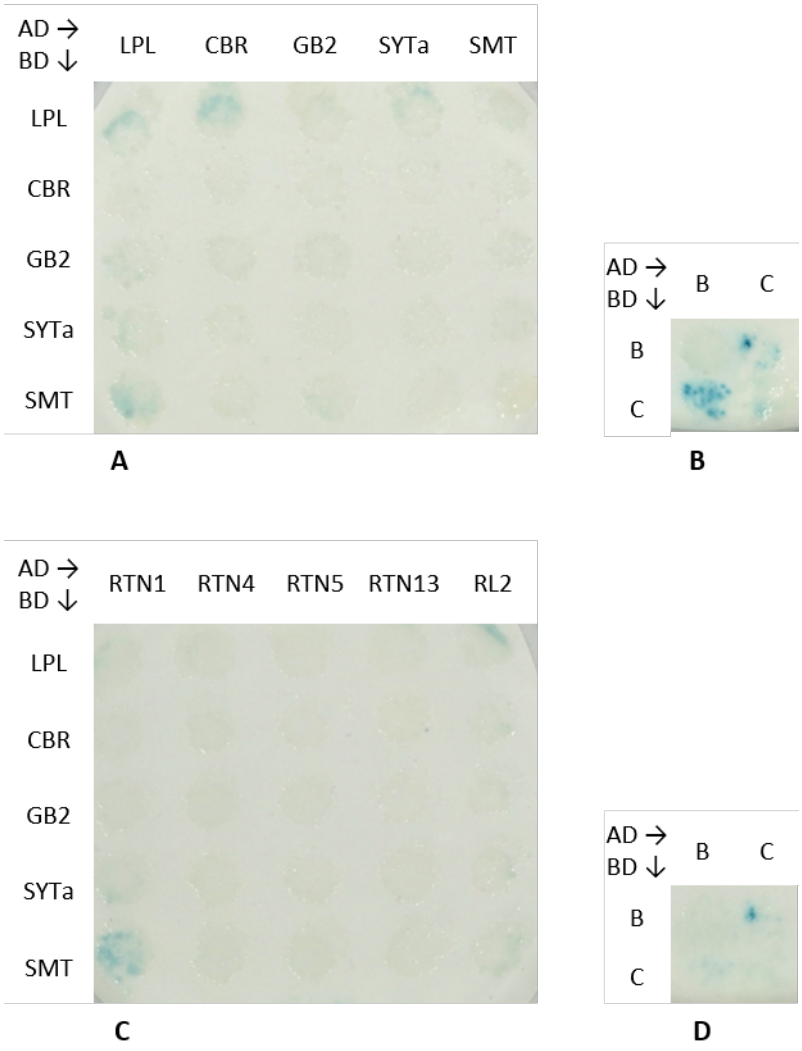

Figure 7.21: ***X-Gal assay 3 and 4****. AD = Activation domain. BD = Binding domain A) Results of assay 3. B) Positive and negative controls of assay 3. B = NFY-B2 and C = NFY-C9. C) Results of assay 4. D) Positive and negative controls of assay 4. B = NFY-B2 and C = NFY-C9.*

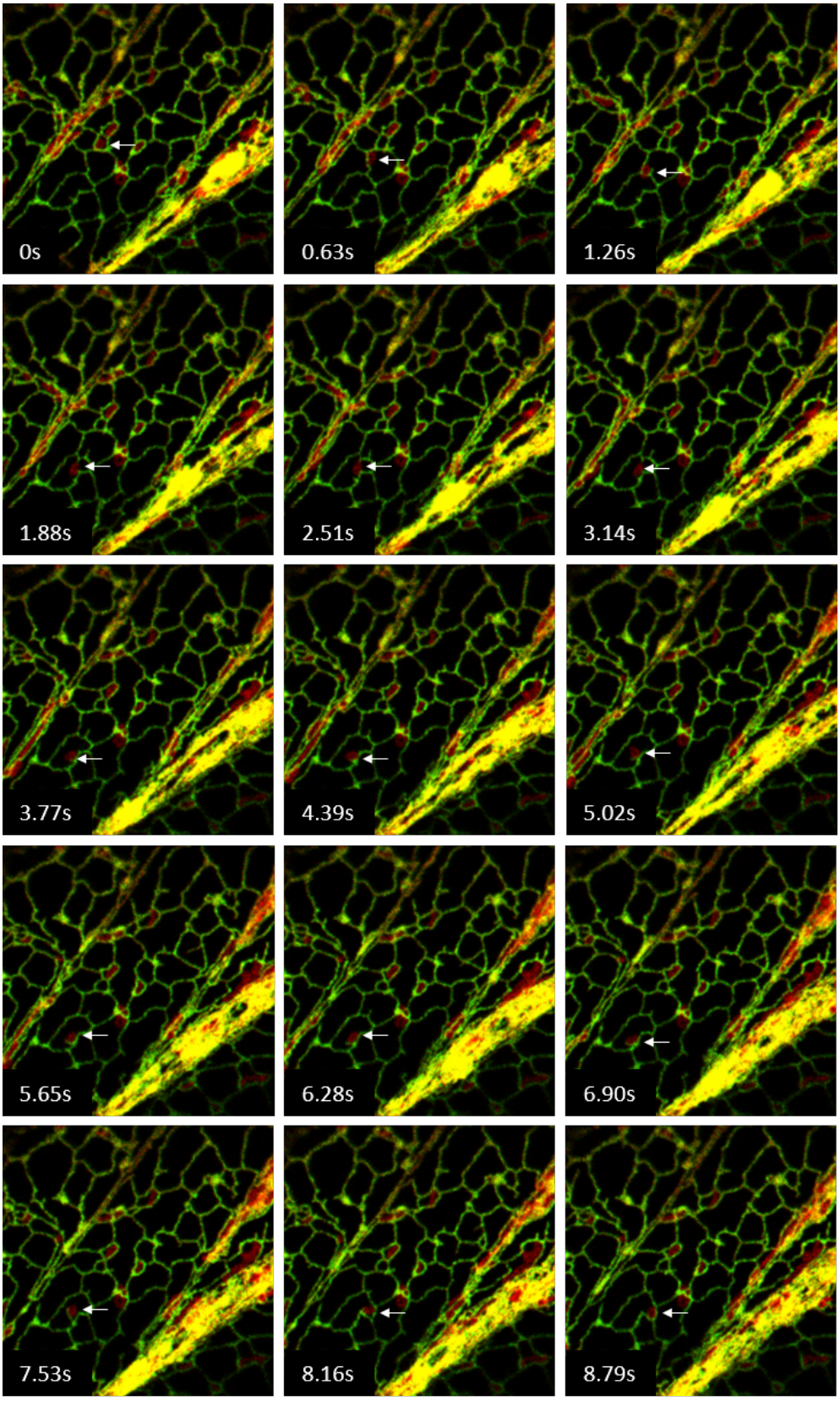

Figure 7.22: ***Time-series showing CBR1-RFP and GFP-HDEL co-expressed.*** *Arrows follow one organelle labelled with CBR1-RFP as it is moved around the cell, and interacting with the ER network.*

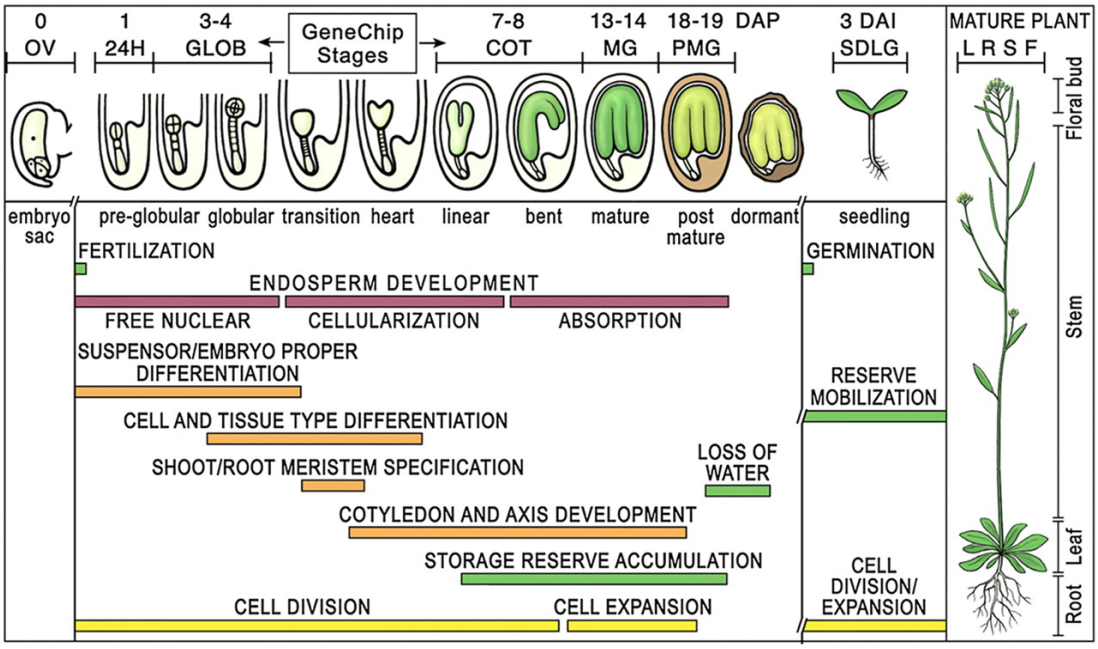

Figure 7.23: ***Arabidopsis thaliana seed development.****. It shows the approximate timeline of seed development and the biochemical events that take place at each stage. Taken from figure 1 of (Le et al., 2010).*

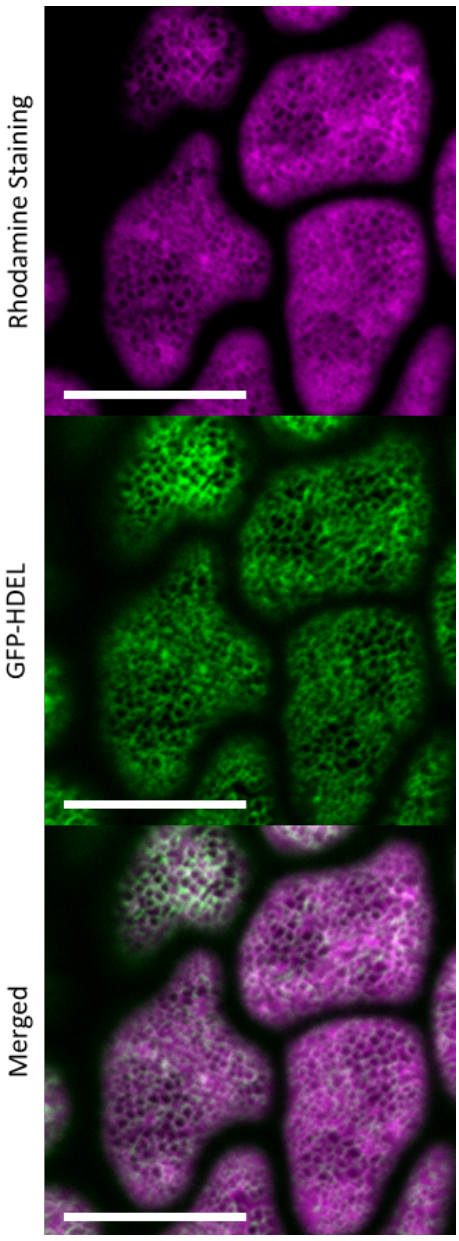

Figure 7.24: ***Rhodamine staining of a mature stage GFP-HDEL A. thaliana embryo.*** *Cells from centre of the cotyledon. This shows that rhodamine b does stain the ER, though the fluorescence background is much higher than when using GFP-HDEL as a label. Scale bars = 10μm.*

Figure 7.25: ***Comparison of uncoated and normal embryos 28 days after being plated.*** *The uncoated embryo are on the left, and had mostly died within 28 days of uncoating, despite their initial germination. The normal embryos are on the right, and have grown into well developed plants after 28 days on being placed onto the petri-dish.*

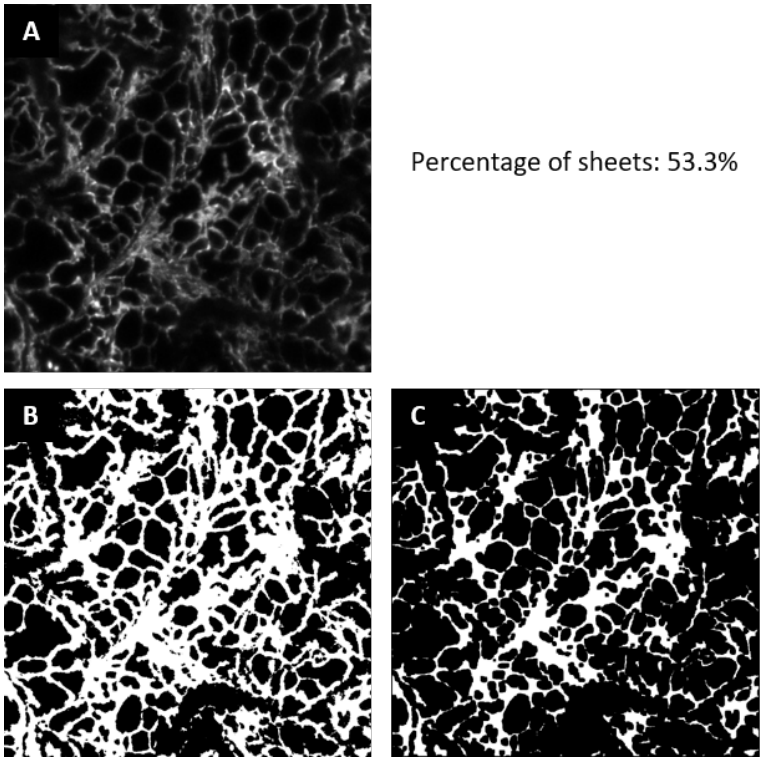

Figure 7.26: ***Example of the macro identifying bundles of tubules as sheets.*** ***A.*** *The original confocal image.* ***B.*** *The binary image highlighting the whole ER.* ***C.*** *The binary image after the erosion function has been applied. Despite the original image having few, if any, sheets in the network, is identified as containing over 50% sheets.*

```
//ER Classifier
//-------------------------------------
//Written by: Natasha Dzimitrowicz
//Edited: 03/04/17
//-------------------------------------
//Purpose: To create a binary image of ER from confocal images.

//Remember: To update the Trainable Weka Segmentation, and update
name in macro
//Remember: To change file pathway for the classifier
//Remember: Download the Color Pixel Counter:
http://imagejdocu.tudor.lu/doku.php?id=plugin:color:color_pixel_cou
nter:start
//And change filename so that each word is capatalised
//Remember: To run Stack to Images or Z-project.

//To find resolution:
run("Show Info...");

//Setup
setOption("Display Label", true); //Image name is in results table
setOption("BlackBackground", true); //Binary images assumed as
white object on black background
run("Colors...", "foreground=white background=black"); //Sets
foreground as white

//Remove noise
run("Duplicate...", "title=Original");
run("Median...", "radius=2");

//Normalise Histogram
run("8-bit");
run("Enhance Contrast...", "saturated=0.05");

//Run Trainable Weka Classifier
run("Trainable Weka Segmentation");
selectWindow("Trainable Weka Segmentation v3.2.5");
waitForUser("Fiji needs a breather. Click OK");
call("trainableSegmentation.Weka_Segmentation.loadClassifier",
"D:\\Program Files\\Fiji.app\\Segmentation_Classifier.model");
//call("trainableSegmentation.Weka_Segmentation.trainClassifier");
waitForUser("Fiji needs another breather. Click OK");
call("trainableSegmentation.Weka_Segmentation.getResult");
selectWindow("Classified image");
rename("BinaryTotal");
run("8-bit");
run("Make Binary");
```

Figure 7.27: ***Image Analysis Macro - Part 1.*** *Green colouring indicates comments which are not executed. Pink colouring indicates the functions used.*

```
//Duplicate binary image to erode
run("Duplicate...", "title=Eroded");
run("Options...", "iterations=3 count=1 black do=Erode");
selectWindow("BinaryTotal");
run("RGB Color");
run("Color Pixel Counter", "color=Green cells=20 pixels=0.2100
minimum=30");
selectWindow("Eroded");
run("RGB Color");
run("Color Pixel Counter", "color=Red cells=20 pixels=0.2100
minimum=30");
IJ.renameResults("Colour Pixel Results")


//Run Edge Analysis
//selectWindow("BinaryTotal");
//run("Duplicate...", "title=Edges");
//run("8-bit");
//run("Outline");
//run("Analyze Particles...");
//IJ.renameResults("Outline Results");

//Run Skeletonise
//selectWindow("BinaryTotal");
//run("Duplicate...", "title=Skeleton");
//run("8-bit");
//run("Skeletonize");
//run("Analyze Skeleton (2D/3D)", "prune=none");
//IJ.renameResults("Skeleton Results");

run("Close All");
```

Figure 7.28: ***Image analysis macro - Part 2.*** *Green colouring indicates comments which are not excecuted. Pink colouring indicates the functions used. The Edge Analysis function and Skeletonise function was coded, but never used in analysis of images.*

Descriptives

Sheet_Percentage

Day	N	Mean	Std. Deviation	Std. Error	Interval for Mean		Minimum	Maximum
					Lower Bound	Upper Bound		
1	14	38.67	6.79	1.81	32.75	40.58	21.49	45.74
2	11	46.26	8.26	2.49	40.71	51.81	34.55	59.61
3	16	74.90	8.50	2.12	70.38	79.43	59.32	87.30
4	14	79.15	5.32	1.42	76.07	82.22	71.19	89.80
5	18	75.60	6.64	1.57	72.29	78.90	61.66	85.87
6	12	55.15	6.95	2.01	50.73	59.56	46.54	68.41
7	12	57.61	7.58	2.19	52.80	62.42	43.56	75.39
Total	**97**	**62.29**	**16.85**	**1.71**	**58.90**	**65.69**	**21.49**	**89.80**

Test of Homogeneity of Variances

Sheet_Percentage

Levene Statistic	df1	df2	Sig.
0.635	6	90	0.702

ANOVA

Sheet_Percentage

	Sum of Squares	df	Mean Square	F	Sig.	F-Crit
Between Groups	22605.77	6	3767.629	72.992	0.000	2.201
Within Groups	4645.53	90	51.617			
Total	27251.30	96				

Is F-crit < F value? TRUE **Then reject H0**

Is p-value <0.05? TRUE **Then reject H0**

Figure 7.29: ***Single Factor ANOVA****; testing the variance in percentage of sheet morphology between days for the GFP-HDEL only line. The Levene statistic shows equal variance between samples. The F value of the ANOVA is larger than the F-crit and therefore the null hypothesis (equal variance) is rejected.*

Multiple Comparisons

(I) Day	(J) Day	Mean Difference (I-J)	Std. Error	Sig.	Interval Lower Bound	Interval Upper Bound	p-value < 0.05
1	2	-9.59500*	2.89472	0.022	-18.3256	-0.8644	TRUE
	3	-38.23938*	2.62926	0.000	-46.1694	-30.3094	TRUE
	4	-42.48071*	2.71548	0.000	-50.6708	-34.2907	TRUE
	5	-38.93278*	2.56018	0.000	-46.6544	-31.2111	TRUE
	6	-18.48250*	2.82637	0.000	-27.0070	-9.9580	TRUE
	7	-20.94583*	2.82637	0.000	-29.4703	-12.4213	TRUE
2	1	9.59500*	2.89472	0.022	0.8644	18.3256	TRUE
	3	-28.64438*	2.81399	0.000	-37.1315	-20.1572	TRUE
	4	-32.88571*	2.89472	0.000	-41.6164	-24.1551	TRUE
	5	-29.33778*	2.74956	0.000	-37.6306	-21.0449	TRUE
	6	-8.88750	2.99898	0.057	-17.9326	0.1576	FALSE
	7	-11.35083*	2.99898	0.005	-20.3959	-2.3057	TRUE
3	1	38.23938*	2.62926	0.000	30.3094	46.1694	TRUE
	2	28.64438*	2.81399	0.000	20.1572	37.1315	TRUE
	4	-4.24134	2.62926	0.674	-12.1713	3.6887	FALSE
	5	-0.69340	2.46854	1.000	-8.1387	6.7519	FALSE
	6	19.75688*	2.74362	0.000	11.4819	28.0318	TRUE
	7	17.29354*	2.74362	0.000	9.0186	25.5685	TRUE
4	1	42.48071*	2.71548	0.000	34.2907	50.6708	TRUE
	2	32.88571*	2.89472	0.000	24.1551	41.6164	TRUE
	3	4.24134	2.62926	0.674	-3.6887	12.1713	FALSE
	5	3.54794	2.56018	0.808	-4.1737	11.2696	FALSE
	6	23.99821*	2.82637	0.000	15.4737	32.5227	TRUE
	7	21.53488*	2.82637	0.000	13.0104	30.0594	TRUE
5	1	38.93278*	2.56018	0.000	31.2111	46.6544	TRUE
	2	29.33778*	2.74956	0.000	21.0449	37.6306	TRUE
	3	0.69340	2.46854	1.000	-6.7519	8.1387	FALSE
	4	-3.54794	2.56018	0.808	-11.2696	4.1737	FALSE
	6	20.45028*	2.67750	0.000	12.3748	28.5258	TRUE
	7	17.98694*	2.67750	0.000	9.9114	26.0625	TRUE
6	1	18.48250*	2.82637	0.000	9.9580	27.0070	TRUE
	2	8.88750	2.99898	0.057	-0.1576	17.9326	FALSE
	3	-19.75688*	2.74362	0.000	-28.0318	-11.4819	TRUE
	4	-23.99821*	2.82637	0.000	-32.5227	-15.4737	TRUE
	5	-20.45028*	2.67750	0.000	-28.5258	-12.3748	TRUE
	7	-2.46333	2.93306	0.980	-11.3096	6.3829	FALSE
7	1	20.94583*	2.82637	0.000	12.4213	29.4703	TRUE
	2	11.35083*	2.99898	0.005	2.3057	20.3959	TRUE
	3	-17.29354*	2.74362	0.000	-25.5685	-9.0186	TRUE
	4	-21.53488*	2.82637	0.000	-30.0594	-13.0104	TRUE
	5	-17.98694*	2.67750	0.000	-26.0625	-9.9114	TRUE
	6	2.46333	2.93306	0.980	-6.3829	11.3096	FALSE

Figure 7.30: ***Difference in means and the output from the Tukey HSD post-hoc test for single ANOVA.*** *The mean difference for each pairwise interaction was calculated and the significance (p-value) was determined. Interactions highlighted as false show that there was no significant difference between those days.*

Tests of Between-Subjects Effects

Dependent Variable:

Source	Type III Sum of Squares	df	Mean Square	F	Sig.	Partial Eta Squared	F-Crit
Corrected Model	42770.393[a]	23	1859.58	32.933	0.000	0.745	
Intercept	1200387.883	1	1200387.88	21258.597	0.000	0.988	
Day	29176.829	5	5835.37	103.343	0.000	0.666	2.249
Line	5034.610	3	1678.20	29.721	0.000	0.256	2.639
Day * Line	5619.493	15	374.63	6.635	0.000	0.278	1.705
Error	14624.694	259	56.47				
Total	1321887.580	283					
Corrected Total	57395.087	282					

a. R Squared = .745 (Adjusted R Squared = .723)

Figure 7.31: ***Two-factor ANOVA*** *shows that the F value is larger than the F-crit for comparision between days, the comparison between lines and the comparison with interaction between days and lines, therefore rejecting the hypothesis that the variance is the same within these groups.*

Descriptive Statistics

Dependent Variable: Sheet_Percentage

Day	Line	Mean	Std. Deviation	N
1	HDEL	36.67	6.79	14
	lnplnp	52.68	4.70	12
	pahpah	59.96	8.43	10
	Triple KO	52.52	8.84	8
	Total	**49.21**	**11.16**	**44**
2	HDEL	46.26	8.26	11
	lnplnp	60.88	4.90	12
	pahpah	66.99	7.56	8
	Triple KO	62.83	8.92	13
	Total	**58.91**	**10.60**	**44**
3	HDEL	74.90	8.50	16
	lnplnp	73.54	5.34	12
	pahpah	86.55	5.05	12
	Triple KO	72.36	9.77	9
	Total	**76.95**	**9.06**	**49**
4	HDEL	79.15	5.32	14
	lnplnp	82.42	2.42	12
	pahpah	79.82	8.31	7
	Triple KO	72.55	6.75	12
	Total	**78.36**	**6.70**	**45**
5	HDEL	75.60	6.84	18
	lnplnp	80.53	10.75	10
	pahpah	76.51	8.17	13
	Triple KO	65.80	7.48	15
	Total	**74.07**	**9.48**	**56**
6	HDEL	55.15	6.95	12
	lnplnp	61.37	6.13	10
	pahpah	65.99	14.01	11
	Triple KO	59.46	7.16	12
	Total	**60.33**	**9.64**	**45**

Figure 7.32: ***Two-factor ANOVA descriptive statistics*** *for each line on each day from A. thaliana germination image analysis.*

Multiple Comparisons - Tukey HSD

Dependent Sheet_Percentage

(I) Line		Mean Difference (I-J)	Std. Error	Sig.	95% Confidence Interval	
					Lower Bound	Upper Bound
HDEL	*lnplnp*	-5.4746*	1.22257	0.000	-8.6359	-2.3133
	pahpah	-10.0492*	1.26094	0.000	-13.3097	-6.7886
	Triple KO	-1.6711	1.21764	0.518	-4.8197	1.4775
lnplnp	HDEL	5.4746*	1.22257	0.000	2.3133	8.6359
	pahpah	-4.5746*	1.32516	0.004	-8.0012	-1.1480
	Triple KO	3.8035*	1.28403	0.017	0.4833	7.1237
pahpah	HDEL	10.0492*	1.26094	0.000	6.7886	13.3097
	lnplnp	4.5746*	1.32516	0.004	1.1480	8.0012
	Triple KO	8.3781*	1.32061	0.000	4.9632	11.7929
Triple KO	HDEL	1.6711	1.21764	0.518	-1.4775	4.8197
	lnplnp	-3.8035*	1.28403	0.017	-7.1237	-0.4833
	pahpah	-8.3781*	1.32061	0.000	-11.7929	-4.9632

Multiple Comparisons - Tukey HSD

Dependent Variable: Sheet_Percentage

(I) Day		Mean Difference (I-J)	Std. Error	Sig.	95% Confidence Interval	
					Lower Bound	Upper Bound
1	2	-9.7041*	1.60207	0.000	-14.3039	-5.1042
	3	-27.7476*	1.56067	0.000	-32.2286	-23.2667
	4	-29.1572*	1.59315	0.000	-33.7314	-24.5830
	5	-24.8593*	1.51382	0.000	-29.2058	-20.5129
	6	-11.1221*	1.59315	0.000	-15.6963	-6.5478
2	1	9.7041*	1.60207	0.000	5.1042	14.3039
	3	-18.0435*	1.56067	0.000	-22.5245	-13.5626
	4	-19.4531*	1.59315	0.000	-24.0273	-14.8789
	5	-15.1552*	1.51382	0.000	-19.5017	-10.8088
	6	-1.4180	1.59315	0.949	-5.9922	3.1562
3	1	27.7476*	1.56067	0.000	23.2667	32.2286
	2	18.0435*	1.56067	0.000	13.5626	22.5245
	4	-1.4095	1.55150	0.944	-5.8642	3.0451
	5	2.8883	1.46993	0.365	-1.3321	7.1087
	6	16.6256*	1.55150	0.000	12.1709	21.0802
4	1	29.1572*	1.59315	0.000	24.5830	33.7314
	2	19.4531*	1.59315	0.000	14.8789	24.0273
	3	1.4095	1.55150	0.944	-3.0451	5.8642
	5	4.2978	1.50437	0.052	-0.0215	8.6171
	6	18.0351*	1.58417	0.000	13.4867	22.5836
5	1	24.8593*	1.51382	0.000	20.5129	29.2058
	2	15.1552*	1.51382	0.000	10.8088	19.5017
	3	-2.8883	1.46993	0.365	-7.1087	1.3321
	4	-4.2978	1.50437	0.052	-8.6171	0.0215
	6	13.7373*	1.50437	0.000	9.4180	18.0566
6	1	11.1221*	1.59315	0.000	6.5478	15.6963
	2	1.4180	1.59315	0.949	-3.1562	5.9922
	3	-16.6256*	1.55150	0.000	-21.0802	-12.1709
	4	-18.0351*	1.58417	0.000	-22.5836	-13.4867
	5	-13.7373*	1.50437	0.000	-18.0566	-9.4180

Figure 7.33: ***Two factor ANOVA post-hoc Tukey analysis.*** *The upper table shows comparison of lines and the lower table shows the comparison of days.*

Multiple Comparisons - Tukey HSD (2 / 2)

Dependent Variable: Sheet_Percentage

Day	Line		Mean Difference (I-J)	Std. Error	Sig.	Interval	
						Lower Bound	Upper Bound
4	HDEL	*lnplnp*	-3.2701	2.25561	0.477	-9.3098	2.7695
		pahpah	-0.6771	2.65416	0.994	-7.7840	6.4297
		Triple KO	6.5949*	2.25561	0.028	0.5552	12.6345
	lnplnp	HDEL	3.2701	2.25561	0.477	-2.7695	9.3098
		pahpah	2.5930	2.72689	0.778	-4.7086	9.8946
		Triple KO	9.8650*	2.34075	0.001	3.5974	16.1326
	pahpah	HDEL	0.6771	2.65416	0.994	-6.4297	7.7840
		lnplnp	-2.5930	2.72689	0.778	-9.8946	4.7086
		Triple KO	7.2720	2.72689	0.051	-0.0296	14.5736
	Triple KO	HDEL	-6.5949*	2.25561	0.028	-12.6345	-0.5552
		lnplnp	-9.8650*	2.34075	0.001	-16.1326	-3.5974
		pahpah	-7.2720	2.72689	0.051	-14.5736	0.0296
5	HDEL	*lnplnp*	-4.9342	3.17760	0.414	-13.3679	3.4994
		pahpah	-0.9115	2.93244	0.989	-8.6944	6.8715
		Triple KO	9.7958*	2.81664	0.006	2.3201	17.2714
	lnplnp	HDEL	4.9342	3.17760	0.414	-3.4994	13.3679
		pahpah	4.0228	3.38882	0.638	-4.9715	13.0170
		Triple KO	14.7300*	3.28913	0.000	6.0003	23.4597
	pahpah	HDEL	0.9115	2.93244	0.989	-6.8715	8.6944
		lnplnp	-4.0228	3.38882	0.638	-13.0170	4.9715
		Triple KO	10.7072*	3.05294	0.005	2.6044	18.8100
	Triple KO	HDEL	-9.7958*	2.81664	0.006	-17.2714	-2.3201
		lnplnp	-14.7300*	3.28913	0.000	-23.4597	-6.0003
		pahpah	-10.7072*	3.05294	0.005	-18.8100	-2.6044
6	HDEL	*lnplnp*	-6.2245	3.89713	0.391	-16.6595	4.2105
		pahpah	-10.8407*	3.79928	0.033	-21.0137	-0.6677
		Triple KO	-4.3075	3.71577	0.655	-14.2569	5.6419
	lnplnp	HDEL	6.2245	3.89713	0.391	-4.2105	16.6595
		pahpah	-4.6162	3.97684	0.655	-15.2646	6.0323
		Triple KO	1.9170	3.89713	0.960	-8.5180	12.3520
	pahpah	HDEL	10.8407*	3.79928	0.033	0.6677	21.0137
		lnplnp	4.6162	3.97684	0.655	-6.0323	15.2646
		Triple KO	6.5332	3.79928	0.327	-3.6398	16.7062
	Triple KO	HDEL	4.3075	3.71577	0.655	-5.6419	14.2569
		lnplnp	-1.9170	3.89713	0.960	-12.3520	8.5180
		pahpah	-6.5332	3.79928	0.327	-16.7062	3.6398

Figure 7.34: ***Two factor ANOVA post-hoc Tukey analysis****. Shows difference in means and significance when comparing lines within each day (for days 1-3). Significance values highlighted in green show significant p-values.*

Multiple Comparisons - Tukey HSD (2 / 2)

Dependent Variable: Sheet_Percentage

Day	Line		Mean Difference (I-J)	Std. Error	Sig.	Interval Lower Bound	Interval Upper Bound
4	HDEL	*lnplnp*	-3.2701	2.25561	0.477	-9.3098	2.7695
		pahpah	-0.6771	2.65416	0.994	-7.7840	6.4297
		Triple KO	6.5949*	2.25561	0.028	0.5552	12.6345
	lnplnp	HDEL	3.2701	2.25561	0.477	-2.7695	9.3098
		pahpah	2.5930	2.72689	0.778	-4.7086	9.8946
		Triple KO	9.8650*	2.34075	0.001	3.5974	16.1326
	pahpah	HDEL	0.6771	2.65416	0.994	-6.4297	7.7840
		lnplnp	-2.5930	2.72689	0.778	-9.8946	4.7086
		Triple KO	7.2720	2.72689	0.051	-0.0296	14.5736
	Triple KO	HDEL	-6.5949*	2.25561	0.028	-12.6345	-0.5552
		lnplnp	-9.8650*	2.34075	0.001	-16.1326	-3.5974
		pahpah	-7.2720	2.72689	0.051	-14.5736	0.0296
5	HDEL	*lnplnp*	-4.9342	3.17760	0.414	-13.3679	3.4994
		pahpah	-0.9115	2.93244	0.989	-8.6944	6.8715
		Triple KO	9.7958*	2.81664	0.006	2.3201	17.2714
	lnplnp	HDEL	4.9342	3.17760	0.414	-3.4994	13.3679
		pahpah	4.0228	3.38882	0.638	-4.9715	13.0170
		Triple KO	14.7300*	3.28913	0.000	6.0003	23.4597
	pahpah	HDEL	0.9115	2.93244	0.989	-6.8715	8.6944
		lnplnp	-4.0228	3.38882	0.638	-13.0170	4.9715
		Triple KO	10.7072*	3.05294	0.005	2.6044	18.8100
	Triple KO	HDEL	-9.7958*	2.81664	0.006	-17.2714	-2.3201
		lnplnp	-14.7300*	3.28913	0.000	-23.4597	-6.0003
		pahpah	-10.7072*	3.05294	0.005	-18.8100	-2.6044
6	HDEL	*lnplnp*	-6.2245	3.89713	0.391	-16.6595	4.2105
		pahpah	-10.8407*	3.79928	0.033	-21.0137	-0.6677
		Triple KO	-4.3075	3.71577	0.655	-14.2569	5.6419
	lnplnp	HDEL	6.2245	3.89713	0.391	-4.2105	16.6595
		pahpah	-4.6162	3.97684	0.655	-15.2646	6.0323
		Triple KO	1.9170	3.89713	0.960	-8.5180	12.3520
	pahpah	HDEL	10.8407*	3.79928	0.033	0.6677	21.0137
		lnplnp	4.6162	3.97684	0.655	-6.0323	15.2646
		Triple KO	6.5332	3.79928	0.327	-3.6398	16.7062
	Triple KO	HDEL	4.3075	3.71577	0.655	-5.6419	14.2569
		lnplnp	-1.9170	3.89713	0.960	-12.3520	8.5180
		pahpah	-6.5332	3.79928	0.327	-16.7062	3.6398

Figure 7.35: ***Two factor ANOVA post-hoc Tukey analysis.*** *Shows difference in means and significance when comparing lines within each day (for days 4-6). Significance values highlighted in green show significant p-values.*

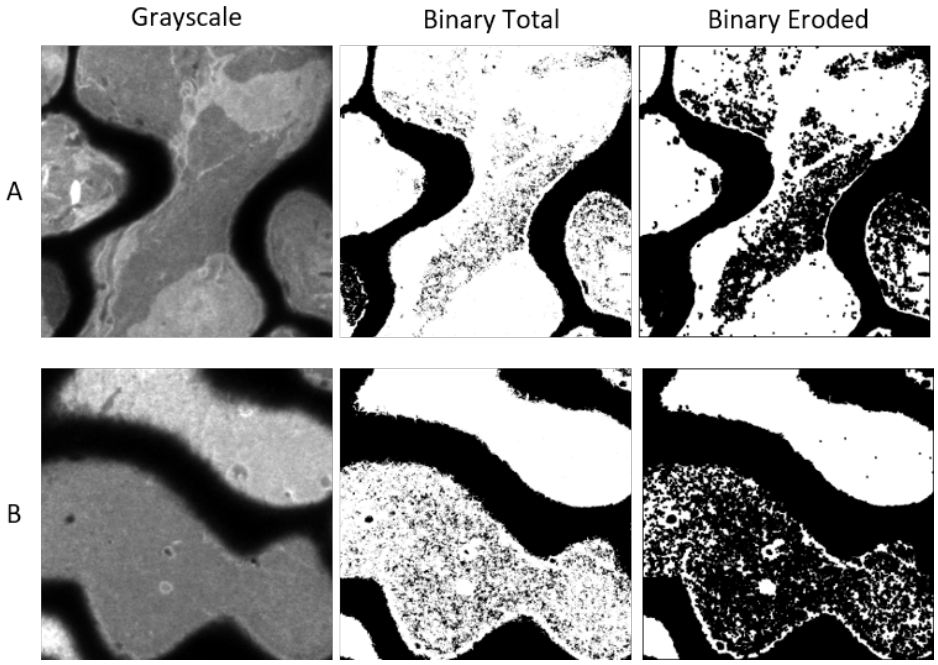

Figure 7.36: ***Example of fault when analysing large sheets with the image analysis macro.*** *These images are from the pah1pah2 mutant image analysis. The series A in figure 7.36 (appendix) resulted in 73.1% of sheet morphology, whereas human analysis would determine it as almost 100%. There is obviously some dependence on fluorescence intensity as seen in the series B of figure 7.36. The upper cell, when analysed on its own gave a value of 92.8% of sheet morphology, whereas the lower cell gave a value of 29.4% of sheet morphology. Due to this, the macro should not be used on the pah1pah2 mutant, particularly in comparison to other lines.*

	Day 2	Day 3	Day 4	Day 5	Day 6
Day 1	-8.21 (p = 0.018)	-20.87 (p = 0.000)	-29.74 (p = 0.000)	-27.86 (p = 0.000)	-8.7 (p = 0.016)
Day 2		-12.66 (p = 0.000)	-21.53 (p = 0.000)	-19.65 (p = 0.000)	-0.49 (p = 1.000)
Day 3			-8.87 (p = 0.008)	-6.99 (p = 0.089)	12.17 (p = 0.000)
Day 4				1.88 (p = 0.978)	21.04 (p = 0.000)
Day 5					19.16 (p = 0.000)

Table 7.1: ***Difference in sheet morphology mean for each day of the lnplnp mutant*** *Highlights difference between each day and the significance of the difference.*

	Day 2	Day 3	Day 4	Day 5	Day 6
Day 1	-7.03 (p = 0.545)	-26.59 (p = 0.000)	-19.87 (p = 0.000)	-16.55 (p = 0.001)	-6.03 (p = 0.619)
Day 2		-19.56 (p = 0.000)	-12.84 (p = 0.068)	-9.52 (p = 0.168)	-0.99 (p = 1.000)
Day 3			-6.73 (p = 0.594)	10.04 (p = 0.063)	20.56 (p = 0.000)
Day 4				3.31 (p = 0.965)	13.83 (p = 0.022)
Day 5					10.52 (p = 0.053)

Table 7.2: ***Difference in sheet morphology mean for each day of the pahpah mutant*** *Highlights difference between each day and the significance of the difference.*

	Day 2	Day 3	Day 4	Day 5	Day 6
Day 1	-10.31 (p = 0.064)	-19.84 (p = 0.000)	-20.03 (p = 0.000)	-13.29 (p = 0.005)	-6.94 (p = 0.423)
Day 2		-9.53 (p = 0.086)	-9.72 (p = 0.042)	-2.97 (p = 0.925)	3.37 (p = 0.902)
Day 3			-0.19 (p =1.000)	6.56 (p = 0.398)	12.9 (p = 0.007)
Day 4				6.75 (p = 0.273)	13.1 (p = 0.002)
Day 5					6.35 (p = 0.339)

Table 7.3: ***Difference in sheet morphology mean for each day of the triple reticulon knockout mutant*** *Highlights difference between each day and the significance of the difference.*

Bibliography

Andersson, M. X., Goksr, M., and Sandelius, A. S. (2007). Optical manipulation reveals strong attracting forces at membrane contact sites between endoplasmic reticulum and chloroplasts. *Journal of Biological Chemistry*, 282(2):1170–1174.

Arabidopsis Genome Initiative, T. (2000). Analysis of the genome sequence of the flowering plant arabidopsis thaliana. *Nature*, 408(6814):796–815.

Arganda-Carreras, I., Kaynig, V., Rueden, C., Schindelin, J., Cardona, A., and Seung, H. S. (2016). Trainable weka segmentation (v3.1.2). Plugin.

Baird, B. A. and Hammes, G. (1976). Chemical cross-linking studies of chloroplast coupling factor 1. *Journal of Biological Chemistry*, 251(22):6953–6962.

Bao, Y. and Howell, S. H. (2017). The unfolded protein response supports plant development and defense as well as responses to abiotic stress. *Frontiers in Plant Science*, 8:344.

Baskin, J. M. and Baskin, C. C. (2004). A classification system for seed dormancy. *Seed Science Research*, 14(1):1–16.

Bassard, J.-E., Richert, L., Geerinck, J., Renault, H., Duval, F., Ullmann, P., Schmitt, M., Meyer, E., Mutterer, J., Boerjan, W., De Jaeger, G., Mely, Y., Goossens, A., and Werck-Reichhart, D. (2012). Protein-protein and protein-membrane associations in the lignin pathway. *The Plant Cell*, 24(11):4465–4482.

Bates, P., Jewell, J., and Browse, J. (2013). Rapid separation of developing arabidopsis seeds from siliques for rna or metabolite analysis. *Plant Methods*, 9(9):1–9.

Baud, S., Boutin, J.-P., Miquel, M., Lepiniec, L., and Rochat, C. (2002). An integrated overview of seed development in arabidopsis thaliana ecotype ws. *Plant Physiology and Biochemistry*, 40(2):151 – 160.

Bendahmane, A., Querci, M., Kanyuka, K., and Baulcombe, D. C. (2000). Agrobacterium transient expression system as a tool for the isolation of disease resistance genes: application to the rx2 locus in potato. *The Plant journal : for cell and molecular biology*, 21:73–81.

Bentsink, L. and Koornneef, M. (2008). Seed dormancy and germination. *The Arabidopsis Book*, page e0119.

Bethke, P. C., Libourel, I. G., Aoyama, N., Chung, Y.-Y., Still, D. W., and Jones, R. L. (2007). The arabidopsis aleurone layer responds to nitric oxide,

gibberellin, and abscisic acid and is sufficient and necessary for seed dormancy. *Plant Physiology*, 143(3):1173–1188.

Bewley, J. D. (1997). Seed germination and dormancy. *The Plant Cell*, 9(7):1055–1066.

Bian, X., Klemm, R. W., Liu, T. Y., Zhang, M., Sun, S., Sui, X., Liu, X., Rapoport, T. A., and Hu, J. (2011). Structures of the atlastin gtpase provide insight into homotypic fusion of endoplasmic reticulum membranes. *PNAS*, 108(10):3976–3981.

Block, M. A. and Jouhet, J. (2015). Lipid trafficking at endoplasmic reticulum-chloroplast membrane contact sites. *Current Opinion in Cell Biology*, 35:21 – 29. Cell organelles.

Bouchekhima, A., Frigerio, L., and Kirkilionis, M. (2009). Geometric quantification of the the plant endoplasmic reticulum. *Journal of Microscopy*, 234(2):158–172.

Brady, J., Claridge, J., Smith, P., and Schnell, J. (2014). A conserved amphipathic helix is required for membrane tubule formation by yop1p. *PNAS*, 112(7):E639–E648.

Brandizzi, F., Irons, S. L., Johansen, J., Kotzer, A., and Neumann, U. (2004). Gfp is the way to glow: bioimaging of the plant endomembrane system. *Journal of Microscopy*, 214(2):138–158.

Breeze, E., Dzimitrowicz, N., Kriechbaumer, V., Brooks, R., Botchway, S. W., Brady, J. P., Hawes, C., Dixon, A. M., Schnell, J. R., Fricker, M. D., and Frigerio, L. (2016). A c-terminal amphipathic helix is necessary for the in vivo tubule-shaping function of a plant reticulon. *PNAS*, 113(39):10902–10907.

Bruce, J. E. (2012). In vivo protein complex topologies: Sights through a cross-linking lens. *Proteomics*, 12(10):1565–1575.

Bücherl, C. A., Bader, A., Westphal, A. H., Laptenok, S. P., and Borst, J. W. (2014). Fret-flim applications in plant systems. *Protoplasma*, 251(2):383–394.

Byrnes, L. and Sondermann, H. (2010). Structural basis for the nucleotide-dependent dimerization of the large g protein atlastin-1/spg3ay1. *PNAS*, 108(6):22162221.

Byrnes, L. J., Singh, A., Szeto, K., Benvin, N. M., O'Donnell, J. P., Zipfel, W. R., and Sondermann, H. (2013). Structural basis for conformational switching and gtp loading of the large g protein atlastin. *The EMBO Journal*, 32(3):369–384.

Calvenzani, V., Testoni, B., Gusmaroli, G., Lorenzo, M., Gnesutta, N., Petroni, K., Mantovani, R., and Tonelli, C. (2012). Interactions and ccaat-binding of arabidopsis thaliana nf-y subunits. *PLOS ONE*, 7(8):1–11.

Capron, A., Chatfield, S., Provart, N., and Berleth, T. (2009). Embryogenesis: Pattern formation from a single cell. *The Arabidopsis Book*, page e0126.

Carland, F., Fujioka, S., and Nelson, T. (2010). The sterol methyltransferases

smt1, smt2, and smt3 influence arabidopsis development through nonbrassinosteroid products. *Plant Physiology*, 153(2):741–756.

Carland, F. M., Berg, B. L., FitzGerald, J. N., Jinamornphongs, S., Nelson, T., and Keith, B. (1999). Genetic regulation of vascular tissue patterning in arabidopsis. *The Plant Cell*, 11:2123–37.

Chen, C.-N., Chu, C.-C., Zentella, R., Pan, S.-M., and David Ho, T.-H. (2002). Athva22 gene family in arabidopsis: phylogenetic relationship, aba and stress regulation, and tissue-specific expression. *Plant Molecular Biology*, 49(6):631–642.

Chen, J., Doyle, C., Qi, X., and Zheng, H. (2012a). The endoplasmic reticulum: A social network in plant cells. *Journal of Integrative Plant Biology*, 54(11):840–850.

Chen, J., Lalonde, S., Obrdlik, P., Noorani Vatani, A., Parsa, S. A., Vilarino, C., Revuelta, J. L., Frommer, W. B., and Rhee, S. Y. (2012b). Uncovering arabidopsis membrane protein interactome enriched in transporters using mating-based split ubiquitin assays and classification models. *Frontiers in Plant Science*, 3:124.

Chen, J., Stefano, G., Brandizzi, F., and Zheng, H. (2011). Arabidopsis rhd3 mediates the generation of the tubular er network and is required for golgi distribution and motility in plant cells. *Journal of cell science*, 124(13):2241–2252.

Chen, S., Desai, T., McNew, J. A., Gerard, P., Novick, P. J., and Ferro-Novick, S. (2015). Lunapark stabilizes nascent three-way junctions in the endoplasmic reticulum. *PNAS*, 112(2):418–423.

Chen, S., Novick, P., and Ferro-Novick, S. (2012c). Er network formation requires a balance of the dynamin-like gtpase sey1p and the lunapark family member lnp1p. *Nat Cell Biol*, 14(7):707–716.

Cheung, A. Y., Chen, C. Y.-h., Glaven, R. H., de Graaf, B. H. J., Vidali, L., Hepler, P. K., and Wu, H.-m. (2002). Rab2 gtpase regulates vesicle trafficking between the endoplasmic reticulum and the golgi bodies and is important to pollen tube growth. *The Plant Cell*, 14(4):945–962.

Chinchilla, D., Zipfel, C., Robatzek, S., Kemmerling, B., Nurnberger, T., Jones, J. D. G., Felix, G., and Boller, T. (2007). A flagellin-induced complex of the receptor fls2 and bak1 initiates plant defence. *Nature*, 448(7152):497–500. 10.1038/nature05999.

Consortium, A. I. M. (2011). Evidence for network evolution in an arabidopsis interactome map. *Science (New York, N.Y.)*, 333(6042):601–607.

Crawford, K. M. and Zambryski, P. C. (2000). Subcellular localization determines the availability of non-targeted proteins to plasmodesmatal transport. *Current Biology*, 10(17):1032–1040.

Cunnac, S., Wilson, A., Nuwer, J., Kirik, A., Baranage, G., and Mudgett, M. B.

(2007). A conserved carboxylesterase is a suppressor of avrbst-elicited resistance in arabidopsis. *The Plant Cell*, 19(2):688–705.

Eastmond, P. J., Quettier, A.-L., Kroon, J. T., Craddock, C., Adams, N., and Slabas, A. R. (2010). Phosphatidic acid phosphohydrolase1 and 2 regulate phospholipid synthesis at the endoplasmic reticulum in arabidopsis. *The Plant Cell*, 22(8):2796–2811.

English, A. R. and Voeltz, G. K. (2013a). Endoplasmic reticulum structure and interconnections with other organelles. *Cold Spring Harbor Perspectives in Biology*, 5(4):1–16.

English, A. R. and Voeltz, G. K. (2013b). Rab10 gtpase regulates er dynamics and morphology. *Nat Cell Biol*, 15(2):169–178. 10.1038/ncb2647.

Evans, D., Irons, S., Graumann, K., and Runions, J. (2009). *Functional Organization of the Plant Nucleus*, volume 14, chapter The plant nuclear envelope, pages 9–27. Springer-Verlag Berlin Heidelberg.

Fanata, W. I. D., Lee, S. Y., and Lee, K. O. (2013). The unfolded protein response in plants: A fundamental adaptive cellular response to internal and external stresses. *Journal of Proteomics*, 93:356 – 368. Special Issue: Translational Plant Proteomics.

Faust, J. E., Desai, T., Verma, A., Ulengin, I., Sun, T.-L., Moss, T. J., Betancourt-Solis, M. A., Huang, H. W., Lee, T., and McNew, J. A. (2015). The atlastin c-terminal tail is an amphipathic helix that perturbs the bilayer structure during endoplasmic reticulum homotypic fusion. *Journal of Biological Chemistry*, 290(8):4772–4783.

Fernandez-Calvino, L., Faulkner, C., Walshaw, J., Saalbach, G., Bayer, E., Benitez-Alfonso, Y., and Maule, A. (2011). Arabidopsis plasmodesmal proteome. *PLOS ONE*, 6(4):1–13.

Finch-Savage, W. E. and Leubner-Metzger, G. (2006). Seed dormancy and the control of germination. *New Phytologist*, 171(3):501–523.

Fricker, M. (2016). Er network analysis program (https:// markfricker.org / 77-2 / software /er-network-analysis / er-network-analysis-download/).

Fukuchi-Mizutani, M., Mizutani, M., Tanaka, Y., Kusumi, T., and Ohta, D. (1999). Microsomal electron transfer in higher plants: Cloning and heterologous expression of nadh-cytochromeb 5reductase from arabidopsis. *Plant Physiology*, 119(1):353–362.

Gao, W., Li, H. Y., Xiao, S., and Chye, M. L. (2010). Acyl-coa-binding protein 2 binds lysophospholipase 2 and lysopc to promote tolerance to cadmium-induced oxidative stress in transgenic arabidopsis. *Plant Journal*, 62(6):989–1003.

Geisler-Lee, J., O'Toole, N., Ammar, R., Provart, N. J., Millar, A. H., and Geisler, M. (2007). A predicted interactome for arabidopsis. *Plant Physiology*, 145(2):317–329.

Goldberg, R. B., De Paiva, G., Yadegari, R., et al. (1994). Plant embryogenesis: zygote to seed. *Science New York then Washington*, pages 605–605.

Gomord, V., Denmat, L.-A., Fitchette-Lain, A.-C., Satiat-Jeunemaitre, B., Hawes, C., and Faye, L. (1997). The c-terminal hdel sequence is sufficient for retention of secretory proteins in the endoplasmic reticulum (er) but promotes vacuolar targeting of proteins that escape the er. *The Plant Journal*, 11(2):313–325.

Grabski, S., de Feigter, A. W., and Schindler, M. (1993). Endoplasmic reticulum forms a dynamic continuum for lipid diffusion between contiguous soybean root cells. *The Plant Cell*, 5:25–38.

Grefen, C., Obrdlik, P., and Harter, K. (2009). *The Determination of Protein-protein Interactions by the Mating-based Split-ubiquitin system (mbSUS)*, pages 217–233. Humana Press, Totowa, NJ.

Han, C. and Yang, P. (2015). Studies on the molecular mechanisms of seed germination. *Proteomics*, 15(10):1671–1679.

Harris, N. and Chrispeels, M. (1980). The endoplasmic reticulum of mung-bean cotyledons: Quantitative morphology of cisternal and tubular er during seedling growth. *Planta*, 148(3):293–303.

Hartmann, M.-A. (1998). Plant sterols and the membrane environment. *Trends in Plant Science*, 3(5):170 – 175.

Hawes, C., Osterrieder, A., Hummel, E., and Sparkes, I. (2008). The plant ergolgi interface. *Traffic*, 9(10):1571–1580.

Hawes, C., Saint-Jore, C., Martin, B., and Zheng, H.-Q. (2001). Er confirmed as the location of mystery organelles in arabidopsis plants expressing gfp! *Trends in Plant Science*, 6(6):245 – 246.

Heazlewood, J. L., Verboom, R. E., Tonti-Filippini, J., Small, I., and Millar, A. H. (2006). Suba: the arabidopsis subcellular database. *Nucleic Acids Research*, 35(Database issue):213 – 218.

Held, M. A., Boulaflous, A., and Brandizzi, F. (2008). Advances in fluorescent protein-based imaging for the analysis of plant endomembranes. *Plant Physiology*, 147(4):1469–1481.

Heldt, H.-W. and Piechulla, B. (2011). *14 - Products of nitrate assimilation are deposited in plants as storage proteins*, pages 349–357. Academic Press, San Diego.

Holdsworth, M. J., Bentsink, L., and Soppe, W. J. J. (2008). Molecular networks regulating arabidopsis seed maturation, after-ripening, dormancy and germination. *New Phytologist*, 179(1):33–54.

Horstman, A., Nougalli Tonaco, I. A., Boutilier, K., and Immink, R. G. H. (2014). A cautionary note on the use of split-yfp/bifc in plant protein-protein interaction studies. *International Journal of Molecular Sciences*, 15(6):9628–9643.

Hu, J., Prinz, W. A., and Rapoport, T. A. (2011). Weaving the web of er tubules. *Cell*, 147(6):1226–1231.

Hu, J. and Rapoport, T. A. (2016). Fusion of the endoplasmic reticulum by membrane-bound gtpases. *Seminars in Cell & Developmental Biology*, pages – .

Hu, J., Shibata, Y., Zhu, P.-P., Voss, C., Rismanchi, N., Prinz, W. A., Rapoport, T. A., and Blackstone, C. (2009). A class of dynamin-like gtpases involved in the generation of the tubular er network. *Cell*, 138(3):549–561.

Husselstein, T., Gachotte, D., Desprez, T., Bard, M., and Benveniste, P. (1996). Transformation of saccharomyces cerevisiae with a cdna encoding a sterol c-methyltransferase from arabidopsis thaliana results in the synthesis of 24-ethyl sterols. *FEBS Letters*, 381(1):87 – 92.

Hwang, H.-H. and Gelvin, S. B. (2004). Plant proteins that interact with virb2, the agrobacterium tumefaciens pilin protein, mediate plant transformation. *The Plant Cell*, 16(11):3148–3167.

Ibl, V. and Stoger, E. (2011). The formation, function and fate of protein storage compartments in seeds. *Protoplasma*, 249(2):379–392.

Jaquinod, M., Villiers, F., Kieffer-Jaquinod, S., Hugouvieux, V., Bruley, C., Garin, J., and Bourguignon, J. (2007). A proteomics dissection of arabidopsis thaliana vacuoles isolated from cell culture. *Molecular & cellular proteomics*, 6:394–412.

Jerabek-Willemsen, M., Wienken, C. J., Braun, D., Baaske, P., and Duhr, S. (2011). Molecular interaction studies using microscale thermophoresis. *Assay and Drug Development Technologies*, 9(4):342–353.

Kim, R. J., Kim, H. J., Shim, D., and Suh, M. C. (2016). Molecular and biochemical characterizations of the monoacylglycerol lipase gene family of arabidopsis thaliana. *The Plant Journal*, 85(6):758–771.

Klockenbusch, C. and Kast, J. (2010). Optimization of formaldehyde cross-linking for protein interaction analysis of non-tagged integrin beta-1. *Journal of Biomedicine and Biotechnology*, page 13.

Koornneef, M., Bentsink, L., and Hilhorst, H. (2002). Seed dormancy and germination. *Current Opinion in Plant Biology*, 5(1):33 – 36.

Kriechbaumer, V., Botchway, S. W., Slade, S. E., Knox, K., Frigerio, L., Oparka, K. J., and Hawes, C. (2015). Reticulomics: Protein-protein interaction studies with two plasmodesmata-localised reticulon family proteins identify binding partners enriched at plasmodesmata, er and the plasma membrane. *Plant Physiology*.

Kumar, R., Wallis, J. G., Skidmore, C., and Browse, J. (2006). A mutation in arabidopsis cytochrome b5 reductase identified by high-throughput screening differentially affects hydroxylation and desaturation. *The Plant Journal*, 48(6):920–932.

Lang-Pauluzzi, I. (2000). The behaviour of the plasma membrane during plasmolysis: a study by uv microscopy. *Journal of Microscopy*, 198(3):188–198.

Laursen, T., Mller, B. L., and Bassard, J.-E. (2015). Plasticity of specialized metabolism as mediated by dynamic metabolons. *Trends in Plant Science*, 20(1):20 – 32.

Le, B. H., Cheng, C., Bui, A. Q., Wagmaister, J. A., Henry, K. F., Pelletier, J., Kwong, L., Belmonte, M., Kirkbride, R., Horvath, S., Drews, G. N., Fischer, R. L., Okamuro, J. K., Harada, J. J., and Goldberg, R. B. (2010). Global analysis of gene activity during arabidopsis seed development and identification of seed-specific transcription factors. *PNAS*, 107(18):8063–8070.

Lee, H., Sparkes, I., Gattolin, S., Dzimitrowicz, N., Roberts, L. M., Hawes, C., and Frigerio, L. (2013). An arabidopsis reticulon and the atlastin homologue rhd3-like2 act together in shaping the tubular endoplasmic reticulum. *New Phytologist*, 197(2):481–489.

Lee, J. S., Kuroha, T., Hnilova, M., Khatayevich, D., Kanaoka, M. M., McAbee, J. M., Sarikaya, M., Tamerler, C., and Torii, K. U. (2012). Direct interaction of ligandreceptor pairs specifying stomatal patterning. *Genes & Development*, 26(2):126–136.

Legland, D. and Arganda-Carreras, I. (2014). Morpholibj. GitHub.

Levy, A., Zheng, J., and Lazarowitz, S. (2015). Synaptotagmin forms er-plasma membrane junctions that are recruited to plasmodesmata for plant virus movement. *Current Biology*, 25(15):2018 – 2025.

Lewis, J. D. and Lazarowitz, S. G. (2010). Arabidopsis synaptotagmin syta regulates endocytosis and virus movement protein cell-to-cell transport. *PNAS*, 107(6):2491–2496.

Liebrand, T. W., Smit, P., Abd-El-Haliem, A., de Jonge, R., Cordewener, J. H., America, A. H., Sklenar, J., Jones, A. M., Robatzek, S., Thomma, B. P., Tameling, W. I., and Joosten, M. H. (2012). Endoplasmic reticulum-quality control chaperones facilitate the biogenesis of cf receptor-like proteins involved in pathogen resistance of tomato. *Plant Physiology*, 159(4):1819–1833.

Lin, C., Zhang, Y., Sparkes, I., and Ashwin, P. (2014). Structure and dynamics of er: Minimal networks and biophysical constraints. *Biophysical Journal*, 107(3):763–772.

Liu, T. Y., Bian, X., Sun, S., Hu, X., Klemm, R. W., Prinz, W. A., Rapoport, T. A., and Hu, J. (2012). Lipid interaction of the c terminus and association of the transmembrane segments facilitate atlastin-mediated homotypic endoplasmic reticulum fusion. *Proceedings of the National Academy of Sciences*, 109(32):E2146E2154.

Lodish, H., Berk, A., Kaiser, C. A., Krieger, M., Scott, M. P., Bretscher, A., Ploegh, H., and Matsudaira, P. (2007). *Molecular Cell Biology*. W. H. Freeman, 6th edition.

Lu, D.-P. and Christopher, D. A. (2008). Light enhances the unfolded protein response as measured by bip2 gene expression and the secretory gfp-2sc marker in arabidopsis. *Physiologia Plantarum*, 134(2):360–368.

Lu, L., Ladinsky, M. S., and Kirchhausen, T. (2009). Cisternal organization of the endoplasmic reticulum during mitosis. *Molecular Biology of the Cell*, 20(15):3471–3480.

Madsen, K., Bhatia, V., Gether, U., and Stamou, D. (2010). Bar domains, amphipathic helices and membrane-anchored proteins use the same mechanism to sense membrane curvature. *FEBS Letters*, 584(9):1848 – 1855. Frontiers in Membrane Biochemistry.

Marquze, B., Berton, F., and Seagar, M. (2000). Synaptotagmins in membrane traffic: Which vesicles do the tagmins tag? *Biochimie*, 82(5):409 – 420.

Martnez, I. M. and Chrispeels, M. J. (2003). Genomic analysis of the unfolded protein response in arabidopsis shows its connection to important cellular processes. *Plant Cell*, 15(2):561.

Mathur, J. (2007). The illuminated plant cell. *Trends in Plant Science*, 12(11):506 – 513.

Meyerowitz, E. M. (2001). Prehistory and history of arabidopsis research. *Plant Physiology*, 125(1):15–19.

Miller, K. E., Kim, Y., Huh, W.-K., and Park, H.-O. (2015). Bimolecular fluorescence complementation (bifc) analysis: advances and recent applications for genome-wide interaction studies. *Journal of molecular biology*, 427(11):2039–2055.

Möller, B., Glaß, M., Misiak, D., and Posch, S. (2016). Mitobo-a toolbox for image processing and analysis. *Journal of Open Research Software*, 4(1).

Moore, I., Diefenthal, T., Zarsky, V., Schell, J., and Palme, K. (1997). A homolog of the mammalian gtpase rab2 is present in arabidopsis and is expressed predominantly in pollen grains and?seedlings. *PNAS*, 94(2):762–767.

Moss, T. J., Andreazza, C., Verma, A., Daga, A., and McNew, J. A. (2011). Membrane fusion by the gtpase atlastin requires a conserved c-terminal cytoplasmic tail and dimerization through the middle domain. *Proceedings of the National Academy of Sciences*, 108(27):11133–11138.

Mueller, S. J. and Reski, R. (2015). Mitochondrial dynamics and the er: The plant perspective. *Frontiers in Cell and Developmental Biology*, 3:78.

Nakamura, Y., Koizumi, R., Shui, G., Shimojima, M., Wenk, M. R., Ito, T., and Ohta, H. (2009). Arabidopsis lipins mediate eukaryotic pathway of lipid metabolism and cope critically with phosphate starvation. *PNAS*, 106(49):20978–20983.

Nebenfhr, A. and Staehelin, L. (2001). Mobile factories: Golgi dynamics in plant cells. *Trends in Plant Science*, 6(4):160 – 167.

Nixon-Abell, J., Obara, C. J., Weigel, A. V., Li, D., Legant, W. R., Xu, C. S., Pasolli, H. A., Harvey, K., Hess, H. F., Betzig, E., Blackstone, C., and Lippincott-Schwartz, J. (2016). Increased spatiotemporal resolution reveals highly dynamic dense tubular matrices in the peripheral er. *Science*, 354(6311).

Nziengui, H., Bouhidel, K., Pillon, D., Der, C., Marty, F., and Schoefs, B. (2007). Reticulon-like proteins in arabidopsis thaliana: Structural organization and er localization. *FEBS letters*, 581(18):3356–3362.

Obrdlik, P., El-Bakkoury, M., Hamacher, T., Cappellaro, C., Vilarino, C., Fleischer, C., Ellerbrok, H., Kamuzinzi, R., Ledent, V., Blaudez, D., Sanders, D., Revuelta, J. L., Boles, E., Andr?, B., and Frommer, W. B. (2004). K+ channel interactions detected by a genetic system optimized for systematic studies of membrane protein interactions. *PNAS*, 101(33):12242–12247.

Oh, Y., Kim, H., Seo, S., Hwang, B., Chang, Y., Lee, J., Lee, D., Sohn, E., Lee, S., Lee, Y., and Hwang, I. (2016). Cytochrome b5 reductase 1 triggers serial reactions that lead to iron uptake in plants. *Molecular Plant*, 9(4):501 – 513.

Palade, G. (1956). The endoplasmic reticulum. *J Biophys Biochem Cytol*, 2(4):85–98.

Palade, G. E. (1965). Transmission electron micrograph of liver cells from a 3-day old rat showing extensive smooth and rough endoplasmic reticulum, and glycogen. Image made available by James D. Jamieson and the Department of Cell Biology, Yale University School of Medicine.

Patching, S. G. (2014). Surface plasmon resonance spectroscopy for characterisation of membrane proteinligand interactions and its potential for drug discovery. *Biochimica et Biophysica Acta (BBA) - Biomembranes*, 1838(1, Part A):43 – 55. Structural and biophysical characterisation of membrane protein-ligand binding.

Pereira-Leal, J. B. and Seabra, M. C. (2001). Evolution of the rab family of small gtp-binding proteins1. *Journal of Molecular Biology*, 313(4):889 – 901.

Perez-Sancho, J., Vanneste, S., Lee, E., McFarlane, H. E., Esteban del Valle, A., Valpuesta, V., Friml, J., Botella, M. A., and Rosado, A. (2015). The arabidopsis synaptotagmin1 is enriched in endoplasmic reticulum-plasma membrane contact sites and confers cellular resistance to mechanical stresses. *Plant Physiology*, 168(1):132–143.

Perin, M. S., Fried, V. A., Mignery, G. A., Jahn, R., and Sudhof, T. C. (1990). Phospholipid binding by a synaptic vesicle protein homologous to the regulatory region of protein kinase c. *Nature*, 345(6272):260.

Peterson, K. M. and Torii, K. U. (2012). Long-term, high-resolution confocal time lapse imaging of arabidopsis cotyledon epidermis during germination. *J Vis Exp*, 70(1):1–4.

Pichette, B. (2010). Color pixel counter (v1.0). Plugin.

Porter, K. R., Claude, A., and Fullam, E. F. (1945). A study of tissue culture cells bu electron microscopy: Methods and preliminary observations.

Porter, K. R. and Thompson, H. P. (1948). A particulate body associate with epithelial cells cultured from ammary carcinomas of mice of a milk-factor strain. *Journal of Experimental Medicine*, 88(1):15–24.

Powers, R. E., Wang, S., Liu, T. Y., and Rapoport, T. A. (2017). Reconstitution of the tubular endoplasmic reticulum network with purified components. *Nature*, 543(7644):257–260.

Puhka, M., Joensuu, M., Vihinen, H., Belevich, I., and Jokitalo, E. (2012). Progressive sheet-to-tubule transformation is a general mechanism for endoplasmic reticulum partitioning in dividing mammalian cells. *Molecular Biology of the Cell*, 23(13):2424–2432.

Prez-Sancho, J., Tilsner, J., Samuels, A. L., Botella, M. A., Bayer, E. M., and Rosado, A. (2016). Stitching organelles: Organization and function of specialized membrane contact sites in plants. *Trends in Cell Biology*, 26(9):705 – 717.

Qi, Y. and Katagiri, F. (2009). Purification of low-abundance arabidopsis plasma-membrane protein complexes and identification of candidate components. *The Plant Journal*, 57(5):932–944.

Radhamony, R. N., Prasad, A. M., and Srinivasan, R. (2004). T-dna insertional mutagenesis in arabidopsis: a tool for functional genomics. *Electronic Journal of Biotechnology*, 8(1).

Reddy, A. S. N. and Day, I. S. (2001). Analysis of the myosins encoded in the recently completed arabidopsis thaliana genome sequence. *Genome Biology*, 2:research0024.1–research0024.17.

Rigaut, G., Shevchenko, A., Rutz, B., Wilm, M., Mann, M., and Seraphin, B. (1999). A generic protein purification method for protein complex characterization and proteome exploration. *Nature biotechnology*, 17:1030–2.

Rismanchi, N., Soderblom, C., Stadler, J., Zhu, P.-P., and Blackstone, C. (2008). Atlastin gtpases are required for golgi apparatus and er morphogenesis. *Human Molecular Genetics*, 17(11):1591.

Roebroek, A. J., van de Velde, H. J., Van Bokhoven, A., Broers, J. L., Ramaekers, F. C., and Van de Ven, W. J. (1993). Cloning and expression of alternative transcripts of a novel neuroendocrine-specific gene and identification of its 135-kda translational product. *Journal of Biological Chemistry*, 268(18):13439–13447.

Rowland, A. A. and Voeltz, G. K. (2012). Endoplasmic reticulum-mitochondria contacts: function of the junction. *Nat Rev Mol Cell Biol*, 13(10):607–625.

Runions, J., Brach, T., Khner, S., and Hawes, C. (2006). Photoactivation of gfp reveals protein dynamics within the endoplasmic reticulum membrane. *Journal of Experimental Botany*, 57(1):43.

Rutherford, S. and Moore, I. (2002). The arabidopsis rab gtpase family: another enigma variation. *Current Opinion in Plant Biology*, 5(6):518–528.

Sandoval, C. O. and Simmen, T. (2012). Rab proteins of the endoplasmic reticulum: functions and interactors. *Biochemical Society Transactions*, 40(6):1426–1432.

Schaeffer, A., Bronner, R., Benveniste, P., and Schaller, H. (2001). The ratio of campesterol to sitosterol that modulates growth in arabidopsis is controlled by sterol methyltransferase 2;1. *The Plant Journal*, 25(6):605–615.

Schaller, H. (2003). The role of sterols in plant growth and development. *Progress in Lipid Research*, 42(3):163 – 175.

Schaller, H. (2004). New aspects of sterol biosynthesis in growth and development of higher plants. *Plant Physiology and Biochemistry*, 42(6):465 – 476.

Schiefelbein, J. W. and Somerville, C. (1990). Genetic control of root hair development in arabidopsis thaliana. *The Plant Cell*, 2(3):235–243.

Schindelin, J., Arganda-Carreras, I., Frise, E., Kaynig, V., Longair, M., Pietzsch, T., Preibisch, S., Rueden, C., Saalfeld, S., Tinevez, J.-Y., White, D. J., Hartenstein, V., Eliceiri, K., Tomancak, P., and Cardona, A. (2012). Fiji: an open-source platform for biological-image analysis. *Nat Meth*, 9(7):676–682.

Schwarz, D. S. and Blower, M. D. (2015). The endoplasmic reticulum: structure, function and response to cellular signaling. *Cellular and Molecular Life Sciences*, 73:79–94.

Schweiger, R., Soll, J., Jung, K., Heermann, R., and Schwenkert, S. (2013). Quantification of interaction strengths between chaperones and tetratricopeptide repeat domain containing membrane proteins. *Journal of Biological Chemistry*.

Sevilem, I., Miyashima, S., and Helariutta, Y. (2013). Cell-to-cell communication via plasmodesmata in vascular plants. *Cell Adhesion & Migration*, 7:27–32.

Shemesh, T., Klemm, R. W., Romano, F. B., Wang, S., Vaughan, J., Zhuang, X., Tukachinsky, H., Kozlov, M. M., and Rapoport, T. A. (2014). A model for the generation and interconversion of er morphologies. *PNAS*, 111(49):E5243–E5251.

Shewry, P. and Halford, N. (2002). Cereal seed storage proteins: structures, properties androle in grain utilization. *Journal of Experimental Botany*, 53(370):947 – 958.

Shibata, Y., Hu, J., Kozlov, M. M., and Rapoport, T. A. (2009). Mechanisms shaping the membranes of cellular organelles. *Annual Review of Cell and Developmental Biology*, 25(1):329–354.

Shibata, Y., Shemesh, T., Prinz, W. A., Palazzo, A. F., Kozlov, M. M., and Rapoport, T. A. (2010). Mechanisms determining the morphology of the peripheral er. *Cell*, 143(5):774–788.

Shibata, Y., Voeltz, G. K., and Rapoport, T. A. (2006). Rough sheets and smooth tubules. *Cell*, 126(3):435–439.

Shibata, Y., Voss, C., Rist, J. M., Hu, J., Rapoport, T. A., Prinz, W. A., and Voeltz, G. K. (2008). The reticulon and dp1/yop1p proteins form immobile oligomers in the tubular endoplasmic reticulum. *Journal of Biological Chemistry*, 283(27):18892–18904.

Shimomura, O., Johnson, F. H., and Saiga, Y. (1962). Extraction, purification and properties of aequorin, a bioluminescent protein from the luminous hydromedusan, aequorea. *Journal of Cellular and Comparative Physiology*, 59(3):223–239.

Siao, W., Wang, P., Voigt, B., Hussey, P. J., and Baluska, F. (2016). Arabidopsis syt1 maintains stability of cortical endoplasmic reticulum networks and vap27-1-enriched endoplasmic reticulumplasma membrane contact sites. *Journal of Experimental Botany*, 67(21):6161.

Sinz, A. (2006). Chemical cross-linking and mass spectrometry to map three-dimensional protein structures and proteinprotein interactions. *Mass Spectrometry Reviews*, 25(4):663–682.

Sparkes, I. (2011). Recent advances in understanding plant myosin function: Life in the fast lane. *Molecular Plant*, 4(5):805 – 812.

Sparkes, I., Hawes, C., and Frigerio, L. (2011). Frontiers: movers and shapers of the higher plant cortical endoplasmic reticulum. *Current opinion in plant biology*, 14(6):658–665.

Sparkes, I., Runions, J., Hawes, C., and Griffing, L. (2009a). Movement and remodeling of the endoplasmic reticulum in nondividing cells of tobacco leaves. *The Plant cell*, 21:3937–49.

Sparkes, I., Runions, J., Kearns, A., and Hawes, C. (2006). Rapid, transient expression of fluorescent fusion proteins in tobacco plants and generation of stably transformed plants. *Nature Protocols*, 1(4):2019–2025.

Sparkes, I., Tolley, N., Aller, I., Svozil, J., Osterrieder, A., Botchway, S., Mueller, C., Frigerio, L., and Hawes, C. (2010). Five arabidopsis reticulon isoforms share endoplasmic reticulum location, topology, and membrane-shaping properties. *The Plant Cell Online*, 22(4):1333–1343.

Sparkes, I. A., Frigerio, L., Tolley, N., and Hawes, C. (2009b). The plant endoplasmic reticulum: a cell-wide web. *Biochemical Journal*, 423(2):145–155.

Sparkes, I. A., Ketelaar, T., De Ruijter, N. C. A., and Hawes, C. (2009c). Grab a golgi: Laser trapping of golgi bodies reveals in vivo interactions with the endoplasmic reticulum. *Traffic*, 10(5):567–571.

Staehelin, L. A. (1997). The plant er: a dynamic organelle composed of a large number of discrete functional domains. *The Plant journal : for cell and molecular biology*, 11:1151–65.

Stefan, C. J., Manford, A. G., and Emr, S. D. (2013). Er–pm connections: sites of information transfer and inter-organelle communication. *Current Opinion in Cell Biology*, 25(4):434–442.

Stefano, G., Hawes, C., and Brandizzi, F. (2014a). Er – the key to the highway. *Current Opinion in Plant Biology*, 22(0):30–38.

Stefano, G., Renna, L., and Brandizzi, F. (2014b). The endoplasmic reticulum exerts control over organelle streaming during cell expansion. *Journal of Cell Science*, 127(5):947–953.

Terasaki, M., Shemesh, T., Kasthuri, N., Klemm, R. W., Schalek, R., Hayworth, K. J., Hand, A. R., Yankova, M., Huber, G., Lichtman, J. W., Rapoport, T. A., and Kozlov, M. M. (2013). Stacked endoplasmic reticulum sheets are connected by helicoidal membrane motifs. *Cell*, 154(2):285–296.

The MathWorks, I. (2017). Matlab and simulink r2017a.

Tisdale, E. J. (1999). A rab2 mutant with impaired gtpase activity stimulates vesicle formation from pre-golgi intermediates. *Molecular Biology of the Cell*, 10(6):1837–1849.

Tolley, N., Sparkes, I., Craddock, C. P., Eastmond, P. J., Runions, J., Hawes, C., and Frigerio, L. (2010). Transmembrane domain length is responsible for the ability of a plant reticulon to shape endoplasmic reticulum tubules in vivo. *The Plant Journal*, 64(3):411–418.

Tolley, N., Sparkes, I. A., Hunter, P. R., Craddock, C. P., Nuttall, J., Roberts, L. M., Hawes, C., Pedrazzini, E., and Frigerio, L. (2008). Overexpression of a plant reticulon remodels the lumen of the cortical endoplasmic reticulum but does not perturb protein transport. *Traffic*, 9(1):94–102.

Uchiyama, A., Shimada-Beltran, H., Levy, A., Zheng, J. Y., Javia, P. A., and Lazarowitz, S. G. (2014). The arabidopsis synaptotagmin syta regulates the cell-to-cell movement of diverse plant viruses. *Frontiers in Plant Science*, 5:584.

Valitova, J. N., Sulkarnayeva, A. G., and Minibayeva, F. V. (2016). Plant sterols: Diversity, biosynthesis, and physiological functions. *Biochemistry (Moscow)*, 81(8):819–834.

van de Velde, H., Roebroek, A., Senden, N., Ramaekers, F., and Van de Ven, W. (1994). Nsp-encoded reticulons, neuroendocrine proteins of a novel gene family associated with membranes of the endoplasmic reticulum. *Journal of Cell Science*, 107(9):2403–2416.

Van Leene, J., Eeckhout, D., Cannoot, B., De Winne, N., Persiau, G., Van De Slijke, E., Vercruysse, L., Dedecker, M., Verkest, A., Vandepoele, K., Martens, L., Witters, E., Gevaert, K., and De Jaeger, G. (2015). An improved toolbox to unravel the plant cellular machinery by tandem affinity purification of arabidopsis protein complexes. *Nat. Protocols*, 10(1):169–187.

Vanholme, R., Cesarino, I., Rataj, K., Xiao, Y., Sundin, L., Goeminne, G., Kim, H., Cross, J., Morreel, K., Araujo, P., Welsh, L., Haustraete, J., McClellan, C., Vanholme, B., Ralph, J., Simpson, G. G., Halpin, C., and Boerjan, W. (2013). Caffeoyl shikimate esterase (cse) is an enzyme in the lignin biosynthetic pathway in arabidopsis. *Science*, 341(6150):1103–1106.

Vernoud, V., Horton, A. C., Yang, Z., and Nielsen, E. (2003). Analysis of the small gtpase gene superfamily of arabidopsis. *Plant Physiology*, 131(3):1191–1208.

Viotti, C. (2014). Er and vacuoles: never been closer. *Frontiers in Plant Science*, 5:20.

Voeltz, G. K., Prinz, W. A., Shibata, Y., Rist, J. M., and Rapoport, T. A. (2006).

A class of membrane proteins shaping the tubular endoplasmic reticulum. *Cell*, 124(3):573–586.

Voeltz, G. K., Rolls, M. M., and Rapoport, T. A. (2002). Structural organization of the endoplasmic reticulum. *EMBO Reports*, 3(10):944–950.

Voinnet, O., Rivas, S., Mestre, P., and Baulcombe, D. (2003). Retracted: An enhanced transient expression system in plants based on suppression of gene silencing by the p19 protein of tomato bushy stunt virus. *The Plant Journal*, 33(5):949–956.

Wan, S. and Jiang, L. (2016). Endoplasmic reticulum (er) stress and the unfolded protein response (upr) in plants. *Protoplasma*, 253(3):753–764.

Wang, A., Yang, H.-C., Friedman, P., Johnson, C., and Dennis, E. (1999). A specific human lysophospholipase: cdna cloning, tissue distribution and kinetic characterization. *Biochimica et Biophysica Acta (BBA) - Molecular and Cell Biology of Lipids*, 1437(2):157 – 169.

Wang, H., Lockwood, S. K., Hoeltzel, M. F., and Schiefelbein, J. W. (1997). The root hair defective3 gene encodes an evolutionarily conserved protein with gtp-binding motifs and is required for regulated cell enlargement in arabidopsis. *Gene & Dev*, 11(6):799–811.

Wang, P., Richardson, C., Hawkins, T. J., Sparkes, I., Hawes, C., and Hussey, P. J. (2016a). Plant vap27 proteins: domain characterization, intracellular localization and role in plant development. *New Phytologist*, 210(4):1311–1326.

Wang, S., Tukachinsky, H., Romano, F. B., and Rapoport, T. A. (2016b). Cooperation of the er-shaping proteins atlastin, lunapark, and reticulons to generate a tubular membrane network. *eLife*, 5:e18605.

Wayne, L. L., Wallis, J. G., Kumar, R., Markham, J. E., and Browse, J. (2013). Cytochrome b5 reductase encoded by cbr1 is essential for a functional male gametophyte in arabidopsis. *The Plant Cell*, 25(8):3052–3066.

West, M., Zurek, N., Hoenger, A., and Voeltz, G. K. (2011). A 3d analysis of yeast er structure reveals how er domains are organized by membrane curvature. *JCB*, 193(2):333–346.

Westrate, L., Lee, J., Prinz, W., and Voeltz, G. (2015). Form follows function: The importance of endoplasmic reticulum shape. *Annual Review of Biochemistry*, 84(1):791–811. PMID: 25580528.

William J. Lucas, Byung-Kook Ham, J.-Y. K. (2009). Plasmodesmata bridging the gap between neighboring plant cells. *Trends in Cell Biology*, 19(10):495 – 503.

Winter, D., Vinegar, B., Nahal, H., Ammar, R., Wilson, G. V., and Provart, N. J. (2007). An "electronic fluorescent pictograph" browser for exploring and analyzing large-scale biological data sets. *PLoS ONE*, 2(8):1–12.

Yamazaki, T., Takata, N., Uemura, M., and Kawamura, Y. (2010). Arabidopsis synaptotagmin syt1, a type i signal-anchor protein, requires tandem c2 do-

mains for delivery to the plasma membrane. *Journal of Biological Chemistry*, 285(30):23165–23176.

Zhang, H. and Hu, J. (2016). Shaping the endoplasmic reticulum into a social network. *Trends in Cell Biology*, pages –.

Zhang, M. and Hu, J. (2013). Homotypic fusion of endoplasmic reticulum membranes in plant cells. *Frontiers in Plant Science*, 4.

Zhang, M., Wu, F., Shi, J., Zhu, Y., Zhu, Z., Gong, Q., and Hu, J. (2013). Rhd3 family of dynamin-like gtpases mediates homotypic endoplasmic reticulum fusion and is essential for arabidopsis development. *Plant Physiology*, 163(2):713–720.

Zhao, X., Alvarado, D., Rainier, S., Lemons, R., Hedera, P., Weber, C. H., Tukel, T., Apak, M., Heiman-Patterson, T., Ming, L., Bui, M., and Fink, J. K. (2001). Mutations in a newly identified gtpase gene cause autosomal dominant hereditary spastic paraplegia. *Nat Genet*, 29(3):326–331.

Zhao, Y., Zhang, T., Huo, H., Ye, Y., and Liu, Y. (2016). Lunapark is a component of a ubiquitin ligase complex localized to the endoplasmic reticulum three-way junctions. *Journal of Biological Chemistry*, 291(35):18252–18262.

Zheng, H., Kunst, L., Hawes, C., and Moore, I. (2004). A gfp-based assay reveals a role for rhd3 in transport between the endoplasmic reticulum and golgi apparatus. *The Plant Journal*, 37(3):398–414.

Zheng, H. and Staehelin, L. A. (2011). Protein storage vacuoles are transformed into lytic vacuoles in root meristematic cells of germinating seedlings by multiple, cell type-specific mechanisms. *Plant Physiology*, 155(4):2023–2035.

Zhu, X., Yu, F., Yang, Z., Liu, S., Dai, C., Lu, X., Liu, C., Yu, W., and Li, N. (2016). In planta chemical cross-linking and mass spectrometry analysis of protein structure and interaction in arabidopsis. *Proteomics*, 16(13):1915–1927.